

---

# Evolutionary Engineering of Green Fluorescent Protein Calcium Biosensors

---



Dissertation der Fakultät für Biologie  
der Ludwig-Maximilians-Universität München

vorgelegt von  
**Thomas Michael Thestrup**  
aus Kopenhagen, Dänemark  
München, den 6. Oktober 2016

Erstgutachter: PD Dr. Oliver Griesbeck  
Zweitgutachter: Prof. Dr. Christian Leibold  
Tag der mündlichen Prüfung: 27. September 2017

# Eidesstattliche Versicherung und Erklärung

Hiermit versichere ich an Eides statt, dass die vorliegende Dissertation von mir selbstständig und ohne unerlaubte Hilfe angefertigt wurde. Zudem wurden keine anderen als die angegebenen Quellen verwendet.

Außerdem versichere ich, dass die Dissertation keiner anderen Prüfungskommission vorgelegt wurde und ich mich nicht anderweitig einer Doktorprüfung ohne Erfolg unterzogen habe.

München, 29.09.2016

---

Thomas Michael Thestrup

# Table of contents

EIDESSTÄTTLICHE VERSICHERUNG UND ERKLÄRUNG .....	I
TABLE OF CONTENTS .....	II
LIST OF PUBLICATIONS .....	IV
CONTRIBUTION TO PUBLICATIONS .....	V
TABLE OF FIGURES .....	VI
ABBREVIATIONS .....	VII
SUMMARY .....	IX
ZUSAMMENFASSUNG .....	XI
CHAPTER 1 .....	1
1 GENERAL INTRODUCTION .....	2
1.1 THE ROLE OF CALCIUM IN CELL PHYSIOLOGY .....	3
1.2 CALCIUM BINDING PROTEINS .....	6
1.3 FLUORESCENT PROTEINS .....	9
1.4 GENETICALLY ENCODED CALCIUM INDICATORS .....	16
1.5 DIRECTED MOLECULAR EVOLUTION OF GENETICALLY ENCODED CALCIUM INDICATORS .....	22
1.6 RESEARCH OBJECTIVES .....	25
CHAPTER 2 .....	26
CORRELATING CALCIUM BINDING, FRET AND CONFORMATIONAL CHANGE IN THE BIOSENSOR TN-XXL .....	26
CHAPTER 3 .....	37
REAL-TIME <i>IN VIVO</i> ANALYSIS OF T CELL ACTIVATION IN THE CENTRAL NERVOUS SYSTEM USING A GENETICALLY ENCODED CALCIUM INDICATOR .....	37
CHAPTER 4 .....	45
OPTIMIZED RATIO-METRIC CALCIUM SENSORS FOR FUNCTIONAL <i>IN VIVO</i> IMAGING OF NEURONS AND T-LYMPHOCYTES .....	45
CHAPTER 5 .....	60
5 DISCUSSION .....	61
5.1 ENGINEERING MINIMAL DOMAIN TWITCH GECIS BASED ON STRUCTURE-FUNCTION STUDIES .....	61

5.2	MODIFICATION AND SCREENING OF TWITCH GECIS USING PEPTIDE LINKERS AND DIRECTED MOLECULAR EVOLUTION	63
5.3	ASSESSMENT OF SCREENING AND SELECTION METHODS	67
5.4	RECORDINGS OF NEURONAL ACTIVITY USING TWITCH GECIS	68
5.5	PERSPECTIVES FOR MINIMAL DOMAIN GECIS	74
5.6	CONCLUSION	76
<b>REFERENCES</b>		<b>77</b>
<b>APPENDIX – CHAPTER 2</b>		<b>87</b>
<b>APPENDIX – CHAPTER 3</b>		<b>94</b>
<b>APPENDIX – CHAPTER 4</b>		<b>114</b>
<b>ACKNOWLEDGEMENTS</b>		<b>132</b>
<b>CURRICULUM VITAE</b>		<b>134</b>

# List of Publications

Daten der vorliegenden Arbeit wurden in folgende Publikationen veröffentlicht oder auf den folgenden Zeitschriften eingereicht:

(The data presented in this thesis was published in, or submitted to, the following journals):

## Publications included in this thesis

Geiger A, Russo L, Gensch T, **Thestrup T**, Becker S, Hopfner KP, Griesinger C, Witte G, Griesbeck O. *Correlating calcium binding, FRET and conformational change in the biosensor TN-XXL*. **Biophys. Journal**. May 2012

Mues M, Bartholomäus I, **Thestrup T**, Griesbeck O, Wekerle H, Kawakami N, Krishnamoorthy G. *Real-time in vivo analysis of T cell activation in the central nervous system using a genetically encoded calcium indicator*. **Nature Medicine**, May 2013

**Thestrup T**, Litzlbauer J, Geiger A, Mues M, Bartholomäus I, Russo L, Griesinger C, Witte G, Chen TW, Kim D, Griesbeck O. *Optimized ratiometric calcium sensors for functional in vivo imaging of neurons and T lymphocytes*. **Nature Methods**, Jan. 2014

**Thestrup T** and Griesbeck O. *Protein-Based Calcium Sensors*. **Optical Probes in Biology**, Jan., 2015 (included as part of the General Introduction)

## Publications not included in this thesis

Y. Kovalchuk, R. Homma, Y. Liang, A. Maslyukov, M. Hermes, **T. Thestrup**, O. Griesbeck, Y. Ninkovic, L. B. Cohen and O. Garaschuk. *In vivo odorant response properties of migrating adult-born neurons in the mouse olfactory bulb*. **Nature Communications**, Feb., 2015

Litzlbauer J, Schifferer M, Ng D, Fabritius A, **Thestrup T**, Griesbeck O. *Large Scale Bacterial Colony Screening of Diversified FRET Biosensors*. **PLOS ONE**, Jun. 2015

Schnaitmann C, Haikala V, Abraham E, Oberhauser V, **Thestrup T**, Griesbeck O and Reiff DF. *Colour opponency processing in Drosophila inner photoreceptor terminals*. **Cell** (Submitted, Dec. 2016)

Mourino PT, Paulat M, **Thestrup T**, Griesbeck O, Griesinger C & Becker S. *The Structural base for FRET in a green fluorescent protein biosensor*. **Science Advances** (Submitted, Jun. 2016)

# Contribution to Publications

## Chapter 2

Geiger A, Russo L, Gensch T, **Thestrup T**, Becker S, Hopfner KP, Griesinger C, Witte G, Griesbeck O (2012). *Biophysical Journal* Volume **102** May 2401–2410

Geiger A designed and cloned the TN-XXL mutants. Geiger A and Thestrup T performed the protein expression and purification. Geiger A, Thestrup T and Witte G collected and interpreted SAXS data. Geiger A and Gensch T performed analytical ultracentrifugation. Russo L and Becker S performed NMR structure determination and interpreted results. Hopfner KP, Griesinger C and Griesbeck O designed and supervised the experiments and data analysis. Geiger A, Russo L, Griesinger C, Witte G, and Griesbeck O wrote the manuscript.

## Chapter 3

Marsilius Mues, Ingo Bartholomäus, **Thomas Thestrup**, Oliver Griesbeck, Hartmut Wekerle, Naoto Kawakami & Gurumoorthy Krishnamoorthy (2013). *Nature Medicine* **19**, 778-783

M.M. established the calcium indicator expression in T cells and performed all experiments except two-photon imaging. I.B. performed the mouse surgery and in vivo two-photon imaging. M.M. and I.B. designed experiments and analyzed data. T.T. and O.G. generated the higher-affinity calcium indicator Twitch-1. H.W., N.K. and G.K. supervised the study. M.M., G.K. and H.W. wrote the manuscript.

## Chapter 4

**Thomas Thestrup**, Julia Litzlbauer, Ingo Bartholomäus, Marsilius Mues, Luigi Russo, Hod Dana, Yuri Kovalchuk, Yajie Liang, Georgios Kalamakis, Yvonne Laukat, Stefan Becker, Gregor Witte, Anselm Geiger, Taylor Allen, Lawrence C Rome, Tsai-Wen Chen, Douglas S. Kim, Olga Garaschuk, Christian Griesinger, Oliver Griesbeck (2014). *Nature Methods* **11**, 175-182

T.T. characterized the minimal domain, cloned constructs and performed protein purifications and in vitro spectroscopic characterizations; J.L. established the bacterial colony screen and performed colony screening and further protein purifications together with T.T.; M.M. and I.B. performed in vivo imaging of T lymphocytes; L.R., S.B., Y. Laukat and C.G. performed NMR structure determination and interpreted results; T.A. and L.C.R. cloned toadfish TnC; A.G. and T.T. collected SAXS data; G.W. calculated SAXS models; H.D. performed in vivo characterization in mouse visual cortex; Y.K., Y. Liang, G.K. and O. Garaschuk planned, performed and interpreted characterization of the sensors in cortical slices in situ and mouse olfactory bulb in vivo; T.T., T.W.C., H.D. and D.S.K. planned, performed and interpreted neuronal screening results. O. Griesbeck designed experiments, supervised sensor engineering and screening and integrated results from the collaborators. T.T., H.D., C.G., O. Garaschuk and O. Griesbeck wrote the manuscript.

# Table of Figures

## CHAPTER 1

Figure 1.1: Overview of neuronal Ca <sup>2+</sup> signaling dynamics	5
Figure 1.2: Ca <sup>2+</sup> -binding and coordination in the EF-hand	7
Figure 1.3: Crystal structure of troponin C from the chicken skeletal muscle	9
Figure 1.4: Crystal structure of GFP	10
Figure 1.5: Jablonski diagram	13
Figure 1.6: Spectral overlap between donor and acceptor	15
Figure 1.7: Schematics of protein-based GECIs	17
Figure 1.8: In vitro emission spectra of ratiometric and single fluorophore GECIs	18
Figure 1.9: Protein fitness landscape	24

## CHAPTER 2

Figure 1: Fluorescence spectroscopy of single tyrosine substitutions in the calcium binding domain of TN-XXL	29
Figure 2: Hydrodynamics of TN-XXL	30
Figure 3: NMR characterization of the calcium-binding domain of TN-XXL	32
Figure 4: Fluorescence lifetime spectroscopy of TN-XXL	33
Figure 5: Temperature and pH dependency	34

## CHAPTER 3

Figure 1: Functional characterization of TN-XXL in EL4 cells	39
Figure 2: Expression and characterization of TN-XXL in primary T cells	39
Figure 3: In vivo imaging in OVA-specific T cells in the lymph node	40
Figure 4: In vivo calcium imaging in extravasated OVA-specific T cells during EAE in the spinal cord	41
Figure 5: In vivo calcium signaling in extravasated 2D2 T cells during EAE	42

## CHAPTER 4

Figure 1: Minimizing the calcium-binding domain in Twitch sensors	47
Figure 2: Structural characterization of Twitch calcium sensors	48
Figure 3: Functional screening of large FRET calcium-biosensor libraries	49
Figure 4: Use of Twitch-3 and Twitch-2B for high-resolution in vivo imaging in the mouse brain	50
Figure 5: In vivo calcium imaging of T lymphocytes with Twitch-1 and Twitch-2B	51

# Abbreviations

°C	degrees Celsius
A	adenine
AAV	adeno-associated Virus
BFP	blue fluorescent protein
BAPTA	1,2-bis-[2-aminophenoxy]ethane-N,N,N',N'-tetraacetic acid
bp	base pair
C	cytosine
Ca <sup>2+</sup>	calcium
CaM	calmodulin
CD	codon diversified
CCD	charge-coupled device
CFP	cyan fluorescent protein
cp	circular permuted
csTnC	chicken skeletal muscle troponin C
$\Delta F/F$	change in fluorescence/ ( $t_0$ ) fluorescence
$\Delta R/R$	change in ratio/ ( $t_0$ ) ratio
DMEM	dulbecco's modified eagle medium
DMSO	dimethyl sulfoxide
DNA	desoxyribonucleic acid
dNTP	deoxyribonucleotid triphosphate
ECFP	enhanced cyan fluorescent protein
EDTA	ethylenediamine tetraacetic acid
EGFP	enhanced green fluorescent protein
EGTA	ethylene glycol-bis [ $\beta$ -amino-ethyl ether] N,N,N',N'-tetraacetic acid
ER	endoplasmatic reticulum
EYFP	enhanced yellow fluorescent protein
FACS	fluorescence-activated cell sorting
FAD	flavin adenine dinucleotide
FRET	Förster/fluorescence resonance energy transfer
g	gram
G	guanine
GEC1	genetically encoded calcium sensor
GFP	green fluorescent protein
HBSS	Hanks' balanced salt solution
HEK	human embryonic kidney
hcTnC	human cardiac muscle troponin C
hsTnC	human skeletal muscle troponin C
IPTG	Isopropyl-beta-D-thiogalactopyranoside
K <sup>+</sup>	potassium
kD	kilodalton

K <sub>D</sub>	dissociation constant
LB	Luria-Bertani broth
M	molar
M13	calmodulin binding peptide
MCS	multi cloning site
Mg <sup>2+</sup>	magnesium
mOK	monomeric Kusabira orange
MOPS	3-(N-morpholino) propanesulfonic acid
mRFP	monomeric red fluorescent protein
mTnC	mouse troponin C
Na <sup>+</sup>	sodium
NADH	nicotinamide adenine dinucleotide (reduced)
NMR	nuclear magnetic resonance spectroscopy
nt	nucleotide
OD	optical density
OGB-1	oregon green BAPTA-1
PBS	phosphate buffered saline
PCR	polymerase chain reaction
pH	reverse logarithmic representation of relative H <sup>+</sup> concentration
R	ratio; donor/acceptor
RFP	red fluorescent protein
R <sub>max</sub>	ratio at maximum calcium concentration
R <sub>min</sub>	ratio at minimum calcium concentration
RT	room temperature
SAXS	single-angle X-ray scattering
SR	sarcoplasmic reticulum
T	thymine
tsTnC	toadfish ( <i>Opsanus tau</i> ) swimbladder troponin C
TnC	troponin C
VOC	voltage operated channel
wt	wild-type
YFP	yellow fluorescent protein
zTnC	zebrafish troponin C
Å	Angström

# Summary

Neurobiology continues to be one of the great frontiers in biological sciences. The number of neurons in the brain, and the complex neuronal circuits they constitute, will keep scientists trying to decipher them challenged for years to come. In the last decade, the use of genetically encoded calcium indicators (GECIs) to monitor and visualize neuronal activity has greatly advanced. Calcium imaging using GECIs has become a principal modality to elucidate neuronal coding and signaling processes. GECIs provide clear advantages over synthetic calcium dyes by enabling long-term expression and chronic imaging in targeted neurons *in vivo*. Whilst most improvements of GECIs have been primarily focusing on faster kinetics, calcium sensitivity, brightness and signal strength; less attention has been on GECIs' likely impact on cellular environments via calcium buffering. Studies have shown that long-term expression of GECIs at high intracellular concentrations can lead to pathological changes and reduced responsiveness in cells.

The objective of this dissertation was to design a new family of GECIs suitable for long-term monitoring of neuronal calcium activity. In contrast to previous optimization strategies, here a new species of calcium binding protein, troponin C from *Opsanus tau*, was used as a basis for the development of a minimal calcium-binding domain. The minimal domain was fused to brighter fluorescent proteins to generate novel GECIs with improved properties. Consequently, the novel GECIs were optimized through iterative rounds of directed molecular evolution and screening, resulting in the Twitch-family of GECIs.

In Chapter 2, we describe the structure-function relationships of a previously published FRET-based calcium indicator, the TN-XXL. The structure-function relationship in FRET-based GECIs is largely uncharacterized due to the artificial and multi-modular composition. By utilizing a combination of protein engineering, spectroscopic and biophysical analyses, we show that two of the four calcium binding sites dominate the FRET output. Furthermore, we found that local conformational changes of these sites match the kinetics of FRET change. We show that TN-XXL changes from a flexible elongated structure to a rigid globular shape upon binding calcium. The insights gained from this work formed the basis for the engineering of the FRET-based GECIs described in this work.

In Chapter 3, a newly developed minimal domain FRET-based GECI, Twitch-1<sup>CD</sup>, was introduced into auto-antigen-specific and non-auto-antigen-specific CD4<sup>+</sup> T cells. We demonstrated for the first time *in vivo* how a GECI is fully expressed in T cells, and thus

allowing for detailed recording and visualization of calcium signaling during T cell antigen-recognition.

In Chapter 4, we orchestrated the evolution of the Twitch-family of GECIs, with better signal-to-noise ratios (SNR), greater dynamic range ( $\Delta R/R$ ) and calcium kinetics. These indicators underwent rational design and directed molecular evolution, followed by bacterial plate screening and a fluorescent imaging screening assay in hippocampal neurons. The novel GECIs were subsequently applied in a series of studies, emphasizing their improvements to previous FRET-based GECIs.

# Zusammenfassung

Die Neurobiologie bringt die Wissenschaft fortlaufend an neue Grenzen. Allein die Anzahl an Neuronen und die komplexen Netzwerke, die sie formen, hat und wird Wissenschaftler noch einige Jahre vor neue Herausforderungen stellen. In der letzten Dekade hat sich die Verwendung von genetisch kodierten Calcium-Indikatoren (GECIs) zur Analyse zellulärer Calciumlevel als Methode etabliert, um neuronale Signalprozesse besser zu verstehen. GECIs bieten durch die Möglichkeit von Langzeitexpression und chronischem Imaging deutliche Vorteile gegenüber synthetischen Calcium-Farbstoffen. Während sich Verbesserungen von GECIs vorrangig auf Kinetik, Sensitivität und Signalstärke konzentrierten, wurden deren Auswirkungen auf die intrazelluläre Calciumkonzentration der Zielzellen meist vernachlässigt. Studien haben jedoch gezeigt, dass Langzeitexpression von Calmodulin-basierten GECIs oder hohe intrazelluläre Konzentrationen anderer GECIs zu pathologischen Veränderungen und reduzierten Antwortverhalten der Zellen führen - ein direkter Calcium-Puffer-Effekt durch die Indikatoren.

Das Ziel dieser Doktorarbeit war die Entwicklung und Verbesserung von GECIs für Langzeitbeobachtungen von neuronaler Calciumaktivität. Im Gegensatz zu früheren Optimierungsstrategien wurde durch die Wahl einer neuen troponin C-Variante und hellerer fluoreszenter Proteine ein neuartiger GECI mit minimaler Calcium-Bindungsdomäne, verbesserten Eigenschaften und reduziertem Puffereffekt entwickelt. Um strukturelle Eigenschaften des Calcium-Bindungsprotein (troponin C) zu verstehen, wurden die Wechselwirkungen der Calcium-Bindungsdomäne mit den fusionierten fluoreszenten Proteinen (FRET Paar) sorgfältig untersucht. Die neuen GECIs wurden folglich durch iterative Runden gerichteter molekularer Evolution und Screening optimiert, dabei entstand die Twitch-Familie von GECIs.

Kapitel 2 beschreibt die Struktur-Funktions-Beziehung eines zuvor veröffentlichten FRET-basierten Calcium-Biosensors, dem TN-XXL. Aufgrund der artifiziellen und multimodalen Beschaffenheit ist dessen Struktur-Funktions-Beziehung weitgehend unbeschrieben. Der Einsatz von Protein-Engineering, spektroskopischen und biophysikalische Analysen zeigt, dass zwei der vier calciumbindenden EF-Hände das FRET-Signal von TN-XXL dominieren und, dass lokale Konformationsänderungen dieser EF-Hände mit der Kinetik des FRET-Signals übereinstimmen. Weiter wird gezeigt, dass TN-XXL durch Bindung von Calcium von einer flexiblen, länglichen Struktur in eine starre kugelförmige Konformation wechselt. Die

Erkenntnisse dieser Arbeit bilden die Grundlage für das rationelle Engineering von FRET-basierten Biosensoren.

Kapitel 3 zeigt, wie ein neu entwickelter FRET-basierter GECI mit minimaler Domäne, Twitch-1<sup>CD</sup>, in den Auto-Antigen-spezifischen und nicht-auto-Antigen-spezifischen CD4+ T-Zellen integriert wurde. Zum ersten Mal wird hier die vollständige Expression eines GECIs in T-Zellen *in vivo* beschrieben, welche detaillierte Aufnahmen von Calcium-Signalen während der Antigen-Erkennung ermöglicht.

Kapitel 4 veranschaulicht die Evolution der Twitch-Familie von GECIs von der frühen Version aus Kapitel III zu fortschrittlicheren Indikatoren mit verbessertem Signal-Rausch-Verhältnis (SNR), höherem  $\Delta R/R$  und besserer Kinetik. Die Indikatoren aus dieser Veröffentlichung wurden rationalem Design und gerichteter molekularer Evolution mittels bakterieller- und neuronaler-Screening-Methoden unterzogen. Anschließend wurde in einer Reihe von Studien deren Verbesserung und Überlegenheit gegenüber früheren FRET-basierten GECIs gezeigt.

# CHAPTER 1

---

**General Introduction**

**Research Objectives**

# 1 General Introduction

The brain is an immensely complex organ. Today, a multitude of different scientific disciplines are focused on unravelling this complexity. Over the last few decades, fluorescence imaging has become one of the most important tools for dissecting and interpreting neurobiological processes. This is mainly due to the development of single-photon and 2-photon fluorescent microscopy techniques, as well as advanced fluorescent  $\text{Ca}^{2+}$  imaging methods that enables long-term expression and cell-specific labeling for chronic monitoring of neuronal activity. Along with the development of genetically encoded calcium indicators (GECIs), 2-photon microscopy has provided a substantial contribution to this advancement (Denk et al., 1990). To detect the fluorescence emission of *in vivo* expressed GECIs in neurons, a 2-photon microscope excites the fluorescent probes in the specimen using a laser light source. Both excitation and emission pathways are separated by optical filters, to ensure high contrast images during recording. The emitted fluorescent light from the GECI is passed through emission filters, if applicable, and collected by a photon detector, such as a CCD chip. 2-photon microscopy differs from epifluorescent and confocal microscopy by using two low-energy photons coming from deep-red or infrared excitation lasers, to excite the fluorescent probes. Lasers in this range penetrate tissues better and are far less prone to light scattering and absorption by endogenous molecules (Svoboda and Yasuda, 2006). The result is a technique that allows fluorescent imaging down to several hundreds of micrometers *in vivo* (Russell, 2011). The latest advancements and contributions to the field are super-resolution microscopy techniques such as STED (Westphal and Hell, 2005), STORM (Rust et al., 2006) and PALM (Betzig et al., 2006). These techniques, together with fluorescent probes, provide the ability to visualize cellular structures and processes with higher resolution than the diffraction limit, as originally described by Ernst Abbe in 1873 (Abbe, 1873; Neice, 2010).

With the advancement of fluorescent imaging techniques, follows an increasing demand for more sophisticated GECIs. GECIs are a class of fluorescent probes used for the non-invasive study of real-time spiking activity of individual or populations of neurons. The non-invasive nature of these probes is possible as GECIs are not loaded into specific tissues (unlike synthetic fluorescent dye counterparts), but rather are constitutively expressed by the cells of interest. GECIs are encoded by stretches of DNA, composed only of amino acids and require no external cofactors or synthetic compounds to function. In combination with

specific promoters, appropriate targeting sequences and approaches to generate transgenic animals, GECIs can be readily applied as a non-invasive method for calcium imaging.

## 1.1 The Role of Calcium in Cell Physiology

### 1.1.1 Calcium signaling

A method to decipher the complex connectivity and signaling pathways in neuronal circuits is to study the role of calcium ( $\text{Ca}^{2+}$ ).  $\text{Ca}^{2+}$  is a vital and omni-present second messenger for intracellular signaling, with regulatory functions influencing nearly every aspect of the cell cycle, such as cellular secretion, expression of genes, cell proliferation and cell death (Berridge et al., 2000). These functions are orchestrated according to the rate, amplitude and spatio-temporal distribution of intracellular  $\text{Ca}^{2+}$  concentrations.

In neurobiology, much  $\text{Ca}^{2+}$  research focus on the underlying signaling mechanisms governing neuronal function and activity in the central nervous system (CNS). Here,  $\text{Ca}^{2+}$  can trigger the release of neurotransmitters from pre-synaptic vesicles for intercellular signal propagation, alter gene up- and down-regulation in neurons, and modulate synaptic plasticity and memory consolidation at the post-synapse in spines (Frazier et al., 2017; Limbäck-Stokin et al., 2004).

$\text{Ca}^{2+}$  signaling may occur intracellularly through the release and uptake from internal stores, or extracellularly via voltage-gated  $\text{Ca}^{2+}$  channels (e.g. acetylcholine and glutamate) (Berridge et al., 2000; Kaufman and Malhotra, 2014; Orrenius et al., 2003) (Figure 1.1). Cells at steady state typically have an intracellular  $\text{Ca}^{2+}$  concentration of 50-100 nM and an extracellular concentration gradient of approximately 1mM (Yamakage and Namiki, 2002). Intracellular  $\text{Ca}^{2+}$  is stored and regulated by either the endoplasmic reticulum (ER) or sarcoplasmic reticulum (SR) organelles. The release of  $\text{Ca}^{2+}$  from ER/SR into the cytoplasm is orchestrated by various channels such as the  $\text{IP}_3\text{R}$  (inositol-1,4,5-triphosphate receptor) and RyR (ryanodine receptor) families. The sarco-endoplasmic  $\text{Ca}^{2+}$ -ATPase (SERCA) pumps the cytosolic  $\text{Ca}^{2+}$  back into the ER/SR at the expense of ATP (Lytton et al., 1992). The influx and efflux of  $\text{Ca}^{2+}$  from external and internal stores are governed by different mechanisms. For example, action potentials (APs) can trigger and release bursts of  $\text{Ca}^{2+}$  through voltage-gated  $\text{Ca}^{2+}$  channels (VGCC). The onset of APs may take as little as 3-5 ms and is followed by the slower  $\text{Ca}^{2+}$  transients, peaking 30-100 ms post AP initiation (Helmchen et al., 1997; Koester and Sakmann, 2000). The mechanism of an AP can be broken down into three phases; depolarization, repolarization and hyperpolarization. An inward current of  $\text{Na}^+$  is responsible for the depolarization phase and the slower outward  $\text{K}^+$

current initiates the repolarization phase.  $\text{Ca}^{2+}$  enters the cell through the numerous VGCCs with slow activation kinetics. Hence, the  $\text{Ca}^{2+}$  currents are only activated near the end of the depolarization phase. The incoming  $\text{Ca}^{2+}$  activates several types of  $\text{Ca}^{2+}$ -activated  $\text{K}^+$  channels, which contribute to the repolarization of the neuron, as well as the shape of the hyperpolarization phase and the after-hyperpolarization (AHP). Other channels include neurotransmitter triggered ionotropic glutamate receptors, nicotinic acetylcholine receptors (nAChR), transient receptor potential type C channels (TRPC) and N-methyl-D-aspartate receptors (NMDA) (Müller and Connor, 1991; Jaffe et al., 1992; Berridge et al., 2000; Fucile, 2004; Ramsey et al., 2006; Higley and Sabatini, 2008). Extended periods of high intracellular  $\text{Ca}^{2+}$  can be cytotoxic and may cause apoptosis.  $\text{Ca}^{2+}$  ions are therefore immediately pumped out via the plasma membrane  $\text{Ca}^{2+}$  ATPase (PMCA) or the  $\text{Na}^+/\text{Ca}^{2+}$  exchanger (NCX).  $\text{Ca}^{2+}$ -binding proteins such as parvalbumin, calretinin, troponin C (TnC) or calmodulin (CaM) act as temporary buffers both in the cytosol and cellular compartments (Grienberger and Konnerth, 2012). During  $\text{Ca}^{2+}$  propagation, the mitochondria too play an important role by rapidly taking up  $\text{Ca}^{2+}$  and slowly releasing it back into the cytosol, modifying and shaping the amplitude and duration of the  $\text{Ca}^{2+}$  signal (Berridge et al., 2000). The time scale of which these signaling processes operates under, ranges from microseconds (neurotransmitter release in synapses) to minutes and hours (gene transcription) (Berridge et al., 2003).

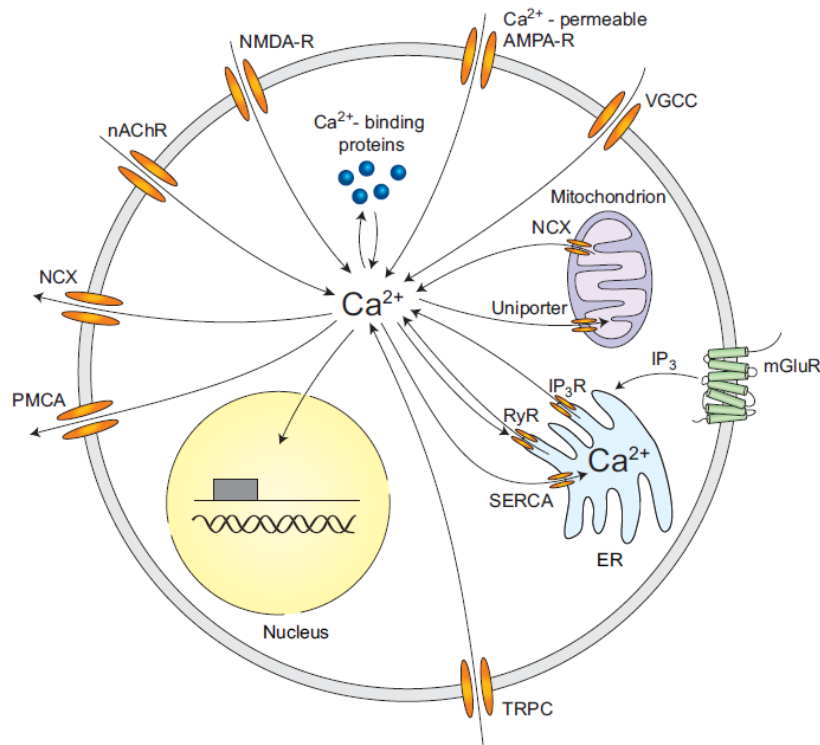


**Figure 1.1. Overview of neuronal  $\text{Ca}^{2+}$  signaling dynamics**

The  $\text{Ca}^{2+}$  concentration at any given moment is balanced by the in- and efflux of  $\text{Ca}^{2+}$  from internal and external stores, transmembrane  $\text{Ca}^{2+}$  channels and cytosolic protein  $\text{Ca}^{2+}$  buffers, such as parvalbumin, calbindin-D28k, calretinin. The  $\text{Ca}^{2+}$  in- and efflux from external stores is orchestrated by  $\text{Ca}^{2+}$ -permeable  $\alpha$ -amino-3-hydroxy-5-methyl-4-isoxazolepropionic acid (AMPA) and N-methyl-D-aspartate (NMDA) glutamate type receptors, voltage-gated  $\text{Ca}^{2+}$  channels (VGCC), nicotinic acetylcholine receptors (nAChR), and transient receptor potential type C (TRPC) channels. The  $\text{Ca}^{2+}$  release from internal stores is facilitated by inositol trisphosphate receptors (IP<sub>3</sub>R) and ryanodine receptors (RyR). Inositol trisphosphate (IP<sub>3</sub>) can be generated by the metabotropic glutamate receptors (mGluR). The plasma membrane located ATPase (PMCA), the  $\text{Na}^{+}/\text{Ca}^{2+}$  exchanger (NCX), and the sarco-/endoplasmic reticulum  $\text{Ca}^{2+}$  ATPase (SERCA) orchestrates  $\text{Ca}^{2+}$  efflux. Figure is adapted from (Grienberger and Konnerth, 2012).

## 1.2 Calcium Binding Proteins

Ca<sup>2+</sup>-binding proteins constitutes a group of proteins involved in Ca<sup>2+</sup> regulation. Their main functions are buffering, Ca<sup>2+</sup> transport and regulation of various enzymatic systems (Krebs and Heizmann, 2007). Some Ca<sup>2+</sup>-binding proteins are essential in biological processes including cell cycle progression, cell growth, cell motility, transcription and cell differentiation (Mäler et al., 2002). The translation of a Ca<sup>2+</sup>-binding event into a conformational change and downstream effect, is directly linked to the highly-conserved protein domain; the EF-hand.

### 1.2.1 The canonical EF-hands

The term “EF-hand” was first introduced in 1972 by Kretsinger and Nockolds, while trying to describe the Ca<sup>2+</sup>-binding domains AB, CD and EF of the parvalbumin protein (Kretsinger and Nockolds, 1973). Typically, an EF-hand consists of a helix-loop-helix motif encoded by approximately 30 amino acids that coordinate and bind Ca<sup>2+</sup> or magnesium (Mg<sup>2+</sup>) ions. Most commonly, the EF-hands appear in pairs, resulting in multiples of 2, 4, or 6 EF-hand domains within the same Ca<sup>2+</sup>-binding protein.

The loop region make up the ion-coordinating structure via charged amino acids. This architecture consists of 12 amino acids with 9 residues composing the loop region and 3 residues extending into the helix of the EF-hand (Figure 1.2). The loop region coordinates the metal ion through a pentagonal bipyramidal arrangement of 7 chelating ligands (Gifford et al., 2007; Lewit-Bentley and Réty, 2000). The highly conserved positions 1, 3 and 5, form the chelating groups at positions +X, +Y, +Z, respectively. The chelating position 7 (–Y) is formed by the carbonyl group in the peptide backbone. The amino acid residue at position 9 (–X) coordinates the Ca<sup>2+</sup> ion directly or via a bridged water molecule. The hydrophobic residue at position 8 (Ile, Val or Leu) plays a key role in stabilizing the EF-hand pair. This is achieved through an anti-parallel  $\beta$ -sheet composed by a corresponding hydrophobic residue in the adjacent EF-hand (Grabarek, 2006). The most conserved residue is located at position 12, where a glutamic acid acts as the –Z coordinating amino acid. The binding of Ca<sup>2+</sup> to the first EF-hand induce a structural rearrangement of the EF-hand domain, which consequently promotes binding to the second EF-hand. The nearly parallel helices in the apo-state (unbound) change conformation into perpendicular helices in the saturated (bound) state (Gifford et al., 2007). The structural interconnection of one EF-hand pair does not extend to other pair(s) in the same protein. As a consequence, EF-hand pairs often

display independent binding properties and functions (Jurado et al., 1999; Lewit-Bentley and Réty, 2000).

Certain EF-hands are capable of binding  $Mg^{2+}$  and are commonly referred to as  $Ca^{2+}/Mg^{2+}$  EF-hands (Tikunova et al., 2001; Gifford et al., 2007). One such protein where  $Mg^{2+}$  can induce a conformational change in EF-hands III and IV, is the troponin C (Filatov et al., 1999; Potter and Gergely, 1975).

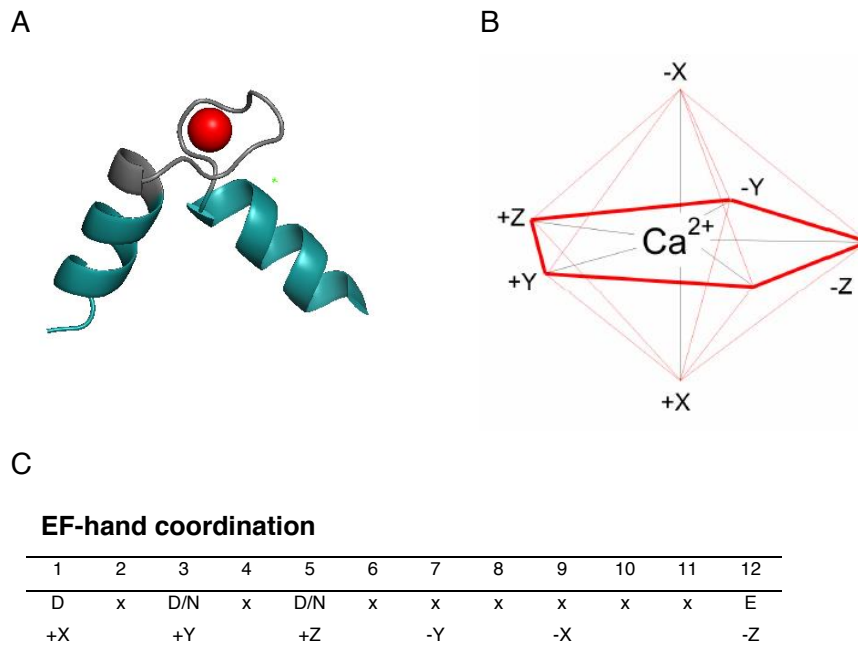


**Figure 1.2.  $Ca^{2+}$ -binding and coordination in the EF-hand**

A)  $Ca^{2+}$  ion (red sphere) coordination in EF-hand III of troponin C (modified PDB file 1TOP, PyMOL), loops in grey and sheets in cyan. B) Pentagonal bipyramid  $Ca^{2+}$  coordination geometry of the canonical EF-hand. C) Consensus sequence for the canonical EF-hand (Adapted from Bertini et al., 2003). The amino acids involved in the coordination of the  $Ca^{2+}$ -binding are located at positions depicted in B) and listed in C). Indicated by numbers are the positions in the linear sequence of the loop region and the letters represent the position in the 3-dimensional protein structure.

### 1.2.2 Troponin C and the troponin complex

Muscle contractions are governed by the proteins actin, tropomyosin and the troponin complex. The troponin complex was discovered by Ebashi and Kodama in 1965. The complex contains three subunits; troponin C (TnC) (Figure 1.3), which constitutes the  $Ca^{2+}$  sensing unit; the globular troponin I (TnI) which binds to actin and inhibits the actomyosin ATPase and; troponin T (TnT), responsible for anchoring the troponin complex to

tropomyosin (Farah and Reinach, 1995; Gordon et al., 2000). Upon muscle contraction caused by APs,  $\text{Ca}^{2+}$  is released in the cytosol of myocytes, where a conformational change in troponin C is triggered, causing the removal of the TnI inhibition of ATPase. Subsequently, ATP hydrolysis occurs and the movement of the two filaments results in muscle contraction (Gordon et al., 2000; Ohtsuki, 2007).

Troponin C is a dumbbell-shaped  $\alpha$ -helical protein (~160 residues) composed of two EF-hand binding pairs separated by a central flexible linker. The four EF-hands are designated I to IV, where I and II make up the N-terminal and III and IV constitute the C-terminal domain (Figure 1.3). EF-hands I and II bind  $\text{Ca}^{2+}$  exclusively, whereas EF-hands III and IV are occupied by either  $\text{Ca}^{2+}$  or  $\text{Mg}^{2+}$  at any given instant (Farah and Reinach, 1995; Mercier et al., 2000). The progression from unbound to bound state, occurs in sequence and in accordance with the individual affinities of the EF-hands. Accordingly, the following binding pattern arises: EF-hand III<sup>1</sup>-IV<sup>2</sup>-I<sup>3</sup>-II<sup>4</sup>. This corresponds to the binding of  $\text{Ca}^{2+}$  to the high-affinity C-terminal, which then promotes the binding of the N-terminal (Mercier et al., 2000). Owing to the high affinity for  $\text{Ca}^{2+}$ , the C-terminal exhibits a slower ion exchange rate than the N-terminal (Berchtold et al., 2000).

In vertebrates, troponin C is primarily found in two isoforms: a slow cardiac muscle troponin C (cTnC) and a fast-skeletal muscle troponin C (sTnC). The slow vertebrate cTnC contains an impaired EF-hand I. The EF-hand I has undergone an evolutionary modification, where a single residue insertion (Val28) drastically amends the EF-hand function. The modification causes the helix-loop-helix to mimic the structure of a bound-state conformation (chelated  $\text{Ca}^{2+}$ ) (Sia et al., 1997; Spyrapoulos et al., 2001). The structure of the skeletal muscle troponin C still entails a full set of functional EF-hand pairs ; both with significantly different  $\text{Ca}^{2+}$  dissociations constants ( $K_D$ ) of ~3  $\mu\text{M}$  and ~50 nM, respectively (Johnson et al., 1994).

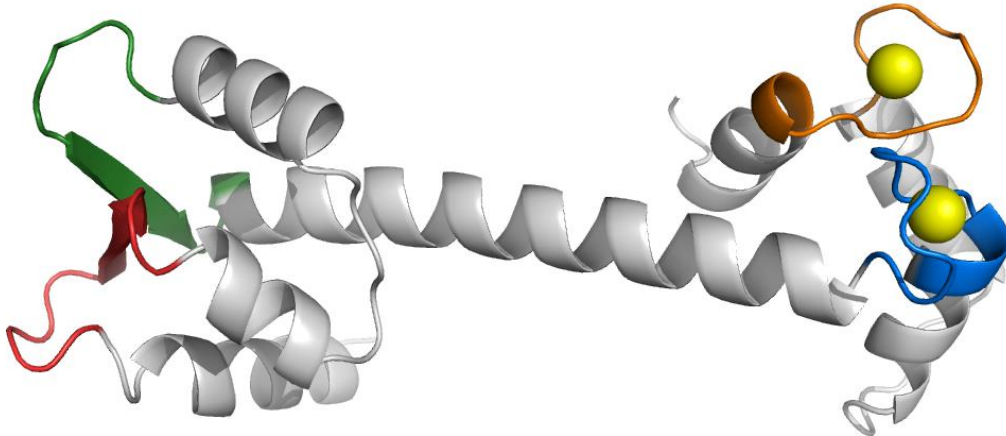


**Figure 1.3. Crystal structure of troponin C from the chicken skeletal muscle**

The structure of chicken skeletal muscle troponin C (csTnC) depicting two pairs of EF-hands located at the N- and C-terminal ends, connected via a long central  $\alpha$ -helix. The EF-hands I, II, III and IV are shown in red, green, blue and orange, respectively. Two  $\text{Ca}^{2+}$  ions (yellow) are bound to EF-hands III and IV. The structure was edited from the PDB file 1TOP using PyMOL.

## 1.3 Fluorescent Proteins

### 1.3.1 The Green Fluorescent Protein

A noteworthy milestone and the beginning of a new era in fluorescent imaging started in 1962, with the discovery of the Green Fluorescent Protein (GFP) from the jellyfish *Aequoria Victoria* (Shimomura et al., 1962). GFP was discovered as a co-factor for transduction of the blue emission of aequorin into green light via Resonance Energy Transfer (RET), a mechanism that in this case involves a non-radiative energy transfer from the bioluminescent aequorin to the GFP protein (Meer et al., 1994). The next big breakthrough came with the cloning of GFP cDNA in 1996 which allowed GFP to be structurally elucidated and used as a biological marker in cells (Yang et al., 1996).

The protein structure of GFP constitutes a distinctive cylindrical arrangement of 11  $\beta$ -sheets forming a  $\beta$ -barrel (Figure 1.4). The dimensions are 30Å in diameter and 40Å in length, with an  $\alpha$ -helix running inside the  $\beta$ -barrel forming a scaffold for the fluorophore. The unique position of the fluorophore provides an effective shielding from the molecular environment and from photochemical damage. The fluorophore constitutes three amino acids; serine65 (S65), tyrosine66 (Y66) and glycine67 (G67) (Tsien, 1998). As the only external maturation co-factor, GFP only requires molecular oxygen for the oxidation of the fluorophore. This

intrinsic property deems GFP very suitable for *in vivo* fluorescent imaging (Heim et al., 1994; Ormö et al., 1996; Reid and Flynn, 1997; Yang et al., 1996).

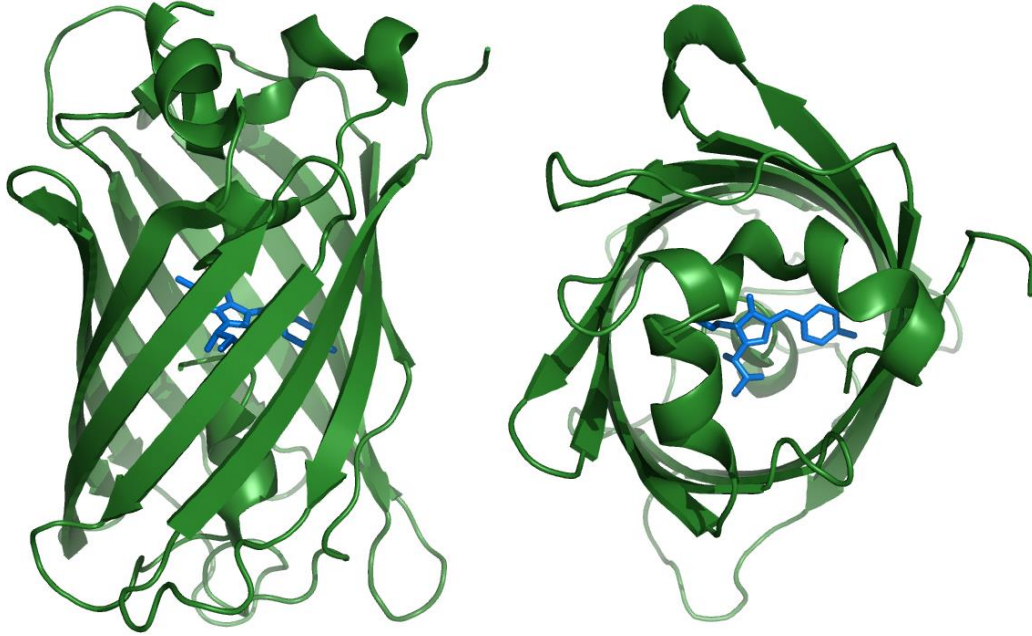


**Figure 1.4. Crystal structure of GFP**

Side view (left) and top view (right) of the  $\beta$ -barrel structure of GFP. The fluorophore is portrayed in the middle of the structure (blue). The protein residues VQCFA have been concealed to expose the fluorophore in the top view (right). The GFP structure was made using the PDB file 4KW4.

Notwithstanding the protective  $\beta$ -barrel structure, the autocatalytic folding and the maturational properties, GFP still entails very complex spectral characteristics. The fluorescence excitation spectrum of wild-type GFP shows two peaks at 395 nm and 475 nm with two emission peaks in proximity; 503 nm and 508 nm. The nature of this phenomenon matches two distinct states of the fluorophore – a protonated state, giving rise to the 395 nm peak and a deprotonated state, instigating the 475 nm peak (Jung et al., 2005; Tsien, 1998). As a consequence of solving the protein structure of GFP, researchers have been modulating and optimizing wild-type GFP in order to develop new variants with improved spectral-, brightness- and photo-stability properties (Cormack et al., 1996; Cramer et al., 1996; Heim et al., 1994). A disadvantageous folding characteristic at 37°C and the dual excitation and emission properties limited the use of GFP as a fluorescent tag. In 1996, Cormack and colleagues managed to optimize the folding at 37°C, by introducing the F64L mutation (Cormack et al., 1996). Additionally, they managed to transform the two excitation

peaks at 395 nm and 475nm, into a single peak at 488 nm, giving rise to the more stable and brighter enhanced GFP (EGFP). By mutating the Y66W residue, the excitation and emission peaks changed to 432 nm and 475 nm, respectively, to yield the cyan fluorescent protein (CFP) (Cormack et al., 1996). Subsequent engineering of the yellow fluorescent protein (YFP) occurred by the introduction of crucial mutations at S65G and T203F. The results were excitation and emission peaks of 514 nm and 527 nm (Wachter et al., 1998). Later, Griesbeck and colleagues developed Citrine, a variant of YFP, with reduced pH and Cl<sup>-</sup> sensitivity, and improved folding and photo-stability (Griesbeck et al., 2001). Iterative engineering of GFP variants led to two successful and widely applied FRET-pairs: the CFP/YFP and ECFP/Citrine (Piston and Kremers, 2007).

### 1.3.2 The Diverse Palette of Fluorescent Proteins (FPs)

As light travels through tissue, photons are likely to become scattered or absorbed, resulting in a loss of photons and ultimately a weaker signal strength (Popp et al., 2003). Absorption occurs when photons encounter molecules endogenous to tissue, with absorption properties in visible light range up to approximately 650 nm. Such endogenous molecules are hemoglobin, melanin, and metabolism related coenzymes such as FAD and NADH (Lakowicz, 2007; Zipfel et al., 2003). Even water may cause absorption of light above 1000 nm (Shcherbo et al., 2007; Shkrob et al., 2005). Correspondingly, the ideal optical range for fluorescent imaging is within the so-called “optical window” (650-1000 nm).

Multiple efforts have been made to address the implications and limitations scattering and absorption bring when imaging in tissue. Fluorescent proteins with red-shifted excitation and emission spectra, may very well be the solution to this challenge. Yet, most red-shifted FPs are dimers or tetramers by nature, limiting their applicability as fluorescent fusion tags or as part of a GECl protein backbone. Therefore, vast efforts are typically needed to optimize red fluorescent proteins. The first monomeric red FP, mRFP, was engineered from DsRed by mutating a staggering 33 residues (Campbell et al., 2002). The red emitting protein DsRed has a similar structure to GFP and originates from an *Anthozoa* species with no bioluminescence (Matz et al., 1999). Later, the well-known “fruit” series of FPs became available through the work of Shaner and colleagues, making DsRed-based FPs available in colors ranging from yellow to red (Shaner et al., 2004). Bright orange tetrameric fluorescent proteins were isolated from the coral *Fungia concinna* and were engineered into the first monomeric variant Kusabira Orange (KO) (Karasawa et al., 2004). This was followed by the fast maturing and brighter mKOK (Tsutsui et al., 2008) and finally mKO2 (Sakae-Sawano et al., 2008). The most recent contributions to the far-red and near-infrared FPs are

the spectrally distinct near-infrared iRFP670, iRFP682, iRFP702 and iRFP720 from bacterial phytochromes (Shcherbakova and Verkhusha, 2013) and a new class of FPs, from the laboratory of the now late Roger Tsien; an allophycocyanin  $\alpha$ -subunit (APC $\alpha$ ) named small ultra-red FP (smURFP) (Rodriguez et al., 2016).

### 1.3.3 Fluorescence

Fluorescence is the characteristics of a molecule to emit photons upon light absorption. The phenomenon occurs when a photon is absorbed and subsequently excites an electron in a fluorophore. Depending on the energy level of the photon, the excited electron in the low energy ground state ( $S_0$ ) will shift to an excited vibrational high energy state ( $S_1$ ,  $S_2$  or  $S_3$ ) (Figure 1.5). From the excited state, an internal energy conversion occurs causing the electron to shed energy and return to its original state ( $S_0$ ), thereby emitting a photon through radiated decay (emission). The temporal occurrence of electron conversion is also known as the fluorescence lifetime ( $T$ ,  $1-10 \times 10^{-9}$ s). Measuring the lifetime of a given fluorophore provide valuable information on the molecular environment. Factors such as ionic strength, hydrophobicity, oxygen concentration, binding of macromolecules, and the proximity of molecules can be determined. These factors can modify the lifetime of a fluorophore. Typically, the release of energy is an emission of fluorescent light: An emitted photon ( $h\nu_{EM}$ ) with lower energy and thus, a longer wavelength than of the absorbed photon ( $h\nu_{A/EX}$ ). This energy difference ( $h\nu_{A/EX} - h\nu_{EM}$ ) is referred to as the Stokes' shift (Lichtman and Conchello, 2005), which was first observed by Sir. G. G. Stokes in 1852 (Stokes, 1852). In some cases, an electron can absorb two photons, which leads to radiated decay of higher energy and thus a shorter wavelength. The Jablonski diagram below provides an illustration of the fluorescence excitation and emission process.

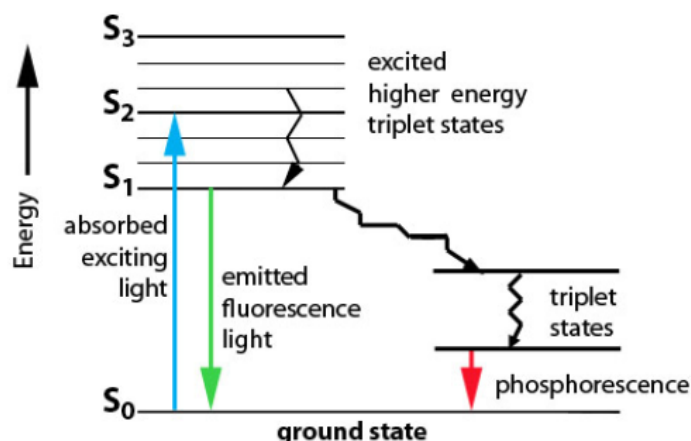


**Figure 1.5. Jablonski diagram**

A schematic illustration of an electron being excited from the ground state ( $S_0$ ) to its excited state ( $S_{1-3}$ ,  $S_n$ ). Dissipating energy causes a drop to the lower excited state ( $S_1$ ). The energy conversion takes place within nanoseconds, from photon emission to when the electron returns to its ground state ( $S_0$ ).

Besides fluorescence lifetime and the internal conversion of the electron energy state, the quantum yield ( $\Phi$ ) is a distinctive property of a fluorophore. The quantum yield is defined as the ratio between emitted and absorbed photons and can be understood as the emission efficiency of a fluorophore, Equation 1.1:

$$\Phi = \frac{hvEM \text{ (photons emitted)}}{hvA \text{ (photons absorbed)}}$$

Alternatively, it can be determined by the rate of emissive and non-emissive decay properties, Equation 1.2:

$$\Phi = \frac{\Gamma}{\Gamma + K_{ne}}$$

Where,

$r$  = rate of emissive decay [ $S^{-1}$ ]

$K_{ne}$  = rate of non-emissive decay [ $S^{-1}$ ], e.g. quenching.

Thus, if  $K_{ne}$  is smaller than  $r$ , the equation for  $\Phi$  approaches 1, which consecutively can be translated as an almost 100% conversion of all absorbed photons to emitted photons. As for

fluorescence lifetime, the environment surrounding the fluorophore can lead to a reduction of the quantum yield. This effect is known as the Quenching Phenomenon.

The most common quenching phenomena is Förster (Fluorescence) Resonance Energy Transfer (FRET) is a non-radiative transfer of the excited state energy to an acceptor molecule. Others quenching phenomena are Collisional Quenching (inactivation of the excited state by contact with other molecules) or Static Quenching (non-fluorescent complexes with other molecules). Further factors worth considering are photoisomerization, photobleaching and the molar extinction coefficient ( $\epsilon$ ).

#### **1.3.4 Fluorescence (Förster) Resonance Energy Transfer (FRET)**

The principle of FRET was first described in the middle of the 20<sup>th</sup> century by Theodor Förster, hence also referred to as Förster Resonance Energy Transfer (Förster, 1948), and was later proven experimentally by Latt et al. (1965). FRET is a phenomenon that occurs when two fluorophores are in proximity of less than 100 Å of each other. A FRET-pair constitutes a donor FP and an acceptor FP. An excited state fluorophore (donor) may transfer its energy through non-radiative means to an acceptor fluorophore that transitions into an excited state. FRET is a radiation-less energy transfer via long-range dipole-dipole interactions (Lakowicz, 2007). The FRET efficiency ( $E$ ) depends not only on the relative orientation ( $\kappa^2$ ) and distance of the two FPs, but also on the FRET-pairs' spectral overlap ( $J$ , donor emission- and acceptor absorption spectra) (Figure 1.6). Additionally, the quantum yield of the donor and the acceptor extinction coefficient and the ratio of the speed of light in a vacuum relative to the speed in the present medium (refraction index ( $n$ )), affects the FRET-efficiency. For an interesting review on genetically encoded FRET-biosensors, please refer to (Lindenburg and Merckx, 2014).

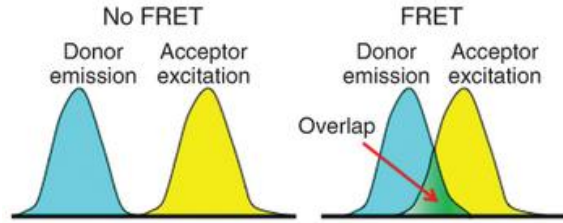


**Figure 1.6. Spectral overlap between donor and acceptor**

A representation of a donor and acceptor FRET-pair, showing the emission and excitation spectra. In the instant when the FRET-pair is within the distance threshold, the emission spectra of the donor will overlap the excitation spectra of the acceptor (shaded in green), resulting in the excitation of the acceptor FP. Adapted from (Broussard et al., 2013).

The Förster radius ( $R_0$ ) is the distance where 50% energy transfer takes place, typically in the proximity of 20-80 Å (2-8 nm), which can be used to determine a FRET-pair's suitability (Piston and Kremers, 2007; Zhang et al., 2002), Equation 1.3:

$$R_0 = 0.211 \cdot [n^{-4} \cdot k^2 \cdot \phi \cdot J]^{\frac{1}{6}}$$

For the refractive index ( $n$ ) the theoretical values of 1.4-1.5 are commonly used (Kuzmenkina et al., 2005; Vörös, 2004). For freely rotating dipoles,  $K^2$  is assumed to be  $2/3$ . The FRET-efficiency ( $E$ ) is dependent on distance (nm) between the two fluorophores ( $r$ ) and is given in Equation 1.4:

$$E = \frac{R_0^6}{R_0^6 + r^6}$$

Commonly used FRET-pairs cover a range of  $R_0$  between 40-60Å. Examples include CFP-YFP ( $R_0 = 50\text{Å}$ ), BFP-GFP and GFP-YFP ( $R_0 = 40\text{Å}$  and  $57\text{Å}$ , respectively). For non-synthetic fluorophores such as fluorescent proteins, the lower limit for  $r$  is approximately 30Å, which is determined by the shape and width of the  $\beta$ -barrel (Akrap et al., 2010; Patterson et al., 2000).

## 1.4 Genetically Encoded Calcium Indicators

*The following section is a variant of the original text written and published as the chapter “Protein-Based Calcium Sensors” (Thestrup & Griesbeck) in the book Optical Probes in Biology (Schultz et al., 2015).*

Today, GECIs pursue two different design avenues to deliver fluorescent signal output upon  $\text{Ca}^{2+}$ -binding: Single fluorescent protein indicators and FRET-based indicators, as illustrated in Figure 1.7 (Lindenburg and Merkx, 2014; Mank and Griesbeck, 2008; Zhang et al., 2002). Single fluorescent protein indicators (also referred to as single-wavelength or intensity-based indicators) often use variants of circularly permuted fluorescent proteins. The signal output comes from a manipulation of the fluorophore protonation state, through  $\text{Ca}^{2+}$ -binding induced opening and closing of a solvent channel in the FP (Baird et al., 1999; Nagai et al., 2001). For FRET-based indicators, the binding of  $\text{Ca}^{2+}$  alters the structural conformation of the indicator and thus, the donor and acceptor emission and fluorescence ratio between the two (Heim and Griesbeck, 2004; Miyawaki et al., 1997).

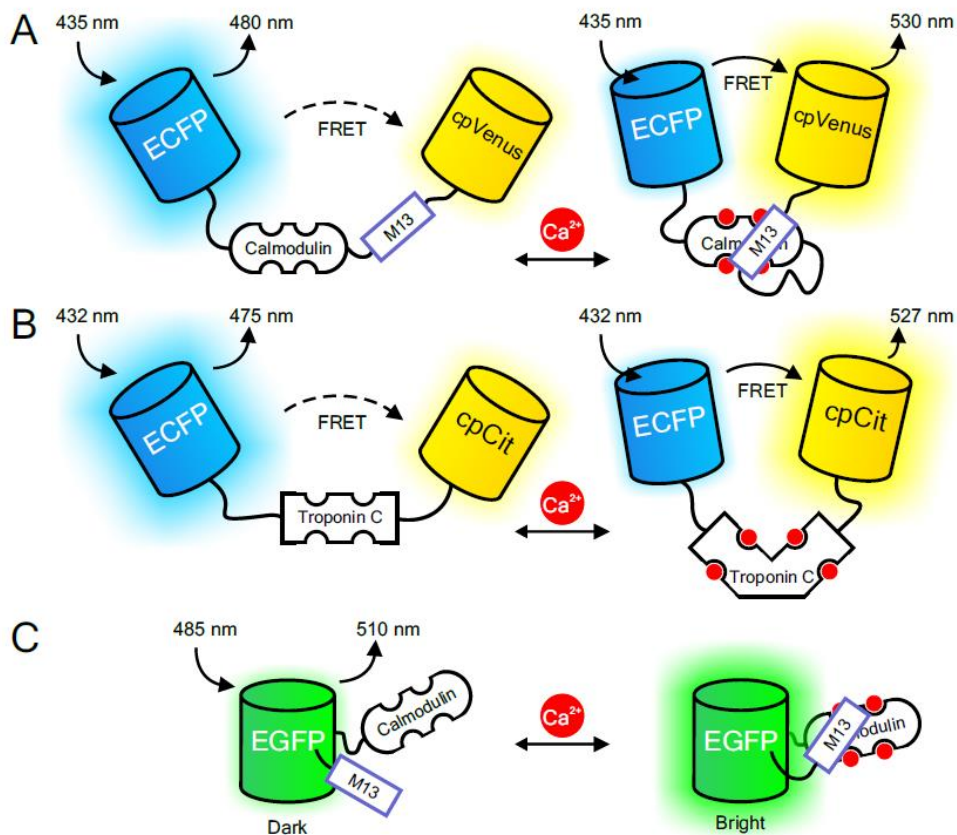


**Figure 1.7. Schematics of protein-based GECIs**

A) A schematic representation of YC3.60, a member of the Yellow Cameleons sensors. Here CaM and M13 are inserted between variants of CFP (donor) and YFP (acceptor). Binding of  $\text{Ca}^{2+}$  to CaM leads to a conformational change and formation of the CaM-M13 complex, bringing the donor and acceptor in close proximity to allow FRET (Nagai et al., 2004a). B) A different family of FRET sensors relies on conformational change of troponin C (TnC) upon  $\text{Ca}^{2+}$ -binding. In TN-XXL, two TnC C-lobes are fused together, forming the  $\text{Ca}^{2+}$  sensing domain between the ECFP and cpCitrine FRET-pair (Mank et al., 2008). C) Schematics of the GCaMP-type  $\text{Ca}^{2+}$  indicator. GCaMPs rely on the formation of the CaM-M13 complex upon  $\text{Ca}^{2+}$ -binding to increase the fluorescence intensity of a circularly permuted GFP protein (Akerboom et al., 2012).

Generally, there will not be one single multi-purpose GECI for all cell types and applications. It is therefore important that the properties of a given indicator match the physiological properties of the targeted cells or organelles. Dynamics such as resting  $\text{Ca}^{2+}$  levels, expected amplitudes of  $\text{Ca}^{2+}$  transients and time-course of  $\text{Ca}^{2+}$  fluctuations, should be considered and match with a suitable GECI.

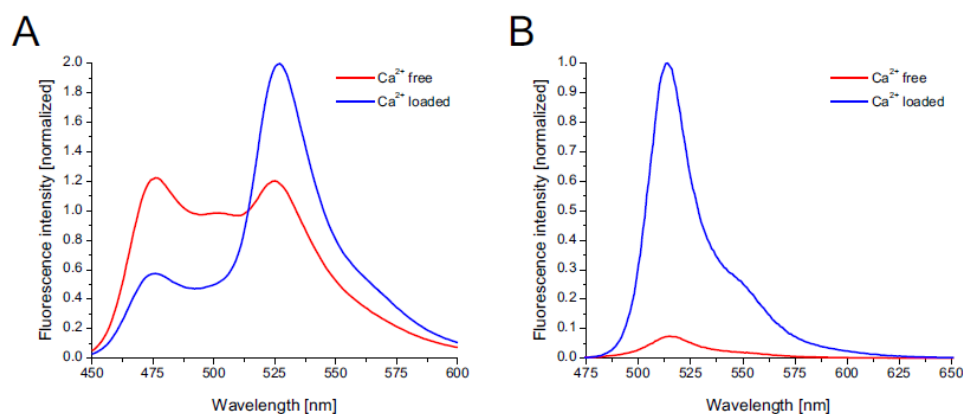


**Figure 1.8. In vitro emission spectra of ratiometric and single fluorophore GECIs**

A) Emission spectrum of the FRET-based TN-XXL at zero  $\text{Ca}^{2+}$  (red line) and at full  $\text{Ca}^{2+}$  saturation (blue line) (Ex. 432 nm). B) Emission spectrum of the single fluorophore indicator GCaMP5G with low baseline fluorescence emission in the  $\text{Ca}^{2+}$ -free state (red line) and a significant emission increase upon  $\text{Ca}^{2+}$ -binding (blue line) (data on GCaMP5G kindly provided by J. Akerboom). Purified recombinant proteins were used to obtain these spectra.

#### 1.4.1 Calmodulin-Based FRET Calcium Indicators

The very first protein-based GECI materialized in the groups of Persechini (Romoser et al., 1997) and Tsien (Miyawaki et al., 1997). FIP- $\text{CB}_{\text{SM}}$  designed by Romoser and colleagues, was based on ratiometric signal output by means of utilizing the CaM-binding sequence from smooth muscle myosin light chain kinase (smMLCK) fused between a pair of modified GFPs; BGFP and RGFP. Via the CaM-dependent modulation, orientation and distance between the donor and acceptor is altered to transmit a  $\text{Ca}^{2+}$  induced change in the emission spectrum of FIP- $\text{CB}_{\text{SM}}$ . The FRET-based Cameleons developed by Miyawaki and co-workers utilized a similar principle, while including both the synthetic M13 peptide and CaM in combination with BFP/GFP (Cameleon-1), EBFP/EGFP (Cameleon-2) and ECFP/EYFP (Yellow Cameleon-2) with enhanced responses (Miyawaki et al., 1997). The family of Yellow Cameleons (YCs) displayed superior cellular imaging properties in comparison to Cameleons-1 and 2 and stands as a great example of how iterative improvements can evolve GECIs into advance imaging tools (Miyawaki et al., 1999).

Intracellular pH changes can have a direct effect on absorbance and fluorescence. Protonated fluorophores are not capable of FRET and the effect can therefore be mistaken and interpreted as changes in  $\text{Ca}^{2+}$  concentration (Habuchi et al., 2002). To tackle the intrinsic pH sensitivity known to EYFPs, two adjacent point mutations, V68L and Q69K, were introduced. This resulted in a lowering of the pKa from 6.9 to 6.1 and consequently giving rise to YC2.1 and YC3.1. Further improvements such as increased photostability, reduced

chloride sensitivity and improved folding at 37°C originated from the evolution of YFP into “Citrine” through the Q69M mutation (Griesbeck et al., 2001). In similar attempts to improve YFP, Nagai and colleagues reported the finding of a beneficial F46L mutation, which greatly improved maturation time by accelerating the oxidation process of the fluorophore at physiological temperatures (37°C) (Nagai et al. 2002). Due to its brightness, this variant of YFP was given the name “Venus” and was incorporated in the YC2.12 construct.

From here on, the evolution of FRET-based Cameleons takes two separate directions, with the design of the noteworthy YC2.6 and YC3.6 (Nagai et al., 2004b) as well as the computationally redesigned “Design” series (Palmer et al., 2006). Palmer and co-workers utilized readily available NMR-based structural data to target six possible salt-bridge interactions between CaM and the M13 peptide (Palmer et al., 2004). This approach was undertaken to design of an indicator targeted to the ER; the Cameleon D1ER, which would require a low Ca<sup>2+</sup> sensitivity. The result was the D1ER variant with a low Ca<sup>2+</sup> affinity of K<sub>D</sub> = 60 μM. Using computational reengineering, steric bumps were introduced in CaM to create a series of circularly permuted Venus (cpV) based indicators (D2cpV, D3cpV and D4cpV) with a wide range of Ca<sup>2+</sup> affinities. D3cpV is the most widely used, providing suitable performance in reporting Ca<sup>2+</sup> transients in the cytosol and mitochondria of HeLa cells, as well as in hippocampal neurons (Palmer et al., 2006). The most recently optimized variants in the Cameleon family are a series of high-affinity (K<sub>D</sub> = 15-140 nM) indicators with alterations in the peptide linker between CaM and M13. These are known as the Yellow Cameleon-Nano or YC-Nano (Horikawa et al., 2010).

#### 1.4.2 Troponin C-Based FRET Calcium Indicators

Despite of great improvements in CaM-based indicators, the concern of cross-reactivity with the endogenous CaM signaling pathway initiated a parallel approach in GECI design based troponin C.

The first attempt came with the creation of TN-L15 (Heim and Griesbeck, 2004). The TN-L15 used a truncated version of chicken skeletal muscle troponin C (csTnC) inserted between CFP and YFP. Whilst TN-L15 lacked the ability to detect small Ca<sup>2+</sup> transients, it proved that TnC was a viable Ca<sup>2+</sup>-binding domain to generate GECIs suitable for *in vivo* imaging of neurons (Heim et al., 2007). Improvements of TnC-based indicators resulted in TN-XL (Mank et al., 2006). The TN-XL showed FRET ratio changes up to 400%, greater kinetics and high selectivity for Ca<sup>2+</sup> over Mg<sup>2+</sup>. However, the low Ca<sup>2+</sup> affinity (K<sub>D</sub> = 2.2 μM) made it less suitable for detecting small cytosolic changes in Ca<sup>2+</sup>. With TN-XXL came the next generation. The fundamental engineering principle of TN-XXL was a doubling of the

Ca<sup>2+</sup>/Mg<sup>2+</sup> sensitive C-terminal domain, while at the same time abolishing magnesium-induced conformation change. The final construct consisted of the C-terminal doubling fused between the two fluorescent proteins; ECFP and the circularly permuted Citrine variant 'Citrine cp174' (Mank et al., 2008). *In vitro* experiments with TN-XXL showed a significantly lower K<sub>D</sub> of 0.8 μM for Ca<sup>2+</sup> compared to TN-XL. *In vivo* experiments in *Drosophila melanogaster* motor neuron boutons showed promising applicability for GECIs such as TN-XXL. By using 2-photon microscopy, changes in intracellular free Ca<sup>2+</sup> could be measured with a maximal FRET ratio of 150% in the *D. melanogaster* neuromuscular junction (Mank et al., 2008). TN-XXL allowed for the first chronic imaging of neuronal response properties in mouse cortex after sensory stimulation over repeated imaging sessions spread over three weeks.

### 1.4.3 Single Fluorescent Protein Indicators

The emergence of single fluorescent protein sensors came with the discovery that large protein fragments could be inserted into sites within the β-barrel of fluorescent proteins, without destroying the folding ability of the FP. As a result, three groups of single fluorescent protein calcium indicators (or single wavelength indicators) using CaM were developed: Camgaroos, Pericams and G-CaMPs (Baird et al., 1999; Nagai et al., 2002; Nakai et al., 2001). The first successful attempt to develop a single fluorophore calcium indicator was made by introducing CaM from *Xenopus*, at the site of the residue tyrosine 145 of EYFP (Baird et al., 1999). The resulting indicator, Camgaroo-1, displayed a change in absorbance spectrum from a peak at 400 nm at zero Ca<sup>2+</sup> to 490 nm by deprotonating the YFP fluorophore at Ca<sup>2+</sup>-binding. Overall, an 8-fold increase in brightness was recorded (Baird et al., 1999; Griesbeck et al., 2001). To date, the most popular family of single wavelength GECIs, G-CAMPs, rely on a similar functional motif. The very first variants of G-CAMPs were developed by means of peptide linker manipulation and point mutations on the M13-cpGFP-CaM construct, giving rise to a series of twenty-six variants. Variants which were all screened for expression efficiency as well as Ca<sup>2+</sup> performance using ATP and charbachol (Nakai et al., 2001). The best variant "G85" (G-CaMP), showed an increase in fluorescence upon cellular stimulation with ATP and an up to 4-fold increase with addition of ionomycin (Nakai et al., 2001). The Ca<sup>2+</sup> induced change in fluorescence intensity of GCaMP arises from the interaction between Ca<sup>2+</sup> and CaM, at the C terminus of cpGFP and the N-terminal M13 peptide (Tallini et al., 2006). As with the Camgaroo indicators, G-CaMP1 suffered from poor fluorescence under physiological temperatures. Therefore, GFP-stabilizing mutations were introduced to improve the maturation of G-CaMP1. The resulting new indicator, G-

CaMP1.6, was a significant improvement, due to its increased brightness as well as being less sensitive to lower pH (Ohkura et al., 2005).

Recently, the structural and functional mechanisms of G-CaMP2 were elucidated in two subsequently published articles by (Wang et al., 2008) and (Akerboom et al., 2009). The crystal structure of G-CaMP2 in the  $\text{Ca}^{2+}$  free and  $\text{Ca}^{2+}$  bound states provided knowledge that allowed for systematic targeted mutagenesis around the crucial GFP-CaM interface and fluorophore. Improvements were achieved with respect to brightness, signal-to-noise ratio,  $\text{Ca}^{2+}$ -response kinetics and fluorescence dynamic range, giving rise to G-CaMP3. With a  $\sim 12$ -fold fluorescence change upon  $\text{Ca}^{2+}$ -binding, threefold larger than GCaMP2, and a  $\text{Ca}^{2+}$  affinity of  $K_D$  of 660 nM, the G-CaMP3 is in many ways a superior indicator compared to G-CaMP2. The increase in dynamic range results from a 2-fold decrease of fluorescence in the  $\text{Ca}^{2+}$ -free state and a 1.5-fold fluorescence increase in the  $\text{Ca}^{2+}$  saturated state (Tian et al., 2009). A series of other attempts were made to improve G-CaMP2 by, for example, introducing GFP “super-folder” mutations (Pédélecq et al., 2005) in the G-CaMP2 scaffold to create the G-CaMP-HS (Muto et al., 2011) or a more recent variant coined G-CaMP4 (Shindo et al., 2010). The engineering of GCaMP5 is a perfect illustration of how complex engineering of protein-based biosensors can be achieved. Here, crystal structures of both GCaMP2 and GCaMP3 were used to identify residues for site-directed mutagenesis at the cpGFP/CaM proto-interface. In addition, targeted library screening at the region of the M13 peptide/cpGFP and cpGFP/CaM linkers and mutations in the M13 peptide and the  $\text{Ca}^{2+}$ -binding loops were tested (Akerboom et al., 2012). The color palette of single-wavelength GECIs has also been expanded (Zhao et al., 2011). Simple error PCR of G-CaMP3 resulted in G-GECO. Incorporation of fluorophore mutations into GCaMP3, followed by random mutagenesis, produced a blue indicator, B-GECO1. Using the red fluorescent protein mApple instead of GFP as a fluorescent backbone, led to the creation of R-GECO1 (Zhao et al., 2011). Intriguingly, during the development of B-GECO1 and improved versions of GCaMP3 (G-GECO1.1 and G-GECO1.2), variants were discovered with ratiometric blue/green emission and excitation (GEM-GECO1 and GEX-GECO1, respectively) (Zhao et al., 2011). The first application attempts using GECOs *in vivo* were however, not encouraging, due to their low quantum yield and decreased dynamic range *in vivo* (Yamada and Mikoshiba, 2012). The latest addition to the GCaMP family are the GCaMP6s, m, and f (slow, medium and fast) (Chen et al., 2013; Dana et al., 2014).

## 1.5 Directed Molecular Evolution of Genetically Encoded Calcium Indicators

The late Roger Tsien won the Nobel Prize for chemistry in 2008 for his work on GFP, which led to a transformation of fluorescent imaging. In his work, directed evolution of proteins played a key role in improving fluorescent proteins in terms of emission and excitation properties, quantum yield, the multimerization state and maturation rate (Campbell et al., 2002; Shaner et al., 2004, 2008).

In nature, it has taken millions of years to evolve proteins with functions tailored to solve specific tasks in living organisms. Indeed, there are more theoretical protein structures, and functions, than atoms in the universe. It is therefore a major challenge for protein engineering to understand and design proteins that will bind a target ligand more efficiently, catalyze a reaction better, interact with other proteins in a specific manner or even outperform natural proteins. Simple trial and error methods are frequently adopted during protein optimization efforts and are in some situations considered to be the only approach to protein optimization. When dealing with theoretical combinations of amino acids ( $20^n$ ,  $n$  = number of amino acids) in a protein, it becomes paramount to exclude all residue combinations that are known to or predetermined to fail (Goldsmith and Tawfik, 2013; Khersonsky et al., 2012). Protein engineering has repeatedly shown that small changes in structure can have significant effects on function. Mutations surrounding, or even distant from the active sites, can have unforeseeable effects on protein properties (Arnold and Volkov, 1999; Romero and Arnold, 2009; Shimotohno et al., 2001).

The assumption “you get what you screen for” is important to keep in mind, as the methodology applied greatly influences the results and knowledge gained in the process. Therefore, the protein engineer must carefully choose a strategy that is both efficient in exploring the sequence space as well as being time- and cost efficient.

### 1.5.1 Strategies for Directed Molecular Evolution

Directed molecular evolution is a highly versatile strategy to modify and create novel proteins through iterative rounds of mutation, screening and selection of the fittest proteins (Farinas et al., 2001; Jäckel et al., 2008; Litzlbauer et al., 2015). In addition, the iterative rounds of screening and selection provides valuable insights into the structure-function relationship, which in turn directs the approach to the final and superior protein product (Wong et al., 2006a, 2006b; Tee and Schwaneberg, 2007).

Protein engineering starts with an objective to optimize or change the function of a parental protein. Depending on the prior structural knowledge, strategies can either take a rational, a semi-rational or a more randomized approach (Bommarius et al., 2011; Litzlbauer et al., 2015). The more preliminary knowledge available, such as the amino acid sequence, active sites, protein stability, target/ligand molecules, three-dimensional structures from SAXS, X-ray crystallography or NMR, the better the initial strategy will be. In cases where structure-function knowledge is limited, directed evolution will take a semi-rational or random approach.

In 1970, John Maynard Smith described what he referred to as the protein fitness landscape, where the evolution of a protein is described as a walk from one functional protein to another in the space of all possible sequences (Smith, 1970), (Figure 1.9). Each protein sequence is assigned a given “fitness” in the landscape, which in nature would be an organism’s chance of survival through reproduction (Wright, 1931). Under artificial laboratory conditions, the fitness of a protein will be determined by the researcher, based on the screening and selection methods, e.g. higher affinity for a substrate or survival of a cellular host organism. The fitness landscape can be explained as a mountainous landscape with peaks and valleys, with each peak representing an alternate fitness. The starting fitness is considered relative to the protein function at the beginning, which therefore can lead to many different landscapes.

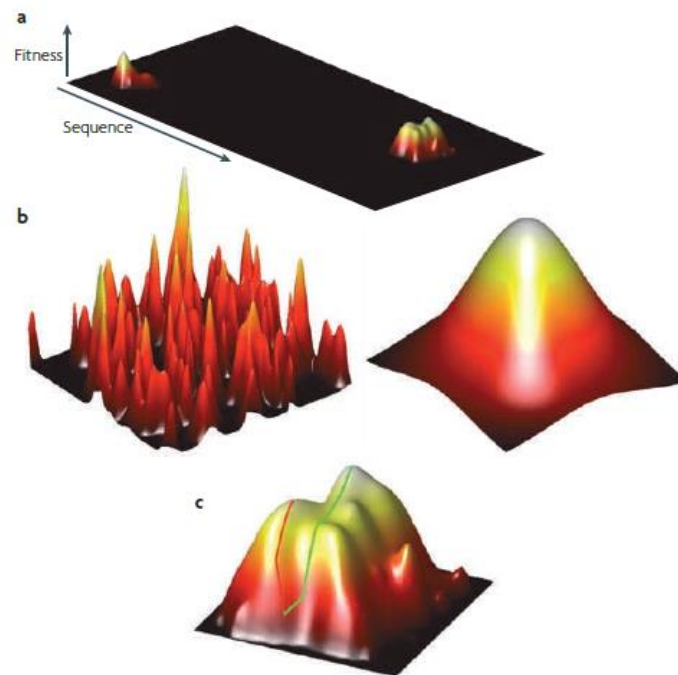


**Figure 1.9. Protein fitness landscape**

Through directed molecular evolution, the protein travels through the fitness landscape in sequence space. A) The plot of fitness against sequence represents the evolutionary landscape. The color coding of the peaks (black–red–orange–yellow) signifies increasing or decreasing fitness. Non-functional proteins are represented in black. Bright yellow are proteins with the best fitness. B) Illustration on how directed evolution moves along grids of fitness peaks differing by a single amino acid. Epistasis occurs as the effect of one mutation depends on another. This leads to randomly scattered peaks (left) or local optima (right). C) The local optima may constrain some beneficial mutations (red line), still, a great number of other paths leaves alternatives to local fitness optima (green line). Adapted from Romero and Arnold, 2009.

It is advisable to start with a parental protein which possesses desirable functionality so that incremental improvements are detectable in a screen (Zhao and Arnold, 1997; Arnold, 1998). Stable parental proteins (high thermal and solvent stability) are generally able to accept more destabilizing residue substitutions, which thus increases the likelihood of identifying beneficial mutations (Bloom et al., 2006; Martínez and Schwaneberg, 2013). On one hand, starting with a stable parental protein with a highly evolved function might also slow the process of identifying improved functionality (Jäckel et al., 2008; Martínez and Schwaneberg, 2013). On the other hand, if one anticipates significant changes in function and fitness, the optimization for novel functions or substrates might increase in rate if fitness peaks are initially lower (Leemhuis et al., 2009). Multi-homologous hybrid parental protein can also be considered. Here proteins are improved by gene recombination through methods like DNA shuffling (Coco et al., 2001; Stemmer, 1994), StEP (Zhao et al., 1998),

SCOPE (O'Maille et al., 2008) or recently by phosphorothioate-based DNA recombination (PTRec) (Marienhagen et al., 2012). A thorough overview on gene diversification can be found in the reviews of Ruff et al., 2013 and Martínez and Schwaneberg, 2013.

To find and select the fittest protein candidates, directed evolution comprises four fundamental steps: 1) Identifying the best parent sequence, 2) mutating the parent at strategic or at random sites to create a mutant library, 3) screen and identify variants with improved function and 4) repeat steps 1-3 until the desired function has been identified. Not all proteins are equally prone to evolution and the process gets more complex when evolving multi-modular proteins such as GECIs (Akerboom et al., 2012; Mank et al., 2008). The creation of mutant libraries is not trivial and is tightly interconnected with the process of screening.

## 1.6 Research Objectives

GECIs, a fluorescent modality for *in vivo* neuronal imaging, are required to bind and release  $\text{Ca}^{2+}$  with fast kinetics to resolve single or multiple APs in single or networks of neurons. They typically require a high specificity towards  $\text{Ca}^{2+}$  ions ( $K_D$ ) and should be non-toxic for constitutively expression in cells. Furthermore, buffering of internal  $\text{Ca}^{2+}$  should be at a minimum and a high signal-to-noise ratio (SNR) is required to improve imaging quality and depth. Protein engineering strategies are conceived based on known protein structures and mutations. Any improvements made should be characterized *in vitro* and *in vivo* to elucidate the improved structure-function relationship.

The objective of this dissertation was to engineer the next generation of FRET-based GECIs through means of rational protein engineering and directed molecular evolution. The next generations of GECIs should entail a novel  $\text{Ca}^{2+}$ -binding domain, with a minimum number of active EF-hands to reduce  $\text{Ca}^{2+}$  buffering, entail brighter fluorescent proteins for an improved SNR, as well as showing a broad range of  $\text{Ca}^{2+}$  affinities for a wide-ranging application. A further objective was to develop and design a functional bacterial plate-screening assay, to evaluate and characterize the thousands of new GECI variants.

# CHAPTER 2

---

## Correlating Calcium Binding, FRET and Conformational Change in the Biosensor TN-XXL

Anselm Geiger, Luigi Russo, Thomas Gensch, **Thomas Thestrup**, Stefan Becker, Karl-Peter Hopfner, Christian Griesinger, Gregor Witte, Oliver Griesbeck

*Biophysical Journal* **102**, 2401-2410 (2012)

# Correlating Calcium Binding, Förster Resonance Energy Transfer, and Conformational Change in the Biosensor TN-XXL

Anselm Geiger,<sup>†</sup> Luigi Russo,<sup>‡</sup> Thomas Gensch,<sup>§</sup> Thomas Thestrup,<sup>†</sup> Stefan Becker,<sup>‡</sup> Karl-Peter Hopfner,<sup>¶</sup> Christian Griesinger,<sup>‡</sup> Gregor Witte,<sup>¶</sup> and Oliver Griesbeck<sup>†\*</sup>

<sup>†</sup>Max-Planck-Institut für Neurobiologie, Martinsried, Germany; <sup>‡</sup>Max-Planck-Institut für biophysikalische Chemie, Göttingen, Germany;

<sup>§</sup>ICS-4, Forschungszentrum Jülich, Jülich, Germany; and <sup>¶</sup>Genzentrum und Department Biochemie, Ludwig-Maximilians-Universität, Munich, Germany

**ABSTRACT** Genetically encoded calcium indicators have become instrumental in imaging signaling in complex tissues and neuronal circuits in vivo. Despite their importance, structure-function relationships of these sensors often remain largely uncharacterized due to their artificial and multimodular composition. Here, we describe a combination of protein engineering and kinetic, spectroscopic, and biophysical analysis of the Förster resonance energy transfer (FRET)-based calcium biosensor TN-XXL. Using fluorescence spectroscopy of engineered tyrosines, we show that two of the four calcium binding EF-hands dominate the FRET output of TN-XXL and that local conformational changes of these hands match the kinetics of FRET change. Using small-angle x-ray scattering and NMR spectroscopy, we show that TN-XXL changes from a flexible elongated to a rigid globular shape upon binding calcium, thus resulting in FRET signal output. Furthermore, we compare calcium titrations using fluorescence lifetime spectroscopy with the ratiometric approach and investigate potential non-FRET effects that may affect the fluorophores. Thus, our data characterize the biophysics of TN-XXL in detail and may form a basis for further rational engineering of FRET-based biosensors.

## INTRODUCTION

Förster resonance energy transfer (FRET) between fluorescent protein variants has become a powerful method to detect protein interactions and conformational change in living cells (1–3). Unimolecular FRET is the read-out mode in a large number of biosensors that employ a donor and acceptor fluorescent protein, predominantly cyan fluorescent protein (CFP) and yellow fluorescent protein (YFP) or improved derivatives thereof (4–6). Genetically encoded calcium indicators (GECIs) enable observation of intracellular signaling in multicellular tissues and neuronal activity in living organisms (7,8). The currently available GECIs can be subdivided into single-wavelength indicators like the GCaMPs (9) and GECOs (10) on the one hand and dual-wavelength indicators based on FRET on the other hand. There has been a strong interest in the continuous improvement of these types of sensors in terms of sensitivity, kinetics, and biocompatibility. The prototypical FRET-based Cameleons (11,12) and the subsequent derivatives YC3.6 (13) or Cameleon-Nano (14) employ calmodulin (CaM) and a CaM-binding peptide such as M13 from myosin light-chain kinase as calcium-dependent interaction domains. Sensors with redesigned interaction interfaces between CaM and its binding peptide have been generated (15). To avoid perturbation of CaM-dependent signal networks inside cells, and to simplify sensor design, Troponin C (TnC) has been used to replace CaM/M13 within biosensors (16). TnC is a calcium-binding protein

specialized in regulating muscle contraction, with no other known signaling function. Ca<sup>2+</sup> binding to chicken skeletal muscle TnC has been extensively studied by exploiting endogenous aromatic amino acid fluorescence (17–19). The protein consists of an N-terminal regulatory lobe with two sites that bind calcium specifically with lower affinity and a C-terminal structural lobe with another two sites that bind calcium with high affinity and also bind magnesium (20). Structural changes in TnC have been followed by circular dichroism spectroscopy (21), NMR (22,23), x-ray scattering (24), and crystallography (25). TnC-based calcium biosensors were subsequently further engineered to abolish magnesium binding and to enhance FRET change by incorporation of a circular permutation of the acceptor fluorescent protein Citrine (26). The latest signal-optimized variant, TN-XXL, arose from domain rearrangement, by which two copies of the C-terminal lobe of chicken skeletal TnC were linked to each other and sandwiched between CFP and cpCitrine (27). This procedure abolished the N-terminal lobe of TnC completely and served as a first step away from the use of naturally occurring calcium-binding proteins to a more synthetic, biocompatible sensor architecture. As a better understanding of sensor biophysics may serve as a basis for further rational improvements of sensor design and performance, we here set out to characterize TN-XXL function in more detail. Our results depict the biophysical parameters of TN-XXL function, give insight into how the initial calcium binding to TN-XXL results in FRET output, and pinpoint optimization potential for further rational sensor engineering.

Submitted January 9, 2012, and accepted for publication March 27, 2012.

\*Correspondence: griesbeck@neuro.mpg.de

Editor: David Yue.

© 2012 by the Biophysical Society  
0006-3495/12/05/2401/10 \$2.00

doi: 10.1016/j.bpj.2012.03.065

## MATERIALS AND METHODS

### Gene construction

TN-XXL and its “Amber” variants were cloned into pRSETB vector (Invitrogen, Carlsbad, CA) using flanking *Bam*HI/*Eco*RI restriction sites. As constructs for tyrosine fluorescence experiments, only the TN-XXL calcium-binding domain, without the FPs, was cloned into pRSETB, changing the flanking restriction sites from *Sph*I/*Sac*I to *Bam*HI/*Eco*RI. Mutant constructs of the indicator variants were generated by site-directed mutagenesis using the primer extension method (Stratagene, La Jolla, CA). For protein expression, indicator constructs were subcloned into a modified version of the pET16b vector (EMD Biosciences, San Diego, CA) containing an N-terminal tobacco etch virus (TEV) protease cleavage site.

### Protein expression and purification

Indicator variants were expressed in *E. coli* BL21 and treated as described previously (16). Clear lysates were purified via HisTrap Ni-NTA columns (GE Healthcare, Waukesha, WI) according to the manufacturer’s protocol. The eluate was incubated with TEV protease in the presence of 5 mM dithiothreitol (DTT) at 4°C overnight for His-tag removal. The cleaved protein was obtained in the flow-through during Ni-NTA affinity chromatography. Protein variants were further purified by size-exclusion chromatography on a Superdex 200 column (16/60, GE Healthcare) equilibrated with the respective measurement buffers. Fractions containing protein were pooled and concentrated using a 10 kD Centricon ultrafiltration device (Millipore, Billerica, MA). Analytical size-exclusion chromatography was performed using a Superose 12 column (10/300, GE Healthcare) equilibrated with buffer A (30 mM MOPS, 100 mM KCl, 100 μM EDTA, 100 μM EGTA, pH 7.5) with EGTA (2 mM, Ca<sup>2+</sup>-free) or CaCl<sub>2</sub> (10 mM, high Ca<sup>2+</sup>). Before chromatographic separation, the samples were pretreated with 2 mM EGTA and 10 mM CaCl<sub>2</sub>, respectively.

For NMR experiments, expression of the uniformly <sup>15</sup>N- and <sup>13</sup>C-labeled histidine-tagged single-lobe domain of TN-XXL (comprising EF-hands 3 and 4) was performed at 37°C in minimal medium with <sup>15</sup>N-ammonium chloride and <sup>13</sup>C<sub>6</sub>-D-glucose as the sole nitrogen and carbon sources. The fusion protein was purified by immobilized metal affinity chromatography on Ni-NTA agarose (Qiagen, Venlo, The Netherlands) and subsequently cleaved with TEV protease. The released EF34 TN-XXL was further purified by reverse-phase HPLC.

### Analytical ultracentrifugation

The sedimentation velocity experiments were performed using an Optima XL-I analytical ultracentrifuge (Beckman Coulter, Brea, CA) equipped with an An-60 Ti rotor and double-sector centerpieces at 20°C. The sample proteins were used at a concentration of 18–23 μM in buffer A (30 mM MOPS, 100 mM KCl, 100 μM EDTA, 100 μM EGTA, pH 7.5) with EGTA (2 mM, Ca<sup>2+</sup> free) or CaCl<sub>2</sub> (10 mM, high Ca<sup>2+</sup>) added. Buffer density and viscosity were measured using a DMA 5000 densitometer and an AMVn viscosimeter, respectively (both from Anton Paar, Graz, Austria). Concentration profiles were measured at 280 nm at a speed of 50,000 rpm, followed by evaluation using the SEDFIT software (version 11.71 (28)) to obtain the diffusion-corrected sedimentation coefficient distributions (c(s)-distributions).

### Fluorescence spectroscopy

Ca<sup>2+</sup> affinity of TN-XXL and variants were measured by steady-state fluorescence spectroscopy using a Cary Eclipse fluorometer (Varian, Palo Alto, CA) with temperature-controlled cuvette holder. Dissociation kinetics were measured with a stopped-flow RX2000 rapid kinetics accessory unit (Applied Photophysics, Leatherhead, UK) with a dead time of ~8 ms,

with excitation at 432 nm and detection at 475 nm and 527 nm. Free Ca<sup>2+</sup> concentrations were calculated using the Maxchelator (<http://maxchelator.stanford.edu>). Ca<sup>2+</sup> titrations were carried out in calcium titration buffer RT (30 mM MOPS, 100 mM KCl, 1 mM MgCl<sub>2</sub>, 10 mM K<sub>2</sub>EGTA, and 0–10 mM CaCl<sub>2</sub>, pH 7.2) according to the methods of Tsieng and Pozzan (29) at a protein concentration of 0.5 μM. Stopped-flow measurements of these variants were conducted at a protein concentration of 0.5 μM with 2 mM Ca<sup>2+</sup> in buffer SF (10 mM MOPS, 50 mM KCl, 1 mM MgCl<sub>2</sub>, and 1 mM DTT, pH 7.5) being rapidly mixed with an equal volume of EGTA (10 mM) in buffer SF (30).

Ca<sup>2+</sup> titrations monitoring tyrosine fluorescence were carried out with the same stopped-flow unit as described above in a 2-mL volume of 1 μM protein in buffer YT (200 mM MOPS to prevent pH changes upon Ca<sup>2+</sup> addition, 100 mM KCl, 2 mM EGTA, 1 mM MgCl<sub>2</sub>, and 1 mM DTT, pH 7.2). Microliter amounts of CaCl<sub>2</sub> solution (250 mM) were added at 30°C with tyrosine fluorescence excited at 275 nm and monitored at 303 nm using the Cary Eclipse fluorometer. The rate of conformational change of the binding domain alone was followed by stopped-flow tyrosine fluorescence at a protein concentration of 5 μM in buffer SF, as described above.

The time-resolved detection of the fluorescence decay of TN-XXL was performed with a Fluotime100 fluorescence spectrophotometer (Picoquant, Berlin, Germany) based on a picoHarp300 unit and using a pulsed diode laser (LDH-440 and LDH-P-C-470; center wavelength, 440 nm and 470 nm; pulse width, 54 ps and 88 ps; repetition frequency, variable, here 10 MHz) as an excitation source. Fluorescence decay curves were measured by time-correlated single-photon counting with a resolution of ≥300 ps (31,32). Decay curves were analyzed by iterative reconvolution of the instrument response function, IRF(t), with an exponential model function, M(t), using the FluoFit software (version 4.4; Picoquant) using:

$$I(t) = \text{IRF}(t) \times M(t) \quad (1)$$

$$M(t) = \sum_{i=1-3} \left[ \alpha_i \times \exp\left(-\frac{t}{\tau_i}\right) \right], \quad (2)$$

where  $\tau_i$  are the characteristic lifetimes and  $\alpha_i$  are the respective intensities. The average lifetime,  $\tau_{\text{ave}}$ , was calculated as

$$\tau_{\text{ave}} = \frac{\sum_{i=1-3} [\alpha_i \times \tau_i]}{\sum_{i=1-3} [\alpha_i]} \quad (3)$$

### Small-angle x-ray scattering

Small-angle x-ray scattering (SAXS) data collection was performed at ID14-3 European Molecular Biology Laboratory (EMBL)/European Synchrotron Radiation Facility (Grenoble, France) and X33 EMBL/Deutsches Elektronen-Synchrotron (Hamburg, Germany) beamlines. TN-XXL samples were purified by size-exclusion chromatography in buffer A (30 mM MOPS, 100 mM KCl, 100 μM EDTA, and 100 μM EGTA, pH 7.5) containing EGTA (2 mM, Ca<sup>2+</sup> free) or 10 mM CaCl<sub>2</sub> (10 mM high Ca<sup>2+</sup>). Protein samples and buffer controls were centrifuged for 10 min at 13,200 × g before data acquisition. Samples were measured in concentrations of 1, 2, 5, and 10 mg/mL. The running buffer of the size-exclusion chromatography (buffer A) was used for buffer correction. No particle interaction or aggregation was observed in the tested concentration range. All samples were checked for radiation damage by comparison of the successive 10-s frames of sample exposure. Raw data were analyzed and processed using the ATSAS package (version 2.4 (33)) according to the literature (34). Sets of independent ab initio models were calculated using GASBOR (35). DAMAVER (36) was used for alignment and averaging. Figures and modeling were carried out using SITUS (37) and UCSF Chimera (38).

## NMR spectroscopy

NMR experiments were carried out at 303 K on Bruker DRX spectrometers equipped with z-gradient cryoprobes operating at different fields (600–800 MHz). NMR samples were prepared at a final protein concentration of 1 mM in 20 mM Bis-Tris (pH 7.0), 100 mM KCl, 10 mM DTT, and 10%  $^2\text{H}_2\text{O}$ . The metal-free and calcium-loaded samples contained 20 mM EDTA/20 mM EGTA and 10 mM  $\text{CaCl}_2$ , respectively. To obtain sequence-specific backbone resonance assignments, a standard set of triple-resonance NMR experiments was performed. The spectra were processed using NMRpipe (39) and analyzed using SPARKY (40) and CARS (41).

## RESULTS

### Correlating calcium binding and FRET output

We first investigated calcium binding to individual EF-hands of the TN-XXL calcium-binding domain via tyrosine fluorescence. The binding domain of TN-XXL comprises two concatenated C-terminal lobes (EF-hands 3 and 4 with residues 94–162) from chicken skeletal muscle TnC, thus consisting of two identical pairs of EF-hands connected by a short linker peptide (Fig. 1 A). To monitor calcium binding to the individual EF-hands of TN-XXL directly, we mutated endogenous phenylalanine residues in the chelating loop of each EF-hand to tyrosines. Tyrosine residues present at the corresponding positions in the related wild-type human cardiac TnC are known to report  $\text{Ca}^{2+}$  binding to one specific EF-hand with an increase of intrinsic fluorescence (30). We generated a series of constructs in which one of the four Phe residues was selectively exchanged (EF3-1, EF4-1, EF3-2, EF4-2), with one control that contained tyrosines in all four binding sites (TN-XXL 4 $\times$ Tyr). TN-XXL 4 $\times$ Tyr showed a calcium affinity and off rate that was indistinguishable from that of TN-XXL when monitored via FRET (Fig. S1, A and B, in the Supporting Material). Direct calcium binding to the individual EF-hands of TN-XXL was monitored at 23°C and pH 7.2. For this purpose, we used the TN-XXL calcium-binding domain without the flanking fluorescent proteins due to the presence of one endogenous tryptophan and 8–10 tyrosines within each fluorescent protein. These four constructs, containing only a single tyrosine residue per construct, were analyzed by steady-state (Fig. 1 B) and stopped-flow fluorescence spectroscopy (Fig. 1 C). Calcium-induced tyrosine fluorescence increases were significantly different in both EF-hand types and varied between ~75% (EF3-1 or 3-2) and only ~6% (EF4-1 and 4-2) (Fig. S1, C and D). For EF3-1 and EF3-2,  $K_d$  values of 690 nM and 820 nM, respectively, were determined, matching the measured  $K_d$  of TN-XXL, which was 830 nM as monitored by FRET. In contrast, EF4-1 and EF4-2 showed  $K_d$  values of 180 nM and 2.05  $\mu\text{M}$ , respectively. Thus, EF3-1 and EF3-2 show a calcium affinity that is in good agreement with the value of TN-XXL and therefore were identified as the major determinants of the sensor's FRET signal. Notably, EF3-1 shows a broader binding curve in comparison to EF3-2, which

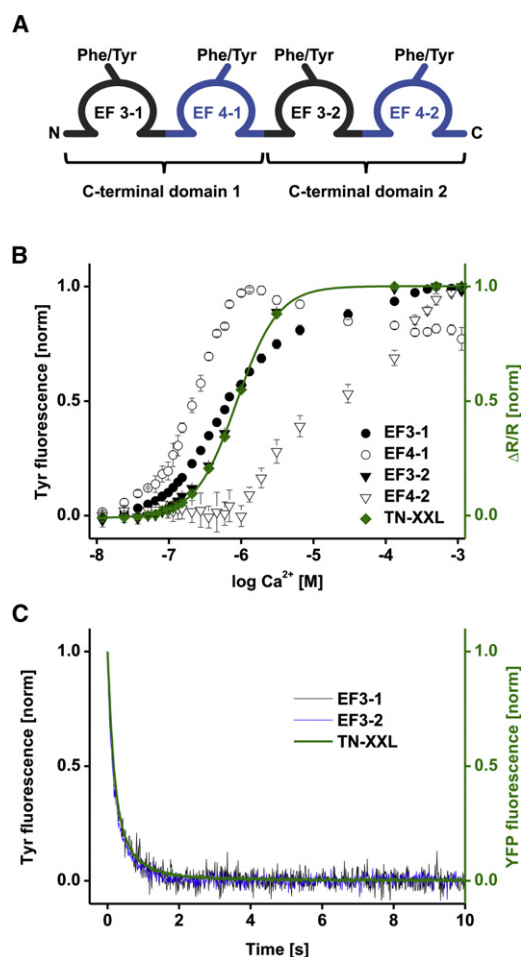


FIGURE 1 Fluorescence spectroscopy of single tyrosine substitutions in the calcium binding domain of TN-XXL. (A) Schematic representation of the four calcium binding EF-hands of the TN-XXL calcium binding domain. Endogenous phenylalanine residues were mutated to tyrosines to report local calcium binding at individual EF-hands. (B) Calcium titrations of single tyrosine substitutions in comparison to TN-XXL FRET. Standard error of the mean depicted as error bars and fluorescence normalized. (C) Calcium-dissociation kinetics of EF3-1 and EF3-2. Tyrosine measurements used excitation at 275 nm with emission recorded at 303 nm. TN-XXL FRET control was performed with excitation at 432 nm and cpCitrate (YFP) emission was recorded at 527 nm. All data are averages of three independent experiments.

suggests structural instability of the first EF-hand due to the lack of an N-terminal fusion partner. The assumption of a less ordered structure is further supported by the NMR results (see Fig. 3 C)  $\text{Ca}^{2+}$  dissociation kinetics were determined for EF3-1 and EF3-2 (Fig. 1 C). Due to their low signal strength and the missing relation to TN-XXL affinity, EF4-1 and EF4-2 were not included in this experiment. The resulting  $\text{Ca}^{2+}$ -dissociation time constants,  $t_{\text{decay}}$ , were calculated using monoexponential fits and compared with the FRET fluorescence decay of TN-XXL. For FRET, a  $t_{\text{decay}}$  of 311 ms was measured, whereas EF3-1 and EF3-2 show  $t_{\text{decay}}$  values of 317 ms and 277 ms, respectively. Thus, unbinding of bound  $\text{Ca}^{2+}$

locally detected at EF-hands 3-1 and 3-2 displayed off-kinetics similar to the global changes reported by FRET.

### Hydrodynamics of TN-XXL

Hydrodynamic analysis of TN-XXL was performed using a multimethod approach to investigate the conformational switch upon  $\text{Ca}^{2+}$  binding underlying the FRET changes. Under both conditions—high calcium (10 mM  $\text{CaCl}_2$ ) or

calcium-free (2 mM EGTA)—recombinant purified TN-XXL remained strictly monomeric (Fig. 2, A–C). Analytical size-exclusion chromatography of TN-XXL showed a large shift of the elution volume,  $V_e$ , indicating a significant change of the hydrodynamic volume with its monomeric status maintained. Further analysis by analytical ultracentrifugation confirmed these results shown as sedimentation-coefficient distributions (Fig. 2 C,  $c(S)$ ). In sedimentation velocity experiments, the sedimentation

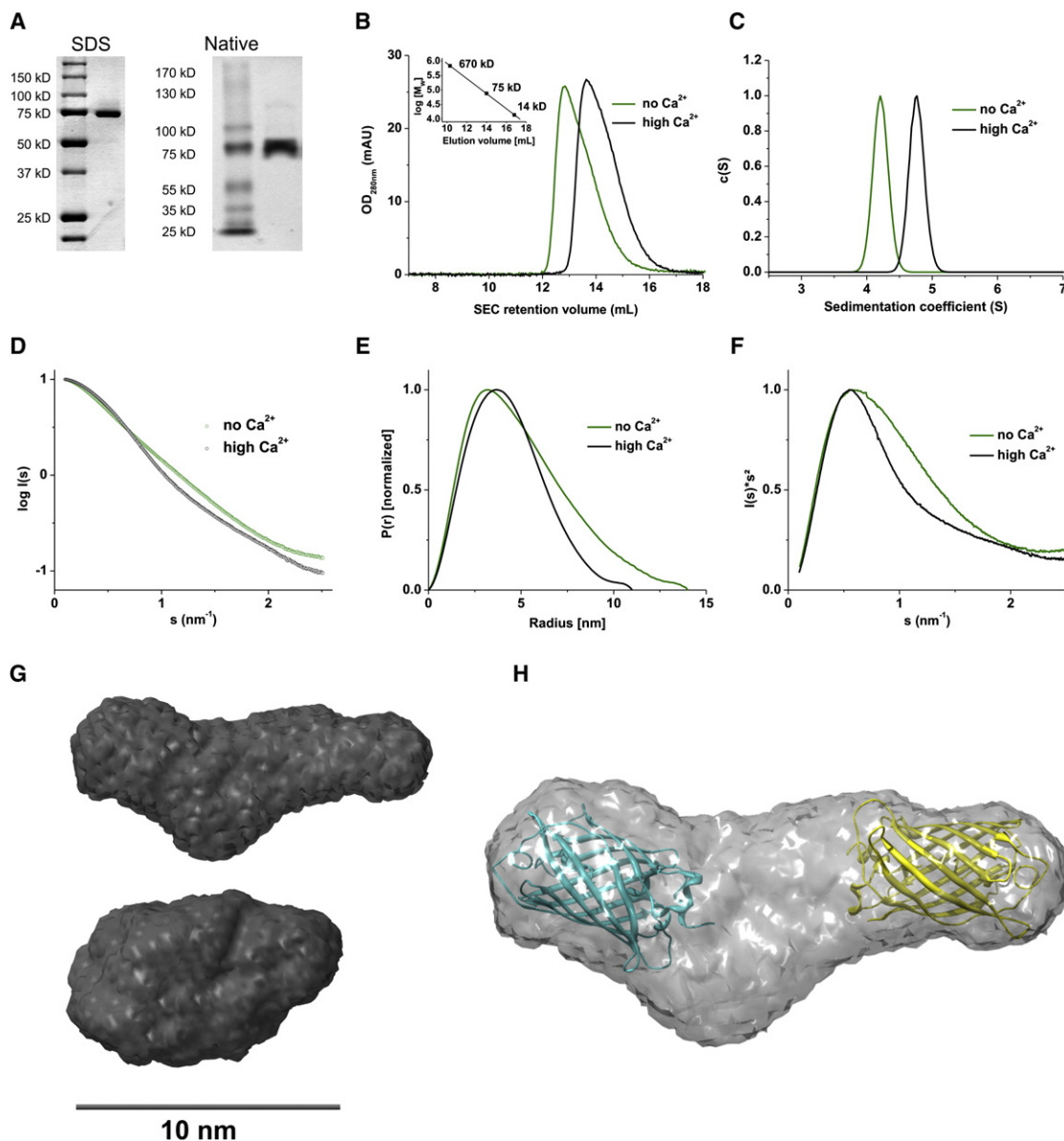


**FIGURE 2** Hydrodynamics of TN-XXL. (A) Coomassie staining of SDS- and native PAGE gels of purified TN-XXL. (B) Size-exclusion chromatography of TN-XXL in  $\text{Ca}^{2+}$ -free and high- $\text{Ca}^{2+}$  conditions on a Superose 12 column (10/300). (C)  $c(S)$  distribution calculated using SEDFIT (28) from sedimentation-velocity experiments in the analytical ultracentrifuge with TN-XXL concentrations of 18 and 23  $\mu\text{M}$  in the presence and absence, respectively, of  $\text{Ca}^{2+}$ . (D) Solution scattering data for TN-XXL in  $\text{Ca}^{2+}$ -free and high- $\text{Ca}^{2+}$  conditions. (E and F) Distance distribution functions  $P(r)$  and Kratky plot, respectively, of TN-XXL in  $\text{Ca}^{2+}$ -free and high- $\text{Ca}^{2+}$  conditions. (G) Final averaged DAMAVER (36) ab initio shapes from independent GASBOR (35) runs of TN-XXL in  $\text{Ca}^{2+}$ -free (upper) and high- $\text{Ca}^{2+}$  (lower) states. (H) Shape of TN-XXL in  $\text{Ca}^{2+}$ -free state manually docked with cartoon representations of crystal structures of ECFP and citrine (PDB 1CV7 and 1HUY). All experiments were carried out in buffer A. Either 2 mM EGTA or 10 mM  $\text{CaCl}_2$  were added for  $\text{Ca}^{2+}$ -free or high- $\text{Ca}^{2+}$  conditions, respectively.

constant  $S_{20,w}$  shifted from 5.05 at high calcium to 4.32 at calcium-free conditions. As a measure for the change in maximal shape asymmetry, calculation of the frictional ratio  $f/f_0$  showed values of 1.2 in the calcium-saturated state, correlating with a rather compact structure, as usually observed for globular proteins, and a frictional ratio  $f/f_0$  of 1.5 in the calcium-depleted state, indicating an elongated shape (42). Molecular masses of TN-XXL in the calcium unbound and bound states determined from broadening of the sedimenting boundary in sedimentation-velocity experiments were 74.1 kDa and 67.8 kDa mol wt, respectively, and are in good agreement with the theoretical molecular mass of a monomer (74.1 kDa). Finally, SAXS allowed us to associate these results with molecular geometry parameters like radius of gyration,  $R_g$ , and maximum diameter,  $D_{max}$ , of the proteins and with approximations of folding status and conformation. The obvious differences in TN-XXL shapes in the presence and absence of  $Ca^{2+}$  can already be seen in the scattering curves (Fig. 2 D), and they are even more pronounced in the interatomic distance distribution function,  $P(r)$  (Fig. 2 E). A radius of gyration,  $R_g$ , of 3.85 nm suggests an elongated calcium-free conformation, in comparison to an  $R_g$  of 3.32 nm for the calcium-saturated state, confirming its more compact structure. Calcium-bound and calcium-free states are clearly folded, as can be judged from the bell-shaped curves (43) in the Kratky plots (Fig. 2 F). Maximum particle size,  $D_{max}$ , values of 14 nm ( $Ca^{2+}$ -free) versus 11 nm ( $Ca^{2+}$ -bound) fit well to possible arrangements of the enhanced CFP (ECFP)/cpCitrine pair, allowing the assumption of a strong distance contribution to the FRET change of TN-XXL. To visualize the results, low-resolution shapes were calculated ab initio from the scattering data (Fig. 2 G). The location of the two  $\beta$ -barrel domains is evident in the outstretched  $Ca^{2+}$ -free form but ambiguous in the compact  $Ca^{2+}$ -bound form. To better illustrate the possible positioning of the two FPs, the available structures for ECFP and citrine (PDB 1CV7 and 1HUY) were manually docked in the shape envelope of the  $Ca^{2+}$ -free form (Fig. 2 H).

### NMR characterization of a single C-lobe domain of TN-XXL

To further investigate the different rigidities under both conditions, we undertook a solution NMR characterization of a single C-terminal lobe of TnC containing one pair of EF-hands from TN-XXL (EF34). The  $^1H$ - $^{15}N$  heteronuclear single-quantum coherence (HSQC) spectrum of the calcium-loaded form (Fig. 3 A) shows that EF34—considering the good dispersion of signals in both proton and nitrogen dimensions—adopts a folded conformation. Moreover, we obtained the complete assignment of HN and  $C_\alpha$  chemical shifts of EF34. On the basis of chemical shift index values (44), we derived a secondary structure prediction, shown in Fig. 3 C, which is essentially identical to that obtained for

the wild-type C-terminal domain of chicken skeletal TnC and consistent with its high-resolution structure, PDB ID code 1TNW19. This finding suggests that the three TN-XXL mutations N108D, D110N, and I130T do not affect the tertiary fold of EF34. This result gains further support from the characteristic amide proton chemical shifts of residues Gly<sup>111</sup> and Gly<sup>147</sup>. As in wild-type TnC, these residues show remarkable downfield chemical shifts in EF34, suggesting that they are similarly involved in a hydrogen bond that stabilizes calcium-binding sites. Finally, to address the role of metal in the domain organization, we also investigated the apo form of EF34. As displayed in Fig. 3 B, there is considerably less signal dispersion in the  $^1H$ - $^{15}N$  HSQC spectrum of the apo form than in the calcium-loaded form. Secondary  $C_\alpha$  chemical shifts are also less pronounced in the metal-free form (Fig. 3 C), even though they still deviate significantly from zero. Taken together, these data indicate that in the absence of calcium, the tertiary structure of protein is partially lost and the secondary structural elements are less stable than in the metal-loaded protein. Notably, the secondary structure, in particular the first  $\alpha$ -helix, of the EF-hand motif (EF3) appears to be more affected than EF4. However, this might also be due to the lack of a stabilizing N-terminal fusion partner.

### Truncations and “Amber” substitutions in TN-XXL

Strong conformational changes such as those demonstrated here might affect fluorescence properties of fused fluorescent proteins by direct conformational coupling onto the  $\beta$ -barrels. To address this issue, which potentially impairs the signal output, we generated a series of four fusion constructs containing only one fluorescent protein (Fig. S2 A). Two constructs contained the calcium-binding domain of TN-XXL fused to one of the fluorescent proteins and lacking the second (TN-XXL  $\Delta$ cpCit and TN-XXL  $\Delta$ ECFP). In two other constructs, one of the FPs was replaced with a defective FP in which an “Amber”-like 67<sup>Cys</sup> mutation (45) prevented fluorophore formation yet retained the fully folded  $\beta$ -barrel structure (TN-XXL cpCit<sup>o</sup> and TN-XXL ECFP<sup>o</sup>). These constructs acted as reporters for fluorescence changes caused by non-FRET mechanisms. We tested the calcium sensitivity of all constructs with steady-state (Fig. S2, B–G) and time-resolved fluorescence spectroscopy (Table S1). The fluorescence emission of ECFP, either alone or in fusion constructs, was minimally reduced by the addition of calcium ( $\approx 2\%$ , Fig. S2, B–D). cpCitrine and all its control constructs maintained stable fluorescence properties at all calcium concentrations (Fig. S2, E–G). Thus, the  $Ca^{2+}$ -dependent conformational change does not affect the fluorescence properties of the single FPs.

### Fluorescence-lifetime calcium titrations of TN-XXL

To correlate the time-resolved fluorescence signal of TN-XXL with the sensor properties obtained for steady-state

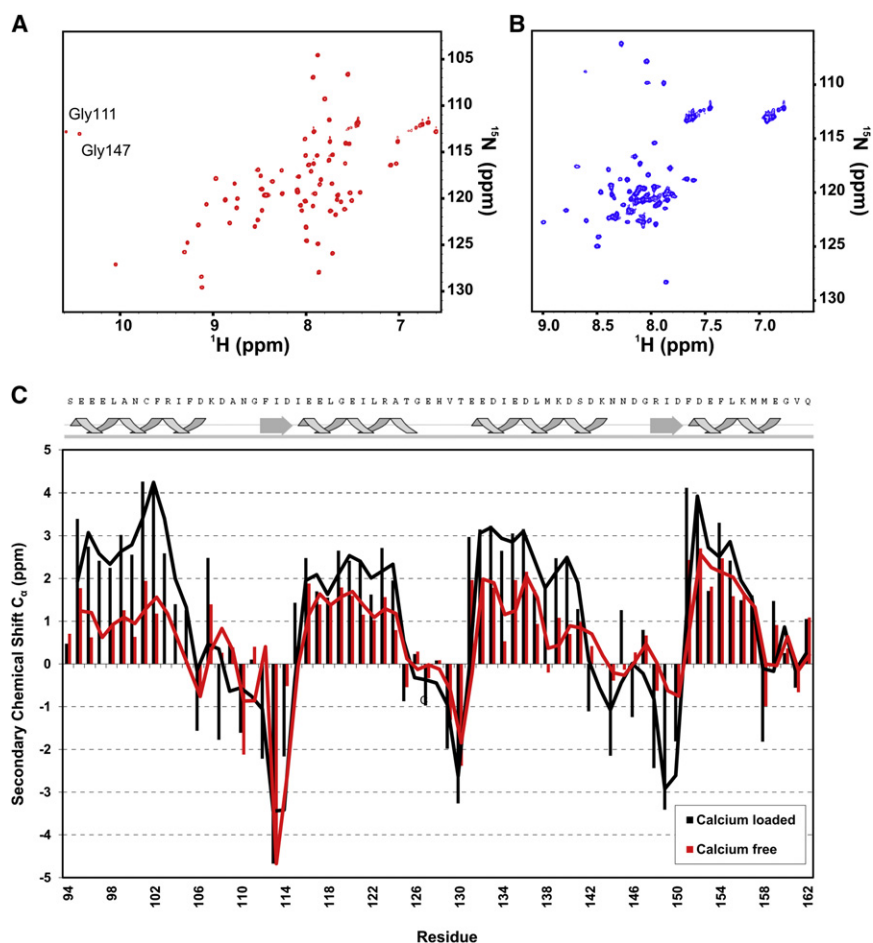


FIGURE 3 NMR characterization of the calcium-binding domain of TN-XXL. (A and B)  $^1\text{H}$ - $^{15}\text{N}$  HSQC spectra of  $^{15}\text{N}$ - $^{13}\text{C}$ -labeled single-lobe EF34 TN-XXL domain (residues 94–162). Data acquisition was performed at 303 K on an 800 MHz spectrometer with the  $\text{Ca}^{2+}$ -loaded (A) and  $\text{Ca}^{2+}$ -free form (B). (C) Upper, Secondary-structure elements ( $\alpha$ -helices and  $\beta$ -strands) in dependence of the sequence in EF34 TN-XXL in the  $\text{Ca}^{2+}$ -loaded form as derived by the chemical shift index based on  $\text{C}_\alpha$  resonance assignments. Lower, Secondary chemical shift analysis for EF34 of TN-XXL in the  $\text{Ca}^{2+}$ -loaded (black) and  $\text{Ca}^{2+}$ -free forms (gray).

FRET spectroscopy, we performed  $\text{Ca}^{2+}$  titrations with both methods in parallel and followed the donor fluorescence decay. Due to initial FRET, the overall donor fluorescence lifetime in TN-XXL in zero calcium was already shorter than that of the control construct TN-XXL cpCit<sup>o</sup>, containing only ECFP (Fig. 4 A, curves 1 and 2, respectively). Upon saturation with  $\text{Ca}^{2+}$ , a further shortening of the fluorescence lifetime could be observed (curve 3). For ECFP fluorescence decay, both biexponential fits (46–48) and triexponential fits (49,50) have been reported in vitro and in living cells. In our experiments, the triexponential fit notably improved the quality for the fit of ECFP decay (Fig. 4 A and  $\chi^2$  values in Table S2). A factorial analysis of the triexponential fit of the  $\text{Ca}^{2+}$  titration yielded a surprising distribution of lifetimes and amplitudes (Fig. 4 B and Table S2). Only the shortest of all three lifetimes showed a significant  $\text{Ca}^{2+}$  dependency, decreasing by >25% from 0.696 to 0.503 ns. The longer lifetimes,  $\tau_2$  and  $\tau_3$ , remained unaffected. The relative amplitude  $\alpha_1$  of the fast lifetime increased by 28% to 64% at calcium saturation, whereas the amplitudes of the longer, invariant lifetimes dropped by 6% for  $\tau_2$  and 22% for  $\tau_3$ . It cannot be excluded that the decay represented by these lifetimes has contributions of both the shorter lifetimes of non-FRET

donor molecules and less efficient FRET processes compared to those described by  $\tau_1$ . However, the longest lifetime,  $\tau_3$ , at high calcium (12%)—nearly identical in TN-XXL and TN-XXL cpCit<sup>o</sup>—is doubtless associated with donor molecules that do not undergo FRET. The value of high-calcium  $\alpha_3$  is in very good agreement with the fraction of the cpCitrine chromophore that is protonated at pH 7.2 (~15%; Fig. S3). Thus, in contrast to earlier studies of other FRET-based GECIs, no fraction of nonfunctional biosensors has to be postulated. Instead, at low calcium, TN-XXL molecules exhibit only low FRET efficiency, whereas at high calcium, all ECFPs undergo FRET except for those that are bound to an acceptor with a protonated chromophore. A second possible explanation for a non-interacting fraction of FRET-based indicators could be the photoconversion of the acceptor upon long and intense illumination (51,52). Under our experimental conditions, we found no indication for a substantial contribution thereof, but under fluorescence lifetime imaging (FLIM) conditions with more continuous illumination, this effect might hamper the  $\Delta\tau_{\text{ave}}$  signal further. The boundary cases for TN-XXL were obtained at calcium concentrations of 0 and 40  $\mu\text{M}$  and yielded average fluorescence lifetimes of 2.11 and 1.26 ns and therefore an average fluorescence lifetime

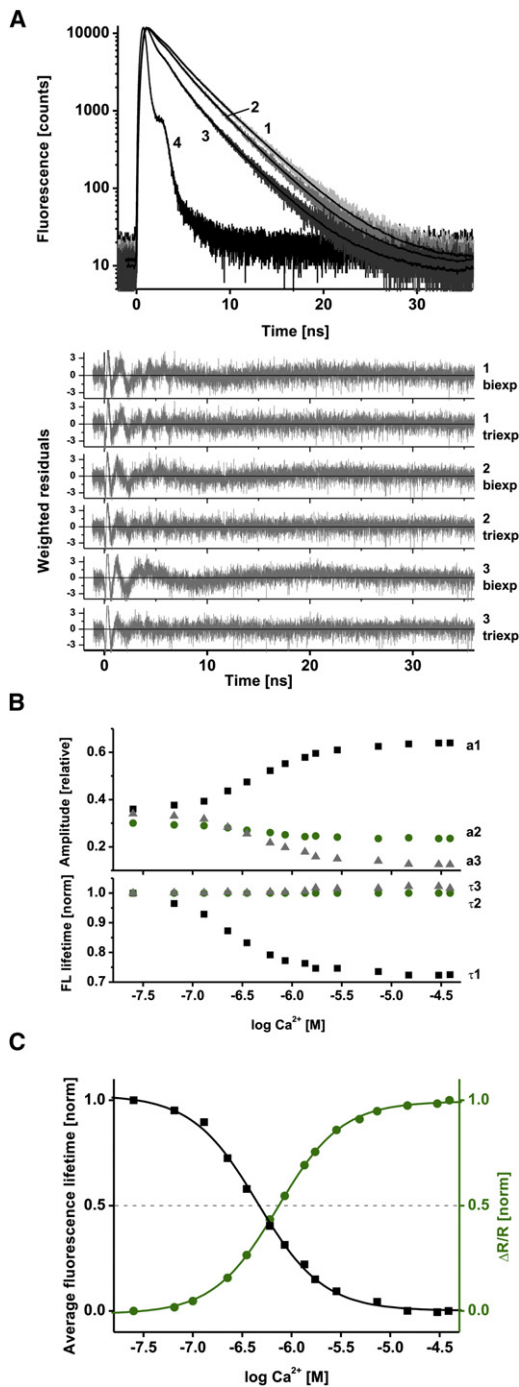


FIGURE 4 Fluorescence lifetime spectroscopy of TN-XXL. (A) *Upper*, Experimental and fitted fluorescence donor decay curves of TN-XXL cpCit<sup>o</sup> control (curve 1), TN-XXL in the Ca<sup>2+</sup>-free state (curve 2), TN-XXL in the high-Ca<sup>2+</sup> state (curve 3), and the instrument response function (curve 4) (excitation of ECFP at 440 nm and donor emission recorded at 475 nm). Experimental data are fitted with multiexponential functions with amplitude  $\alpha_i$  and lifetimes  $\tau_i$ . *Lower*, Weighted residuals of bi- and triexponential fits. All resulting parameters are listed in Table S2. (B) Ca<sup>2+</sup> dependence of relative amplitudes from the triexponential fit (*upper*) and normalized fluorescence lifetimes (*lower*). (C) Ca<sup>2+</sup> dependence of the normalized average fluorescence lifetime  $\tau_{ave}$  (*black*). Ratiometric steady-state titration of TN-XXL with ECFP and cpCit<sup>o</sup> fluorescence measured with excitation at 432 nm and emission recorded at 475/527 nm (*gray*). The dotted line represents the half-maximal signal change.

change,  $\Delta\tau_{ave}$ , of 0.85 ns without prior subtraction of subpopulations. The Ca<sup>2+</sup> titration of  $\Delta\tau_{ave}$  showed a sigmoidal curve corresponding to the titration curve obtained by ratiometric spectroscopy (Fig. 4 C). The apparent  $K_d$  obtained with the lifetime analysis was 453 nM, in contrast to the  $K_d$  of 830 nM determined by intensity-based measurements.

### Effects of pH and temperature on TN-XXL

To estimate the sensor performance under different environmental conditions, we tested pH and temperature effects on affinity and kinetics of TN-XXL (Fig. 5 and Table S3). Three temperatures were tested with a constant pH of 7.2. Although the affinity decreased slightly ( $K_d$  rising slightly from 830 to 1210 nM, Fig. 5 A), the off-kinetics, represented by the monoexponentially fitted Ca<sup>2+</sup> dissociation time constant,  $t_{decay}$ , decreased drastically from 620 ms at 23°C to only 129 ms at 37°C (Fig. 5 C). pH values tested at a constant temperature of 23°C ranged from pH 6.5 to 8.0. TN-XXL affinity increased with pH, dropping from 1030 nM at pH 6.5 to 451 nM at pH 8.0 (Fig. 5 B). The Ca<sup>2+</sup> dissociation time constant,  $t_{decay}$ , hereby changed from 620 ms to 425 ms with increasing pH (Fig. 5 D).

### DISCUSSION

Here, we present a biophysical analysis of the FRET-based calcium biosensor TN-XXL (27) using a variety of approaches. The aim of these efforts was to increase our understanding of the modular build-up of a FRET-based calcium sensor to identify optimization potential for rational engineering.

We monitored calcium binding to individual EF-hands of the calcium-binding moiety of TN-XXL by engineering a number of mutants with tyrosine substitutions. This allowed us to determine the affinity and kinetics for binding events in each EF-hand separately. We could divide the four EF-hands of the binding domain of TN-XXL into two distinct classes: EF-hands 3-1 and 3-2 dominate the FRET output of the indicator, whereas calcium binding to EF-hands 4-1 and 4-2 does not contribute detectably to the FRET signal and may have more of a stabilizing function. One avenue of further improvement would be to eliminate completely calcium binding to EF-hands 4-1 and 4-2, thus reducing the buffer capacity of the sensor. As EF-hands typically function in high-affinity binding as pairs that stabilize each other (24), it will be important to maintain the supporting scaffolding function the hands exert on EF-hands 3-1 and 3-2, similar to mutational inactivation of the first of the EF-hands in the N-terminal lobe of human cardiac TnC (53). Our tyrosine fluorescence data show that fusion of fluorescent proteins to the binding domain does not affect sensor kinetics at a detectable level. The matching dissociation time constants suggest a model with concerted slow conformational change of the entire binding domain

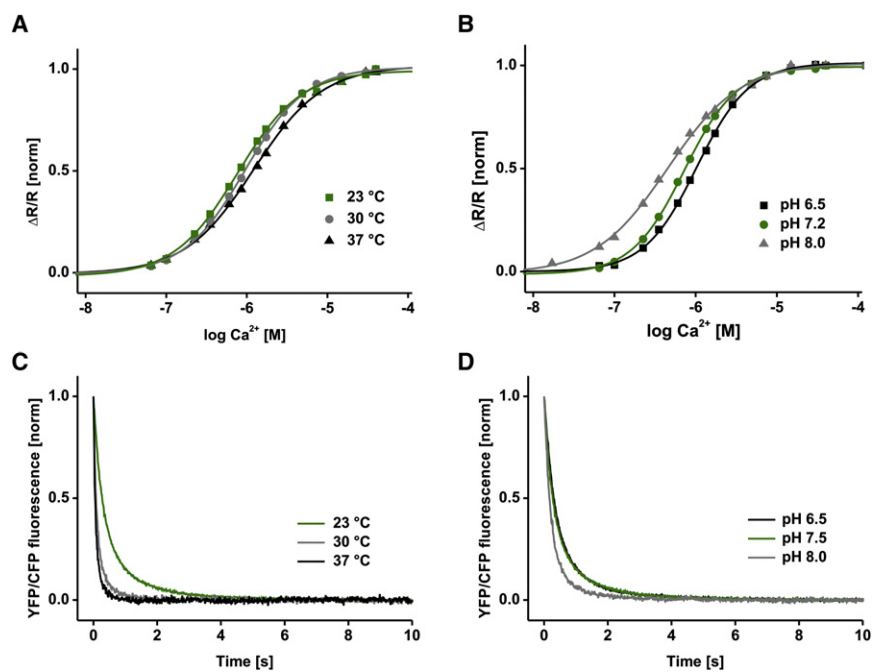


FIGURE 5 Temperature and pH dependency. (A and B)  $Ca^{2+}$  titration curve of TN-XXL at different temperatures (A) and pH values (B). (C and D)  $Ca^{2+}$ -dissociation kinetics of TN-XXL at different temperatures (C) and pH values (D) (excitation at 432 nm and emission recorded at 475/527 nm). All data are normalized averages of three independent experiments in buffer A. All resulting values are summarized in Table S3.

triggered by initial  $Ca^{2+}$  dissociation rather than with sequential transduction of the conformational change.

We also showed that the large FRET change in TN-XXL after calcium binding is associated with a distinct conformational change of the protein and cannot be related to orientational changes between the fluorophores alone. Analytical ultracentrifugation, size-exclusion chromatography, and SAXS consistently reported an outstretched calcium-free conformation and a large structural change upon calcium binding to a more compact, globular calcium-saturated conformation. The fluorescent donor and acceptor proteins, presumably localized at opposite ends of the elongated structure at zero calcium, thereby move several nanometers closer to each other and associate in close proximity. We complemented our results from SAXS analysis with NMR data on the single C-terminal lobe domain in TN-XXL, indicating that the binding domain adopts a compact folded conformation in the calcium-bound form that is partially lost in the absence of calcium. We conclude that the engineering potential to further improve the indicator's signal strength is twofold. The FRET efficiency in the flexible calcium-free form is more affected by the distance between the two FPs than by a specific orientation. Hence, reducing FRET in the unbound state can most likely be achieved by prolonging the linker sequence. Enhancing the FRET efficiency of the already compact calcium-bound state, however, requires the improvement of the alignment of the two FP  $\beta$ -barrels toward an optimal  $\kappa^2$  value according to the Förster equation. In this case, the binding domain's rigid conformation supports the concept of a confined and optimized orientation. For both strategies, the vast combinatorial possibilities of the required modifications in the amino

acid sequence will necessitate high-throughput screening to ensure maximum signal optimization.

The conformational change in TN-XXL does not induce structural distortions of the fluorophores. Using defective donor or acceptor proteins that incorporate the Amber mutation (45), we could observe no additional  $Ca^{2+}$ -dependent effect on the fluorescence of ECFP and cpCitrine (Fig. S2). Steady-state fluorescence spectroscopy revealed a strong temperature dependence of the off-kinetics, as well as a pH dependence of off-kinetics and affinity (Fig. 5).

Furthermore, the change of the average fluorescence lifetime,  $\Delta\tau_{ave}$ , of 0.85 ns (YC3.6 shows only 0.46 ns (48)) together with an apparent  $K_d$  of 453 nM (Fig. 4 C) make TN-XXL a good starting point to generate GECIs tailor-made for FLIM applications. The apparently higher calcium affinity determined for TN-XXL by titration of the donor fluorescence lifetime compared to that of the fluorescence intensity ratio of acceptor and donor can be explained by the existence of fast FRET processes with rates of 1/300 ps or larger. Indeed, processes in this order of magnitude are faster than the instrument response function of the setup; they therefore cannot be resolved and detected and will be missed in the donor fluorescence lifetime titration. Such efficient FRET processes would shift the apparent fluorescence lifetime change toward lower calcium concentrations and can explain the discrepancy in the  $K_d$  values determined by lifetime and ratio. In fact, this difference points toward an experimental problem in microscopic FLIM-FRET studies in cells and tissue. The time resolution practically achievable in measurements in cells and tissue in such studies is even lower (500 ps or longer) compared to measurements of purified GECIs in aqueous solution due

to experimental limitations, e.g., lower count numbers or larger scattering amplitudes. As a consequence, fluorescence lifetime calibration of FRET-based biosensors should always be carried out in the same microscope setup and using the same conditions under which the measurements in cells will be performed. Despite the progress in GECI development and their exciting *in vivo* use in modern fluorescence microscopy studies (8), high impact FLIM applications do not exist yet. This can be mainly attributed corruption of the  $\Delta\tau_{\text{ave}}$  due to the low dynamic range of the lifetime change (here 40%, often only 10–20% at most) and the frequently observed complexity of the multi-exponential donor fluorescence decay and noninteracting fraction in FRET constructs. Next-generation GECIs might employ improved CFPs such as the latest Cerulean (54) or mTurquoise variants (55), with higher fluorescence quantum yields and monoexponential fluorescence decays.

In conclusion, this study characterizes the genetically encoded calcium indicator TN-XXL in detail and identifies several options that might be bases for further engineering of sensors with improved signal strength, faster kinetics, and reduced buffering potential.

## SUPPORTING MATERIAL

Three tables and three figures are available at [http://www.biophysj.org/biophysj/supplemental/S0006-3495\(12\)00406-7](http://www.biophysj.org/biophysj/supplemental/S0006-3495(12)00406-7).

The authors thank S. Balfanz, Y. Laukat, B. Kunkel, and A. Moritz for technical assistance, and S. Uebel for help with analytical ultracentrifugation. We acknowledge the synchrotron beam time allocation at X33 (EMBL/DESY Hamburg, Germany) and ID14-3 (ESRF, Grenoble, France), and we thank the respective staffs for excellent support.

This work was supported by the Max-Planck-Society. Additional support came from grants from the European Union Framework 7 program (Euro-Vision) to O.G., the Deutsche Forschungsgemeinschaft (SFB 870) to O.G., the DFG Graduiertenkolleg (GRK1721) to G.W. and K.P.H., and the National Institutes of Health U19 (AI083025) to K.P.H.

## REFERENCES

- Heim, R., and R. Y. Tsien. 1996. Engineering green fluorescent protein for improved brightness, longer wavelengths and fluorescence resonance energy transfer. *Curr. Biol.* 6:178–182.
- Pollok, B. A., and R. Heim. 1999. Using GFP in FRET-based applications. *Trends Cell Biol.* 9:57–60.
- Miyawaki, A., and R. Y. Tsien. 2000. Monitoring protein conformations and interactions by fluorescence resonance energy transfer between mutants of green fluorescent protein. *Methods Enzymol.* 327:472–500.
- Yasuda, R. 2006. Imaging spatiotemporal dynamics of neuronal signaling using fluorescence resonance energy transfer and fluorescence lifetime imaging microscopy. *Curr. Opin. Neurobiol.* 16:551–561.
- Miyawaki, A. 2011. Development of probes for cellular functions using fluorescent proteins and fluorescence resonance energy transfer. *Annu. Rev. Biochem.* 80:357–373.
- Newman, R. H., M. D. Fosbrink, and J. Zhang. 2011. Genetically encodable fluorescent biosensors for tracking signaling dynamics in living cells. *Chem. Rev.* 111:3614–3666.
- Mank, M., and O. Griesbeck. 2008. Genetically encoded calcium indicators. *Chem. Rev.* 108:1550–1564.
- Gensch, T., and D. Kaschuba. 2012. Fluorescent genetically encoded calcium indicators and their *in vivo* application. In *Fluorescent Proteins II: From Fundamental Research to Bioanalytics*. G. Jung, editor. Springer-Verlag, Berlin, Germany. 125–162.
- Nakai, J., M. Ohkura, and K. Imoto. 2001. A high signal-to-noise  $\text{Ca}^{2+}$  probe composed of a single green fluorescent protein. *Nat. Biotechnol.* 19:137–141.
- Zhao, Y., S. Araki, ..., R. E. Campbell. 2011. An expanded palette of genetically encoded  $\text{Ca}^{2+}$  indicators. *Science.* 333:1888–1891.
- Miyawaki, A., J. Llopis, ..., R. Y. Tsien. 1997. Fluorescent indicators for  $\text{Ca}^{2+}$  based on green fluorescent proteins and calmodulin. *Nature.* 388:882–887.
- Miyawaki, A., O. Griesbeck, ..., R. Y. Tsien. 1999. Dynamic and quantitative  $\text{Ca}^{2+}$  measurements using improved cameleons. *Proc. Natl. Acad. Sci. USA.* 96:2135–2140.
- Nagai, T., S. Yamada, ..., A. Miyawaki. 2004. Expanded dynamic range of fluorescent indicators for  $\text{Ca}^{2+}$  by circularly permuted yellow fluorescent proteins. *Proc. Natl. Acad. Sci. USA.* 101:10554–10559.
- Horikawa, K., Y. Yamada, ..., T. Nagai. 2010. Spontaneous network activity visualized by ultrasensitive  $\text{Ca}^{2+}$  indicators, yellow Camleon-Nano. *Nat. Methods.* 7:729–732.
- Palmer, A. E., C. Jin, ..., R. Y. Tsien. 2004. Bcl-2-mediated alterations in endoplasmic reticulum  $\text{Ca}^{2+}$  analyzed with an improved genetically encoded fluorescent sensor. *Proc. Natl. Acad. Sci. USA.* 101:17404–17409.
- Heim, N., and O. Griesbeck. 2004. Genetically encoded indicators of cellular calcium dynamics based on troponin C and green fluorescent protein. *J. Biol. Chem.* 279:14280–14286.
- Pearlstone, J. R., W. D. McCubbin, ..., L. B. Smillie. 1992. Spectroscopic analysis of a methionine-48 to tyrosine mutant of chicken troponin C. *Biochemistry.* 31:9703–9708.
- Sorenson, M. M., A. C. da Silva, ..., F. C. Reinach. 1995. Concerted action of the high affinity calcium binding sites in skeletal muscle troponin C. *J. Biol. Chem.* 270:9770–9777.
- VanScyoc, W. S., B. R. Sorensen, ..., M. A. Shea. 2002. Calcium binding to calmodulin mutants monitored by domain-specific intrinsic phenylalanine and tyrosine fluorescence. *Biophys. J.* 83:2767–2780.
- Filatov, V. L., A. G. Katrukha, ..., N. B. Gusev. 1999. Troponin: structure, properties, and mechanism of functioning. *Biochemistry (Mosc.).* 64:969–985.
- Li, M. X., M. Chandra, ..., L. B. Smillie. 1994. Properties of isolated recombinant N and C domains of chicken troponin C. *Biochemistry.* 33:917–925.
- Slupsky, C. M., and B. D. Sykes. 1995. NMR solution structure of calcium-saturated skeletal muscle troponin C. *Biochemistry.* 34:15953–15964.
- Tsuda, S., A. Miura, ..., B. D. Sykes. 1999. Low-temperature-induced structural changes in the Apo regulatory domain of skeletal muscle troponin C. *Biochemistry.* 38:5693–5700.
- Gifford, J. L., M. P. Walsh, and H. J. Vogel. 2007. Structures and metal-ion-binding properties of the  $\text{Ca}^{2+}$ -binding helix-loop-helix EF-hand motifs. *Biochem. J.* 405:199–221.
- Houdusse, A., M. L. Love, ..., C. Cohen. 1997. Structures of four  $\text{Ca}^{2+}$ -bound troponin C at 2.0 Å resolution: further insights into the  $\text{Ca}^{2+}$ -switch in the calmodulin superfamily. *Structure.* 5:1695–1711.
- Mank, M., D. F. Reiff, ..., O. Griesbeck. 2006. A FRET-based calcium biosensor with fast signal kinetics and high fluorescence change. *Biophys. J.* 90:1790–1796.
- Mank, M., A. F. Santos, ..., O. Griesbeck. 2008. A genetically encoded calcium indicator for chronic *in vivo* two-photon imaging. *Nat. Methods.* 5:805–811.
- Schuck, P. 2000. Size-distribution analysis of macromolecules by sedimentation velocity ultracentrifugation and lamm equation modeling. *Biophys. J.* 78:1606–1619.

29. Tsien, R., and T. Pozzan. 1989. Measurement of cytosolic free  $\text{Ca}^{2+}$  with quin2. *Methods Enzymol.* 172:230–262.
30. Swindle, N., and S. B. Tikunova. 2010. Hypertrophic cardiomyopathy-linked mutation D145E drastically alters calcium binding by the C-domain of cardiac troponin C. *Biochemistry.* 49:4813–4820.
31. Kaneko, H., I. Putzier, ..., T. Gensch. 2002. Determination of intracellular chloride concentration in dorsal root ganglion neurons by fluorescence lifetime imaging. In *Calcium-Activated Chloride Channels*. C. M. Fuller, editor. Elsevier Academic, San Diego. 167–189.
32. Gensch, T., K. E. Komolov, ..., K. W. Koch. 2007.  $\text{Ca}^{2+}$ -dependent conformational changes in the neuronal  $\text{Ca}^{2+}$ -sensor recoverin probed by the fluorescent dye Alexa647. *Proteins.* 66:492–499.
33. Konarev, P. V., M. V. Petoukhov, ..., D. I. Svergun. 2006. ATSAS 2.1, a program package for small-angle scattering data analysis. *J. Appl. Crystallogr.* 39:277–286.
34. Putnam, C. D., M. Hammel, ..., J. A. Tainer. 2007. X-ray solution scattering (SAXS) combined with crystallography and computation: defining accurate macromolecular structures, conformations and assemblies in solution. *Q. Rev. Biophys.* 40:191–285.
35. Svergun, D. I., M. V. Petoukhov, and M. H. Koch. 2001. Determination of domain structure of proteins from x-ray solution scattering. *Biophys. J.* 80:2946–2953.
36. Volkov, V. V., and D. I. Svergun. 2003. Uniqueness of ab initio shape determination in small-angle scattering. *J. Appl. Crystallogr.* 36: 860–864.
37. Wriggers, W., and P. Chacón. 2001. Using Situs for the registration of protein structures with low-resolution bead models from x-ray solution scattering. *J. Appl. Crystallogr.* 34:773–776.
38. Pettersen, E. F., T. D. Goddard, ..., T. E. Ferrin. 2004. UCSF Chimera—a visualization system for exploratory research and analysis. *J. Comput. Chem.* 25:1605–1612.
39. Delaglio, F., S. Grzesiek, ..., A. Bax. 1995. NMRPipe: a multidimensional spectral processing system based on UNIX pipes. *J. Biomol. NMR.* 6:277–293.
40. Goddard, T. D., and D. G. Kneller. 1999. Sparky 3. University of California, San Francisco.
41. Keller, R. 2004. The Computer Aided Resonance Assignment Tutorial. Cantina-Verlag, Goldau, Switzerland.
42. Lebowitz, J., M. S. Lewis, and P. Schuck. 2002. Modern analytical ultracentrifugation in protein science: a tutorial review. *Protein Sci.* 11:2067–2079.
43. Mertens, H. D. T., and D. I. Svergun. 2010. Structural characterization of proteins and complexes using small-angle x-ray solution scattering. *J. Struct. Biol.* 172:128–141.
44. Wishart, D. S., and D. A. Case. 2001. Use of chemical shifts in macromolecular structure determination. *Methods Enzymol.* 338:3–34.
45. Koushik, S. V., H. Chen, ..., S. S. Vogel. 2006. Cerulean, Venus, and VenusY67C FRET reference standards. *Biophys. J.* 91:L99–L101.
46. Tramier, M., I. Gautier, ..., M. Coppey-Moisan. 2002. Picosecond-hetero-FRET microscopy to probe protein-protein interactions in live cells. *Biophys. J.* 83:3570–3577.
47. Millington, M., G. J. Grindlay, ..., S. W. Magennis. 2007. High-precision FLIM-FRET in fixed and living cells reveals heterogeneity in a simple CFP-YFP fusion protein. *Biophys. Chem.* 127:155–164.
48. Borst, J. W., S. P. Laptinok, ..., A. J. Visser. 2008. Structural changes of yellow Cameleon domains observed by quantitative FRET analysis and polarized fluorescence correlation spectroscopy. *Biophys. J.* 95: 5399–5411.
49. Habuchi, S., M. Cotlet, ..., F. C. De Schryver. 2002. Resonance energy transfer in a calcium concentration-dependent cameleon protein. *Biophys. J.* 83:3499–3506.
50. Villoing, A., M. Ridhoir, ..., H. Pasquier. 2008. Complex fluorescence of the cyan fluorescent protein: comparisons with the H148D variant and consequences for quantitative cell imaging. *Biochemistry.* 47:12483–12492.
51. Valentin, G., C. Verheggen, ..., E. Bertrand. 2005. Photoconversion of YFP into a CFP-like species during acceptor photobleaching FRET experiments. *Nat. Methods.* 2:801.
52. Kirber, M. T., K. Chen, and J. F. Keaney, Jr. 2007. YFP photoconversion revisited: confirmation of the CFP-like species. *Nat. Methods.* 4:767–768.
53. Farah, C. S., and F. C. Reinach. 1995. The troponin complex and regulation of muscle contraction. *FASEB J.* 9:755–767.
54. Markwardt, M. L., G.-J. Kremers, ..., M. A. Rizzo. 2011. An improved cerulean fluorescent protein with enhanced brightness and reduced reversible photoswitching. *PLoS ONE.* 6:e17896.
55. Goedhart, J., L. van Weeren, ..., T. W. Gadella, Jr. 2010. Bright cyan fluorescent protein variants identified by fluorescence lifetime screening. *Nat. Methods.* 7:137–139.

# CHAPTER 3

---

## Real-time *in vivo* analysis of T cell activation in the central nervous system using a genetically encoded calcium indicator

Marsilius Mues, Ingo Bartholomäus, **Thomas Thestrup**, Oliver Griesbeck, Hartmut Wekerle, Naoto Kawakami & Gurumoorthy Krishnamoorthy

*Nature Medicine* **19**, 778-783 (2013)

## Real-time *in vivo* analysis of T cell activation in the central nervous system using a genetically encoded calcium indicator

Marsilius Mues<sup>1,5</sup>, Ingo Bartholomäus<sup>1</sup>, Thomas Thestrup<sup>2</sup>, Oliver Griesbeck<sup>2</sup>, Hartmut Wekerle<sup>1</sup>, Naoto Kawakami<sup>1,3,4</sup> & Gurumoorthy Krishnamoorthy<sup>1,4</sup>

**To study T cell activation *in vivo* in real time, we introduced a newly developed fluorescence resonance energy transfer-based, genetically encoded calcium indicator into autoantigen-specific and non-autoantigen-specific CD4<sup>+</sup> T cells. Using two-photon microscopy, we explored the responses of retrovirally transduced calcium indicator-expressing T cells to antigen in the lymph nodes and the central nervous system. In lymph nodes, the administration of exogenous antigen caused an almost immediate arrest of T cells around antigen-presenting cells and an instant rise of cytosolic calcium. In contrast, encephalitogenic T cells entering the leptomeningeal space, one main portal into the central nervous system parenchyma during experimental autoimmune encephalomyelitis, showed elevated intracellular calcium concentrations while still meandering through the space. This approach enabled us to follow the migration and activation patterns of T cells *in vivo* during the course of the disease.**

T lymphocytes show a remarkable degree of functional plasticity. During their lifetime, they pass through different tissue milieus, making contact with a variety of neighboring cells. Communication between cells may involve antigens presented by facultative or professional antigen-presenting cells (APCs), or the communication may be sterile, such as lymphocyte contact with vascular structures during recirculation. Irrespective of their nature, most of these interactions involve signaling that is mediated by variations in intracellular calcium concentrations<sup>1</sup>. Past research has established that short-lasting triggers, such as transient T cell receptor ligation, mobilize the calcium stored in the endoplasmic reticulum. Depletion of these calcium stores results in the opening of calcium release-activated calcium channels located in the plasma membrane, which sets off a signaling cascade that ultimately leads to activation-dependent gene induction<sup>2</sup>. Traditionally, fluctuations in intracellular calcium concentrations in T cells have been followed in real time by imaging with synthetic calcium indicators, which are applicable to short-term investigations

*in vitro*<sup>3</sup> or *in vivo*<sup>4</sup>. However, because of their limited intracellular persistence, synthetic indicators cannot be used in T cells for sustained *in vivo* work. A powerful alternative is a self-replenishing, genetically encoded calcium indicator (GECI), such as TN-XXL<sup>5</sup>.

TN-XXL has been successfully used for a range of studies, from the mapping of neurons in the *Drosophila* optic system<sup>6</sup> and the monitoring of neurotransmitter release in the rodent cortex *in vivo*<sup>7</sup> to the visualization of neuronal changes in mouse experimental autoimmune encephalomyelitis (EAE), an animal model for multiple sclerosis<sup>8</sup>. However, GECIs have not been used for *in vivo* calcium imaging in lymphocytes. Unexpectedly, we found that the original TN-XXL construct cannot be expressed efficiently in immune cells using retroviral transduction. This report describes a new, modified variant of this GECI that is fully expressed by T cells. We used these GECI-expressing cells to characterize the initial activation events in autoantigen-specific and non-autoantigen-specific T cells in peripheral lymph nodes and the leptomeningeal area, a key entry port for T cells into the central nervous system (CNS) during EAE<sup>9</sup>.

### RESULTS

#### Expression of TN-XXL in immortalized cells

Although short-term calcium imaging in living cells has been performed using synthetic calcium indicator dyes, these dyes are unsuitable for extended-period imaging *in vivo* owing to their rapid expulsion from labeled cells<sup>10</sup> (**Supplementary Fig. 1a,b**). As an alternative to bypass this problem, fluorescence resonance energy transfer (FRET)-based GECI TN-XXL<sup>5</sup>, which is genetically encoded and thus self-replenishing, was examined for calcium imaging in lymphocytes *in vivo*. TN-XXL is composed of two fluorescent proteins: cyan fluorescent protein (CFP) as the FRET donor and cpCitrine as the FRET acceptor. These proteins are linked by the calcium-sensitive double C-terminal lobe of troponin C (TnC). After the binding of free calcium, TnC undergoes a reversible conformational change that leads to energy transfer from the donor to the acceptor fluorophore (**Fig. 1a**), resulting in a drop in CFP fluorescence and an increase in cpCitrine fluorescence. This ratiometric change in fluorescence intensities is

<sup>1</sup>Department of Neuroimmunology, Max Planck Institute of Neurobiology, Martinsried, Germany. <sup>2</sup>Research Group of Cellular Dynamics, Max Planck Institute of Neurobiology, Martinsried, Germany. <sup>3</sup>Institute of Clinical Neuroimmunology, Ludwig Maximilians University, Munich, Germany. <sup>4</sup>These authors contributed equally to this work. <sup>5</sup>Present address: University of California–San Francisco, San Francisco, California, USA. Correspondence should be addressed to H.W. ([hwekerle@neuro.mpg.de](mailto:hwekerle@neuro.mpg.de)).

Received 18 May 2012; accepted 27 November 2012; published online 12 May 2013; doi:10.1038/nm.3180

**Figure 1** Functional characterization of TN-XXL in EL4 cells. (a) Schematic representation of the calcium indicator TN-XXL, containing donor fluorophore CFP, cpCitrine acceptor and calcium-sensitive domain TnC, before and after binding of calcium. (b) Spectrophotometric analysis of lysate from TN-XXL-expressing EL4 cells before and after addition of 1 mM calcium. Excitation was at 430 nm. FI, fluorescence intensity; AU, arbitrary units. (c) FACS-based measurement of calcium influx in TN-XXL-expressing EL4 cells after stimulation with 4  $\mu$ M ionomycin (downward arrowheads). Fluorescence intensities and fractional fluorescence changes in the emission ratio ( $\Delta R/R$ ) are plotted as function of time. Results are representative of at least three similar experiments.

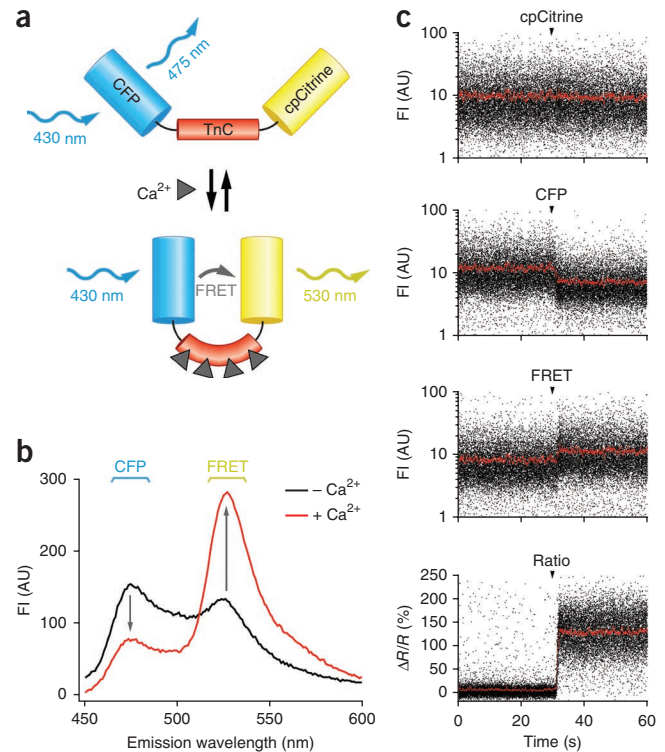
a direct measurement of the change in calcium concentration in the cytoplasm at a given time<sup>5</sup>.

We first examined the applicability of TN-XXL to calcium imaging in lymphoid cells in EL4 lymphoma cells stably transfected with TN-XXL. The spectrophotometric measurement of lysates from these cells revealed a strong fluorescence ratio change after the addition of saturating concentrations of calcium (Fig. 1b). FACS analysis (Fig. 1c) and fluorescence microscopy (Supplementary Fig. 2a,b and Supplementary Video 1) of TN-XXL-expressing EL4 cells showed a high fluorescence ratio change after the addition of the calcium ionophore ionomycin.

To achieve expression of the calcium indicator in *ex vivo*-isolated lymphocytes, we intended to introduce TN-XXL into primary mouse T cells using retroviral transduction. Whereas TN-XXL was expressed readily in Phoenix packaging cells (data not shown), all attempts to introduce TN-XXL into T cells by retroviral transduction were unsuccessful (Fig. 2a). A systematic dissection of TN-XXL components revealed that the individual elements (for example, cpCitrine, one of the tandem fluorophores) were expressed readily in T cells in the expected amounts. However, the combination of both fluorophores, with or without the TnC domain, was not expressed, suggesting that it is the combination of CFP-cpCitrine that hinders expression of the calcium indicator in T cells (Fig. 2a).

**Optimization of TN-XXL for expression in primary T cells**

CFP and cpCitrine are both derived from jellyfish GFP<sup>11</sup> and share a sequence homology of 97%. Suspecting that this high homology was a key obstacle to efficient TN-XXL expression in T cells, we replaced CFP with coral-derived blue fluorescent protein (BFP)<sup>12</sup>, which has



only 62% homology with cpCitrine. Indeed, this exchange restored the desired expression of cpCitrine in primary T cells (Fig. 2a); however, because BFP and cpCitrine do not form an efficient FRET pair, BFP cannot be used to replace CFP for calcium imaging.

Therefore, we used codon diversification to reduce the sequence homologies between CFP and cpCitrine, and also between the repetitive lobes of TnC<sup>5</sup>, while maintaining the original amino acid sequence (Supplementary Fig. 3). This reduced the homology between CFP and cpCitrine to 80% and the homology between the lobes of TnC to 75%. The codon-diversified calcium indicator TN-XXL<sup>CD</sup> showed a tenfold increase in the proportion of transduced T cells compared with the unmodified TN-XXL (Fig. 2a). Expression of TN-XXL<sup>CD</sup> was enhanced further by truncating the retroviral vector size (Supplementary Fig. 4), resulting in a sevenfold increase in the fluorescence intensity (Fig. 2a).

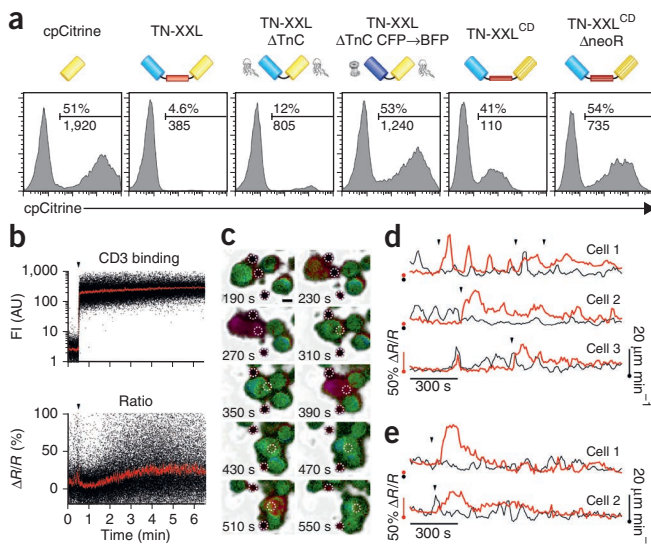


**Figure 2** Expression and characterization of TN-XXL in primary T cells. (a) Schematic representation of TN-XXL and its derivatives (top), and the corresponding expression levels in wild-type CD4<sup>+</sup> T cells after retroviral transduction (bottom). Percentages of transduced T cells and mean fluorescence intensities are indicated. (b) FACS-based calcium measurements in TN-XXL<sup>CD</sup>-expressing 2D2 T cells. Binding of complexes between anti-CD3-biotin and streptavidin-allophycocyanin (downward arrowheads) as seen by a rapid increase in allophycocyanin fluorescence (top) induces calcium mobilization in T cells (bottom). (c) Series of sample images of a 2D2 T cell interacting with anti-CD3/CD28 beads taken from cell 1 of Supplementary Video 2. Beads are encircled with white dotted lines, the timestamps given are in s; scale bar, 10  $\mu$ m. (d) Sample tracks of intracellular calcium concentrations and cell velocities of T cells engaging with anti-CD3/CD28 beads; dots depict zero levels of ratio (red) and velocity (black). (e) Example tracks of intracellular calcium concentrations and velocities of T cells interacting with antigen-pulsed IgH<sup>MOG</sup> B cells. The time points of contact initiation are indicated (downward arrowheads), and dots depict zero levels of ratio (red) and velocity (black). Results are representative of at least three similar experiments.



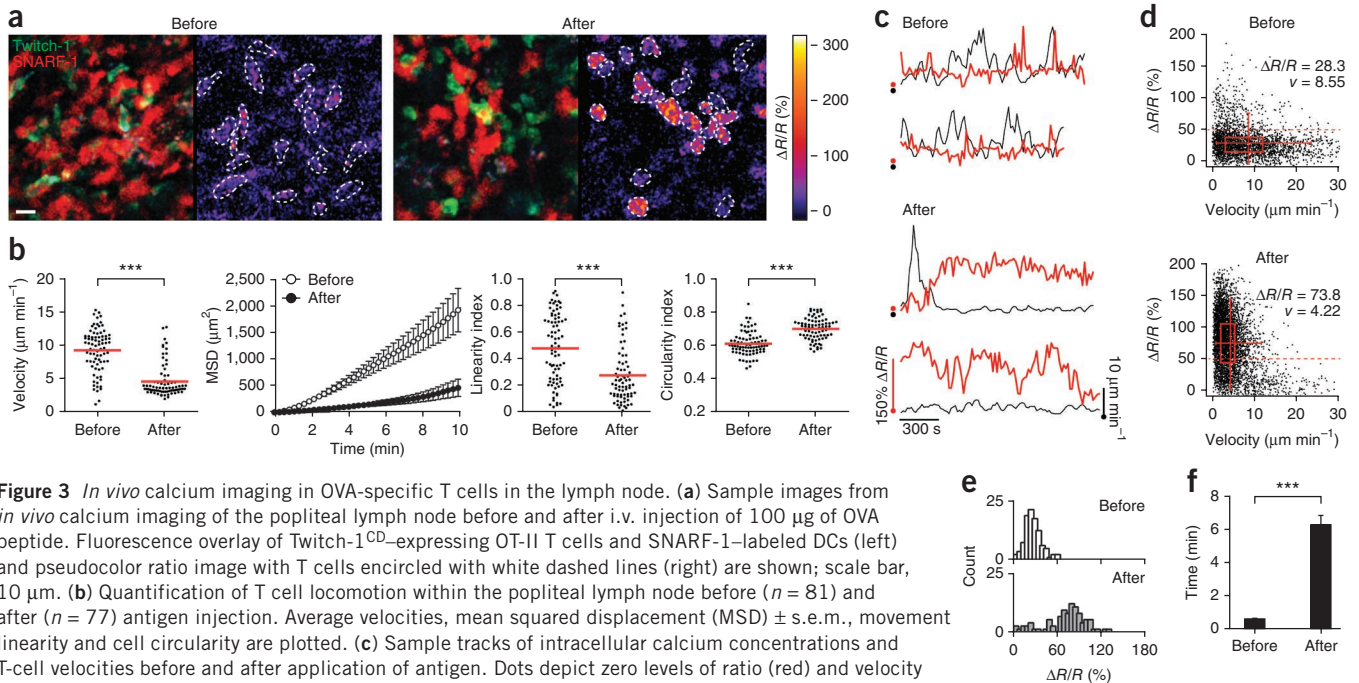


**Figure 3** *In vivo* calcium imaging in OVA-specific T cells in the lymph node. (a) Sample images from *in vivo* calcium imaging of the popliteal lymph node before and after i.v. injection of 100  $\mu$ g of OVA peptide. Fluorescence overlay of Twitch-1<sup>CD</sup>-expressing OT-II T cells and SNARF-1-labeled DCs (left) and pseudocolor ratio image with T cells encircled with white dashed lines (right) are shown; scale bar, 10  $\mu$ m. (b) Quantification of T cell locomotion within the popliteal lymph node before ( $n = 81$ ) and after ( $n = 77$ ) antigen injection. Average velocities, mean squared displacement (MSD)  $\pm$  s.e.m., movement linearity and cell circularity are plotted. (c) Sample tracks of intracellular calcium concentrations and T-cell velocities before and after application of antigen. Dots depict zero levels of ratio (red) and velocity (black). (d) Scatter plots showing cell velocity versus calcium-indicator ratio change for each individual timepoint analyzed before ( $n = 3,139$ ) and after ( $n = 5,136$ ) antigen injection. Mean values for  $\Delta R/R$  and velocity ( $v$ ) are indicated along with a two-dimensional box plot. (e) Distribution of average intracellular calcium concentration. (f) Duration of increased calcium concentrations with a  $\Delta R/R$  above 50%. Data are presented as the mean  $\pm$  s.e.m. \*\*\* $P < 0.001$ . Results represent one of three similar experiments.

**Characterization of calcium indicator-expressing T cells**

We assessed the functionality of the calcium indicator in retrovirally transduced CD4<sup>+</sup> T cells from 2D2 mice<sup>13</sup> and TCR<sup>1640</sup> mice<sup>14</sup>, both of which are transgenic for a T cell receptor (TCR) specific for myelin oligodendrocyte glycoprotein (MOG), and in retrovirally transduced ovalbumin (OVA)-specific CD4<sup>+</sup> T cells from OT-II mice<sup>15</sup>. Calcium mobilization after CD3 stimulation was detectable at the population level (Fig. 2b) as well as in individual cells. The activation of individual TN-XXL<sup>CD</sup>-expressing T cells by beads coated with antibodies to CD3 and CD28 (anti-CD3/CD28 beads) was reflected by a prompt ratiometric increase that indicated a rapid rise in cytoplasmic calcium (Fig. 2c,d and Supplementary Video 2). We obtained similar results with MOG-pulsed IgH<sup>MOG</sup> B cells<sup>16</sup> as APCs (Fig. 2e and Supplementary Video 3). The transduction rates of CD4<sup>+</sup> T cells were consistently greater than 30%, and the fluorescence intensities remained stable after the adoptive transfer of T cells (Supplementary Fig. 5). However, despite the efficient expression in T cells, our initial attempts to use TN-XXL<sup>CD</sup> to visualize calcium concentration changes in T cells *in vivo* resulted in only scarce and faint signals (data not shown). To increase the sensitivity, we used an advanced version of TN-XXL, termed Twitch-1. Similar to TN-XXL, Twitch-1 contains CFP and cpCitrine as a FRET pair, but it features a minimal-domain single TnC C-terminal lobe with a higher calcium affinity (T.T. and O.G., unpublished data). Twitch-1 was equally codon diversified to produce Twitch-1<sup>CD</sup> (Supplementary Fig. 6), which again allowed for the efficient transduction of primary T cells (Supplementary Fig. 7a). The *in situ* calcium calibration revealed that Twitch-1<sup>CD</sup> showed a 3.5-fold higher calcium affinity. Therefore, Twitch-1<sup>CD</sup> was more suitable for measuring physiologically relevant intracellular calcium concentration changes in T cells (Supplementary Fig. 7b).

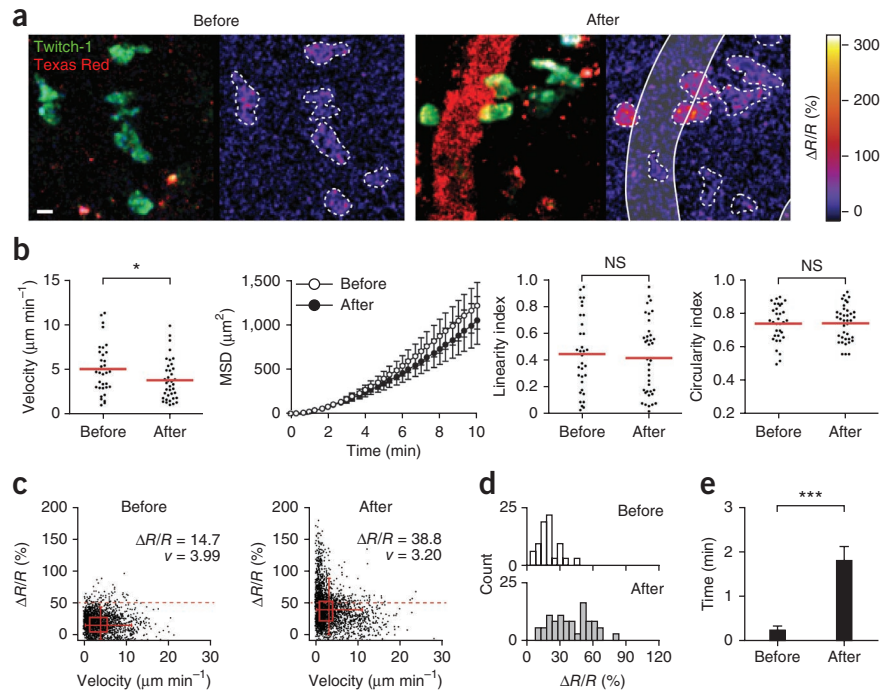
As shown in previous studies<sup>17</sup>, retroviral transduction did not interfere with T cell function. The activation markers on T cells

cultured *in vitro* were indistinguishable between TN-XXL<sup>CD</sup>- or Twitch-1<sup>CD</sup>-expressing T cells and control T cells (Supplementary Fig. 8a), and the frequencies of the calcium indicator-expressing cells remained stable over time (Supplementary Fig. 8b). Furthermore, the expression of cytokines (Supplementary Fig. 8c) and the proliferation of T cells (Supplementary Fig. 8d) were comparable. Most notably, the encephalitogenic potential of MOG-specific T cells was unaffected by calcium indicator expression. The adoptive transfer of TN-XXL<sup>CD</sup>-transduced, Twitch-1<sup>CD</sup>-transduced or control TCR<sup>1640</sup> T cells into SJL/J recipients triggered transfer EAE with similar outcomes in severity and disease course (Supplementary Fig. 9).

**Calcium dynamics in T cells in peripheral lymph nodes**

Initially, we used Twitch-1<sup>CD</sup> to trace the antigen-dependent activation of OT-II T cells by dendritic cells (DCs) in lymph nodes *in vivo* before and after intravenous (i.v.) injection of OVA<sub>323-339</sub> peptide (Fig. 3a and Supplementary Video 4). In the absence of cognate antigen, the OT-II T cells showed a high motility and a large displacement (Fig. 3b) accompanied by a generally very low calcium signature with a few short-lasting peaks (Fig. 3c). This changed notably after i.v. injection of OVA peptide. In minutes, the T cells engaged with DCs, greatly reduced their motility and showed a more rounded phenotype (Fig. 3b). Furthermore, the calcium concentrations in T cells increased markedly and eventually began a continuous oscillation (Fig. 3c). These calcium responses were associated with sustained T cell contact with DCs (Supplementary Video 5). The quantification of calcium concentrations revealed a strong inverse correlation with cell motility: T cells with low calcium concentrations were highly motile, whereas T cells with elevated calcium slowed down considerably (Fig. 3d). Furthermore, the overall distribution of average calcium concentrations was skewed markedly toward higher values after injection of OVA peptide (Fig. 3e). Whereas the T cells showed

**Figure 4** *In vivo* calcium imaging in extravasated OVA-specific T cells during EAE in the spinal cord. **(a)** Sample images from *in vivo* calcium imaging of OT-II T cells in the spinal cord during EAE before and after *i.v.* injection of 100  $\mu\text{g}$  of OVA peptide and Texas Red dextran. Fluorescence overlay of Twitch-1<sup>CD</sup>-expressing OT-II T cells with *i.v.*-infused Texas Red dextran (left) and pseudocolor ratio image with T cells encircled with white dashed lines and blood vessel walls retraced (right) are shown; scale bar, 5  $\mu\text{m}$ . **(b)** Quantification of T cell locomotion within the spinal cord before ( $n = 33$ ) and after ( $n = 38$ ) antigen injection. Average velocities, MSD  $\pm$  s.e.m., movement linearity and cell circularity are plotted. NS, not significant. **(c)** Scatter plots showing cell velocity versus calcium-indicator ratio change for each individual timepoint before ( $n = 2,749$ ) and after ( $n = 3,460$ ) antigen injection. Mean values for  $\Delta R/R$  and velocity ( $v$ ) are indicated along with a two-dimensional box plot. **(d)** Distribution of average intracellular calcium concentrations. **(e)** Duration of increased calcium concentrations with a  $\Delta R/R$  above 50%. Data are presented as the mean  $\pm$  s.e.m. \* $P < 0.05$ , \*\*\* $P < 0.001$ . Results represent one of three similar experiments.



only short-lived calcium peaks in the absence of antigen, antigen encounter triggered an increase in calcium that persisted over several minutes (Fig. 3f).

Second, to test the universal applicability of Twitch-1<sup>CD</sup>, we used myelin-specific 2D2 T cells in an identical *in vivo* imaging setting. Similar to OT-II T cells, Twitch-1<sup>CD</sup>-transduced 2D2 T cells showed high mobility within the lymph node tissue in the absence of cognate antigen (Supplementary Fig. 10a). It is known that 2D2 T cells recognize two brain autoantigens, MOG and NF-M<sup>18</sup>, and show a heteroclitic, stronger responsiveness to NF-M<sup>19</sup>. Again, injection of NF-M<sub>11-34</sub> peptide induced strong calcium signals in T cells (Supplementary Video 6). The 2D2 T cells also notably reduced their velocity after antigen injection; this reduction in velocity again correlated with increased calcium concentrations (Supplementary Fig. 10b–d).

### Presentation of cognate antigen in the inflamed CNS

The presentation of autoantigen by leptomeningeal APCs is a key event in the initiation of EAE. However, the identity of local APCs may differ from classic peripheral DCs<sup>9,20</sup>. To assess directly their antigen-presenting potential, we visualized the presentation of OVA to Twitch-1<sup>CD</sup>-transduced OT-II cells in the leptomeninges. OT-II cells, like all non-self-specific T cells, are generally excluded from the brain. However, they can be piloted into autoimmune CNS infiltrates by encephalitogenic T cells.

Two-photon imaging confirmed that in the absence of antigen, Twitch-1<sup>CD</sup>-transduced OT-II T cells migrated randomly through the leptomeningeal space (Fig. 4a,b and Supplementary Video 7), and their calcium signatures were generally very low (Fig. 4c). However, promptly after *i.v.* injection of OVA peptide, a substantial proportion of the OT-II T cells was arrested, and as seen in the lymph nodes, many of the immobilized T cells had increased calcium concentrations (Fig. 4c,d) that persisted over several minutes (Fig. 4e). This increase was pronounced particularly in those T cells closely associated with blood vessels (Supplementary Video 7); however, the overall motility

of these cells was less drastically affected by antigen application (Fig. 4b) than that of T cells in the lymph node setting.

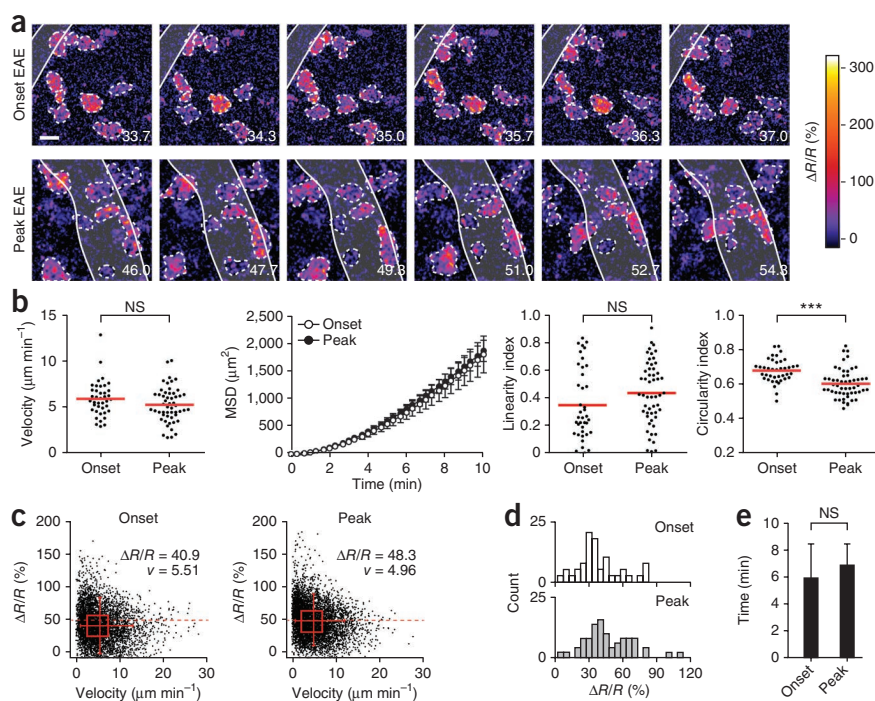
### Calcium dynamics in encephalitogenic T cells in the CNS

Previously, we proposed that leptomeningeal APCs sequentially activate freshly arriving effector T cells by presenting myelin autoantigen at limiting doses. However, the evidence supporting this theory remained circumstantial<sup>9</sup>. To record the calcium dynamics in CNS autoantigen-specific T cells directly, we transferred Twitch-1<sup>CD</sup>-transduced 2D2 T cells into *Rag2*<sup>-/-</sup> mice, which lack T and B cells.

During incipient EAE (score 0.5), *in vivo* imaging showed extravasated T cells crawling within the perivascular space or freely migrating through the leptomeningeal milieu. Unlike in OT-II T cells, increased intracellular calcium concentrations and ongoing calcium oscillations were seen in clustered as well as migratory 2D2 T cells (Fig. 5a and Supplementary Video 8). Notably, during peak EAE (score >2), the calcium signaling in extravasated T cells assumed a similar pattern (Supplementary Video 9). Again, a number of T cells arrested in cell clusters showed increased intracellular calcium concentrations and calcium oscillations (Fig. 5a). 2D2 T cells migrated randomly through the leptomeningeal space at the onset as well as at the peak of EAE (Fig. 5b). These encephalitogenic T cells showed elevated calcium concentrations over several minutes without demonstrable arrests (Fig. 5c–e). In addition, we noted some migrant T cells that were stopping to interact with antigen-presenting phagocytes, resulting in sustained intracellular calcium signaling (Supplementary Fig. 11a). Furthermore, in some T cells, subcellular calcium signaling was observed. Some stationary T cells had increased calcium in the perikarya but not in the uropod-like processes (Supplementary Fig. 11b), a behavior reminiscent of chemokine-directed locomotion<sup>21</sup>.

Supplementary Figure 12 summarizes the different calcium responses of OVA-specific OT-II T cells and encephalitogenic self-reactive 2D2 T cells in the lymph nodes and the CNS. Many of the migrant 2D2 T cells maintained increased calcium concentrations

**Figure 5** *In vivo* calcium signaling in extravasated 2D2 T cells during EAE. (a) Calcium signals in extravasated clusters of T cells in the inflamed spinal cord during EAE onset (top, **Supplementary Video 8**) and peak EAE (bottom, **Supplementary Video 9**). Pseudocolor ratio images with T cells encircled with white dashed lines and blood vessel walls retraced are shown. The time intervals given are in min; scale bar, 10  $\mu\text{m}$ . (b) Quantification of T cell locomotion in the spinal cord at the onset ( $n = 40$ ) and peak ( $n = 53$ ) of EAE. Average velocities, MSD  $\pm$  s.e.m., movement linearity, and cell circularity are plotted. (c) Scatter plots showing cell velocity versus calcium-indicator ratio change for each individual time point analyzed at the onset ( $n = 5,497$ ) and peak ( $n = 6,565$ ) of EAE. Mean values for  $\Delta R/R$  and velocity ( $v$ ) are indicated along with a two-dimensional box plot. (d) Distribution of average intracellular calcium concentration. (e) Duration of increased calcium concentrations with a  $\Delta R/R$  above 50%. Data are presented as the mean  $\pm$  s.e.m. \*\*\* $P < 0.001$ . NS, not significant. Results represent one of at least three similar experiments.



while navigating through the leptomeninges. The pronounced inverse correlation of T cell motility and intracellular calcium concentration, which was so clear-cut in the T cells in the lymph nodes, was not apparent in the encephalitogenic 2D2 T cells in the leptomeninges.

**DISCUSSION**

Calcium is an essential second messenger in cascades induced by signals from the surrounding milieu. Like most other cell types, lymphocytes communicate with their surroundings through membrane structures such as adhesion molecules and receptors for soluble factors. However, they also use specialized receptors to sense specific antigens. Typically, received signals lead to an immediate change in intracellular calcium concentration, which can trigger immune cell responses or initiate cell differentiation<sup>22</sup>. Hence, monitoring calcium concentrations in living immune cells offers a way to monitor in real time an unfolding immune response *in vitro* as well as *in vivo*.

Until recently, researchers relied on synthetic indicator molecules to measure calcium in T cells. This method is applicable to short-term experimentation *in vitro* but fails in extended *in vivo* studies owing to active export of synthetic indicators from loaded cells<sup>23</sup>. Instead, a new generation of GECIs has become available for *in vivo* studies. Single-GFP variants, such as GCaMPs, are useful for studying stationary cells<sup>24</sup> but less suitable for motile cells, such as lymphocytes, as locomotion affects the fluorescence intensity and thus generates false signals. This problem does not limit FRET-based ratiometric indicators such as TN-XXL<sup>5</sup>.

We found that the original TN-XXL construct was functionally expressed in numerous tissues and cells but, unexpectedly, was not expressed in primary T cells. This failure was noted both in transduced T cells and in TN-XXL transgenic mice<sup>25</sup>. We suspected that the extensive sequence homology of the two fluorophores in the indicator might have contributed to the failed expression. Indeed, a previous study of retroviral vectors with large direct sequence repeats found that all the expressed retroviruses had deletions of those repeats<sup>26</sup>. These deletions are most probably introduced by the high rate of

intramolecular template-switching activity of reverse transcriptase, resulting in the loss of homologous sequences<sup>27</sup>. In the case of TN-XXL, our efforts to diversify the codons of one TN-XXL fluorophore gave rise to TN-XXL<sup>CD</sup>, which was efficiently expressed in T cells after retroviral transduction.

We improved the affinity of the calcium sensor by replacing the TnC domain with a higher affinity calcium-binding moiety, resulting in the highly sensitive Twitch-1<sup>CD</sup>. Notably, although Twitch-1 features a 3.5-fold higher calcium affinity than TN-XXL, the intracellular concentrations of GECIs are lower compared with those of synthetic dyes, which have been shown to have adverse effects on normal cell physiology at high concentrations<sup>28</sup>. Acetoxymethyl ester derivatives of synthetic indicators usually have an intracellular concentration 100-fold higher than the extracellular loading concentration<sup>29</sup>, resulting in an intracellular concentration of about 200  $\mu\text{M}$ <sup>30</sup>. GECIs, in contrast, are expressed in the range of 5 to 20  $\mu\text{M}$ <sup>31</sup> and are therefore less likely to lead to calcium-buffering effects. In line with this, we have not noted any adverse effects of long-term GECI expression in our Twitch-1<sup>CD</sup>-expressing T cells.

The strength and rhythm of calcium signaling determine the activation of transcription factors and implicitly the cellular response<sup>32</sup>. In T cells, calcium elevation is not exclusively related to antigen recognition events. We noted, for example, that in antigen-free lymph nodes, both OVA-specific OT-II T cells and MOG-specific 2D2 T cells showed scattered transient calcium peaks. A similar behavior was described previously *in vivo*, where contacts between MOG-specific T cells and DCs were essential for maintaining T cell reactivity<sup>33</sup>.

A central aim of our study was to characterize the activation events in encephalitogenic T cells as they pass through the blood-brain barrier. Previously, we showed that T cells that have crossed the blood-brain barrier establish contacts with perivascular phagocytes, which present myelin autoantigen at low doses<sup>9,34</sup>. In this study, we directly followed the activation events in T cells through calcium imaging *in vivo*. In the leptomeningeal milieu, the portal to the CNS target tissue, the immigrant T cells had elevated intracellular calcium



concentrations that were maintained throughout the T-cell migration within the spinal cord. This was in stark contrast to the behavior of T cells recognizing exogenous antigen in peripheral lymph nodes, which coincides with an immediate and sustained elevation in intracellular calcium and an arrest of migratory T cells<sup>35,36</sup>.

We suggest that encephalitogenic T cells enter the leptomeningeal space and recognize small limiting amounts of local myelin autoantigen presented by the leptomeningeal phagocytes. In fact, previous studies have shown that antigen potency controls the contact period between APCs and CD8<sup>+</sup> T cells<sup>37</sup> or CD4<sup>+</sup> T cells<sup>38</sup>, and as indicated by functional assays, phagocytes that are freshly isolated from the leptomeninges present local myelin antigens at minimal doses<sup>9</sup>. Low autoantigen-dependent activation is too weak to arrest effector T cells in contact with APCs over extended periods. However, it may be sufficient to warrant induction and expression of surface structures required for directing cells to their ultimate destination. We hypothesize that this limited activation may guide the movement of newly invading T cells from the vascular wall into the target tissue.

In summary, we show here a universally applicable tool, Twitch-1<sup>CD</sup>, which will be useful for retracing in detail the multiple antigen-dependent and antigen-independent cell contacts of T cells as they move into and within their target tissues.

## METHODS

Methods and any associated references are available in the [online version of the paper](#).

Note: Supplementary information is available in the [online version of the paper](#).

## ACKNOWLEDGMENTS

This work was supported by the Deutsche Forschungsgemeinschaft (Sonderforschungsbereich 571, projects B6 and C6), the German Competence Network on Multiple Sclerosis (KKNMS), the Novartis Foundation for Therapeutic Research and the Max Planck Society. O.G. and T.T. were supported by the Deutsche Forschungsgemeinschaft (Sonderforschungsbereich 870) and the EuroVision EU FP7 grant. We thank I. Arnold-Ammer, L. Penner, and B. Kunkel for technical assistance.

## AUTHOR CONTRIBUTIONS

M.M. established the calcium indicator expression in T cells and performed all experiments except two-photon imaging. I.B. performed the mouse surgery and *in vivo* two-photon imaging. M.M. and I.B. designed experiments and analyzed data. T.T. and O.G. generated the higher-affinity calcium indicator Twitch-1. H.W., N.K. and G.K. supervised the study. M.M., G.K. and H.W. wrote the manuscript.

## COMPETING FINANCIAL INTERESTS

The authors declare no competing financial interests.

Reprints and permissions information is available online at <http://www.nature.com/reprints/index.html>.

1. Vig, M. & Kinet, J.P. Calcium signaling in immune cells. *Nat. Immunol.* **10**, 21–27 (2009).
2. Oh-hora, M. & Rao, A. Calcium signaling in lymphocytes. *Curr. Opin. Immunol.* **20**, 250–258 (2008).
3. Lioudyno, M.I. *et al.* Orai1 and STIM1 move to the immunological synapse and are upregulated during T-cell activation. *Proc. Natl. Acad. Sci. USA* **105**, 2011–2016 (2008).
4. Wei, S.H. *et al.* Ca<sup>2+</sup> signals in CD4<sup>+</sup> T cells during early contacts with antigen-bearing dendritic cells in lymph node. *J. Immunol.* **179**, 1586–1594 (2007).
5. Mank, M. *et al.* A genetically encoded calcium indicator for chronic *in vivo* two-photon imaging. *Nat. Methods* **5**, 805–811 (2008).
6. Reiff, D.F., Plett, J., Mank, M., Griesbeck, O. & Borst, A. Visualizing retinotopic half-wave rectified input to the motion detection circuitry of *Drosophila*. *Nat. Neurosci.* **13**, 973–978 (2010).
7. Nguyen, Q.T. *et al.* An *in vivo* biosensor for neurotransmitter release and *in situ* receptor activity. *Nat. Neurosci.* **13**, 127–132 (2010).

8. Siffrin, V. *et al.* *In vivo* imaging of partially reversible Th17 cell-induced neuronal dysfunction in the course of encephalomyelitis. *Immunity* **33**, 424–436 (2010).
9. Bartholomäus, I. *et al.* Effector T-cell interactions with meningeal vascular structures in nascent autoimmune CNS lesions. *Nature* **462**, 94–98 (2009).
10. Sommer, F., Bischof, S., Röllinghoff, M. & Lohoff, M. Demonstration of organic anion transport in T lymphocytes. L-lactate and fluo-3 are target molecules. *J. Immunol.* **153**, 3523–3532 (1994).
11. Prasher, D.C., Eckenrode, V.K., Ward, W.W., Prendergast, F.G. & Cormier, M.J. Primary structure of the *Aequorea victoria* green-fluorescent protein. *Gene* **111**, 229–233 (1992).
12. Subach, O.M. *et al.* Conversion of red fluorescent protein into a bright blue probe. *Chem. Biol.* **15**, 1116–1124 (2008).
13. Bettelli, E. *et al.* Myelin oligodendrocyte glycoprotein-specific T-cell receptor transgenic mice develop spontaneous autoimmune optic neuritis. *J. Exp. Med.* **197**, 1073–1081 (2003).
14. Pöllinger, B. *et al.* Spontaneous relapsing-remitting EAE in the SJL/J mouse: MOG-reactive transgenic T cells recruit endogenous MOG-specific B cells. *J. Exp. Med.* **206**, 1303–1316 (2009).
15. Barnden, M.J., Allison, J., Heath, W.R. & Carbone, F.R. Defective TCR expression in transgenic mice constructed using cDNA-based  $\alpha$ - and  $\beta$ -chain genes under the control of heterologous regulatory elements. *Immunol. Cell Biol.* **76**, 34–40 (1998).
16. Litzemberger, T. *et al.* B lymphocytes producing demyelinating autoantibodies: development and function in gene-targeted transgenic mice. *J. Exp. Med.* **188**, 169–180 (1998).
17. Flügel, A., Willem, M., Berkowicz, T. & Wekerle, H. Gene transfer into CD4<sup>+</sup> T lymphocytes: green fluorescent protein engineered, encephalitogenic T cells used to illuminate immune responses in the brain. *Nat. Med.* **5**, 843–847 (1999).
18. Krishnamoorthy, G. *et al.* Myelin-specific T cells also recognize neuronal autoantigen in a transgenic mouse model of multiple sclerosis. *Nat. Med.* **15**, 626–632 (2009).
19. Rosenthal, K.M. *et al.* Low two-dimensional CD4 T-cell receptor affinity for myelin sets in motion delayed response kinetics. *PLoS ONE* **7**, e32562 (2012).
20. Kivisäkk, P. *et al.* Localizing central nervous system immune surveillance: meningeal antigen-presenting cells activate T cells during experimental autoimmune encephalomyelitis. *Ann. Neurol.* **65**, 457–469 (2009).
21. Colvin, R.A. *et al.* Synaptotagmin-mediated vesicle fusion regulates cell migration. *Nat. Immunol.* **11**, 495–502 (2010).
22. Feske, S. Calcium signaling in lymphocyte activation and disease. *Nat. Rev. Immunol.* **7**, 690–702 (2007).
23. Homolya, L. *et al.* Fluorescent cellular indicators are extruded by the multidrug-resistance protein. *J. Biol. Chem.* **268**, 21493–21496 (1993).
24. Zhao, Y. *et al.* An expanded palette of genetically encoded Ca<sup>2+</sup> indicators. *Science* **333**, 1888–1891 (2011).
25. Drenth, S. *et al.* Biocompatibility of a genetically encoded calcium indicator in a transgenic mouse model. *Nat. Commun.* **3**, 1031 (2012).
26. Rhode, B.W., Emerman, M. & Temin, H.M. Instability of large direct repeats in retrovirus vectors. *J. Virol.* **61**, 925–927 (1987).
27. Delviks-Frankenberry, K. *et al.* Mechanisms and factors that influence high frequency retroviral recombination. *Viruses* **3**, 1650–1680 (2011).
28. Helmchen, F., Imoto, K. & Sakmann, B. Ca<sup>2+</sup> buffering and action potential-evoked Ca<sup>2+</sup> signaling in dendrites of pyramidal neurons. *Biophys. J.* **70**, 1069–1081 (1996).
29. Tsien, R.Y., Pozzan, T. & Rink, T.J. Calcium homeostasis in intact lymphocytes: cytoplasmic free calcium monitored with a new, intracellularly trapped fluorescent indicator. *J. Cell Biol.* **94**, 325–334 (1982).
30. Owen, C.S. Quantitation of lymphocyte intracellular free calcium signals using indo-1. *Cell Calcium* **9**, 141–147 (1988).
31. Hires, S.A., Tian, L. & Looger, L.L. Reporting neural activity with genetically encoded calcium indicators. *Brain Cell Biol.* **36**, 69–86 (2008).
32. Dolmetsch, R.E., Lewis, R.S., Goodnow, C.C. & Healy, J.I. Differential activation of transcription factors induced by Ca<sup>2+</sup> response amplitude and duration. *Nature* **386**, 855–858 (1997).
33. Hochweller, K. *et al.* Dendritic cells control T cell tonic signaling required for responsiveness to foreign antigen. *Proc. Natl. Acad. Sci. USA* **107**, 5931–5936 (2010).
34. Odoardi, F., Kawakami, N., Klinkert, W.E.F., Wekerle, H. & Flügel, A. Blood-borne soluble protein antigen intensifies T cell activation in autoimmune CNS lesions and exacerbates clinical disease. *Proc. Natl. Acad. Sci. USA* **104**, 18625–18630 (2007).
35. Mempel, T.R., Henrickson, S.E. & von Andrian, U.H. T-cell priming by dendritic cells in lymph nodes occurs in three distinct phases. *Nature* **427**, 154–159 (2004).
36. Shakhur, G. *et al.* Stable T cell–dendritic cell interactions precede the development of both tolerance and immunity *in vivo*. *Nat. Immunol.* **6**, 707–714 (2005).
37. Henrickson, S.E. *et al.* T cell sensing of antigen dose governs interactive behavior with dendritic cells and sets a threshold for T cell activation. *Nat. Immunol.* **9**, 282–291 (2008).
38. Skokos, D. *et al.* Peptide-MHC potency governs dynamic interactions between T cells and dendritic cells in lymph nodes. *Nat. Immunol.* **8**, 835–844 (2007).



## ONLINE METHODS

**Mice.** 2D2 (ref. 13), IgH<sup>MOG</sup> (ref. 16), TCR<sup>1640</sup> (ref. 14), OT-II (ref. 15), and *Rag2*<sup>-/-</sup> (Jackson Laboratories) mice, along with C57BL/6 and SJL/J mice, were bred in the facilities of the Max Planck Institute of Neurobiology. All procedures were in accordance with the guidelines of the committee on animals of the Max Planck Institute of Neurobiology and were approved by the Regierung von Oberbayern.

**Retroviral transduction of T cells.** We transfected Phoenix ecotropic packaging cells using the calcium phosphate–chloroquine method with 12 µg of pMSCV and 3.5 µg of pCL-Eco plasmid. The virus-containing supernatant was collected 48 h later, replaced with fresh medium and centrifuged at 6,000 r.c.f. overnight. We resuspended the pellets in fresh supernatant from the transfected Phoenix cells and passed them through a 0.45-µm pore-sized filter before the filtrate was used for transduction. Splenocyte suspensions were prepared by forcing spleens through 40-µm strainers (BD Biosciences) followed by erythrocyte lysis using 0.83% NH<sub>4</sub>Cl. For the transduction of wild-type T cells, we purified CD4<sup>+</sup> T cells using the MagCollect CD4<sup>+</sup> T Cell Isolation Kit (R&D) and stimulated them using plate-bound antibodies to CD3 and CD28 (BD Biosciences). The next day, the T cells were suspended in retrovirus supernatant supplemented with 8 µg ml<sup>-1</sup> polybrene (Sigma-Aldrich) and 10 ng ml<sup>-1</sup> IL-2 (PeproTech) and were spin-infected at 450 r.c.f. for 90 min at room temperature. For the transduction of TCR transgenic T cells, we cultured 2D2 × IgH<sup>MOG</sup>, TCR<sup>1640</sup> × IgH<sup>MOG</sup> or OT-II splenocytes in the presence of 20 µg ml<sup>-1</sup> recombinant MOG or 10 µg ml<sup>-1</sup> OVA<sub>323–339</sub> peptide. After 48 h, the cultures were depleted of B cells using Dynabeads Mouse Pan B (Invitrogen) and transduced as described above.

**In vivo two-photon microscopy.** We performed time-lapse, two-photon laser-scanning microscopy using a SP2 confocal microscope (Leica) equipped with a 10 W Millennia/Tsunami laser (Newport Spectra Physics). The laser was tuned to 835 nm and routed through a Leica ×25 water immersion objective (numerical aperture 0.95). Typically, 240 × 240 µm areas were scanned, and 25–30 µm *z*-stacks were acquired using a 3–4 µm *z*-step. The acquisition rate was at 16- to 20-s intervals, with images averaged twice. The fluorescence signals were detected using non-descanned photomultiplier tube (PMT) detectors (Hamamatsu) equipped with 475/50 nm (CFP), 537/26 nm (FRET), and 630/69 nm (SNARF-1, Texas Red) band-pass filters (Semrock). We kept the

PMT voltage settings for CFP and FRET fluorescence identical in all experiments. The bleed-through of CFP into the FRET channel was determined to be 44%. The fraction of cpCitrine emission in the CFP channel and direct excitation of cpCitrine at 835 nm was negligible. We anesthetized mice by i.p. injection with fentanyl, midazolam and medetomidine (50, 50 and 500 µg per kg body weight, respectively), intubated and ventilated them with 1.5% isoflurane. The popliteal lymph nodes were exposed by cutting the skin at the hollow of the knee and dissecting the adductor musculature. For EAE imaging, we prepared a spinal cord window at level Th12/L1. After a midline skin incision, the paravertebral musculature was detached and a laminectomy on one spinal disc was done. The mice were stabilized in a custom-made stage, and their body temperatures were regulated using a heated pad (37.5 °C). We recorded electrocardiograms and constantly monitored physiological parameters. Blood vessels were visualized by i.v. infusion of Texas Red–conjugated dextran (50 µg; 70 kDa; Invitrogen).

**Statistical analyses.** We acquired time-lapse images using Leica LCS software and subsequently processed them by and analyzed them with ImageJ software (US National Institutes of Health). To obtain two-dimensional videos, we applied a Gaussian blur filter and made maximum intensity *z*-projections. Artifacts from tissue drift were removed using the StackReg/TurboReg plugin for ImageJ. Ratiometric pseudocolor pictures were generated by dividing the FRET by the CFP channel and applying a fire lookup table. For analysis, we manually outlined the cell shape at each time point in the maximum projection picture and calculated the average signal intensities within this area. The computing of motility parameters and calcium signals was performed using Excel (Microsoft). We corrected the FRET signal for CFP bleed-through, cFRET = FRET – 0.44 × CFP, and normalized the ratios of cFRET/CFP to show the fractional change in the emission ratio as  $\Delta R/R = (R - R_0)/R_0$  (*R*, actual ratio; *R*<sub>0</sub>, ratio at zero calcium). Because accurate calcium calibration *in vivo* is error prone, calcium concentration changes are not translated into definite intracellular calcium concentrations. The box plots overlaid on the scatter plots depict the twenty-fifth and seventy-fifth percentiles with the box, whereas the whiskers represent the fifth and ninety-fifth percentiles. The linearity index is defined as the sum of the total displacement divided by the path length of a cell and the circularity index is defined as  $4\pi(\text{area}/\text{perimeter}^2)$ . The cell trajectories were calculated from the obtained coordinates and aligned for the starting position. All statistical analysis (Mann-Whitney *U*-test) was done with GraphPad Prism software.

# CHAPTER 4

---

## Optimized Ratiometric Calcium Sensors for Functional *In Vivo* Imaging of Neurons and T-Lymphocytes

**Thomas Thestrup**, Julia Litzlbauer, Ingo Bartholomäus, Marsilius Mues, Luigi Russo, Hod Dana, Yuri Kovalchuk, Yajie Liang, Georgios Kalamakis, Yvonne Laukat, Stefan Becker, Gregor Witte, Anselm Geiger, Taylor Allen, Lawrence C Rome, Tsai-Wen Chen, Douglas S. Kim, Olga Garaschuk, Christian Griesinger, Oliver Griesbeck

*Nature Methods* **11**, 175-182 (2014)

# Optimized ratiometric calcium sensors for functional *in vivo* imaging of neurons and T lymphocytes

Thomas Thestrup<sup>1,2</sup>, Julia Litzlbauer<sup>1</sup>, Ingo Bartholomäus<sup>1</sup>, Marsilius Mues<sup>1</sup>, Luigi Russo<sup>3</sup>, Hod Dana<sup>2</sup>, Yuri Kovalchuk<sup>4</sup>, Yajie Liang<sup>4</sup>, Georgios Kalamakis<sup>4</sup>, Yvonne Laukat<sup>3</sup>, Stefan Becker<sup>3</sup>, Gregor Witte<sup>5</sup>, Anselm Geiger<sup>1</sup>, Taylor Allen<sup>6</sup>, Lawrence C Rome<sup>7,8</sup>, Tsai-Wen Chen<sup>2</sup>, Douglas S Kim<sup>2</sup>, Olga Garaschuk<sup>4</sup>, Christian Griesinger<sup>3</sup> & Oliver Griesbeck<sup>1,2</sup>

**The quality of genetically encoded calcium indicators (GECIs) has improved dramatically in recent years, but high-performing ratiometric indicators are still rare. Here we describe a series of fluorescence resonance energy transfer (FRET)-based calcium biosensors with a reduced number of calcium binding sites per sensor. These ‘Twitch’ sensors are based on the C-terminal domain of *Opsanus* troponin C. Their FRET responses were optimized by a large-scale functional screen in bacterial colonies, refined by a secondary screen in rat hippocampal neuron cultures. We tested the *in vivo* performance of the most sensitive variants in the brain and lymph nodes of mice. The sensitivity of the Twitch sensors matched that of synthetic calcium dyes and allowed visualization of tonic action potential firing in neurons and high resolution functional tracking of T lymphocytes. Given their ratiometric readout, their brightness, large dynamic range and linear response properties, Twitch sensors represent versatile tools for neuroscience and immunology.**

Imaging with GECIs has become a widely used method in physiology and neuroscience<sup>1–3</sup>. According to readout mode, the design of the sensors has followed two different pathways, leading to single-wavelength sensors and FRET-based ratiometric sensors<sup>4–8</sup>. Among the most popular single-wavelength sensors are the G-CaMPs<sup>9–13</sup>, R-CaMPs<sup>14</sup> and GECOs<sup>15</sup>. FRET sensors include yellowameleon 3.60 (refs. 16,17), D3cpv<sup>18</sup>, yellowameleon Nano<sup>19</sup> and TN-XXL<sup>20</sup>.

Quantification by ratiometric FRET imaging is more accurate than single-channel measurements and may be more suitable for long-term functional imaging studies, as it is less influenced by changes in optical path length, excitation light intensity and indicator expression level and by tissue movement and growth during development. In addition, FRET indicators are substantially brighter than single-wavelength sensors at rest, allowing better identification of expressing cells and their subcellular structures.

Another practical feature of FRET-based indicators is their ability to measure basal Ca<sup>2+</sup> levels within cells, for example, to distinguish between resting and continuously spiking neurons—something that cannot easily be achieved with single-wavelength indicators<sup>21</sup>. Increased basal Ca<sup>2+</sup> levels within the brain are also observed at the onset of neurodegenerative processes, and ratiometric FRET calcium imaging has been used in these conditions to monitor disease progression<sup>22,23</sup>. Moreover, ratiometric indicators are advantageous for monitoring calcium in motile cells.

Both calmodulin and troponin C (TnC), the calcium binding proteins within the various GECIs, consist of two globular domains connected by a central linker<sup>24,25</sup>. Each domain possesses two calcium-binding EF hand motifs. Thus, currently available GECIs are highly nonlinear sensors binding up to four calcium ions per sensor. Identification of a smaller calcium-binding domain with fewer binding sites could help to reduce buffering during long-term chronic GECI expression<sup>26</sup>, make the sensor smaller and further minimize the risk of cytotoxicity. It may also help to simplify response properties and facilitate the biophysical modeling of sensor behavior.

Here we report several improvements of FRET-based calcium sensors for *in vivo* imaging. First, we identified a minimal calcium binding motif based on the C-terminal domain of TnC with only two or one remaining calcium binding sites per sensor molecule, thus reducing the overall calcium buffering of the sensors. Second, by sampling TnCs from various species we identified a new TnC variant from the toadfish *Opsanus tau*, which offered the possibility of generating minimal domains with high-affinity calcium binding. Third, we used a large-scale, two-step functional screen to optimize the FRET changes in the sensor by linker diversification. This approach allowed us to identify Twitch sensors with a superior FRET change and may become useful for optimizing other types of FRET sensors. Finally, we improved brightness and photostability of the sensors by incorporating enhanced donor and acceptor fluorescent protein variants. Taken together, these

<sup>1</sup>Max Planck Institute of Neurobiology, Martinsried, Germany. <sup>2</sup>Janelia Farm Research Campus, Howard Hughes Medical Institute, Ashburn, Virginia, USA. <sup>3</sup>Max Planck Institute for Biophysical Chemistry, NMR-based Structural Biology, Göttingen, Germany. <sup>4</sup>Institute of Physiology II, University of Tübingen, Tübingen, Germany. <sup>5</sup>Gene Center, Department of Biochemistry, University of Munich, Munich, Germany. <sup>6</sup>Oberlin College, Oberlin, Ohio, USA. <sup>7</sup>Department of Biology, University of Pennsylvania, Philadelphia, Pennsylvania, USA. <sup>8</sup>The Whitman Center, Marine Biological Lab, Woods Hole, Massachusetts, USA. Correspondence should be addressed to O. Griesbeck (griesbeck@neuro.mpg.de).

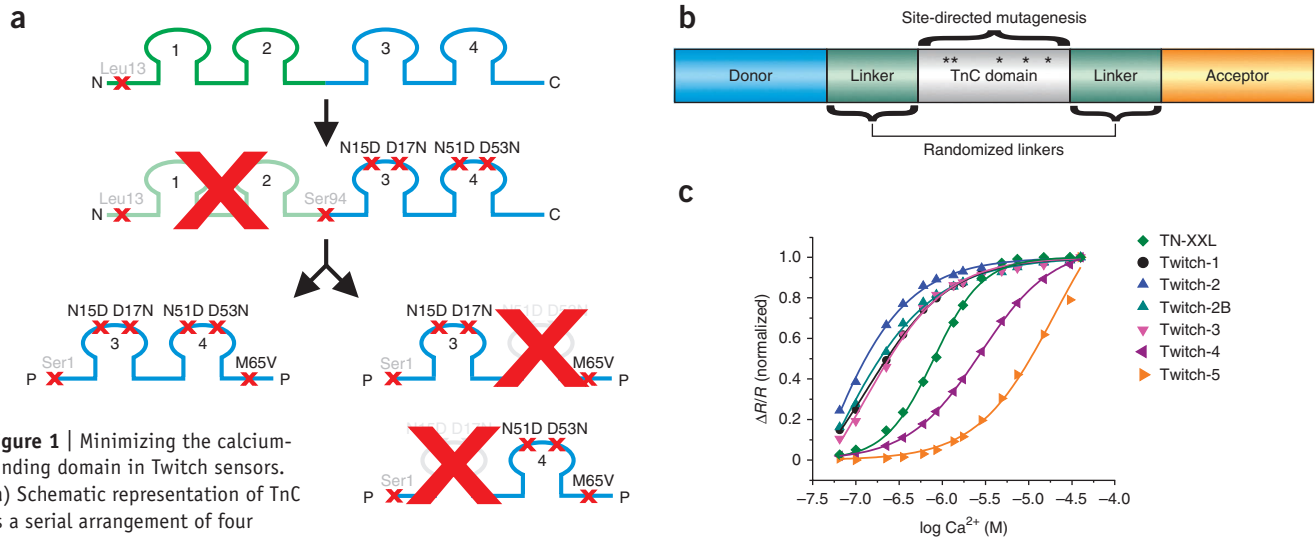


**Figure 1** | Minimizing the calcium-binding domain in Twitch sensors. (a) Schematic representation of TnC as a serial arrangement of four calcium-binding EF hands, depicted as loops (1–4). Removal of the N-terminal domain (green) creates a minimal calcium-binding domain (blue). Mutations (indicated by small ‘x’) are introduced into the EF hands to render them specific for calcium over magnesium. Within the minimal domain, one of the remaining EF hands can be crippled by mutagenesis to generate ‘single-hand’ sensors in which response properties are dominated by calcium binding to the remaining binding site. (b) Schematic representation of Twitch calcium sensors. The minimal domain is sandwiched between a donor and an acceptor fluorescent protein connected by amino acid linkers. Linker sequences can be randomized and screened for optimal calcium-induced FRET change. In addition, other sites within the minimal domain are targeted by site-directed mutagenesis to optimize sensor properties. (c) Calcium-affinity titrations of selected Twitch calcium biosensors (**Supplementary Table 3**).

improvements resulted in FRET-based calcium sensors that have sensitivities similar to synthetic calcium indicators and modern single-wavelength GECIs but that allow the valuable possibility of ratiometric imaging.

## RESULTS

### Design of minimal domains for calcium sensing

Calmodulin and TnC both consist of two globular domains that have different calcium binding properties and distinct biological function<sup>24,25,27</sup>. The dual-domain organization suggested to us that it might be feasible to generate sensors consisting of single domains instead of the full calcium-binding protein. The overall strategy that we followed to reduce GECI calcium binding sites is depicted in **Figure 1**. We found that the N-terminal regulatory domain of TnC resulted in sensors that showed only small FRET changes in response to calcium. Therefore we focused on the C-terminal domains, which in our hands were responsible for almost all the conformational changes seen in the native protein in response to calcium. Domains isolated from the chicken skeletal muscle troponin C<sup>20</sup> did not show sufficiently high affinity for calcium. We thus sampled the sequence diversity of TnC genes from various species and found that TnC derived from swim bladder and white muscle of *O. tau* (tsTnC) (**Supplementary Figs. 1 and 2**) allowed constructing minimal domain sensors with high-affinity calcium binding ( $K_d = 140\text{--}400\text{ nM}$ ). We tested a series of truncations to the C-terminal domain, searching for variants that would optimally fit the calcium binding domain into the FRET sensor. The fragment we chose ranged from Ser93 to Gln161. We subsequently changed the residue numbering of wild-type tsTnC in our constructs for simplicity, renumbering Ser93 as Ser1. Additional point mutations into the original EF hands 3 (N15D, D17N) and 4 (N51D, D53N) were introduced to minimize magnesium binding<sup>28</sup> (**Fig. 1a,b**). To generate lower-affinity sensors such as Twitch-4 and Twitch-5,

we created a small library of sensors with amino acid insertions into EF hand 3 or 4 (**Figs. 1a and 2**). These mutants possessed only one functional EF hand with calcium affinities of  $K_d$  2.8  $\mu\text{M}$  to 250  $\mu\text{M}$  (**Fig. 1c**). FRET signal change was initially improved by screening a small library of sensors with polyproline linkers inserted at the N and C termini of the domain (**Supplementary Fig. 3**). A minimal domain with a flanking proline on each side and a serendipitous beneficial mutation M65V that increased fluorescence ratio change led to the first prototypical minimal domain sensor, which we called Twitch-1. Twitch-1 had a maximal ratio change of ~400% and a  $K_d$  of 250 nM (**Fig. 1c**).

### Structural basis of Twitch calcium sensors

For the development of Twitch sensors, we investigated the properties of different prototypes by solution NMR spectroscopy and small-angle X-ray scattering (SAXS). The solution NMR structural characterization was performed with the minimal C-terminal lobe domain of tsTnC in the calcium-loaded and calcium-free forms (the latter in presence of magnesium) (**Supplementary Fig. 4**). When calcium was present, tsTnC showed well-dispersed resonances in its <sup>1</sup>H-<sup>15</sup>N HSQC spectra (**Supplementary Fig. 4**). A nearly complete assignment of backbone and C $\beta$  chemical shifts was obtained by using standard triple-resonance experiments. Secondary structure elements were initially identified by the analysis of the chemical shift index<sup>29</sup>, and then confirmed by <sup>3</sup>JH<sub>N</sub>H $\alpha$  coupling values (**Supplementary Fig. 4**). The structure calculation for the protein was performed using a considerable number of structural restraints (**Supplementary Table 1**). A high-quality structure was obtained (**Fig. 2a–c**) consisting of a well-defined globular domain (r.m.s. deviation<sub>bb</sub><sup>2–65</sup> = 0.90 Å) with the typical topology known from the C-terminal domain of chicken skeletal TnC<sup>30</sup> (**Supplementary Fig. 5**) with four helices ( $\alpha$ 1, Glu2–Phe12;  $\alpha$ 2, Arg22–Thr32;  $\alpha$ 3, Asp38–Ser48;

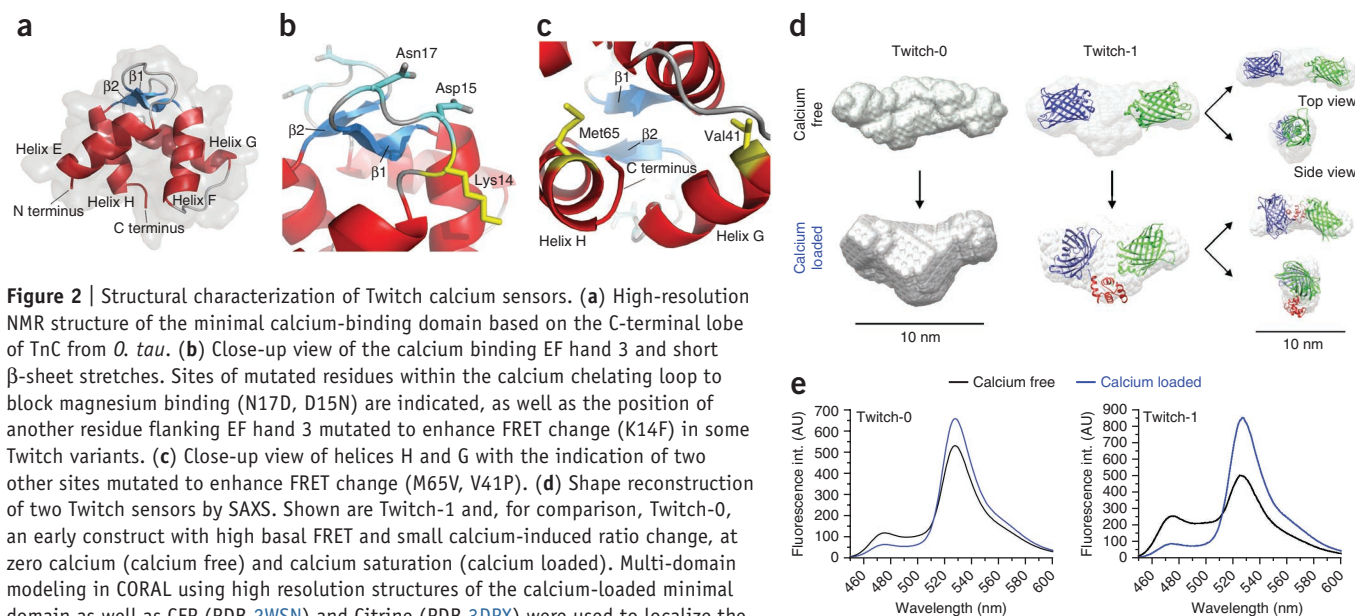


**Figure 2** | Structural characterization of Twitch calcium sensors. **(a)** High-resolution NMR structure of the minimal calcium-binding domain based on the C-terminal lobe of TnC from *O. tau*. **(b)** Close-up view of the calcium binding EF hand 3 and short  $\beta$ -sheet stretches. Sites of mutated residues within the calcium chelating loop to block magnesium binding (N17D, D15N) are indicated, as well as the position of another residue flanking EF hand 3 mutated to enhance FRET change (K14F) in some Twitch variants. **(c)** Close-up view of helices H and G with the indication of two other sites mutated to enhance FRET change (M65V, V41P). **(d)** Shape reconstruction of two Twitch sensors by SAXS. Shown are Twitch-1 and, for comparison, Twitch-0, an early construct with high basal FRET and small calcium-induced ratio change, at zero calcium (calcium free) and calcium saturation (calcium loaded). Multi-domain modeling in CORAL using high resolution structures of the calcium-loaded minimal domain as well as CFP (PDB 2WSN) and Citrine (PDB 3DPX) were used to localize the proteins within the SAXS structures. Shown are views from three angles. Twitch-1 changes from an extended structure, in which the fluorescent proteins are best fitted to scale to the opposite ends, to a compact structure upon calcium binding, thereby reorienting the fluorescent protein moieties for increased FRET. **(e)** Corresponding emission spectra of Twitch-0 and Twitch-1 at zero calcium and calcium saturation.

$\alpha 4$ , Phe58–Val68) and the two calcium binding EF hands 3 and 4 connected by a short antiparallel  $\beta$ -sheet ( $\beta 1$ , Phe19–Ile20–Asp21;  $\beta 2$ , Arg55–Ile56–Val57). The N and the C terminus are close together, at a distance of only 15 Å. By contrast, the magnesium-loaded form in the absence of calcium is fully unfolded, which places the N and C termini at a distance of 5.2 nm, on average, assuming a random coil distribution of conformations similar to ubiquitin<sup>31</sup>.

SAXS allowed us to monitor the shape and conformational change of the biosensor Twitch-1 including the attached fluorescent proteins CFP and cpCitrine (Fig. 2d,e). We obtained results on molecular geometry parameters such as radius of gyration ( $R_g$ ), and maximum particle diameter ( $D_{max}$ ), of the proteins, with approximations of folding status and conformation (Supplementary Table 2 and Supplementary Fig. 6). Algorithms for multidomain modeling<sup>32</sup> using the high-resolution structures of the calcium-loaded minimal domain (Fig. 2a) and available structures for the fluorescent proteins permitted us to generate speculative fits of the probable localization of the proteins within the SAXS structure (Fig. 2d and Supplementary Fig. 7). At the given resolution, there will be an ensemble of possible orientations for the fluorescent proteins with respect to each other, and only one structure is represented here. In the absence of calcium, Twitch-1 forms an elongated structure, with the two fluorescent proteins located at the respective ends. Upon calcium saturation, the protein shortens and becomes more compact, increasing the proximity of the fluorophores. The fits allow ambiguities about the precise distance between the fluorophores in the calcium-bound form, so we did not try to further relate the changes in geometry to changes in FRET. Overall, the shape changes detected here grossly resemble the shape changes reported for the biosensor TN-XXL<sup>33</sup>. Thus, this analysis shows that a minimal TnC domain of 68 amino acids is sufficient to initiate a strong calcium-induced conformational change and can be useful for the construction of FRET biosensors.

### Screening of diversified FRET calcium-sensor libraries

We then created a large library of sensors with diversified linkers between the minimal calcium binding domain and the adjacent fluorophores (Fig. 1b and Supplementary Fig. 8). Additionally, we selected several residues as hotspots for mutagenesis by examining the solved NMR structure (Figs. 1b and 2a), focusing on potential hinge regions where helices interact and nonchelating residues within the binding loops (Fig. 2 and Supplementary Fig. 8). To identify sensors with large responses, we implemented a two-step screening strategy (Fig. 3a). A functional bacterial colony prescreening assay was developed that allowed us to sample up to 1,000 colonies per plate, each expressing a diversified minimal domain sensor variant. As FRET sensors were not efficiently exported to the periplasmic space<sup>15</sup>, we developed a permeabilization protocol that allowed us to efficiently introduce calcium into the bacterial cytosol while collecting  $R_{min}$  and  $R_{max}$  values of the sensors (Online Methods). FRET changes were monitored by wide-field imaging with a charge-coupled device (CCD) camera (Supplementary Fig. 9). Overall, we screened about 100,000 bacterial colonies for optimal linker configurations and initially purified about 1,000 of those (Fig. 3a,b). We selected the best-performing linker configurations and then performed additional hotspot mutagenesis within the minimal domain, thereby screening another 70,000 colonies and purifying another 1,000 proteins for further improvements in ratio change on a smaller scale (Fig. 3a,b). Notably, we were able to find minimal domain sensor variants that showed ratio changes of up to or more than 1,000%, from no calcium to calcium saturation. We selected approximately 120 variants that showed the highest maximal ratio change as well as a small number of sensors with lower affinity and undertook a secondary screen in primary hippocampal neurons (Fig. 3c–e). Neurons expressing the variants were exposed to electrical field stimulation consisting of 1–160 individual pulses (Fig. 3c–e). Two variants showed strong improvements over TN-XXL and Twitch-1 in detecting subtle elevations in the cytosolic free

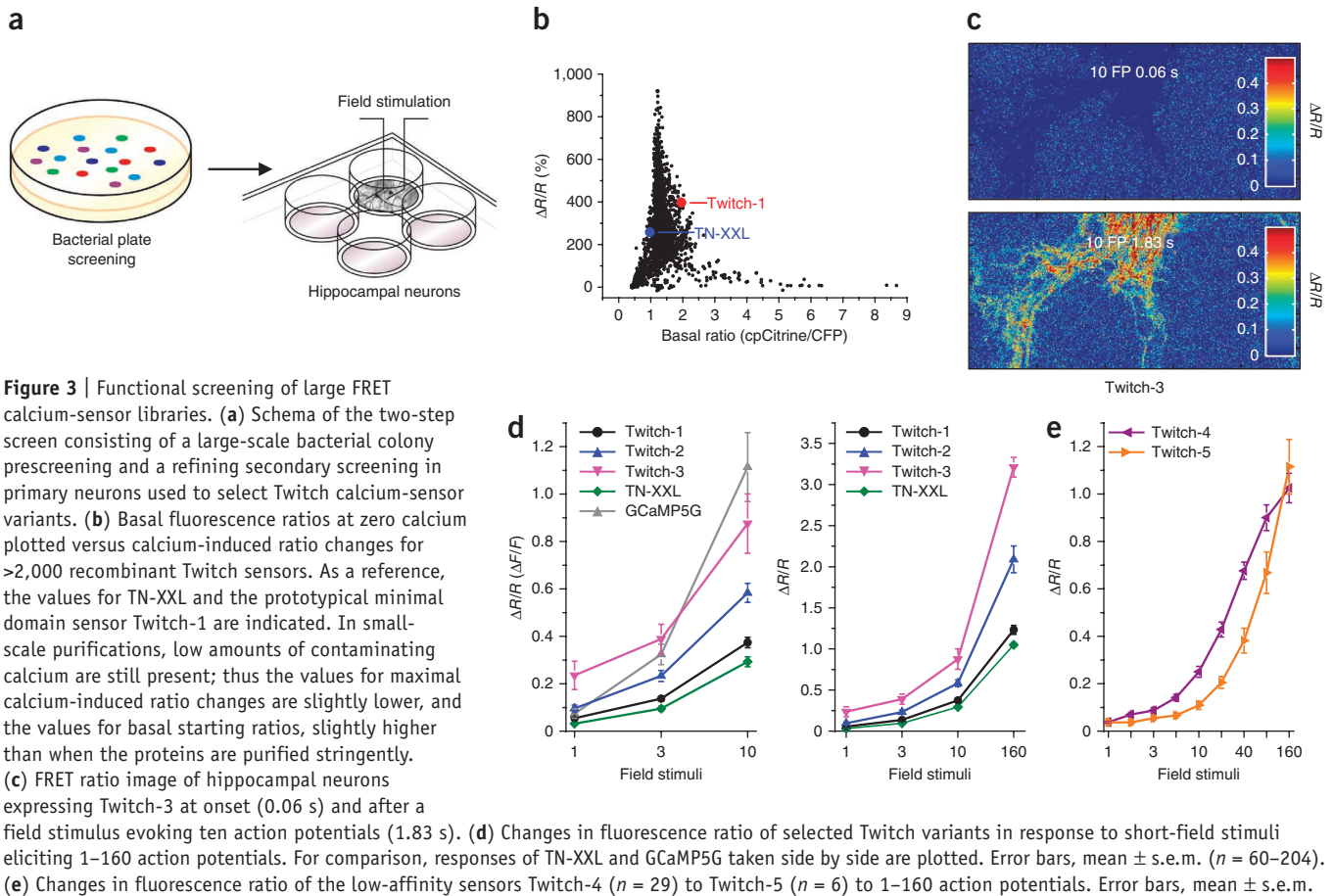


**Figure 3** | Functional screening of large FRET calcium-sensor libraries. **(a)** Schema of the two-step screen consisting of a large-scale bacterial colony prescreening and a refining secondary screening in primary neurons used to select Twitch calcium-sensor variants. **(b)** Basal fluorescence ratios at zero calcium plotted versus calcium-induced ratio changes for >2,000 recombinant Twitch sensors. As a reference, the values for TN-XXL and the prototypical minimal domain sensor Twitch-1 are indicated. In small-scale purifications, low amounts of contaminating calcium are still present; thus the values for maximal calcium-induced ratio changes are slightly lower, and the values for basal starting ratios, slightly higher than when the proteins are purified stringently. **(c)** FRET ratio image of hippocampal neurons expressing Twitch-3 at onset (0.06 s) and after a field stimulus evoking ten action potentials (1.83 s). **(d)** Changes in fluorescence ratio of selected Twitch variants in response to short-field stimuli eliciting 1–160 action potentials. For comparison, responses of TN-XXL and GCaMP5G taken side by side are plotted. Error bars, mean  $\pm$  s.e.m. ( $n = 60$ –204). **(e)** Changes in fluorescence ratio of the low-affinity sensors Twitch-4 ( $n = 29$ ) to Twitch-5 ( $n = 6$ ) to 1–160 action potentials. Error bars, mean  $\pm$  s.e.m.

calcium concentration and were named Twitch-2 and Twitch-3 sensors (Fig. 3d). The maximal response of Twitch-2 and Twitch-3 was also improved compared to TN-XXL. We also found two sensors, Twitch-4 and Twitch-5, that showed lower affinity and sensitivity for calcium in the neurons, but that had faster response kinetics (Fig. 3e). These sensors may be useful for quantifying larger calcium fluxes in cells. In a separate set of neuronal screening experiments, Twitch-3 was compared to other known FRET-based calcium sensors (Supplementary Fig. 10). The core *in vitro* characteristics of selected Twitch indicators are summarized in Supplementary Table 3.

### Imaging neuronal activity *in vivo* with Twitch sensors

To test the performance of Twitch sensors *in vivo*, we first expressed Twitch-3 in mouse primary visual cortex (V1) using adeno-associated virus (AAV) vector-mediated gene transfer<sup>11</sup> and monitored calcium changes of neurons in V1 in response to presentation of moving gratings of differing orientations (Fig. 4a–e and Supplementary Figs. 11 and 12). We compared the *in vivo* properties of Twitch-3 to that of the established FRET based GECI YC3.60 (ref. 16). At comparable average laser powers Twitch-3 was brighter than YC3.60 (Supplementary Fig. 12). The total fraction of V1 neurons that responded to visual stimuli was larger in experiments using Twitch-3 ( $34.8 \pm 8.6\%$ , mean  $\pm$  weighted s.d.) than in those using YC3.60 (ref. 16) ( $19.2 \pm 9.4\%$ , weighted s.d.), and the number of responding cells expressing Twitch-3 equaled the numbers of the synthetic fluorescent calcium indicator OGB-1 ( $36 \pm 4\%$ , weighted s.d.) (Fig. 4e, note that OGB-1 data

were acquired with slower acquisition rate and presumably higher signal-to-noise ratio; details in Online Methods).

New variants of cyan fluorescent protein such as mCerulean3 (ref. 34) or mTurquoise2 (ref. 35) have recently been generated. Both proteins have high quantum yields and improved photostability. We sought to improve the brightness of the Twitch sensors further by exchanging ECFP with these brighter donors and cpCitrine with cpVenus<sup>CD</sup> (ref. 36), a codon-diversified variant of the YFP variant Venus<sup>37</sup>. Although the proteins were almost identical, the exchange had a surprisingly negative impact on the FRET changes observed in the sensors (data not shown). We overcame this by screening additional libraries of extended linkers. In this way, we developed Twitch-2B, which retained the high FRET change of its precursor but was approximately twofold brighter in the donor emission channel than the previous Twitch sensors (Twitch-2B has cpVenus<sup>CD</sup> and mCerulean3 as a FRET pair; Supplementary Fig. 13). Twitch-2B had a Hill coefficient of 1.3 and reported action potentials (APs) in cortical neurons in acute tissue slices in a fairly linear manner (Fig. 4f,g). In this preparation, the mean change in fluorescence ratio ( $\Delta R/R$ ) in response to a single action potential stimulation was  $26.5 \pm 3.8\%$  (s.e.m.,  $n = 11$ ; Fig. 4g) and the increase in the amplitude of the signal with increasing numbers of action potentials was well approximated by a linear fit with the slope of 12.5% ratio change/AP.

We further investigated the properties of Twitch-2B and Twitch-3 *in vivo* by imaging sensory-evoked calcium signals in adult-born juxtglomerular neurons of the mouse olfactory bulb<sup>21</sup> after lentivirus-mediated gene transfer. The amplitude of

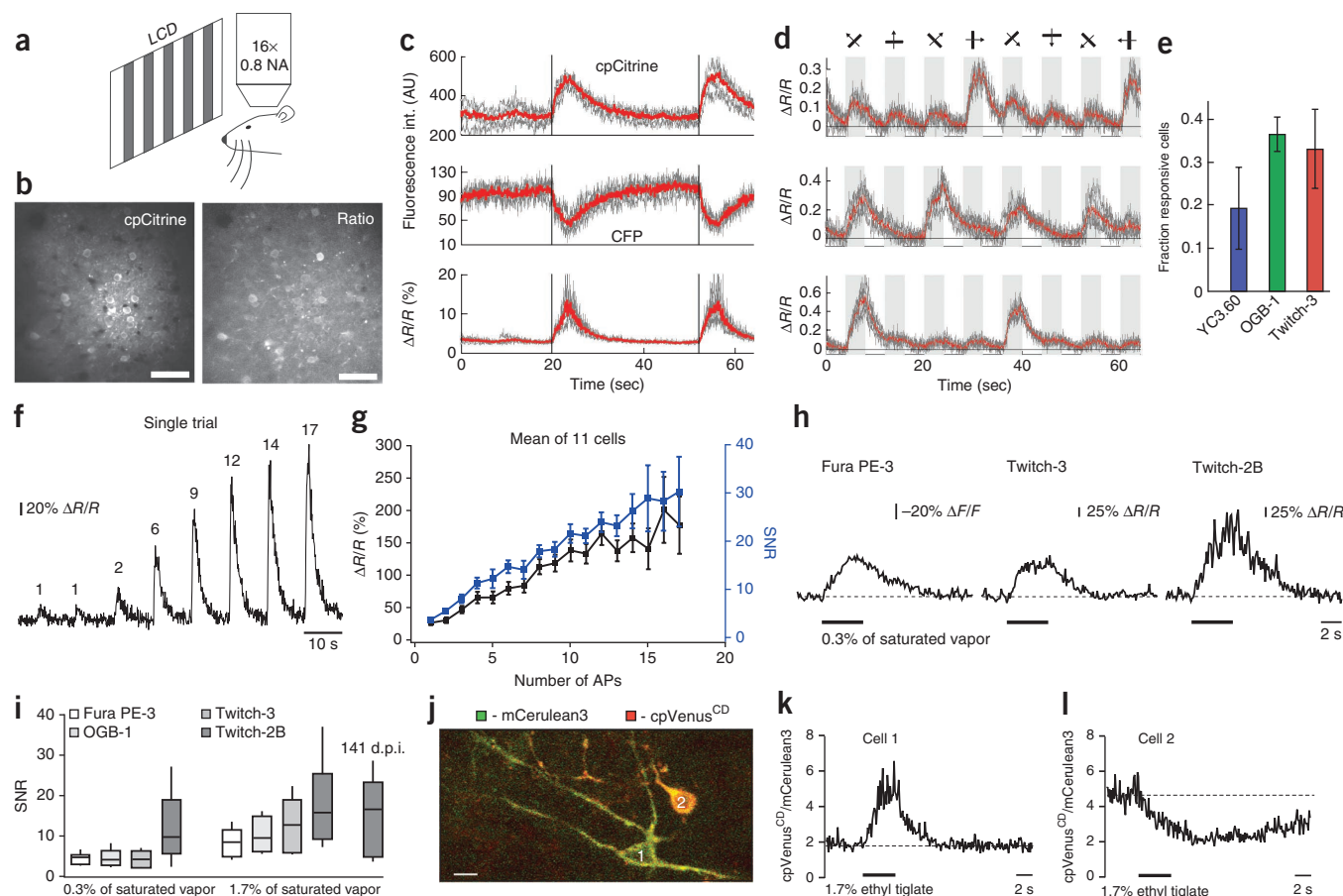


**Figure 4** | Use of Twitch-3 and Twitch-2B for high-resolution *in vivo* imaging in the mouse brain. (a) Schematic showing experimental setup for recording visually evoked calcium signals. (b) Twitch-3 cpCitrine fluorescence in layer 2/3 neurons 4 weeks after AAV injection (left) and ratio cpCitrine/CFP image (right). Scale bars, 50  $\mu\text{m}$ . (c) Measured cpCitrine (top) and CFP (middle) channels for five repetitions of visual stimuli consisting of moving gratings. Bottom, the ratio between these two channels. Gray, single trials; red, trial average; vertical lines show the preferred stimulus start time. (d) Responses of three cells to eight different moving grating stimuli. (e) Fraction of visually responsive neurons in *in vivo* experiments when using three different calcium indicators (OGB-1,  $36 \pm 4\%$ ; YC3.60,  $19.2 \pm 9.4\%$ ; Twitch-3,  $34.8 \pm 8.6\%$ ; mean  $\pm$  weighted s.d.; neuropil compensation factor = 0.7, data for OGB-1 from ref. 11). Significances were determined according to Mann-Whitney test. YC3.60, Twitch-3  $P = 0.052$ ; OGB-1, YC3.60  $P = 0.143$ ; OGB-1, Twitch-3  $P = 0.548$ ; data for YC3.60, Twitch-3 and OGB-1 are from five, six and three animals, respectively (Online Methods). (f) Single trial example (of a total of 11 cells) of the relationship between the emission-ratio change of Twitch-2B and the number of underlying action potentials recorded from a layer 2/3 pyramidal neuron in a cortical slice at 35  $^{\circ}\text{C}$ . (g) Relationship between the mean amplitude of Twitch-2B-mediated calcium transients as well as mean signal-to-noise ratio (SNR, see Online Methods) and the number of underlying action potentials in a cortical slice ( $n = 11$ , data from four animals, mean  $\pm$  s.e.m.). (h) Representative (from 15, 7 and 12 cells, respectively) sensory-evoked calcium transients in juxtglomerular neurons of the *in vivo* olfactory bulb recorded with three different calcium sensors, as indicated. At this low concentration, odorants evoke calcium transients in cells labeled both with synthetic (for example, Fura PE-3) and with genetically encoded (Twitch-2B and Twitch-3) indicators. (i) Representative box plots showing SNRs measured *in vivo* in olfactory bulb neurons labeled with four different indicators in response to two odorant concentrations, as indicated (from left to right,  $n = 15, 38, 7, 12, 15, 32, 9, 15, 11$  cells, respectively; data from ten mice). For all data sets involving GECIs, recordings were conducted at 35–37 d after infection (d.p.i.). The last box plot shows data obtained at 141 d.p.i. from one mouse also imaged at 35–37 d.p.i. The significances for differences in SNR values were determined according to Mann-Whitney test (for 0.3% saturated vapor, Twitch-2B, Fura PE-3  $P = 0.005$ ; Twitch-2B, OGB-1  $P = 0.0016$ ; Twitch-2B, Twitch-3  $P = 0.015$ ; for 1.7% saturated vapor, Twitch-2B, Fura PE-3  $P = 0.003$ ; Twitch-2B, OGB-1  $P = 0.0045$ ; Twitch-2B, Twitch-3  $P = 0.156$ ; Twitch-2B, Twitch-2B 141 d.p.i.  $P = 0.54$ ).  $P > 0.05$  for all other possible comparisons. Boxes drawn from 75th percentile (top) to 25th percentile (bottom); whiskers, 85th percentile to 10th percentile. (j) Image of two adult-born juxtglomerular neurons taken 37 d after the injection of lentiviral vectors encoding Twitch-2B. Scale bar, 10  $\mu\text{m}$ . (k, l) On application of the odorant (ethyl tiglate), cell 1 (k) shows an increased calcium response, whereas cell 2 (l) shows a decreased response.

Twitch-3 signals was comparable to that of signals reported by the synthetic calcium indicator dye Fura PE-3 (Fig. 4h), whereas Twitch-2B signals were stronger than those of both Twitch-3 and Fura PE-3. Signal-to-noise ratios were calculated for Twitch-2B and Twitch-3 as well as Fura PE-3 and OGB-1 in the labeled neurons and in response to two different odorant concentrations (Fig. 4i). In both conditions, Twitch-2B showed higher signal-to-noise ratios than synthetic indicators whereas the signal-to-noise

ratios obtained using Twitch-3 were comparable to those of Fura PE-3 and OGB-1.

One of the main advantages of Twitch sensors compared to other GECIs is their potential for use in long-term imaging experiments. To assess this, we compared the responses of Twitch-2B in adult-born olfactory neurons to the same odorant stimuli at two different time points *in vivo*. We observed that the quality of Twitch-2B-mediated responses did not change over time

(Fig. 4i), suggesting that this indicator is well suited for long-term chronic imaging (Fig. 4i). In addition, we looked for signs of toxicity in these mice, and at 141 d after infection, we found that only 2 out of 63 juxtglomerular neurons analyzed had filled

nuclei, a potential morphological indication of unhealthy cells. In addition, owing to its high dynamic range, Twitch-2B allowed visualization of neurons with different levels of basal activity (Fig. 4j–l). Out of two cells shown in Figure 4j, cell 1 shows low

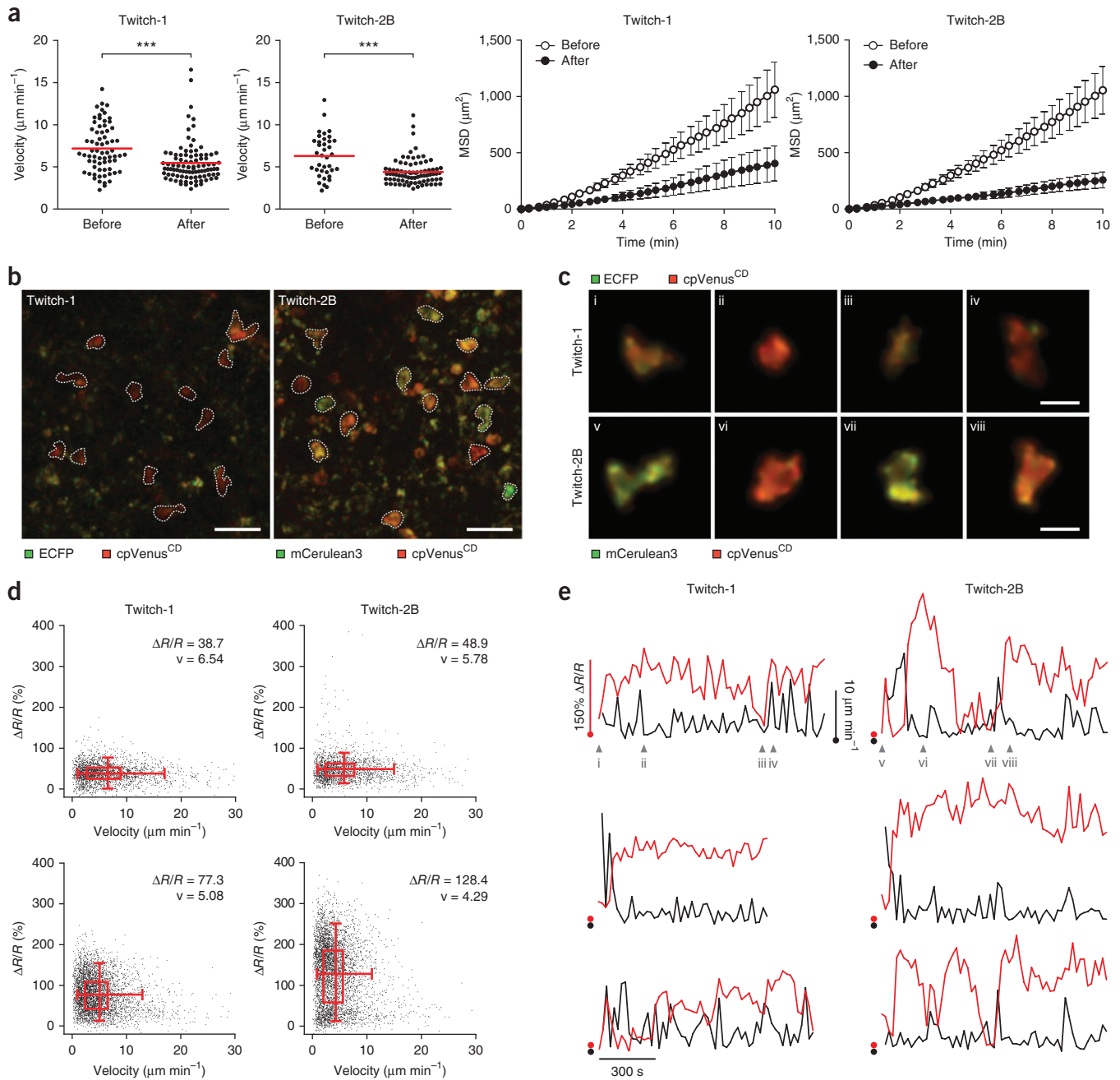


**Figure 5** | *In vivo* calcium imaging of T lymphocytes with Twitch-1 and Twitch-2B. **(a)** Quantification of T lymphocyte locomotion within the popliteal lymph node before and after i.v. injection of 100  $\mu\text{g}$  of OVA peptide antigen. Average velocities and the mean squared displacement (m.s.d.  $\pm$  s.e.m.) for Twitch-1- and Twitch-2B-expressing T lymphocytes.  $n = 68$  and 94 cells (Twitch-1) and 37 and 80 cells (Twitch-2B) for control and antigen-supplemented conditions, respectively. For every condition, data were obtained from three animals.  $***P < 0.0001$  (Mann-Whitney *U* test). Red lines in the left two graphs indicate mean values. **(b)** Sample images from *in vivo* calcium imaging of OT-II T lymphocytes in the popliteal lymph node after antigen injection. Overlay of donor and acceptor fluorescence shown. Scale bars, 30  $\mu\text{m}$ . **(c)** Selected time-lapse series of individual cells expressing Twitch-1 or Twitch-2B, oscillating through minimal and maximal  $\Delta R/R$ . Numbers indicate time points in **e**. Scale bars, 10  $\mu\text{m}$ . Data are representative traces of experiments done in three animals. **(d)** Scatter plots of cell velocity versus calcium-indicator ratio change for each time point analyzed before (top) and after (bottom) antigen injection. Mean values for  $\Delta R/R$  and velocity ( $v$ ) are indicated along with a two-dimensional box plot. Box plot indicates the 25th and 75th percentiles, and the whiskers represent the 5th and 95th percentiles.  $P < 0.001$ . **(e)** Sample tracks of intracellular calcium levels (red) and T cell velocities (black) after the application of antigen. Top, the two cells from **c**. Dots in **e** depict zero levels for ratio (red) and velocity (black). Results from three animals before and after antigen exposure are shown.

cpVenus<sup>CD</sup>/mCerulean3 ratio (1.9), whereas cell 2 shows high cpVenus<sup>CD</sup>/mCerulean3 ratio (4.6), presumably because of the high basal firing rate of the neuron<sup>21</sup>. In response to the same sensory stimulus, cell 1 responded with an increase in calcium signal (Fig. 4k), and cell 2 responded with a decrease (Fig. 4l) in the intracellular free calcium concentration. Cells with decreased responses were encountered five times during this study. In total, such cells comprise 12% of the odor-responsive population of juxtglomerular neurons<sup>21</sup>.

### Imaging T lymphocyte activation *in vivo* using Twitch-2B

Autoreactive T lymphocytes cause autoimmune diseases and are highly motile cells. As such, they offer an ideal platform to test the usefulness of ratiometric calcium indicators for functional imaging in moving samples<sup>38</sup>. Because T cells are highly motile and quickly change their location within the inhomogeneous tissue environment, their brightness will continuously vary over time. To normalize for this effect, only ratiometric calcium indicators are suitable. We previously worked out parameters to express FRET calcium indicators in autoantigen-specific T cells and protocols to image them<sup>36</sup>. To test the performance of the advanced Twitch variants, we imaged immune cells during antigen recognition *in vivo*. Antigen recognition by T cells triggers a swift rise of the intracellular free calcium concentration, which can be used as an indication of T cell activation<sup>39</sup>. We transduced antigen-specific T cells from OT-II mice<sup>40</sup> with retroviruses expressing Twitch-1 or Twitch-2B and compared the antigen-dependent activation of these T cells by dendritic cells (DC) in *in vivo* mouse lymph nodes. In the absence of antigen, both cell lines showed comparable motility and displacement and had low intracellular free Ca<sup>2+</sup> concentration (Fig. 5a,d). After intravenous (i.v.) injection of the cognate OVA peptide antigen, both cell lines reduced their motility and displayed elevated calcium levels (Fig. 5a,b,d). Cells expressing Twitch-2B displayed a ratio change of >300% *in vivo* and showed a higher dynamic range of the sensor output than cells expressing Twitch-1 (Fig. 5b,d). The cells expressing Twitch-2B showed clear fluctuations from green to yellow fluorescence, allowing visual estimation of changes in calcium level without the need for pseudocoloring (Fig. 5b,c). The increased dynamic range of Twitch-2B improved the resolution of the calcium oscillation events in T cells (Fig. 5c,e).

### DISCUSSION

Here we describe a series of optimized FRET-based calcium indicators for ratiometric *in vivo* imaging. We based our work on previous sensors based on TnC—the calcium sensor from skeletal and cardiac muscle—as calcium-binding moiety<sup>6,20</sup>. We illustrate the usefulness of optimized Twitch variants by monitoring neuronal activity and studying activation patterns of T lymphocytes *in vivo* with high sensitivity. This approach may be easily extended to other motile cell types such as B lymphocytes or thrombocytes and could become very valuable for studying the interactions that these cells encounter as they move through tissue microenvironments within the body.

We identified the C-terminal lobe domain of TnC as the smallest possible domain for generating GECIs that exhibits a large conformational change upon calcium binding. Sensors based on this domain are smaller, can lead to reduced sensor-induced buffering during long-term chronic expression and minimize the risk of

cytotoxicity. Reducing the size of the calcium-binding domain may also help to simplify response properties compared to other sensors. *In vitro* titrations of Twitch-2B, for example, showed improved Hill coefficient values compared, for example, to recent G-CaMP5 variants<sup>11</sup>. As with other GECIs, a trade-off can be seen in Twitch sensors between high-affinity binding and fast response kinetics. Whereas sensors with somewhat lower affinity such as Twitch-5 ( $K_d = 9.25 \mu\text{M}$ ,  $\tau = 0.16 \text{ s}$ ) show relatively fast kinetics, the most sensitive variants, such as Twitch-3 ( $K_d = 250 \text{ nM}$ ,  $\tau = 1.5 \text{ s}$ ), are relatively slow. Although slow kinetics may increase sensitivity, as more signal photons are generated, sensitive indicators with brisker responses are also required and will need to be developed.

Finally, to optimize the FRET change of the sensors, we developed a strategy for sensor prescreening in bacterial colonies that allowed us to assay a relatively large number of modified sensors and identify interesting candidates for further analysis. In this way we improved the overall FRET change of Twitch sensors upon calcium binding, from 10–20% ratio change initially to >1,000%. Similar screening techniques might be useful to improve some of the existing FRET biosensors for other signal molecules, many of which currently show modest maximal ratio changes.

### METHODS

Methods and any associated references are available in the [online version of the paper](#).

**Accession codes.** Biological Magnetic Resonance Data Bank: chemical shift assignments are available under accession number [19285](#). Protein Data Bank: the final atomic coordinates are available under accession number [2m97](#). Addgene: Twitch-2B (in pcDNA3) is available under accession number [48203](#). GenBank: the Twitch-2B sequence has been deposited under the accession number [KF843821](#).

*Note: Any Supplementary Information and Source Data files are available in the online version of the paper.*

### ACKNOWLEDGMENTS

This work was funded by the Max Planck Society, the Howard Hughes Medical Institute, Deutsche Forschungsgemeinschaft (DFG) grant SFB 870 (to O. Griesbeck), DFG grant GRK1721 (to G.W.), EU FP7 EuroV1sion grant (to O. Griesbeck), US National Science Foundation grant IBN-9985315 (to T.A.), US National Science Foundation grant IOS 1145981 (to L.C.R.) and the DFG Center for Integrative Neuroscience (to O. Garaschuk).

### AUTHOR CONTRIBUTIONS

T.T. characterized the minimal domain, cloned constructs and performed protein purifications and *in vitro* spectroscopic characterizations; J.L. established the bacterial colony screen and performed colony screening and further protein purifications; M.M. and I.B. performed *in vivo* imaging of T lymphocytes; L.R., S.B., Y. Laukat and C.G. performed NMR structure determination and interpreted results; T.A. and L.C.R. cloned toadfish TnC; A.G. and T.T. collected SAXS data; G.W. calculated SAXS models; H.D. performed *in vivo* characterization in mouse visual cortex; Y.K., Y. Liang, G.K. and O. Garaschuk planned, performed and interpreted characterization of the sensors in cortical slices *in situ* and mouse olfactory bulb *in vivo*; T.T., T.W.C., H.D. and D.S.K. planned, performed and interpreted neuronal screening results. O. Griesbeck designed experiments, supervised sensor engineering and screening and integrated results from the collaborators. T.T., H.D., C.G., O. Garaschuk and O. Griesbeck wrote the manuscript.

### COMPETING FINANCIAL INTERESTS

The authors declare no competing financial interests.

Reprints and permissions information is available online at <http://www.nature.com/reprints/index.html>.

1. Palmer, A.E., Quin, Y., Park, J.G. & McCombs, J.E. Design and application of genetically encoded biosensors. *Trends Biotechnol.* **29**, 144–152 (2011).
2. Looger, L.L. & Griesbeck, O. Genetically encoded neural activity indicators. *Curr. Opin. Neurobiol.* **22**, 18–23 (2012).
3. Knöpfel, T. Genetically encoded optical indicators for the analysis of neuronal circuits. *Nat. Rev. Neurosci.* **13**, 687–700 (2012).
4. Mank, M. & Griesbeck, O. Genetically encoded calcium indicators. *Chem. Rev.* **108**, 1550–1564 (2008).
5. Miyawaki, A. *et al.* Fluorescent indicators for Ca<sup>2+</sup> based on green fluorescent proteins and calmodulin. *Nature* **388**, 882–887 (1997).
6. Heim, N. & Griesbeck, O. Genetically encoded indicators of cellular calcium dynamics based on troponin C and green fluorescent protein. *J. Biol. Chem.* **279**, 14280–14286 (2004).
7. Wang, Q., Shui, B., Kotlikoff, M.I. & Sondermann, H. Structural basis for calcium sensing by GCaMP2. *Structure* **16**, 1817–1827 (2008).
8. Akerboom, J. *et al.* Crystal structures of the GCaMP calcium sensor reveal the mechanism of fluorescence signal change and aid rational design. *J. Biol. Chem.* **284**, 6455–6464 (2009).
9. Nakai, J., Ohkura, M. & Imoto, K. A high signal-to-noise Ca<sup>2+</sup> probe composed of a single green fluorescent protein. *Nat. Biotechnol.* **19**, 137–141 (2001).
10. Tian, L. *et al.* Imaging neural activity in worms, flies and mice with improved GCaMP calcium indicators. *Nat. Methods* **6**, 875–881 (2009).
11. Akerboom, J. *et al.* Optimization of a GCaMP calcium indicator for neural activity imaging. *J. Neurosci.* **32**, 13819–13840 (2012).
12. Zariwala, H.A. *et al.* A Cre-dependent GCaMP3 reporter mouse for neuronal imaging *in vivo*. *J. Neurosci.* **32**, 3131–3141 (2012).
13. Ohkura, M. *et al.* Genetically encoded green fluorescent Ca<sup>2+</sup> indicators with improved detectability for neuronal Ca<sup>2+</sup> signals. *PLoS ONE* **7**, e51286 (2012).
14. Akerboom, J. *et al.* Genetically encoded calcium indicators for multi-color neural activity imaging and combination with optogenetics. *Front. Mol. Neurosci.* **6**, 2 (2013).
15. Zhao, Y. *et al.* An expanded palette of genetically encoded Ca<sup>2+</sup> indicators. *Science* **333**, 1888–1891 (2011).
16. Nagai, T., Yamada, S., Tominaga, T., Ichikawa, M. & Miyawaki, A. Expanded dynamic range of fluorescent indicators for Ca<sup>2+</sup> by circularly permuted yellow fluorescent proteins. *Proc. Natl. Acad. Sci. USA* **101**, 10554–10559 (2004).
17. Lütcke, H. *et al.* Optical recording of neuronal activity with a genetically encoded calcium indicator in anesthetized and freely moving mice. *Front. Neural Circuits* **4**, 9 (2010).
18. Palmer, A.E. *et al.* Ca<sup>2+</sup> indicators based on computationally redesigned calmodulin-peptide pairs. *Chem. Biol.* **13**, 521–530 (2006).
19. Horikawa, K. *et al.* Spontaneous network activity visualized by ultrasensitive Ca<sup>2+</sup> indicators, yellow Cameleon-Nano. *Nat. Methods* **7**, 729–732 (2010).
20. Mank, M. *et al.* A genetically encoded calcium indicator for chronic *in vivo* two-photon imaging. *Nat. Methods* **5**, 805–811 (2008).
21. Homma, R. *et al.* *In vivo* functional properties of juxtglomerular neurons in the mouse olfactory bulb. *Front. Neural Circuits* **7**, 23 (2013).
22. Kuchibhotla, K.V. *et al.* Aβ plaques lead to aberrant regulation of calcium homeostasis *in vivo* resulting in structural and functional disruption of neuronal networks. *Neuron* **59**, 214–225 (2008).
23. Siffrin, V. *et al.* *In vivo* imaging of partially reversible Th17 cell-induced neuronal dysfunction in the course of encephalomyelitis. *Immunity* **33**, 424–436 (2010).
24. Vassilyev, D.G. *et al.* Crystal structure of troponin C in complex with troponin I fragment at 2.3-angstrom resolution. *Proc. Natl. Acad. Sci. USA* **95**, 4847–4852 (1998).
25. Gordon, A.M., Homsher, E. & Regnier, M. Regulation of contraction in striated muscle. *Physiol. Rev.* **80**, 853–924 (2000).
26. Drenth, S. *et al.* Biocompatibility of a genetically encoded calcium indicator in a transgenic mouse model. *Nat. Commun.* **3**, 1031 (2012).
27. DeMaria, C.D., Soong, T.W., Alseikhan, B.A., Alvania, R.S. & Yue, D.T. Calmodulin bifurcates the local Ca<sup>2+</sup> signal that modulates P/Q-type Ca<sup>2+</sup> channels. *Nature* **411**, 484–489 (2001).
28. Mank, M. *et al.* A FRET-based calcium biosensor with fast signal kinetics and high fluorescence change. *Biophys. J.* **90**, 1790–1796 (2006).
29. Wishart, D.S. & Case, D.A. Use of chemical shifts in macromolecular structure determination. *Methods Enzymol.* **338**, 3–34 (2001).
30. Slupsky, C.M. & Sykes, B.D. NMR solution structure of calcium-saturated skeletal muscle troponin C. *Biochemistry* **34**, 15953–15964 (1995).
31. Huang, J.R. & Grzesiek, S. Ensemble calculations of unstructured proteins constrained by RDC and PRE data: a case study of urea-denatured ubiquitin. *J. Am. Chem. Soc.* **132**, 694–705 (2010).
32. Petoukhov, M.V. *et al.* New developments in the ATSAS program package for small-angle scattering data analysis. *J. Appl. Cryst.* **45**, 342–350 (2012).
33. Geiger, A. *et al.* Correlating calcium binding, Förster resonance energy transfer, and conformational change in the biosensor TN-XXL. *Biophys. J.* **102**, 2401–2410 (2012).
34. Markwardt, M.L. *et al.* An improved cerulean fluorescent protein with enhanced brightness and reduced reversible photoswitching. *PLoS ONE* **6**, e17896 (2011).
35. Goedhart, J. *et al.* Bright cyan fluorescent protein variants identified by fluorescence lifetime screening. *Nat. Methods* **7**, 137–139 (2010).
36. Mues, M. *et al.* Real-time *in vivo* analysis of T cell activation in the central nervous system using a genetically encoded calcium indicator. *Nat. Med.* **19**, 778–783 (2013).
37. Nagai, T. *et al.* A variant of yellow fluorescent protein with fast and efficient maturation for cell-biological applications. *Nat. Biotechnol.* **20**, 87–90 (2002).
38. Bousso, P. & Moreau, H.D. Functional immunoimaging: the revolution continues. *Nat. Rev. Immunol.* **12**, 858–864 (2012).
39. Feske, S., Skolnik, E.Y. & Prakriya, M. Ion channels and transporters in lymphocyte function and immunity. *Nat. Rev. Immunol.* **12**, 532–547 (2012).
40. Barnden, M.J. *et al.* Defective TCR expression in transgenic mice constructed using cDNA-based α- and β-chain genes under the control of heterologous regulatory elements. *Immunol. Cell Biol.* **76**, 34–40 (1998).

## ONLINE METHODS

**Gene construction and biosensor library design.** cDNA of toadfish troponin C (tsTnC) retrieved from white muscle and swim bladder was used as starting material for designing the new minimal domain calcium indicators. To generate the Twitch single C-terminal domain the region from amino acid Ser93 to Gln161 of tsTnC was amplified and cloned in between the FRET fluorescent protein variants. Point mutations were introduced by site-directed mutagenesis using the primer extension method similar to the QuickChange method (Stratagene) and by error-prone PCR (Jena Error-Prone Kit). Proline and random linkers were introduced via PCR using primer extensions fused to tsTnC at the 5' and 3' ends of the C-terminal domain. The general structure of the calcium biosensors described herein is as follows: ECFP/Cer3/mTurquoise2-SphI-linker-minimal calcium binding domain-linker-SacI-Met cpCitrine174/cpVenus<sup>CD</sup>-Stop (**Fig. 1**). For specific point mutations and linkers of Twitch variants, see **Supplementary Figure 8** and **Supplementary Table 3**. Constructs encoding Twitch calcium sensors can be viewed at [http://www.addgene.org/Oliver\\_Griesbeck/](http://www.addgene.org/Oliver_Griesbeck/)

**Cloning of toadfish troponin C.** Total RNA was isolated from 0.1 g toadfish swim bladder muscle following homogenization in presence of 0.9 ml TRIzol in accordance with accompanying instructions (Invitrogen, California). From an aliquot of total RNA, a lambda gt11 cDNA library was constructed with the CapSwitch Kit (ClonTech, California). The library was amplified once, and aliquots of the amplified library were screened by PCR for TnC sequences. The same was done for construction of a toadfish white muscle cDNA library.

For screening, a degenerate primer for TnC was paired with a primer specific to the lambda vector. The degenerate primer was designed with the help of the Blocks and CODEHOP algorithms ([blocks.fhcrc.org/blocks/codehop.html](http://blocks.fhcrc.org/blocks/codehop.html)), and the oligonucleotide recognized a distinct, highly conserved motif of the TnC protein: 5'-CGACTTCGACGAGTTCCTGGTATGATGGT-3', recognizing the motif DFEEFLVMM at the start of helix D, after the second calcium-binding loop in the N-terminal half of TnC. Sequence information obtained from this amplification allowed design of primers specific for toadfish TnC. These primers were subsequently paired with lambda-specific primers to amplify the remainder of the full-length cDNA. As a verification of the sequence data, full-length cDNA was then amplified from total RNA following reverse transcription, and the amplified product was sequenced.

**NMR spectroscopy.** The expression of the uniformly <sup>15</sup>N- and <sup>13</sup>C-labeled histidine-tagged minimal C-terminal lobe domain of *Opsanus* TnC (tsTnC), comprising EF hands 3 and 4, was performed at 37 °C in minimal medium with <sup>15</sup>N-ammonium chloride and <sup>13</sup>C<sub>6</sub>-d-glucose as the sole nitrogen and carbon sources. The fusion protein was purified by immobilized metal affinity chromatography on Ni-NTA agarose (Qiagen, Venlo, The Netherlands) and subsequently cleaved with TEV protease. The released tsTnC was further purified by reverse-phase HPLC.

NMR samples for structure determination of tsTnC were prepared at a final concentration of 1 mM in 20 mM Bis-Tris (pH 7.0), 100 mM KCl, 10 mM DTT, 10 mM CaCl<sub>2</sub> and 10% <sup>2</sup>H<sub>2</sub>O. The calcium-free sample in presence of magnesium contained 10 μM tsTnC, 100 μM EGTA and 1 mM MgCl<sub>2</sub>.

NMR experiments were carried out at 303 K on a 700-MHz Bruker DRX spectrometer equipped with a z-gradient cryoprobe and 900-MHz spectrometer with a triple resonance 5-mm cryoprobe with a z-axis pulsed field gradient. Triple resonance NMR experiments including 3D HNCA (refs. 41,42), 3D CBCANH (ref. 43) and 3D CBCA(CO)NH (ref. 42) were collected to obtain sequence-specific backbone and Cβ resonances assignment. Vicinal (three-bond) H<sub>N</sub>-H<sub>α</sub> coupling constants (<sup>3</sup>J<sub>H<sub>N</sub>H<sub>α</sub>) were evaluated from cross-peak intensities in quantitative J-correlation (HNHA) spectra<sup>44</sup>. Residual dipolar couplings <sup>1</sup>D<sub>NH</sub> RDCs were measured by taking the difference in the one-bond <sup>1</sup>H-<sup>15</sup>N splittings (<sup>1</sup>J<sub>NH</sub> + <sup>1</sup>D<sub>NH</sub>) in aligned (~20 mg/ml) phage pf1 (ref. 45) and isotropic media using an in-phase/anti-phase (IPAP) HSQC experiment<sup>46</sup>. The spectra were processed using NMRpipe<sup>47</sup> and analyzed by SPARKY (<http://www.cgl.ucsf.edu/home/sparky/>) and CARA<sup>48</sup>. <sup>1</sup>H, <sup>13</sup>C and <sup>15</sup>N chemical shifts were calibrated indirectly by external DSS references.</sub>

The structure calculation was performed with CS-RDC-Rosetta<sup>49,50</sup> using as structural restraints the residual dipolar couplings, torsion angles φ/ψ derived from TALOS+ database and the complete backbone and Cβ chemical shifts of those residues indicated by TALOS+ to be rigid in picosecond timescale with an order parameter S<sup>2</sup> > 0.7. A set of 200 fragment candidates matching these chemical shifts was used to calculate 3,000 structures in Rosetta. The energy of these Rosetta structures was then rescored against the observed chemical shifts and the 20 conformers with the lowest rescored energy were selected for the ensemble. The structures were visualized and evaluated using PyMOL (<http://www.pymol.org/>), MOLMOL<sup>51</sup>, CHIMERA<sup>52</sup>, PROCHECK-NMR<sup>53</sup> and MolProbity<sup>54</sup>. The chemical shift assignments are available from the Biological Magnetic Resonance Data Bank (accession number 19285), and the final atomic coordinates are available from the Protein Data Bank (2m97). The distance between the N and C terminus was measured to be 14.7 Å for the calcium-loaded globular conformation. For the calcium-free form, average distances between N and C terminus of ~50 Å were extrapolated from urea-disordered ubiquitin, which has a similar amino acid number as TnC<sup>31</sup>.

The GFP molecule is ~4 nm in length and ~2 nm wide. Depending on how the two β-barrels encounter each other, *d*<sup>chromophore</sup> is ~2–4 nm. The Förster radius is normally around R<sub>0</sub> = 5 nm for GFP variants. Thus, in the calcium-free form, a distance of (5.2 + *d*<sup>chromophore</sup> + 5) nm would be expected for the FRET effect, and in the calcium-loaded form (1.5 + *d*<sup>chromophore</sup> + 5) nm is expected. This distance change provides a ratio of 4–6 between the FRET effects, which agrees reasonably well with the observed FRET changes for Twitch-1. Owing to the r<sup>-6</sup> averaging of FRET, only the closest 20% of the conformations are taken into account:

$$\frac{\text{FRET folded}}{\text{FRET unfolded}} = \frac{(d_{\text{chromophore}} + d_{\text{TnC folded}} + R_0)^{-6}}{p_{\text{TnC unfolded closest 20\%}}(d_{\text{chromophore}} + d_{\text{TnC unfolded 20\%}} + R_0)^{-6}}$$

**SAXS.** Small-angle-scattering data were collected on the ID14-3 beamline of the European Synchrotron Radiation Facility ESRF (Grenoble, France). Twitch samples were purified by size exclusion chromatography in buffer A (30 mM MOPS, 100 mM KCl, 100 mM EDTA and 100 mM EGTA, pH 7.5) then taken up either in buffer containing EGTA (2 mM, Ca<sup>2+</sup> free) or 10 mM CaCl<sub>2</sub> (10 mM high Ca<sup>2+</sup>) and centrifuged before the SAXS measurements. Samples were measured at concentrations of 1, 5, 10 and 20 mg/ml, with the running buffer of the size exclusion chromatography used as reference for buffer correction. No particle interactions or radiation damage could be observed for the used data. Raw data processing was performed using the ATSAS package<sup>55</sup> as described in ref. 56, for example. Sets of independent *ab initio* models were calculated using GASBOR<sup>57</sup>, and DAMAVER<sup>58</sup> was used for alignment and averaging. Modeling of the calcium-bound state of Twitch-0 and Twitch-1 was done using CORAL<sup>59</sup> with ECFP (PDB: 2WSN), Citrine (PDB: 3DPX), the minimal domain structure described here and the respective SAXS data. To avoid clashes, we allowed up to five linker residues between the rigid bodies to account for the fact that the termini of the respective crystal structures might be flexible or change their conformation if the minimal domain folds upon Ca<sup>2+</sup> binding and, thus, might also influence the conformation of the directly neighboring residues of the fluorescent proteins. Figures were prepared using USCF Chimera<sup>60</sup>.

**Bacterial plate pre-screening of FRET calcium sensors.** Libraries of biosensor mutants were subcloned into pRSETB (Invitrogen) and transformed into *E. coli* XL-1 Blue cells. The cells were plated on LB agar plates containing 50 µg/ml ampicillin with an average colony density of approximately 800–1,000 colonies per plate and incubated overnight at 37 °C. After 1 d at 4 °C, the biosensor mutants were fully mature and could be analyzed. For this purpose, colonies were blotted onto Whatman filter paper and imaged using a Lambda LS/30 Stand Alone Xenon Arc Lamp and Power Supply, a Lambda 10-2 Optical Filter Changer (both Sutter Instrument), and a CoolSNAP ES2 CCD Camera. The excitation filter used was D 436/40×, and the emission filters were D 480/40 (CFP, Cerulean3 and mTurquoise2) and HQ 535/30 (cpCitrine 174) (all from Chroma). Cell Profiler version 10415 Cell Image Analysis Software was used for automated region of interest (ROI) selection, and the acquired data was processed with MetaFluor version 7.7.0. The Whatman paper containing the colonies was sprayed with a solution of polylysine (50 µg/ml) and ionomycin (50 µg/ml) in a buffer of 30 mM MOPS, 100 mM KCl, pH 7.5, to open the bacterial cell membrane. The whole membrane was dampened with the solution by spraying 4–5 times using 30-ml plastic spray bottles (Rotert, Germany). After 5 min of incubation and acquisition of baseline fluorescence, a solution of 100 mM CaCl<sub>2</sub> was sprayed on the cells. The change in FRET was acquired for 5 min. Data from the plate screening were analyzed in MatLab R2011b, 10–20 of the best-performing colonies were picked, and plasmids were isolated for further analysis. Our selection criteria were lowest basal starting ratio, highest calcium-induced ratio change and the intersection of variants that ranked high in both categories. We identified the best-performing variants (top 1% fraction per plate) using as selection criteria a starting ratio  $R_0$  of ~1 under basal conditions and increased FRET change ( $\Delta R/R$ ) upon calcium addition.

**Expression and purification of proteins.** For protein expression and purification, genes encoding the Twitch biosensors were subcloned into pRSETb (Invitrogen) and transformed in *E. coli* BL21 cells. Purification of the protein of interest was achieved by using either His Mag Sepharose Ni magnetic beads (GE Healthcare) for small-scale purification, or Ni-NTA 30 polypropylene columns (Qiagen), both capable of chelating the His<sub>6</sub> tag. The suspension was washed with column-washing buffer containing 20 mM imidazole. Proteins were eluted by replacement of the bound protein with imidazole using column-elution buffer containing 250 mM imidazole.

**Calcium titration.** To determine the  $K_d$  value, purified protein was used and a pre-warmed (room temperature) titration kit was applied as follows. Two stock solutions were prepared in accordance with previous literature<sup>61</sup>: (i) for zero calcium, a solution of 1 ml of zero-calcium buffer with one volume of protein solution (~0.2–1 µM protein, directly in cuvette); (ii) for high calcium, a solution of 6 ml of 39.8 µM free calcium buffer with six volumes of protein solution. A spectral baseline was recorded using a fluorescence spectrophotometer (Varian Cary Eclipse). The excitation wavelength for the CFP/YFP-FRET pair was 432 nm. The emission was determined in the range from 450 nm to 600 nm (all bandwidths 5 nm). The  $K_d$  value was calculated by fitting a sigmoidal dose response curve to the plotted log<sub>10</sub> values of the free calcium points (in M) versus the normalized signal (normalized to 39.8 µM free calcium). Ratio changes ( $\Delta R/R$ ) were calculated according to the formula

$$\text{FRET Ratio Change} = \frac{\Delta R}{R} = \frac{R_{Ca^{2+} \text{ saturated}} - R_{Ca^{2+} \text{ free}}}{R_{Ca^{2+} \text{ free}}}$$

**Stopped-flow measurements.** To determine the kinetics ( $K_{off}$  and  $K_{on}$ ) of the calcium indicators, a Varian Cary Eclipse fluorescence spectrophotometer fitted with an Applied Photophysics RX pneumatic drive unit was used. Two stock solutions were prepared as follows: calcium-saturated indicator (5 ml), 10 mM MOPS, 4 mM CaCl<sub>2</sub>, 2 mM MgCl<sub>2</sub>, 50 mM KCl, ~0.2–1 µM indicator (pH 7.5); BAPTA solution (5 ml), 10 mM MOPS, 50 mM KCl, 20 mM BAPTA (pH 7.5). The stopped-flow experiment was carried out at room temperature (~23 °C) and the two solutions were mixed with an injection pressure of 3.5 bar. Excitation was set to 432 nm (bandwidth 5 nm) for CFP. Emission spectra of the two individual channels were taken in an alternated manner at 475 nm (for CFP, bandwidth 10 nm) and 527 nm (for YFP, bandwidth 10 nm) respectively. Acquisition time was set to 12.5 ms, duration to >10 s and mixing volume to 400 µl with a mixing dead time of the instrument of 8 ms. An average of the individual channels and the acceptor/donor ratio was calculated. The decay time ( $\tau$ , sec) was determined by fitting with a single- or double-exponential curve to the acceptor/donor ratio using OriginLab 7.5.

**Screening of calcium biosensors in neonatal cultured primary rat hippocampal neurons.** Neuronal screening was performed essentially as reported previously<sup>11,62</sup>, with minor adaptations for FRET ratiometric imaging. Genes encoding Twitch biosensors were subcloned into a hippocampal neuron screening vector pGP-SIV-hsyn1-IRES-nls-mCherry-WPRE-SV40 (hsyn1: human

synapsin-1 promoter) using blunt-end cloning. Cultures of primary hippocampal neurons were obtained from P0 rat pups by dissection, papain-based dissociation and plating onto Matrigel-coated (BD Biosciences), 24-well glass-bottom plates (MatTek) and then cultured in DMEM/B27 medium (Invitrogen). The SIV-based lentiviral vectors containing Twitch biosensors were produced through transfection of HEK293T packaging cells in 10-cm plates. On day 3 *in vitro* the hippocampal neuronal cultures were infected *in vitro* for 16 h using newly harvested lentiviral particles, and medium was replaced with DMEM/B27 with 4 mM AraC (Invitrogen and Sigma). On day 16–18 *in vitro* infected neurons were stimulated using a custom-built, 24-well multiplexed field stimulator with platinum wires and imaged using an Olympus IX81 motorized, inverted microscope (10× objective, 0.4 NA with optical filters 436/20 for CFP excitation, 455 longpass (LP), 520 LP dichroic, 485/30 emission for CFP and FITC-TxRed emission for YFP; all optical filters and dichroic mirrors by Semrock); Prior Scientific H117 ProScanII motorized stage; a cyan (505 nm) LED illumination source (Cairn); and an EMCCD camera (AndoriXon 897, 34.8 frames per second). Field stimuli were delivered in 40-V, 83-Hz, 1-ms pulses for the following trains: 1, 2, 3, 5, 10, 20, 40, 80 and 160 field stimuli. The whole system was automated using MetaMorph (MM; Molecular Devices) and MATLAB (MathWorks) software. Imaging buffer included the following (in mM): 145 NaCl, 2.5 KCl, 10 glucose, 10 HEPES (pH 7.4), 2 CaCl<sub>2</sub>, 1 MgCl<sub>2</sub>, 0.01 3-(2-carboxypiperazin-4-yl)-propyl-1-phosphonic acid (cPP, Tocris Bioscience), 0.01 6-cyano-7-nitroquinoxaline-2,3-dione (CNQX, Tocris Bioscience), 0.01 gabazine (Tocris Bioscience) and 1-methyl-4-carboxyphenylglycine (MCPG, Tocris Bioscience). Images were processed and analyzed using custom software.

#### Transfection of primary cultured cells and dissociated neurons.

Twitch indicators were delivered to primary cell cultures using Lipofectamine. 2–3 µg of plasmid DNA were added to 250 µl of Opti-MEM I. In parallel, 10 µl of Lipofectamine 2000 were mixed with 250 µl of Opti-MEM I and incubated for 5 min at room temperature. The two separate solutions containing DNA and Lipofectamine were mixed and incubated for an additional 20 min at room temperature to form vesicles of DNA. The DNA-Lipofectamine solution was added to cells growing in 30-mm glass bottom dishes, and the transfection was allowed to proceed for 3 h incubating at 37 °C with 5% CO<sub>2</sub>. After a 3 h of incubation, cells were washed with 1 ml PBS and 2 ml of DMEM (10% FCS, 1% Pen/Strep) were added. Cells were allowed to recover from the treatment and to express the Twitch indicators overnight and were ready to use the next day.

**Mouse preparation for *in vivo* imaging.** All procedures were in accordance with protocols approved by the Janelia Farm Research Campus Institutional Animal Care and Use Committee and by the state governments of Baden-Württemberg and Upper Bavaria, Germany. C57bl mice (males and females) were used in all studies and were 2.5–3.5 months old at the start of experiments. Mice were anesthetized either with isoflurane (2.5% for induction, 1.25–1.75% during surgery) or by intraperitoneal injection of a mixture of ketamine and xylazine (80 µg and 8 µg per gram of body weight, respectively). In all cases, an animal was excluded if the cranial window quality was low.

For data shown in **Figure 4a–e** and **Supplementary Figure 11**, after skin removal and thinning of the skull, AAV encoding Twitch-3 or YC3.60 was injected through the thinned bone to the left visual cortex (2.5 and 2.9 mm lateral and 0.2 anterior to lambda, 250 µm deep, 25 nl per injection site). 3–4 weeks following injections, a circular craniotomy (2–3 mm diameter) was placed above the injection site. A custom titanium head post was fixed to the skull using black dental cement (Contemporary Ortho-Jet). The craniotomy was covered with 1% agarose and a round glass coverslip (Warner Instrument, 3 mm diameter, number 1 thickness) was cemented to the skull to reduce motion of the exposed brain. The animal was then transferred to the imaging setup, where it was placed on a warm blanket (37 °C) and kept anesthetized using 0.25–0.5% isoflurane and sedated with chlorprothixene (20–40 µl at 0.33 mg/ml, intramuscular (i.m.))<sup>63</sup>.

For data shown in **Fig. 4h,i**: the HIV-based lentiviruses (FUGW as the backbone, Addgene plasmid number 14883; virus titer  $\geq 10^8$  colony-forming units per ml) containing Twitch-2B or Twitch-3 biosensors were stereotactically injected (3.0 mm anterior to bregma, 0.84 mm lateral, 2.9 mm deep,  $\leq 1$  µl) into the rostral migratory stream of C57BL/6 mice for transduction of adult-born cells moving toward the olfactory bulb. The transduced juxtglomerular neurons in the olfactory bulb were imaged after their arrival to and settling in the glomerular layer of the olfactory bulb, at 35–37 d after infection. To study sensor function after long-term chronic expression, mice expressing Twitch-2B were imaged again at 141 d after infection. On the day of imaging, a mouse was anesthetized by intraperitoneal injection of a mixture of ketamine and xylazine (80 µg and 8 µg, respectively, per gram of body weight), for induction; 40 µg and 4 µg, respectively, per gram of body weight for maintenance). A custom-made recording chamber was glued to the skull. The mouse was transferred to the imaging setup, where it was placed on a warm blanket (37 °C). The chamber was fixed in an *xy* table and perfused with warm (38 °C) standard extracellular solution containing (in mM): 125 NaCl, 4.5 KCl, 26 NaHCO<sub>3</sub>, 1.25 NaH<sub>2</sub>PO<sub>4</sub>, 2 CaCl<sub>2</sub>, 1 MgCl<sub>2</sub> and 20 glucose (pH 7.4) when bubbled with 95% O<sub>2</sub> and 5% CO<sub>2</sub>. A craniotomy (typical size about 1 mm × 0.5 mm) was made using a 30-gauge syringe needle; the dura was left intact (see reference 21 for details). To reduce the movement artifacts, the craniotomy was filled with 2% agarose.

In a separate set of experiments, the area under the cranial window (prepared as described above) was stained either with Oregon Green 488 BAPTA-1 a.m. (OGB-1, Invitrogen, Carlsbad, CA) or Fura PE-3 a.m. (TEFLAB, Austin, TX) using multicell bolus loading technique<sup>64</sup>.

Odorants were applied for 4 s through a custom-made flow-dilution olfactometer positioned in front of the snout of freely breathing mice as described previously<sup>21</sup>.

***In vivo* mouse imaging.** For data shown in **Figure 4a–e** and **Supplementary Figure 11**, a custom-built two-photon microscope with a resonant galvanometric scanner was used for imaging (designs available at <http://research.janelia.org/Svoboda/>). The light source was a Mai Tai HP 100-fs pulsed laser (Spectra-Physics) running at 860 nm for Twitch-3 and at 870 nm for YC 3.60 imaging. The objective was a 16× 0.8 NA (Nikon). Image acquisition was performed using ScanImage 4 (<http://www.scanimage.org>)<sup>65</sup>. Images (512 pixels × 512 pixels, 250 µm

× 250 μm) were collected at 15 Hz from two channels (using 505-nm longpass dichroic mirror, 480/40 filter for CFP channel, and 535/50 filter for cpCitrine channel, Chroma). Mice were randomly chosen to be injected with Twitch-3 or YC3.60. The investigator was blinded to the group allocations for injection of the given AAV. Functional imaging experiments were performed 21–30 d after viral injection. Moving gratings in eight different orientations were displayed to the right eye of lightly anesthetized mice<sup>11,63,66</sup>. Simultaneous two-photon imaging in the contralateral layer 2/3 neurons of V1 revealed bright cellular fluorescence expression as well as neuropil staining. Notably, Twitch-3 imaging required lower excitation intensity than YC 3.60 (20 mW versus 45 mW average laser power for depth of 150 μm under the brain surface) to maintain a similar SNR. Ratio images exhibit robustness to small sample movements; moreover, pixel values were more uniformly distributed than the corresponding fluorescence images pixel values. Therefore, ratio images emphasize regions with lower fluorescence signal. The fraction of responsive cells was larger for Twitch-3 than for YC 3.60 (1,264/3,633 from six animals for Twitch-3, 414/2,149 from 5 animals for YC 3.60). The majority of the responsive cells had a preferred stimulus orientation (856/1,264 for Twitch-3, 258/414 for YC 3.60; **Fig. 4** and **Supplementary Fig. 11**) in agreement with previous studies<sup>11,63</sup>. Data for OGB-1 were obtained from three animals (fraction of responsive cells was 1,297/3,606).

For data shown in **Fig. 4h,i**, imaging was performed with a customized two-photon microscope based on Olympus FV1000 system (Olympus, Tokyo, Japan) and MaiTai Deep See Laser (Spectra Physics, Mountain View, CA). In this case the experimenter was not blinded to the type of GECI injected. Ten mice in total were used for this analysis with between 10 and 40 experiments performed for each indicator. The emitted light was collected with the Zeiss 20× water immersion objective (NA 1.00), and separated with a 515 LP dichroic mirror and two band-pass filters: 475/64 and 500LP for CFP and YFP channels respectively. Images were collected at 7–20 Hz (depending on the size of the imaging frame).

**Mouse visual stimuli.** Moving grating stimuli were shown to mice from the Psychophysics Toolbox<sup>67,68</sup> generated in MATLAB. Each trial consisted of a 4-s blank stimulus period (uniform gray at mean luminance) followed by 4 s of drifting sinusoidal grating stimulus (0.05 cycles per degree, 1 Hz temporal frequency). The visual stimuli were synchronized to individual image frames using frame-start pulses provided by ScanImage 4. The gratings were shown on an LCD monitor (30 cm × 40 cm) 25 cm in front of the center of the right eye of the mouse. The monitor subtended an angle of ± 38° horizontally and ± 31° vertically around the mouse's eye.

**Image analysis.** *Mouse visual cortex.* Analyses were performed in MATLAB. ROIs corresponding to cell bodies were chosen using a semiautomated algorithm<sup>11</sup>. Ring-shaped or circular ROIs were placed at cell cytosolic regions (excluding the nucleus) or on cell somata, respectively, according to each cell's staining pattern. Fluorescence traces for each cell were measured by averaging all pixels within the ROI. The neuropil contamination was corrected as previously described<sup>66</sup>; briefly, the neuropil signal  $F_{\text{neuropil}}(t)$  surrounding each cell was measured by averaging the pixel signals

within a 20-μm radius from the cell center (excluding all selected cells). The true fluorescence signal of a cell body was then estimated as follows:

$$F_{\text{cell\_true}}(t) = F_{\text{cell\_measured}}(t) - r \cdot F_{\text{neuropil}}(t)$$

with  $r = 0.7$  used throughout the study. After neuropil correction, the  $\Delta R/R_0$  of each trial was calculated as  $(R - R_0)/R_0$ , where  $R_0$  is the baseline ratio between fluorescence signal from cpCitrine and CFP channels, averaged over a 2-s period immediately before the start of sensory stimulation, and  $R$  is the ratio between these two channels in each time point. Visually responsive neurons were defined as cells with  $\Delta R/R_0 > 0.05$  during at least one stimulus period, and using ANOVA across blank and eight direction periods (averaged over 2 s,  $P < 0.01$ )<sup>69</sup>.

**Olfactory bulb.** Data inspection during the experiment was carried out using Fluoview (Olympus, Tokyo, Japan), and NeuroPlex (RedShirtImaging LLC, Decatur, GA) software. Detailed data analysis was performed offline using a combination of Fluoview, NeuroPlex, ImageJ (<http://rsb.info.nih.gov/ij/>) with the WCIF plug-in (Wright Cell Imaging Facility, Toronto, Canada), MetaMorph (Molecular Devices, West Chester, PA) and Excel (Microsoft, Redmond, WA), as well as custom-made programs written for Labview (National Instruments, Austin, TX), Igor Pro (WaveMetrics, Portland, OR) or IDL (ITT, Boulder, CO).

Signal-to-noise ratios were measured as mean peak amplitude of the transients divided by the s.d. of the baseline noise.

**Whole-cell recordings.** Whole-cell recordings were made from layer 2/3 pyramidal cells using an EPC-10 patch-clamp amplifier (HEKA, Lambrecht, Germany) as described previously<sup>70</sup>. The HIV-based lentiviruses (FUGW as the backbone, Addgene 14883; virus titer  $\geq 10^8$  colony forming units/ml) encoding for Twitch-2B were stereotactically injected (2 mm posterior to bregma, 1.5 mm lateral, 0.5 mm deep,  $\leq 1 \mu\text{l}$ ) into the cortex. 1–2 weeks after viral transfection, animals were decapitated, and coronal cortical slices of 300-μm thickness were cut in ice-cold standard extracellular solution. Slices were incubated in this solution for at least 1 h before being transferred to the setup. Patch pipettes were made from borosilicate glass (Hilgenberg GmbH, Malsfeld, Germany) and had resistances of 7–10 MΩ when filled with the intracellular pipette solution containing (in mM): 140 Potassium gluconate, 12 KCl, 4 NaCl, 4 Mg-ATP, 0.4 Na-GTP and 10 HEPES (pH 7.3). Experiments were performed at 35 °C. Membrane potential was held at -70 mV. Single action potentials and bursts thereof were evoked by depolarizing current steps of different duration (5–300 ms).

**Mice for functional imaging of T lymphocytes.** C57BL/6 and OT-II mice<sup>40</sup> were bred in the facilities of the Max Planck Institute of Neurobiology. All animal procedures were in accordance with the guidelines of the committee on animals of the Max Planck Institute of Neurobiology and were approved by the state government of Upper Bavaria, Germany.

**Retrovirus supernatant production.** The replication-deficient ecotropic retrovirus producer cells (Phoenix) were transfected using the calcium-phosphate/chloroquine method with 12 μg of pMSCV retroviral vector and 3.5 μg of pCL-Eco packaging

plasmid. After 48 h the virus-containing culture supernatant was collected, replaced with fresh culture medium and concentrated by centrifugation at 6,000 RCF for 18 h at 4 °C. Pellets were resuspended in fresh virus supernatant from the transfected Phoenix cells and filtered through a 0.45- $\mu$ m pore-sized filter, and the filtrate was immediately used for the retroviral transduction of target cells or snap frozen on dry ice and stored at -80 °C.

**Retroviral transduction of T lymphocytes.** Single-cell suspensions were prepared from spleens by mechanical disruption by forcing the spleen through 40- $\mu$ m cell strainers (BD Biosciences) followed by erythrocyte lysis using hypotonic 0.83%  $\text{NH}_4\text{Cl}$ . For the transduction of wild-type T lymphocytes,  $\text{CD4}^+$  cells were purified using the MagCelect  $\text{CD4}^+$  cell Isolation Kit (R&D) and were stimulated using plate-bound anti-CD3 and anti-CD28 (BD Biosciences). After 24 h, the T lymphocytes were suspended in retrovirus supernatant supplemented with 8  $\mu\text{g}/\text{ml}$  polybrene (Sigma-Aldrich) and 10 ng/ml IL-2 (PeproTech), seeded onto RetroNectin-coated (Takara) wells, and spin-infected by centrifugation at 450 RCF for 90 min at room temperature. For the transduction of TCR transgenic T lymphocytes, OT-II splenocyte suspensions were cultured in presence of 10  $\mu\text{g}/\text{ml}$  OVA<sub>323-339</sub> peptide. After 48 h, Dynabeads Mouse Pan B (B220) (Invitrogen) were used to deplete the cultures of B cells, followed by transduction as described above.

**T lymphocyte transfer for lymph node imaging.** One day after retroviral transduction,  $5 \times 10^6$ – $15 \times 10^6$  OT-II T cells were adoptively transferred via i.v. injection into the tail vein of mildly irradiated (20 Gy) C57BL/6 mice. The mice were allowed to recover for one week before the adoptive transfer of antigen-presenting cells. Bone marrow dendritic cells (BMDCs) were obtained from the femurs of C57BL/6 mice and were cultured in the presence of GM-CSF producing hybridoma-conditioned medium with repeated medium exchange to deplete the nonadherent cells. After 8 d in culture, the BMDCs were trypsinized and activated overnight in fresh medium supplemented with 1  $\mu\text{g}/\text{ml}$  LPS. The activated BMDCs were labeled using 4  $\mu\text{M}$  SNARF-1 (Invitrogen), and  $2 \times 10^6$  BMDCs were injected subcutaneously into the lower leg. Imaging of the draining popliteal lymph node was performed 1 d later.

**In vivo two-photon microscopy calcium imaging of T lymphocytes.** Time-lapse two-photon laser-scanning microscopy was performed essentially as reported previously<sup>36</sup> using an SP2 confocal microscope (Leica) equipped with a 10 W Millennia/Tsunami laser (Newport Spectra Physics). The laser wavelength was set to 835 nm for CFP excitation and directed through a Leica 25 $\times$  water immersion objective (NA 0.95). Areas measuring 240  $\mu\text{m} \times 240 \mu\text{m}$  were scanned, and z-stacks (25–30  $\mu\text{m}$ ) were acquired using a 3- to 4- $\mu\text{m}$  z-step. The acquisition rate was at intervals of 16–20 s, with images averaged twice. The fluorescence signals were recorded using non-descanned photomultiplier tube (PMT) detectors (Hamamatsu) equipped with 475/50 nm (CFP), 537/26 nm (FRET), and 630/69 nm (SNARF-1, Texas Red) band-pass filters (Semrock). The PMT settings for CFP and FRET fluorescence were kept identical during all experiments. To estimate FRET ratios, CFP bleed-through was corrected. The CFP bleed-through into the FRET channel was determined to 44%. The fraction of cpCitrine emission in the CFP channel and direct

excitation of cpCitrine at 835 nm was negligible. The mice were anaesthetized by i.p. injection with fentanyl, midazolam, medetomidine (50  $\mu\text{g}$ , 50 mg, and 500  $\mu\text{g}$  per kilogram of body weight, respectively), intubated and ventilated with 1.5% isoflurane. To expose the popliteal lymph nodes the skin was cut at the hollow of the knee followed by a careful dissection of the adductor musculature. Animals were stabilized in a custom-made microscope stage, and the body temperature was regulated using a heat pad (37.5 °C). Physiological parameters and electrocardiograms were constantly monitored and recorded during the imaging. Blood vessels were visualized by the i.v. infusion of Texas Red-conjugated dextran (50  $\mu\text{g}$ ; 70 kDa; Invitrogen).

**Imaging data analysis (T lymphocytes).** Images were acquired using Leica LCS software and subsequently processed and analyzed by ImageJ (<http://rsb.info.nih.gov/ij/>). A Gaussian blur filter was applied and maximum intensity z-projections were made to obtain two-dimensional videos. In the images shown in **Figure 5**, the CFP channel is depicted as green and the YFP channel as red. For analysis, cell shapes at each time point were manually outlined in the maximum projection picture, and the average signal intensities of all pixels for the area were calculated. The calculation of motility and calcium signals was done using Excel (Microsoft). The FRET signal was corrected for CFP bleed-through,  $\text{cFRET} = \text{FRET} - 0.44 \times \text{CFP}$ , and the ratios of  $\text{cFRET}/\text{CFP}$  were normalized to display the fractional ratio change  $\Delta\text{R}/\text{R}_0$  ( $\text{R}_0$  for Twitch-1 = 0.8; Twitch-2B 0.5). Values were arbitrarily chosen for Twitch-1 so that only a tiny fraction of cells would be lower than this threshold. For Twitch-2B,  $\text{R}_0$  was adjusted to match the baseline population to the same level than Twitch-1). The overlaid box plots on the scatter plots in **Figure 5** indicate the 25th and 75th percentiles, and the whiskers represent the 5th and 95th percentiles. All statistical analysis (Mann-Whitney *U* test) was performed with GraphPad Prism.

- Ikura, M., Kay, L.E. & Bax, A. A novel approach for sequential assignment of 1H, 13C, and 15N spectra of proteins: heteronuclear triple-resonance three-dimensional NMR spectroscopy. Application to calmodulin. *Biochemistry* **29**, 4659–4667 (1990).
- Grzesiek, S. & Bax, A. An efficient experiment for sequential backbone assignment of medium sized isotopically enriched proteins. *J. Magn. Reson.* **99**, 201–207 (1992).
- Grzesiek, S. & Bax, A. Correlating backbone amide and sidechain resonances in larger proteins by multiple relayed triple resonance NMR. *J. Am. Chem. Soc.* **114**, 6291–6293 (1992).
- Vuister, G.W. & Bax, A. Quantitative J correlation: a new approach for measuring homonuclear three bond J(HNH $\alpha$ ) coupling constants in 15N-enriched proteins. *J. Am. Chem. Soc.* **115**, 7772–7777 (1993).
- Hansen, M.R., Mueller, L. & Pardi, A. Tunable alignment of macromolecules by filamentous phage yields dipolar coupling interactions. *Nat. Struct. Biol.* **5**, 1065–1074 (1998).
- Ottiger, N., Delaglio, F. & Bax, A. Measurement of J and dipolar couplings from simplified two-dimensional NMR spectra. *J. Magn. Reson.* **131**, 373–378 (1998).
- Delaglio, F. *et al.* NMRPipe: a multidimensional spectral processing system based on UNIX pipes. *J. Biomol. NMR* **6**, 277–293 (1995).
- Keller, R.L.J. *The Computer Aided Resonance Assignment Tutorial* (Cantina, 2004).
- Shen, Y. *et al.* Consistent blind protein structure generation from NMR chemical shift data. *Proc. Natl. Acad. Sci. USA* **105**, 4685–4690 (2008).
- Raman, S. *et al.* NMR structure determination for larger proteins using backbone-only data. *Science* **327**, 1014–1018 (2010).
- Koradi, R., Billeter, M. & Wuthrich, K. MOLMOL: a program for display and analysis of macromolecular structures. *J. Mol. Graph.* **14**, 51–55 (1996).

52. Pettersen, E.F. *et al.* UCSF Chimera—a visualization system for exploratory research and analysis. *J. Comput. Chem.* **25**, 1605–1612 (2004).
53. Laskowski, R.A., Rullmann, J.A., MacArthur, M.W., Kaptein, R. & Thornton, J.M. AQUA and PROCHECK-NMR: programs for checking the quality of protein structures solved by NMR. *J. Biomol. NMR* **8**, 477–486 (1996).
54. Davis, I.W. *et al.* MolProbity: all-atom contacts and structure validation for proteins and nucleic acids. *Nucleic Acids Res.* **35**, W375–W383 (2007).
55. Konarev, P.V., Petoukhov, M.V., Volkov, V.V. & Svergun, D.I. ATSAS 2.1, a program package for small-angle scattering data analysis. *J. Appl. Cryst.* **39**, 277–286 (2006).
56. Putnam, C.D., Hammel, M., Hura, G.L. & Tainer, J.A. X-ray solution scattering (SAXS) combined with crystallography and computation: defining accurate macromolecular structures, conformations and assemblies in solution. *Q. Rev. Biophys.* **40**, 191–285 (2007).
57. Svergun, D.I., Petoukhov, M.V. & Koch, M.H.J. Determination of domain structure of proteins from X-ray solution scattering. *Biophys. J.* **80**, 2946–2953 (2001).
58. Volkov, V.V. & Svergun, D.I. Uniqueness of *ab initio* shape determination in small-angle scattering. *J. Appl. Cryst.* **36**, 860–864 (2003).
59. Petoukhov, M.V. *et al.* New developments in the ATSAS program package for small-angle scattering data analysis. *J. Appl. Cryst.* **45**, 342–350 (2012).
60. Wriggers, W. & Chacon, P. Using Situs for the registration of protein structures with low-resolution bead models from X-ray solution scattering. *J. Appl. Cryst.* **34**, 773–776 (2001).
61. Tsien, R. & Pozzan, T. Measurement of cytosolic free Ca<sup>2+</sup> with quin2. *Methods Enzymol.* **172**, 230–262 (1989).
62. Wardill, T.J. *et al.* A neuron-based screening platform for optimizing genetically encoded calcium indicators. *PLoS ONE* **8**, e77728 (2013).
63. Niell, C.M. & Stryker, M.P. Highly selective receptive fields in mouse visual cortex. *J. Neurosci.* **28**, 7520–7536 (2008).
64. Stosiek, C., Garaschuk, O., Holthoff, K. & Konnerth, A. *In vivo* two-photon calcium imaging of neuronal networks. *Proc. Natl. Acad. Sci. USA* **100**, 7319–7324 (2003).
65. Pologruto, T.A., Yasuda, R. & Svoboda, K. Monitoring neural activity and [Ca<sup>2+</sup>] with genetically encoded Ca<sup>2+</sup> indicators. *J. Neurosci.* **24**, 9572–9579 (2004).
66. Kerlin, A.M., Andermann, M.L., Berezovskii, V.K. & Reid, R.C. Broadly tuned response properties of diverse inhibitory neuron subtypes in mouse visual cortex. *Neuron* **67**, 858–871 (2010).
67. Brainard, D.H. The psychophysics toolbox. *Spat. Vis.* **10**, 433–436 (1997).
68. Pelli, D.G. The VideoToolbox software for visual psychophysics: transforming numbers into movies. *Spat. Vis.* **10**, 437–442 (1997).
69. Ohki, K., Chung, S., Ch'Ng, Y.H., Kara, P. & Reid, R.C. Functional imaging with cellular resolution reveals precise micro-architecture in visual cortex. *Nature* **433**, 597–603 (2005).
70. Garaschuk, O., Hanse, E. & Konnerth, A. Developmental profile and synaptic origin of early network oscillations in the CA1 region of rat neonatal hippocampus. *J. Physiol. (Lond.)* **507**, 219–236 (1998).

# CHAPTER 5

---

**Discussion**

**Conclusion**

# 5 Discussion

Fluorescence imaging techniques for *in vivo* visualization of neuronal activity often entail the use of GECIs as reporter tools. GECIs currently rely on two distinct designs: the single fluorophore based (single-wavelength) indicators, such as GCaMPs, or FRET-based indicators, such as the Twitch indicators reported herein. The work presented in this dissertation is the culmination of multidisciplinary research that has resulted in a significant contribution to the field of fluorescence imaging of neuronal activity.

The results are represented in three papers (Chapter 2, 3 and 4). In our first study (Chapter 2), we deciphered the underlying structural mechanisms taking place during  $\text{Ca}^{2+}$ -binding in a troponin C-based FRET indicator, TN-XXL. The data gathered during this study laid the foundation for our design strategy for a new minimal domain GECI. In Chapter 3, the product of our first functional minimal domain Twitch-1 GECI was used to elucidate the calcium signaling of motile T cells during epitope recognition on dendritic cells. The output of this work was the visualization of calcium oscillations of T cells for the first time *in vivo*. In Chapter 4, we present a new functional bacterial screening assay to screen and evaluate thousands of genetically modified GECI variants, as well as the result of efforts - a family of Twitch GECIs with minimal  $\text{Ca}^{2+}$ -binding domains, suitable for chronic imaging and detection of single APs *in vivo*.

## 5.1 Engineering minimal domain Twitch GECIs based on structure-function studies

The principal work outlined herein, was to design and engineer a new generation of FRET-based GECIs with a minimum of  $\text{Ca}^{2+}$ -binding sites (minimal domain). The inspiration for this work was derived from synthetic dyes, such as Fura-2 and OGB-1 (Grynkiewicz et al., 1985), and from previous FRET-based indicators (Mank et al., 2006; Mank et al., 2008).

To better understand the underlying mechanisms of FRET-based GECIs, we used TN-XXL as a model to study the interplay between the two identical C-terminal domains. TN-XXL is currently the only GECI with this unique design. We also considered investigating the mechanisms of the related Yellow Cameleons (YCs) (Horikawa et al., 2010). The Yellow Cameleons are based on CaM, which altogether offers a different modular and mechanistic behavior, compared to TN-XXL. The binding of  $\text{Ca}^{2+}$  to CaM and its M13 subunit in Yellow

Cameleons is illustrated in Figure 1.7. Moreover, the structural interplay between CaM and the M13 subunit has been extensively investigated in both FRET-based and single GFP-based indicators. Crystal structures from different generations of GCaMPs have been essential in the development of improvements of these indicators (Akerboom et al., 2009). For the troponin-based GECIs, we solely relied on independent crystal structures of GFP molecules and various troponin C species. *In silico* modelling of independent non-related protein structures provides some, although limited, insight on how the characteristics of the GECI ultimately will be. In Chapter 2 we elucidated, for the first time, the mechanism and Ca<sup>2+</sup>-binding dynamics utilized by a troponin C-based GECI. We studied the interplay by monitoring the binding of Ca<sup>2+</sup> to individual EF-hands via tyrosine fluorescence (Chapter 2, Figure 1). Endogenous phenylalanine residues (Phe) were substituted by tyrosines (Tyr) to determine the Ca<sup>2+</sup> affinity (K<sub>D</sub>) and kinetics for binding events in each EF-hand separately (Swindle and Tikunova, 2010). The results indicate that the first C-terminal lobe (EF-hands 3-1 and 3-2) is the primary contributor to FRET-signal output, whereas EF-hands 4-1 and 4-2 presumably take on a stabilizing function (Appendix Chapter 2, Figure S1). This was a key finding, as it provided the fundamental understanding of the underlying mechanism for this GECI. In addition, it revealed that a structural basis for a minimal domain existed within the TnC domain, under the right stereochemical conditions. Subsequently this led to the design strategy for the Twitch GECIs.

Henceforth, we considered two main design avenues. The first avenue was to physically abolish the unfavorable domain (N- or C-terminal) from the wild-type troponin C. Another avenue, inspired by EF-hand 1 in human cardiac troponin C (hcTnC) (Farah and Reinach, 1995), was to render the EF-hand(s) inactive, while preserving structural function and cooperativity. By introducing an aspartic acid (Asp) residue into the EF-hand, we could render the binding domain inactive in manner that resembles a bound state EF-hand, while still maintaining the physical structure to promote Ca<sup>2+</sup>-binding in the neighboring EF-hand. During our studies of TN-XXL, we used SAXS in combination with NMR, analytical ultracentrifugation and size-exclusion chromatography. From these assays, we could investigate the structural arrangements of TN-XXL before and after binding of Ca<sup>2+</sup>, as well as correlate the data with the FRET output. It was necessary to combine all these methods, as each method alone, would yield only a fraction of the complete structural understanding. Figure 2G and Figure 3C in Chapter 2, clearly shows the distinct conformational change that TN-XXL undergoes during binding events.

It became apparent from our data that the interplay of the two C-terminal lobes in TN-XXL constitutes a complex series of structural reorientations upon Ca<sup>2+</sup>-binding. The data

provides some explanation as to why prior attempts to engineer minimal domain GECIs based on csTnC were unsuccessful. These attempts relied mainly on truncations of troponin C at various locations around the binding domains, down to a single physical EF-hand. Many of our attempts failed or showed very little promise. We now know that the inter-cooperativity between EF-hands is essential and must be considered, when designing minimal domains. Our previous attempts were therefore suboptimal due to the removal of stabilizing EF-hands and the subsequent loss of cooperativity (Nelson et al., 2002).

Our efforts of shortening the troponin C domain resulted in high initial FRET in the unbound state – a poor quality for an improved signal-to-noise ratio indicator (Chapter 4, Figure 2e). We know from Chapter 2 and 4 (Geiger et al., 2012; Thestrup et al., 2014) that FRET-based GECIs are unstable structures in the unbound state that transition into a compact and rigid form in the bound state. With the introducing of peptide linkers, we enhanced FRET efficiency (Equation 1.4) by aligning the fluorophores (FP  $\beta$ -barrels). Notably, designing peptide linkers that add beneficial characteristics to the GECI under both bound and unbound conditions, provides an additional dimension for structural improvements. Nevertheless, this possibility is prohibitively complex without detailed modelling and abundant structural knowledge. Residues from a synthetic peptide linker can easily interact with neighboring residues, influencing the indicator under both conditions.

Considerable attention should also be paid to the choice of fluorophore pairs. With TN-XXL, the use of a circular permuted variant of Citrine (cpCitrine) had a positive effect on the FRET efficiency (Mank et al., 2008). We conducted screens of different fluorophores to optimize not only the FRET efficiency, but also the brightness. Finally, our research shows an evident effect on GECI performance under varying pH and temperatures. These studies were conducted as cellular environments can expose the indicators to a range of temperatures and different pH levels. Figure 5 in Chapter 2 shows how temperature and pH can affect the performance of a GECI.

## 5.2 Modification and screening of Twitch GECIs using peptide linkers and directed molecular evolution

The first functional minimal domain Twitch GECI, Twitch-1 (Chapter 3 and 4), was a result of a proline linker screening assay. The two most important parameters we sought to optimize were the proximity and orientation of the FPs. We initially targeted the linkers, hypothesizing that we would see a greater effect, screening for  $R_0$  and  $\Delta R/R$ .

Peptide linkers serve many functions in nature, such as enhancing protein folding, adding stability and forming protein-protein interactions (George and Heringa, 2002; Reddy Chichili et al., 2013). Flexible linkers, such as GGS with various lengths, were found to be successful in optimizing FRET-based RNA biosensors conducted in our laboratory (Schiffener and Griesbeck, 2012). Linkers consisting of glycine (G) and serine (S) are flexible due to their small side chains and consequently can take multiple conformational forms in both unbound and bound states. In our attempt to improve the dynamic range of the Twitch indicators, we initially probed the use of flexible linkers, however these were found to have no or only limited effect on  $\Delta R/R$  (10-30%). Considering the initial proof-of-concept results, we decided to utilize proline (Pro) linkers in lieu of flexible linkers to test the effect. The advantage of the proline residue is its predictable end-to-end distance over a length of more than 100 residues (Schimmel and Flory, 1967). A poly-proline chain has a strict steric conformation with reduced rotational freedom, making it a suitable molecular ruler. It can be used to measure distances of energy transfer between molecules in the size of 12-46Å (Isied et al., 1992; Stryer and Haugland, 1967). Furthermore, proline linkers were also chosen due to their inability to participate in secondary structures and donate hydrogen bonds. Finally, proline residues have an ability to induce conformational turns, known as *cis*-Pro isomers, depending on the adjacent residues (George and Heringa, 2002). For our indicators, a rigid extension was perfectly suitable to modulate the FRET signal. In contrast, Horikawa and colleagues (2010) used a flexible Gly-Ser based linker between CaM and M13 in their YC-Nanos, to increase FRET and sensitivity. CaM-M13 is a two-component interaction, whereas Twitches are single component and thus having a different stereochemistry. We cloned and analyzed a small linker library of Twitch indicators with 1-6 poly-proline linkers at the 5' and 3' termini (Chapter 4, Figure 1b; Appendix Chapter 4, Figure 3b, c). Here we clearly demonstrated that the orientation of FPs had the biggest impact on indicator  $\Delta R/R$  and to a lesser extent the distance (Chapter 4, Figure 2e). Adding only a single proline residue at each terminal end of the minimal domain and a single point mutation (M65V) in the last helix region, we altered  $\Delta R/R$  from approximately 60% to 400% (Twitch-1). This was an interesting achievement, compared to TN-XXL with a  $\Delta R/R$  of approximately 250%. The affinity was additionally improved with a  $K_D$  of 250 nM for Twitch-1 versus the  $K_D$  of 800 nM for TN-XXL.

To increase our screening throughput, we established a new bacterial plate screening assay that was both cost effective and efficient (Litzlbauer et al., 2015; Chapter 4). With knowledge acquired during our proline linker screening, combined with the structural insights from the experiments performed in Chapter 2, we utilized our screening platform to screen a large

diversified linker library (Appendix Chapter 4, Figure 8C). The aim of the screening was to reduce the initial high  $R_0$  observed in Twitch-1 and additionally, to enhance the orientation of the fluorophores to maximize  $\Delta R/R$  even further.

For our library of random linkers, we used degenerate codons of 1-4 residues in length (Chapter 4, Figure 1b; Appendix Chapter 4, Figure 8C). This gave rise to a substantial number of diversified variants:  $16^{20}$ , with 16 possible linker combinations each with 20 different amino acid combinations (incl. stop codons). Initially, we did not consider stop codons to be a significant problem for our screening, however, we found that their inclusion led to false-positives. A stop codon before an acceptor will lead to a high donor signal, as no energy transfer occurs, and ultimately a false  $R_0$  signal. An obvious refinement of the assay would be the use degenerate codons (NNN) without stop-codons. NNN codons codes for all residues with a strong bias to certain amino acids, as well as increasing the likelihood of stop codons (Acevedo-Rocha and Reetz, 2014; Linhart and Shamir, 2005, 2007). Combining both screening in bacteria with fluorescent imaging in cultured neurons as a two-steps qualification procedure, could potentially have revealed certain biases in our screening methodology, at an early stage. In total, we screened approximately 100,000 indicator variants in this round and identified several successful linker combinations. Of the 100,000 variants, we thoroughly analyzed 1,142 in terms of  $\Delta R/R$  and  $R_0$  *in vitro*. The best variants were sequenced. This analysis revealed that the best peptide linkers were short (1-2 amino acids) and that linkers attached to the C-terminal tended to be longer than N-terminal linkers. In the sequence analysis, we found that aspartic acid (Asp) was frequent in the N-terminal linkers. This either indicated that this residue was beneficial in terms of dynamic range and starting ratio ( $\Delta R/R$ ,  $R_0$ ) or that using NNN degenerate primers would bias towards certain residues.

Besides screening a range of random linker combinations, we also conducted multiple screening rounds focusing on certain key areas of the Twitch  $Ca^{2+}$ -binding domain. We call these selected areas 'Hotspots'. The Hotspots are specific residues involved in the structural rearrangement of the binding domain or have a direct role in chelating  $Ca^{2+}$  ions (Figure 1.2). The hotspots were identified during early rounds of random mutagenesis, literature studies and from structural data on troponin C species. In total, we focused on 16 hotspots. Eight of these targeted residues; K14, G16, G18, F19, I20, R22, V41 and F58, and all contributed to improvements in the screened mutants. Residues 14-22 were chosen in order to alter kinetics and  $Ca^{2+}$  affinity, due to their position in the first chelating EF-hand 3. Our screening quickly revealed that substitutions in the binding loop altered the  $Ca^{2+}$ -binding properties, as expected, but could similarly result in dramatic improvements of  $\Delta R/R$ . This was unexpected;

however, we speculate that changes in the EF-hand might have caused side chain interactions or changes in the micro-milieu of binding pocket, which accordingly could promote tighter interlock of the whole structure. Detailed crystal structures would be needed to elucidate these effects. This highlights the importance and necessity of a thorough screening assay that evaluates several parameters simultaneously. Other hotspots residing around EF-hand 4, such as V41, F58 and the previous mentioned M65V, were selected based on the crystal structure of Ca<sup>2+</sup>-loaded troponin C and error-prone PCR. The crystal structure revealed different helix-helix interactions with these and neighboring residues. We rationalized that we could promote a tighter interlock between the helices in the Ca<sup>2+</sup>-bound state by altering the residues in the interface positions. Rationalizing that linkers have a significant effect on surrounding structures, structural data on the optimal linker variants would have been valuable, as these could have orchestrated more interesting interface mutations. Two of the most successful GECIs discovered in these screening rounds were named Twitch-2 and Twitch-3 (Appendix Chapter 4, Table S3), with mutations in positions K14 and V41, respectively.

The third round of screening focused on brighter GECIs, better overall dynamic range and Ca<sup>2+</sup> dissociation kinetics. Here, we exchanged the original donor (ECFP) with the brighter variants mCerulean3 and mTurquoise2 (Goedhart et al., 2010; Markwardt et al., 2011), as well as introducing the codon diversified cpVenus<sup>CD</sup> (Mues et al., 2013). As described in Chapter 4, the exchange of the FPs had a negative impact on the FRET signal. To overcome this, we designed a new round of screening, hypothesizing that extending the linkers could recover the lost dynamic range ( $R_0$  to  $R_{max}$ ). The best Twitch variants from the previous rounds of screening were used as parental templates and NNN-linkers were added to the already existing linkers, following the previous applied protocol. We added up to three additional residues at each N and C-terminal troponin C-FP interface. In the example of mCerulean3-Twitch-2, we screened approximately 30,000 variants and 500 promising candidates were analyzed *in vitro*. The best candidate was named Twitch-2B ( $K_D = 200$  nM, Hill slope = 1,31,  $\Delta R/R = 800\%$ ).

At this point, we had screened more than 250,000 GECIs and introduced a variety of different linkers and point mutations. If a parental gene contains multiple mutations, the interpretation of an isolated cause and effect from one such mutation is challenging. A method known as mutational cleaning is used for isolating advantageous mutations. Mutational cleaning implies the removal of neutral- and non- favorable mutations from the parental gene of each new round, to identify the key mutation(s) (Bloom et al., 2006). Separate small libraries could have been screened to test different residue combinations

among the advantageous mutations. Due to time constraints, we did not pursue this in detail. In addition to evaluating effects based on mutational cleaning, a thorough structural study of the mutations K14F and M65V in NMR, could have been valuable. Other intermediate strategies are the exploration of neighboring or nearby residues of active sites, as well as revisiting hotspots. A mutation at a key hotspot may lead to essential stereochemical changes in the backbone and side chain microenvironment, altering the key structural interactions. It is therefore not trivial to investigate changes in binding pockets, key residues and neighboring residues as they could either improve or impair the already advantageous mutations (Fasan et al., 2008).

### 5.3 Assessment of screening and selection methods

The linker design and screening came with certain biases, such as suboptimal NNN primer design, the slightly uneven distribution of  $\text{Ca}^{2+}$  loaded MOPS buffer and pre-assumed thresholds for  $R_0$  and  $\Delta R/R$ . Post introduction of the new donor FPs, mCerulean3 and mTurquoise2, we speculated whether it would have been appropriate to repeat the first linker screening due to the altered peptide environment. It would be appropriate to assume that we could have obtained similar FRET changes with a shorter linker. However, based on the array of functional indicators already developed, we opted for adding additional residues to recover the loss of dynamic range.

Having identified >150 new GECI variants from screening approximately 250,000 mutants, we needed to assess their performance in mammalian cells. For this, we used the validated setup applied during GCaMP screening (Akerboom et al., 2012). In terms of sensitivity and kinetics, screening in hippocampal neurons revealed a number of surprises. Several variants performed significantly better under cell culture conditions, compared to the anticipated performance based on available *in vitro* data. We screened variants of GECIs that, by our criteria and thresholds, performed well in bacteria and MOPS solutions. We anticipated that the *in vitro* performance we observed in the cuvette would translate into *in vivo*-like settings. Still, some variants we deemed non-functional or less favorable *in vitro*, could potentially have been performing well under the intended conditions in neurons. The hippocampal neuronal screen did, to some extent, point to this fact. We expect some potential mammalian-optimized GECIs were not selected due to our bacteria plate screening. Other factors contributing to poor performance could be suboptimal protein expression and purification process, leading to degraded proteins and smaller yields. Efforts on how our screening assay was further improved can be found in detail in Litzlbauer et al. (2015).

Factors that could lead to false-positives include the statistical weighting we assigned to  $\Delta R/R$  and  $R_0$  values; the  $R_0$  value is particularly critical. Our screening took both  $\Delta R/R$  and  $R_0$  into account, however the  $R_0$  values could produce misleading artifacts, as mentioned earlier. One should also not exclude human error. Manually picking colonies from plates with more than 700-800 colonies can lead to 'mispicks'.

Overall, the screening for improved FRET-based GECIs was to a large extent a success. Measured by output, we generated an entirely new family of indicators embodying a broad range of  $Ca^{2+}$  affinities, dynamic ranges (500-1000%) and  $R_0$  values below around and below 1. Yet, there is still significant room for improvements. The relatively imprecise bacterial screening allows a high throughput, but requires some supplementary screening steps to be conducted either *in vitro* or in mammalian cells. Furthermore, the screening currently only measures  $\Delta R/R$  and  $R_0$ , while completely neglecting kinetics and  $Ca^{2+}$  affinity properties. Rough estimates on kinetics performance could perhaps be achieved by using caged  $Ca^{2+}$  in bacteria or in cell lysate (Faas and Mody, 2012). A powerful flash of light could trigger the  $Ca^{2+}$  release from within the bacterial cells, giving rise to an acceptable  $Ca^{2+}$  on/off curve (Ellis-Davies, 2008; McCray et al., 1992). Ultimately, the screening should be conducted only in the mammalian cells, ensuring that any evolutionary driver would be from an intended environment and not an intermediate host cell (i.e. bacteria). This will most likely favor mutations different to those we find in *E. coli*. With similar screening methods as those we conducted in hippocampal neurons and those by Akerboom et al., (2012) and Chen et al., (2013), we could screen for variants optimal under fast, medium and slow field stimulations, exemplified by GCaMP-6s, m and f.

## 5.4 Recordings of neuronal activity using Twitch GECIs

Throughout the engineering process of the Twitch-family, we aimed to address concerns related to fluorescent imaging in neurons using GECIs. For imaging in neurons, challenges and limitations will be depending on the experimental setup, the cell types and the intended duration of the experiment. Essentially, GECIs should fulfill a set of general criteria to be applicable in modern imaging experiments: A) The GECI coding sequence should be able to fit into commonly applied transgenesis vector backbones and be readily expressed at satisfactory levels in targeted cells. B) The GECI should not interfere with cellular physiology, causing buffering of  $Ca^{2+}$  and unintended side effects. The use of suitable promoters and targeting sequences can minimize the chances of this happening. For the Twitch indicators,

we aimed to reduce the buffering effect by offering one or two active  $\text{Ca}^{2+}$ -binding sites, of a TnC species not expressed in mammalian neurons. C) By introducing the bright mCerulean-3 (Markwardt et al., 2011) in Twitch-2B, we addressed the importance of bright indicators. Twitch is significantly brighter than existing FRET-based GECIs and represents an improvement over GECIs such as YC3.60 (Nagai et al. 2004), YC-Nano variants (Horikawa et al., 2010) and the early single-wavelength GCaMPs (Akerboom et al., 2012; Tian et al., 2009). A bright indicator will, besides increasing the signal-to-noise ratio, allow for easier detection of expressing cells at steady state. This further eases the identification of structural details in tissues and reduces photobleaching. Photobleaching can be limited by using brighter fluorophores with better quantum yield, as the light exposure necessary to excite the fluorophore into fluorescing is reduced. D) A GECI should be sensitive and fast enough to report neuronal activity during firing of single APs or bursts hereof. While bursts are relatively easy to detect (Chen et al., 2013; Hendel et al., 2008; Horikawa et al., 2010), single APs on the other hand are notoriously difficult. Depending on the initial stimuli, single APs may trigger small or vast changes in intracellular  $\text{Ca}^{2+}$ . Where large changes are trans-cytosolic, small changes might be limited to a small fraction of the cytosol, which only activates a partial population of the expressed GECIs. Through our efforts invested in designing the Twitch GECIs, we eventually showed that we can resolve single APs with these indicators (Chapter 4, Figure 4f). E) Optimally, a GECI should additionally display a linear relationship between the fluorescent change and changes in free  $\text{Ca}^{2+}$ . A reduced number of  $\text{Ca}^{2+}$ -binding sites is thought to provide a more linear response, thus enabling quantification of changes in  $\text{Ca}^{2+}$  concentration (Rose et al., 2014). The binding dynamics of GECIs with four EF-hands are non-linear due to the close cooperativity of the binding sites. Synthetic dyes with a single binding site show this linearity. By reducing the EF-hands in the Twitch indicators, we managed to linearize the binding dynamics. Twitch-2B shows a clear linear relationship between APs from 1-15 APs and the fluorescence signal (Chapter 4, Figure 4f, g). This is more linear than the newest generation for GCaMPs (Chen et al., 2013). Whether it is the reduced stoichiometry of TnC itself that results in a linear response or instead the structural properties reflected in the interaction between two binding sites, we cannot yet exclude. Nonetheless, with a Hill coefficient of 1.31, Twitch-2B approximates synthetic dyes by being close to 1. OGB-1, with a single  $\text{Ca}^{2+}$ -binding site exhibits a Hill coefficient of 0.97 (Hendel et al., 2008). In contrast, GCaMP-6 variants range from 2.5-4.0. A Hill coefficient of  $>1$  indicates a positive cooperative binding, where the binding event in one position increases the ligand affinity for the second binding site (Rose et al., 2014; Stefan and Novère, 2013). This aligns with our findings in Chapter 2, and it reflects the

nature of the cooperative high affinity two  $\text{Ca}^{2+}$ -binding site domain engineered into Twitch-1 to Twitch-3. For Twitch-4, which is a pseudo single EF-hand GECI, we measured a Hill coefficient of 1.06. This indicates some positive cooperative binding between the binding sites, reflecting the effect of the inserted residue at position 18, which intends to mimic the bound state of the first EF-hand to promote binding in the second EF-hand. For future research on single EF-hand Twitch indicators, a thorough investigation on binding dynamics would be advised.

Aside from optimizing binding kinetics and fluorescent properties, it is our concern that the potential negative side effects related to expressing GECIs *in vivo* have been somewhat neglected. One should not disregard that sensitive GECIs ( $K_D < 250 \text{ nM}$ ) could, when expressed in high concentrations, alter local  $\text{Ca}^{2+}$  signaling transients and ultimately alter cellular behavior and physiology. This effect was clearly observed by Helmchen and colleagues in 1996, where dendritic  $\text{Ca}^{2+}$  dynamics were measured. Here the synthetic dye Fura-2 (Grynkiewicz et al., 1985) was loaded at different concentrations (20 $\mu\text{M}$ -250 $\mu\text{M}$ ), causing the AP amplitudes and decay times to drastically change in response to high dye concentrations (Helmchen et al., 1996). By using histamine to induce  $\text{Ca}^{2+}$  transients in YC3.1 expressing HeLa cells, at different concentrations (150 $\mu\text{M}$  and 500 $\mu\text{M}$ ), Miyawaki and colleagues observed a clear transient reduction in cells with high indicator expressing (Miyawaki et al., 1999). In support of this, similar effects have been observed in HEK293 cells expressing the TnC-based TN-L15 (Heim and Griesbeck, 2004). During field stimulation of cultured hippocampal neurons, we observed that bright cells (high expression level) did not respond as well, or not at all, compared to dim low-expressing cells. This was also observed in astrocytes expressing variants of Twitch indicators. In unpublished work, we observed the effects using the single EF-hand Twitch indicators, Twitch-4 and -5. What we found was a clear improvement in terms of brightness versus response. Owing to their low  $K_D$  of 2.80  $\mu\text{M}$  and 9.25  $\mu\text{M}$ , respectively, Twitch-4 and 5 could be very suitable for  $\text{Ca}^{2+}$  imaging in organelles like mitochondria, ER or the trans-Golgi network (TGN) (Crevenna et al., 2016; Samtleben et al., 2013).

However, even with a single binding site indicator, GECI or synthetic dye, high levels of expression have a negative impact on  $\text{Ca}^{2+}$  signaling. Throughout our work, we did not have the possibility to quantify all indicators in detail, however, we did put forward the basis for minimal domain GECIs with the potential to minimize systemic interference. It would be interesting to conduct an extensive study of all currently available GECIs focusing on their intrinsic buffering capacity, long-term toxicity and expression levels.

In a recent study addressing concerns related to long-term expression and GECI expression levels, a transgenic mouse was created using the ubiquitous CAG promoter to express the TN-XXL. The effects of expressing the indicator were thoroughly investigated by means of gene expression profiling, physiological conditions, anatomy and behavioral tests (Direnberger et al., 2012). Their findings suggested mild signatures of indicator expression, as the TN-XXL expressing mice showed compromised chronotropic competence and lower maximal heart rates compared to wild-type mice. Considering the comparative differences between TN-XXL and the new Twitch-family, we still do not know the long-term effects of an indicator like Twitch in a transgenic organism.

To ensure the Twitch indicators would perform satisfactorily *in vivo*, we conducted several *in vivo* studies using primarily Twitch-1, -2B and -3. We performed chronic imaging over more than 141 d.p.i. in olfactory bulb neurons responding to odorants (Chapter 4, Figure 4i), which shows responding cells and a stable signal-to-noise ratio at 141 d.p.i.. Long-term expression of GCaMP6s 158 d.p.i. has revealed breakdown of nuclear exclusion of the GECI and an increasing number of filled nuclei with abnormal responses upon stimulation (Rose et al., 2014).

Twitch-2B, which is challenged in terms of kinetics, was expressed in layer II/III excitatory neurons in wake head-restrained mice on a treadmill and recorded 28 days after transduction. Despite showing strong signals, Twitch-2B suffers from being slow compared to e.g. GCaMP6f. At AP bursts, cumulative fluorescence reaches GECI saturation and thus information about the underlying activity is lost. Experiments linking neuronal activity with episodic stimulation or behavioral events may suffer from so called response ‘bleed-through’: AP activity leading to a fluorescence change that is still ongoing during the onset of the next episode. Separation of neuronal events thus becomes challenging and hence, a faster indicator may be more suitable.

Despite advantages of FRET-based GECIs, they require a larger proportion of the wavelength bandwidth compared to their single-wavelength counterparts, and therefore reduce the possibility of using and visualizing additional fluorescent markers. On the upside, as FRET is measured as a change in ratio between two fluorophores, these indicators are less sensitive to movement artifacts. Where FRET-microscopy setup traditionally comes with an increased cost by needing extra optic filters, there is no need to conduct cumbersome motion blur and fluorescence intensity correction calculations. On the biological level, FRET-based GECIs is a larger molecule and thus, has a longer coding DNA sequences. This will in some cases, challenge the packaging into viral vectors, due to their larger size.

In the study conducted by Mues et al. (2013), real-time *in vivo* imaging of T cells (T lymphocytes) was made possible by using an optimized version of Twitch-1. T cells play a key role in targeting and eradicating infectious malignant cells and microorganisms in the body. As T cells recognize an antigen, they activate, proliferate and differentiate and travel to the sites of infection. Here they will exert their function on the infected cell, by initiating cell lysis or cytokine production (Hoekstra et al., 2015). To investigate  $\text{Ca}^{2+}$  transients in activated T cells, Twitch-1 was modified. Previously attempts to introduce TN-XXL (Mank et al., 2008) into T cells using retroviral transduction revealed that the combination of two homologous proteins, such as ECFP and cpCitrine in TN-XXL, failed to express due to a likely high rate of reverse transcriptase that resulted in the deletion of one of the FPs. By codon diversifying (CD) both cpCitrine and a variant hereof, cpVenus, as well as the  $\text{Ca}^{2+}$ -binding domain for mouse codon usage, we ultimately made a Twitch-1<sup>CD</sup> variant that expressed well and was more sensitive than the similarly codon diversified TN-XXL<sup>CD</sup>. These efforts allowed the recording of  $\text{Ca}^{2+}$  transients in T cells (Mues et al., 2013). The intermolecular template switching by reverse transcriptase may be the cause (Gustafsson et al., 2012; Simon-Loriere and Holmes, 2011). A recent study suggests methods of optimizing CFP and YFP based FRET biosensors that are delivered by use of lentivirus or retrovirus (Komatsubara et al., 2015). Komatsubara and colleagues found that codon diversification might not only solve expression problems, but they also suggest that a shorter spacer between the FP pair may be favorable.

In subsequent studies in Chapter 4, we demonstrate the improvements of Twitch-2B in T cell *in vivo* imaging. This led to improved resolution of T cell  $\text{Ca}^{2+}$  oscillation tracing, which had not previously been recorded *in vivo*. The  $\text{Ca}^{2+}$  oscillations occurring in T cells during immune response are yet to be deciphered. However, they may play a critical role as an early differentiator or predictor of downstream events of T cell activation (van Panhuys et al., 2014; Waite et al., 2013). Many preceding studies employed synthetic dyes to investigate T cell activation and behavior, however with the limitations proscribed to dyes (Christo et al., 2015), GECIs and especially FRET-based GECIs are now the tools of choice to elucidate the underlying biology of T cell  $\text{Ca}^{2+}$  oscillations. The reduced sensitivity to movement artifacts and its bright fluorophores, make the Twitch-2B well suited for imaging such motile cells as T cells. The next generation of Twitch-2B targeted to mobile T cells should excel in being more sensitive, while having a low  $R_0$  to compensate for FRET at low  $\text{Ca}^{2+}$  concentrations. A red-shifted variant would additionally allow for co-expression to sub-sets of T cell as wells as improved tracking in deeper tissue layers (Tang et al., 2013). What is specifically interesting about the results presented in our T cell studies, Chapter 3 and 4, is

that we have enabled the study of T cell  $\text{Ca}^{2+}$  signaling and behavior *in vivo*. And with an ever-growing activity in immuno-related fields, the Twitch GECIs could potentially play an important role in the onwards studies of immune system dynamics. For many disease indications, it is becoming clear that mixed types of T cells are involved and interconverted in the adaptations of the immune responses in different microenvironments (Dutoit et al., 2016). This also indicates that better understanding of surface markers, effector molecules, transcriptional regulators and functions of T cell subsets is required. In particular, fields such as immuno-oncology and multiple sclerosis (MS) could benefit from basic research on T cell signaling and plasticity (Bianchini et al., 2017; Scharping and Delgoffe, 2016).

## 5.5 Perspectives for minimal domain GECIs

For both single fluorophore and FRET-based GECIs, progress has been substantial within the last decade. Nevertheless, there is still room for improvement. We believe that our recent contribution to the field plays an important role in the forward evolution of GECIs. Despite reported concerns related to *in vivo* imaging (Helmchen et al., 1996), such as buffering of  $\text{Ca}^{2+}$  ions and pH dependent fluorescence, many studies fail to address these topics in detail (Yamada and Mikoshiba, 2012; Sun et al., 2013; Podor et al., 2015). Intracellular buffering of  $\text{Ca}^{2+}$  might not be of concern in simple *in vitro* experiments, even though the effect is measurable (Miyawaki et al., 1999). It is nevertheless much more concerning when expressing GECIs in transgenic mice, where long-term buffering could have physiological consequences (Direnberger et al., 2012; Rose et al., 2014). With the Twitch GECIs we show that it is possible to develop less invasive  $\text{Ca}^{2+}$  monitoring tools with properties that will allow for extensive chronic imaging.

In terms of pure performance ( $K_D$ , kinetics and  $\Delta F/F$ ), members of the GCaMP family such as GCaMP6s, m, f from Janelia Farm (Chen et al., 2013) and the name-sharing GCaMP6, 7 and 8 from Saitama University (Ohkura et al., 2012), are currently providing an extremely versatile GECI toolbox. Most efforts in optimizing these GECIs has predominantly focused on brightness and binding properties. As explained in the introduction, FPs with exposed fluorophores might be sensitive to pH changes and GCaMPs do show different  $pK_a$  values in  $\text{Ca}^{2+}$  free and  $\text{Ca}^{2+}$  bound states (Chen et al., 2013). This can lead to fluorescent quenching and loss of signal. Even FRET indicators might show small changes in signal output upon changes in acidity or alkalinity, depending on the FRET-pair (Chapter 2). One advantage that Twitch GECIs hold against GCaMPs is their brightness at steady state. GCaMPs rely on an increase in fluorescence intensity upon  $\text{Ca}^{2+}$ -binding. Some of these GECIs suffer from being very dim at low concentrations of  $\text{Ca}^{2+}$ .

Where it additionally becomes evident that our research and Twitch GECIs have contributed to the field, relates to the development of a new minimal domain single fluorophore GECI, named NTnC (Barykina et al., 2016). The fundamentals of NTnC comes from the minimal domain design of *O. tau* tsTnC fused to a modified mNeonGreen FP. NTnC is the first reported GECI of this class with a minimal domain, with reduced pH sensitivity and an inverted  $\Delta F/F$ . An inverted change in fluorescence intensity overcomes the downsides of GCaMPs' reduced brightness at resting state, as the signal goes from bright to dim. There is no doubt that this GECI and whichever variants that may follow, have a huge potential in providing an alternative to the current GCaMP family. The challenge remains to develop

superior red-shifted GECIs for deep tissue imaging. Still, contributions such as NTnC, RCaMPs and R-GECOs, will provide a solid foundation for the next generation of single fluorophore-based GECIs. Regrettably for FRET-based GECIs, the red-shifted variants are still challenging to develop. Several attempts have been conducted in our laboratory with a variety of different FRET-pairs, e.g. T-Sapphire – mKO<sub>K</sub> or with the photoswitchable FP Dreiklang. The best variant to date consisted of Dreiklang, mKO<sub>K</sub> and the minimal tsTnC domain. The FRET-pairs with red-shifted FPs suffer from poor FRET efficiency. Here crystal structures or NMR will be beneficial for further development.

In the most recent efforts to obtain structural knowledge to improve Twitch performance, Trigo-Mourino et al. (submitted 2016) and our laboratory succeeded in solving the complete crystal structure of Twitch-2B at a resolution of 2.5 Å in the calcium bound state. The insight gained from this study has already led to a new indicator called Twitch-6 ( $\Delta R/R = 1100\%$ ,  $K_D = 100$  nM) as well as interesting new insights on FRET-pair and tsTnC domain interactions. This new indicator shows considerably slower kinetics compared to other Twitch indicators. Slow indicators like this could be useful for quantifying slow regulation of resting calcium or dysregulation as a hallmark of disease (Breckwoldt et al., 2014; Gopal et al., 2015). Noteworthy is the fact that having a new structure of Twitch could allow for the development of the new red-shifted variant.

## 5.6 Conclusion

The research presented in this dissertation led to the development of a new family of FRET-based GECs – The Twitch-family. The Twitch GECs show improved properties compared to previous generations of FRET-based GECs and entail a novel engineered calcium binding protein, the minimal domain. We succeeded in engineering a domain that binds calcium using one or two EF-hands from the *O. tau* tsTnC C-lobe. This novel approach has already paved the way to a new class of single fluorophore GEC, the NTnC (Barykina et al., 2016). Furthermore, we have shown that the Twitch design provides a more linear response characteristic, a broad range of properties (Twitch-1 to Twitch-5) and allows for long-term expression in neurons, with limited negative side effects. Moreover, we introduced brighter and more photostable fluorescent proteins to increase the signal-to-noise ratio and dynamic range and hence, the over-all applicability of these GECs. Finally, we designed a high throughput bacterial screening assay to evaluate hundreds of thousands of mutant GECs (Thestrup et al., 2014; Litzlbauer et al., 2015). The applicability of the Twitch GECs was applied in several *in vivo* studies (Kovalchuk et al., 2015; Mues et al., 2013; Thestrup et al., 2014; Rose et al., 2014).

# References

- Abbe, E. (1873). Beiträge zur Theorie des Mikroskops und der mikroskopischen Wahrnehmung.
- Acevedo-Rocha, C.G., and Reetz, M.T. (2014). Assembly of designed oligonucleotides: a useful tool in synthetic biology for creating high-quality combinatorial DNA libraries. *Methods Mol. Biol.* *1179*, 189–206.
- Akerboom, J., Rivera, J.D.V., Guilbe, M.M.R., Malavé, E.C.A., Hernandez, H.H., Tian, L., Hires, S.A., Marvin, J.S., Looger, L.L., and Schreiter, E.R. (2009). Crystal structures of the GCaMP calcium sensor reveal the mechanism of fluorescence signal change and aid rational design. *J. Biol. Chem* *284*, 6455–6464.
- Akerboom, J., Chen, T.-W., Wardill, T.J., Tian, L., Marvin, J.S., Mutlu, S., Calderón, N.C., Esposti, F., Borghuis, B.G., Sun, X.R., et al. (2012). Optimization of a GCaMP Calcium Indicator for Neural Activity Imaging. *J. Neurosci.* *32*, 13819–13840.
- Akrap, N., Seidel, T., and Barisas, B.G. (2010). Förster distances for fluorescence resonant energy transfer between mCherry and other visible fluorescent proteins. *Anal. Biochem.* *402*, 105–106.
- Arnold, F.H. (1998). Design by Directed Evolution. *ACCOUNTS OF CHEMICAL RESEARCH* *31*, 125–131.
- Arnold, F.H., and Volkov, A.A. (1999). Directed evolution of biocatalysts. *Current Opinion in Chemical Biology* *3*, 54–59.
- Baird, G.S., Zacharias, D.A., and Tsien, R.Y. (1999). Circular permutation and receptor insertion within green fluorescent proteins. *Proc Natl Acad Sci U S A* *96*, 11241–11246.
- Barykina, N.V., Subach, O.M., Doronin, D.A., Sotskov, V.P., Roshchina, M.A., Kunitsyna, T.A., Malyshev, A.Y., Smirnov, I.V., Azieva, A.M., Sokolov, I.S., et al. (2016). A new design for a green calcium indicator with a smaller size and a reduced number of calcium-binding sites. *Scientific Reports* *6*, 34447.
- Berchtold, M.W., Brinkmeier, H., and Müntener, M. (2000). Calcium ion in skeletal muscle: its crucial role for muscle function, plasticity, and disease. *Physiol Rev* *80*, 1215–1265.
- Berridge, M.J., Lipp, P., and Bootman, M.D. (2000). The versatility and universality of calcium signalling. *Nat Rev Mol Cell Biol* *1*, 11–21.
- Berridge, M.J., Bootman, M.D., and Roderick, H.L. (2003). Calcium signalling: dynamics, homeostasis and remodelling. *Nat Rev Mol Cell Biol* *4*, 517–529.
- Betzig, E., Patterson, G.H., Sougrat, R., Lindwasser, O.W., Olenych, S., Bonifacino, J.S., Davidson, M.W., Lippincott-Schwartz, J., and Hess, H.F. (2006). Imaging Intracellular Fluorescent Proteins at Nanometer Resolution. *Science* *313*, 1642–1645.
- Bianchini, E., De Biasi, S., Simone, A.M., Ferraro, D., Sola, P., Cossarizza, A., and Pinti, M. (2017). Invariant natural killer T cells and mucosal-associated invariant T cells in multiple sclerosis. *Immunol. Lett.* *183*, 1–7.
- Bloom, J.D., Labthavikul, S.T., Otey, C.R., and Arnold, F.H. (2006). Protein stability promotes evolvability. *Proc Natl Acad Sci U S A* *103*, 5869–5874.
- Bommarius, A.S., Blum, J.K., and Abrahamson, M.J. (2011). Status of protein engineering for biocatalysts: how to design an industrially useful biocatalyst. *Curr Opin Chem Biol* *15*, 194–200.
- Breckwoldt, M.O., Pfister, F.M.J., Bradley, P.M., Marinković, P., Williams, P.R., Brill, M.S., Plomer, B., Schmalz, A., St Clair, D.K., Naumann, R., et al. (2014). Multiparametric optical analysis of mitochondrial redox signals during neuronal physiology and pathology in vivo. *Nat. Med.* *20*, 555–560.

- Broussard, J.A., Rappaz, B., Webb, D.J., and Brown, C.M. (2013). Fluorescence resonance energy transfer microscopy as demonstrated by measuring the activation of the serine/threonine kinase Akt. *Nat. Protocols* **8**, 265–281.
- Campbell, R.E., Tour, O., Palmer, A.E., Steinbach, P.A., Baird, G.S., Zacharias, D.A., and Tsien, R.Y. (2002). A monomeric red fluorescent protein. *Proc. Natl. Acad. Sci. U.S.A.* **99**, 7877–7882.
- Chen, T.-W., Wardill, T.J., Sun, Y., Pulver, S.R., Renninger, S.L., Baohan, A., Schreiter, E.R., Kerr, R.A., Orger, M.B., Jayaraman, V., et al. (2013). Ultra-sensitive fluorescent proteins for imaging neuronal activity. *Nature* **499**, 295–300.
- Christo, S.N., Diener, K.R., and Hayball, J.D. (2015). The functional contribution of calcium ion flux heterogeneity in T cells. *Immunol. Cell Biol.*
- Coco, W.M., Levinson, W.E., Crist, M.J., Hektor, H.J., Darzins, A., Pienkos, P.T., Squires, C.H., and Monticello, D.J. (2001). DNA shuffling method for generating highly recombined genes and evolved enzymes. *Nat Biotech* **19**, 354–359.
- Cormack, B.P., Valdivia, R.H., and Falkow, S. (1996). FACS-optimized mutants of the green fluorescent protein (GFP). *Gene* **173**, 33–38.
- Cramer, A., Whitehorn, E.A., Tate, E., and Stemmer, W.P.C. (1996). Improved green fluorescent protein by molecular evolution using DNA shuffling. *Nature Biotechnology* **14**, 315–319.
- Crevenna, A.H., Blank, B., Maiser, A., Emin, D., Prescher, J., Beck, G., Kienzle, C., Bartnik, K., Habermann, B., Pakdel, M., et al. (2016). Secretory cargo sorting by Ca<sup>2+</sup>-dependent Cab45 oligomerization at the trans-Golgi network. *J Cell Biol* **213**, 305–314.
- Dana, H., Chen, T.-W., Hu, A., Shields, B.C., Guo, C., Looger, L.L., Kim, D.S., and Svoboda, K. (2014). Thy1-GCaMP6 Transgenic Mice for Neuronal Population Imaging In Vivo. *PLoS One* **9**.
- Denk, W., Strickler, J.H., and Webb, W.W. (1990). Two-photon laser scanning fluorescence microscopy. *Science* **248**, 73–76.
- Direnberger, S., Mues, M., Micale, V., Wotjak, C.T., Dietzel, S., Schubert, M., Scharr, A., Hassan, S., Wahl-Schott, C., Biel, M., et al. (2012). Biocompatibility of a genetically encoded calcium indicator in a transgenic mouse model. *Nature Communications* **3**, 1031.
- Dutoit, V., Migliorini, D., Dietrich, P.-Y., and Walker, P.R. (2016). Immunotherapy of Malignant Tumors in the Brain: How Different from Other Sites? *Front Oncol* **6**, 256.
- Ebashi, S., and Kodama, A. (1965). A new protein factor promoting aggregation of tropomyosin. *J. Biochem.* **58**, 107–108.
- Ellis-Davies, G.C.R. (2008). Neurobiology with caged calcium. *Chem. Rev* **108**, 1603–1613.
- Faas, G.C., and Mody, I. (2012). Measuring the kinetics of calcium binding proteins with flash photolysis. *Biochim. Biophys. Acta* **1820**, 1195–1204.
- Farah, C.S., and Reinach, F.C. (1995). The troponin complex and regulation of muscle contraction. *FASEB J* **9**, 755–767.
- Farinas, E.T., Bulter, T., and Arnold, F.H. (2001). Directed enzyme evolution. *Curr. Opin. Biotechnol.* **12**, 545–551.
- Fasan, R., Meharena, Y.T., Snow, C.D., Poulos, T.L., and Arnold, F.H. (2008). Evolutionary history of a specialized P450 propane monooxygenase. *J Mol Biol* **383**, 1069–1080.
- Filatov, V.L., Katrukha, A.G., Bulargina, T.V., and Gusev, N.B. (1999). Troponin: structure, properties, and mechanism of functioning. *Biochemistry Mosc.* **64**, 969–985.

- Förster, T. (1948). Zwischenmolekulare Energiewanderung und Fluoreszenz" [Intermolecular energy migration and fluorescence. *Annalen der Physik* 55–75.
- Frazier, H.N., Maimaiti, S., Anderson, K.L., Brewer, L.D., Gant, J.C., Porter, N.M., and Thibault, O. (2017). Calcium's role as nuanced modulator of cellular physiology in the brain. *Biochem. Biophys. Res. Commun.* 483, 981–987.
- Fucile, S. (2004). Ca<sup>2+</sup> permeability of nicotinic acetylcholine receptors. *Cell Calcium* 35, 1–8.
- Geiger, A., Russo, L., Gensch, T., Thestrup, T., Becker, S., Hopfner, K.-P., Griesinger, C., Witte, G., and Griesbeck, O. (2012). Correlating Calcium Binding, Förster Resonance Energy Transfer, and Conformational Change in the Biosensor TN-XXL. *Biophysical Journal* 102, 2401–2410.
- George, R.A., and Heringa, J. (2002). An analysis of protein domain linkers: their classification and role in protein folding. *Protein Eng.* 15, 871–879.
- Gifford, J.L., Walsh, M.P., and Vogel, H.J. (2007). Structures and metal-ion-binding properties of the Ca<sup>2+</sup>-binding helix-loop-helix EF-hand motifs. *Biochem. J* 405, 199–221.
- Goedhart, J., van Weeren, L., Hink, M.A., Vischer, N.O.E., Jalink, K., and Gadella, T.W.J. (2010). Bright cyan fluorescent protein variants identified by fluorescence lifetime screening. *Nat Meth* 7, 137–139.
- Goldsmith, M., and Tawfik, D.S. (2013). Enzyme engineering by targeted libraries. *Meth. Enzymol.* 523, 257–283.
- Gopal, S., Søgaard, P., Multhaupt, H.A.B., Pataki, C., Okina, E., Xian, X., Pedersen, M.E., Stevens, T., Griesbeck, O., Park, P.W., et al. (2015). Transmembrane proteoglycans control stretch-activated channels to set cytosolic calcium levels. *J Cell Biol* 210, 1199–1211.
- Gordon, A.M., Homsher, E., and Regnier, M. (2000). Regulation of contraction in striated muscle. *Physiol Rev* 80, 853–924.
- Grabarek, Z. (2006). Structural Basis for Diversity of the EF-hand Calcium-binding Proteins. *Journal of Molecular Biology* 359, 509–525.
- Grienberger, C., and Konnerth, A. (2012). Imaging Calcium in Neurons. *Neuron* 73, 862–885.
- Griesbeck, O., Baird, G.S., Campbell, R.E., Zacharias, D.A., and Tsien, R.Y. (2001). Reducing the environmental sensitivity of yellow fluorescent protein. Mechanism and applications. *J. Biol. Chem* 276, 29188–29194.
- Gryniewicz, G., Poenie, M., and Tsien, R.Y. (1985). A new generation of Ca<sup>2+</sup> indicators with greatly improved fluorescence properties. *J. Biol. Chem.* 260, 3440–3450.
- Gustafsson, C., Minshull, J., Govindarajan, S., Ness, J., Villalobos, A., and Welch, M. (2012). Engineering Genes for Predictable Protein Expression. *Protein Expr Purif* 83, 37–46.
- Habuchi, S., Cotlet, M., Hofkens, J., Dirix, G., Michiels, J., Vanderleyden, J., Subramaniam, V., and De Schryver, F.C. (2002). Resonance energy transfer in a calcium concentration-dependent cameleon protein. *Biophys. J.* 83, 3499–3506.
- Heim, N., and Griesbeck, O. (2004). Genetically Encoded Indicators of Cellular Calcium Dynamics Based on Troponin C and Green Fluorescent Protein. *THE JOURNAL OF BIOLOGICAL CHEMISTRY* 279, 14280–14286.
- Heim, N., Garaschuk, O., Friedrich, M.W., Mank, M., Milos, R.I., Kovalchuk, Y., Konnerth, A., and Griesbeck, O. (2007). Improved calcium imaging in transgenic mice expressing a troponin C-based biosensor. *Nat Meth* 4, 127–129.
- Heim, R., Prasher, D.C., and Tsien, R.Y. (1994). Wavelength mutations and posttranslational autoxidation of green fluorescent protein. *Proc Natl Acad Sci U S A.* 91, 12501–12504.

- Helmchen, F., Imoto, K., and Sakmann, B. (1996). Ca<sup>2+</sup> buffering and action potential-evoked Ca<sup>2+</sup> signaling in dendrites of pyramidal neurons. *Biophys J* 70, 1069–1081.
- Helmchen, F., Borst, J.G., and Sakmann, B. (1997). Calcium dynamics associated with a single action potential in a CNS presynaptic terminal. *Biophys J* 72, 1458–1471.
- Hendel, T., Mank, M., Schnell, B., Griesbeck, O., Borst, A., and Reiff, D.F. (2008). Fluorescence Changes of Genetic Calcium Indicators and OGB-1 Correlated with Neural Activity and Calcium In Vivo and In Vitro. *J. Neurosci.* 28, 7399–7411.
- Higley, M.J., and Sabatini, B.L. (2008). Calcium signaling in dendrites and spines: practical and functional considerations. *Neuron* 59, 902–913.
- Hoekstra, M.E., Dijkgraaf, F.E., Schumacher, T.N., and Rohr, J.C. (2015). Assessing T lymphocyte function and differentiation by genetically encoded reporter systems. *Trends in Immunology* 36, 392–400.
- Horikawa, K., Yamada, Y., Matsuda, T., Kobayashi, K., Hashimoto, M., Matsu-ura, T., Miyawaki, A., Michikawa, T., Mikoshiba, K., and Nagai, T. (2010). Spontaneous network activity visualized by ultrasensitive Ca<sup>2+</sup> indicators, yellow Cameleon-Nano. *Nat Meth* 7, 729–732.
- Isied, S.S., Ogawa, M.Y., and Wishart, J.F. (1992). Peptide-mediated intramolecular electron transfer: long-range distance dependence. *Chem. Rev.* 92, 381–394.
- Jäckel, C., Kast, P., and Hilvert, D. (2008). Protein design by directed evolution. *Annu Rev Biophys* 37, 153–173.
- Johnson, J.D., Nakkula, R.J., Vasulka, C., and Smillie, L.B. (1994). Modulation of Ca<sup>2+</sup> exchange with the Ca(2+)-specific regulatory sites of troponin C. *J Biol Chem* 269, 8919–8923.
- Jung, G., Wiehler, J., and Zumbusch, A. (2005). The photophysics of green fluorescent protein: influence of the key amino acids at positions 65, 203, and 222. *Biophys. J.* 88, 1932–1947.
- Jurado, L.A., Chockalingam, P.S., and Jarrett, H.W. (1999). Apocalmodulin. *Physiol. Rev.* 79, 661–682.
- Karasawa, S., Araki, T., Nagai, T., Mizuno, H., and Miyawaki, A. (2004). Cyan-emitting and orange-emitting fluorescent proteins as a donor/acceptor pair for fluorescence resonance energy transfer. *Biochem J.* 381, 307–312.
- Kaufman, R.J., and Malhotra, J.D. (2014). Calcium trafficking integrates endoplasmic reticulum function with mitochondrial bioenergetics. *Biochim Biophys Acta* 1843, 2233–2239.
- Khersonsky, O., Kiss, G., Röthlisberger, D., Dym, O., Albeck, S., Houk, K.N., Baker, D., and Tawfik, D.S. (2012). Bridging the gaps in design methodologies by evolutionary optimization of the stability and proficiency of designed Kemp eliminase KE59. *Proc Natl Acad Sci U S A* 109, 10358–10363.
- Koester, H.J., and Sakmann, B. (2000). Calcium dynamics associated with action potentials in single nerve terminals of pyramidal cells in layer 2/3 of the young rat neocortex. *J Physiol* 529, 625–646.
- Komatsubara, A.T., Matsuda, M., and Aoki, K. (2015). Quantitative analysis of recombination between YFP and CFP genes of FRET biosensors introduced by lentiviral or retroviral gene transfer. *Sci Rep* 5, 13283.
- Krebs, J., and Heizmann, C.W. (2007). Calcium-binding proteins and the EF-hand principle. In *New Comprehensive Biochemistry*, Joachim Krebs and Marek Michalak, ed. (Elsevier), pp. 51–93.
- Kretsinger, R.H., and Nockolds, C.E. (1973). Carp Muscle Calcium-binding Protein. II. STRUCTURE DETERMINATION AND GENERAL DESCRIPTION. *J. Biol. Chem.* 248, 3313–3326.
- Kuzmenkina, E.V., Heyes, C.D., and Nienhaus, G.U. (2005). Single-molecule Förster resonance energy transfer study of protein dynamics under denaturing conditions. *Proc Natl Acad Sci U S A* 102, 15471–15476.
- Lakowicz, J.R. (2007). *Principles of Fluorescence Spectroscopy* (Springer Science & Business Media).

- Latt, S.A., Cheung, H.T., and Blout, E.R. (1965). Energy Transfer. A System with Relatively Fixed Donor-Acceptor Separation. *J. Am. Chem. Soc.* *87*, 995–1003.
- Leemhuis, H., Kelly, R.M., and Dijkhuizen, L. (2009). Directed evolution of enzymes: Library screening strategies. *IUBMB Life* *61*, 222–228.
- Lewit-Bentley, A., and Réty, S. (2000). EF-hand calcium-binding proteins. *Curr Opin Struct Biol* *10*, 637–643.
- Lichtman, J.W., and Conchello, J.-A. (2005). Fluorescence microscopy. *Nat Meth* *2*, 910–919.
- Limbäck-Stokin, K., Korzus, E., Nagaoka-Yasuda, R., and Mayford, M. (2004). Nuclear calcium/calmodulin regulates memory consolidation. *J. Neurosci.* *24*, 10858–10867.
- Lindenburg, L., and Merx, M. (2014). Engineering genetically encoded FRET sensors. *Sensors (Basel)* *14*, 11691–11713.
- Linhart, C., and Shamir, R. (2005). The degenerate primer design problem: theory and applications. *J. Comput. Biol.* *12*, 431–456.
- Linhart, C., and Shamir, R. (2007). Degenerate primer design: theoretical analysis and the HYDEN program. *Methods Mol. Biol.* *402*, 221–244.
- Litzlbauer, J., Schifferer, M., Ng, D., Fabritius, A., Thestrup, T., and Griesbeck, O. (2015). Large Scale Bacterial Colony Screening of Diversified FRET Biosensors. *PLoS ONE* *10*, e0119860.
- Lytton, J., Westlin, M., Burk, S.E., Shull, G.E., and MacLennan, D.H. (1992). Functional comparisons between isoforms of the sarcoplasmic or endoplasmic reticulum family of calcium pumps. *J. Biol. Chem.* *267*, 14483–14489.
- Mäler, L., Sastry, M., and Chazin, W.J. (2002). A structural basis for S100 protein specificity derived from comparative analysis of apo and Ca<sup>2+</sup>-calcyclin. *Journal of Molecular Biology* *317*, 279–290.
- Mank, M., and Griesbeck, O. (2008). Genetically Encoded Calcium Indicators. *Chemical Reviews* *108*, 1550–1564.
- Mank, M., Reiff, D.F., Heim, N., Friedrich, M.W., Borst, A., and Griesbeck, O. (2006). A FRET-Based Calcium Biosensor with Fast Signal Kinetics and High Fluorescence Change. *Biophysical Journal* *90*, 1790–1796.
- Mank, M., Santos, A.F., Drenberger, S., Mrcic-Flogel, T.D., Hofer, S.B., Stein, V., Hendel, T., Reiff, D.F., Levelt, C., Borst, A., et al. (2008). A genetically encoded calcium indicator for chronic in vivo two-photon imaging. *Nat Meth advanced online publication*.
- Marienhagen, J., Dennig, A., and Schwaneberg, U. (2012). Phosphorothioate-based DNA recombination: an enzyme-free method for the combinatorial assembly of multiple DNA fragments. *BioTechniques* *52*.
- Markwardt, M.L., Kremers, G.-J., Kraft, C.A., Ray, K., Cranfill, P.J.C., Wilson, K.A., Day, R.N., Wachter, R.M., Davidson, M.W., and Rizzo, M.A. (2011). An Improved Cerulean Fluorescent Protein with Enhanced Brightness and Reduced Reversible Photoswitching. *PLoS ONE* *6*, e17896.
- Martínez, R., and Schwaneberg, U. (2013). A roadmap to directed enzyme evolution and screening systems for biotechnological applications. *Biol. Res.* *46*, 395–405.
- Matz, M.V., Fradkov, A.F., Labas, Y.A., Savitsky, A.P., Zaraisky, A.G., Markelov, M.L., and Lukyanov, S.A. (1999). Fluorescent proteins from nonbioluminescent Anthozoa species. *Nat. Biotechnol.* *17*, 969–973.
- McCray, J.A., Fidler-Lim, N., Ellis-Davies, G.C., and Kaplan, J.H. (1992). Rate of release of Ca<sup>2+</sup> following laser photolysis of the DM-nitrophen-Ca<sup>2+</sup> complex. *Biochemistry* *31*, 8856–8861.
- Meer, B.W.V.D., III, G.C., and Chen, S.-Y.S. (1994). *Resonance Energy Transfer: Theory and Data* (Wiley).

- Mercier, P., Li, M.X., and Sykes, B.D. (2000). Role of the Structural Domain of Troponin C in Muscle Regulation: NMR Studies of Ca<sup>2+</sup> Binding and Subsequent Interactions with Regions 1-40 and 96-115 of Troponin I. *Biochemistry* *39*, 2902–2911.
- Miyawaki, A., Llopis, J., Heim, R., McCaffery, J.M., Adams, J.A., Ikura, M., and Tsien, R.Y. (1997). Fluorescent indicators for Ca<sup>2+</sup> based on green fluorescent proteins and calmodulin. *Nature* *388*, 882–887.
- Miyawaki, A., Griesbeck, O., Heim, R., and Tsien, R.Y. (1999). Dynamic and quantitative Ca<sup>2+</sup> measurements using improved cameleons. *Proceedings of the National Academy of Sciences of the United States of America* *96*, 2135–2140.
- Mues, M., Bartholomäus, I., Thestrup, T., Griesbeck, O., Wekerle, H., Kawakami, N., and Krishnamoorthy, G. (2013). Real-time in vivo analysis of T cell activation in the central nervous system using a genetically encoded calcium indicator. *Nat Med advance online publication*.
- Muto, A., Ohkura, M., Kotani, T., Higashijima, S., Nakai, J., and Kawakami, K. (2011). Genetic visualization with an improved GCaMP calcium indicator reveals spatiotemporal activation of the spinal motor neurons in zebrafish. *PNAS* *108*, 5425–5430.
- Nagai, T., Sawano, A., Park, E.S., and Miyawaki, A. (2001). Circularly permuted green fluorescent proteins engineered to sense Ca<sup>2+</sup>. *PNAS* *98*, 3197–3202.
- Nagai, T., Ibata, K., Park, E.S., Kubota, M., Mikoshiba, K., and Miyawaki, A. (2002). A variant of yellow fluorescent protein with fast and efficient maturation for cell-biological applications. *Nat. Biotechnol.* *20*, 87–90.
- Nagai, T., Yamada, S., Tominaga, T., Ichikawa, M., and Miyawaki, A. (2004a). Expanded dynamic range of fluorescent indicators for Ca<sup>2+</sup> by circularly permuted yellow fluorescent proteins. *Proc Natl Acad Sci U S A* *101*, 10554–10559.
- Nagai, T., Yamada, S., Tominaga, T., Ichikawa, M., and Miyawaki, A. (2004b). Expanded dynamic range of fluorescent indicators for Ca<sup>2+</sup> by circularly permuted yellow fluorescent proteins. *Proceedings of the National Academy of Sciences of the United States of America* *101*, 10554–10559.
- Nakai, J., Ohkura, M., and Imoto, K. (2001). A high signal-to-noise Ca<sup>2+</sup> probe composed of a single green fluorescent protein. *Nat Biotech* *19*, 137–141.
- Neice, A. (2010). Chapter 3 - Methods and Limitations of Subwavelength Imaging. In *Advances in Imaging and Electron Physics*, P.W. Hawkes, ed. (Elsevier), pp. 117–140.
- Nelson, M.R., Thulin, E., Fagan, P.A., Forsén, S., and Chazin, W.J. (2002). The EF-hand domain: A globally cooperative structural unit. *Protein Sci* *11*, 198–205.
- Ohkura, M., Matsuzaki, M., Kasai, H., Imoto, K., and Nakai, J. (2005). Genetically Encoded Bright Ca<sup>2+</sup> Probe Applicable for Dynamic Ca<sup>2+</sup> Imaging of Dendritic Spines. *Anal. Chem.* *77*, 5861–5869.
- Ohkura, M., Sasaki, T., Sadakari, J., Gengyo-Ando, K., Kagawa-Nagamura, Y., Kobayashi, C., Ikegaya, Y., and Nakai, J. (2012). Genetically Encoded Green Fluorescent Ca<sup>2+</sup> Indicators with Improved Detectability for Neuronal Ca<sup>2+</sup> Signals. *PLOS ONE* *7*, e51286.
- Ohtsuki, I. (2007). Troponin: structure, function and dysfunction. *Adv. Exp. Med. Biol.* *592*, 21–36.
- O'Maille, P.E., Malone, A., Dellas, N., Andes Hess, B., Smentek, L., Sheehan, I., Greenhagen, B.T., Chappell, J., Manning, G., and Noel, J.P. (2008). Quantitative exploration of the catalytic landscape separating divergent plant sesquiterpene synthases. *Nat Chem Biol* *4*, 617–623.
- Ormö, M., Cubitt, A.B., Kallio, K., Gross, L.A., Tsien, R.Y., and Remington, S.J. (1996). Crystal structure of the *Aequorea victoria* green fluorescent protein. *Science* *273*, 1392–1395.
- Orrenius, S., Zhivotovsky, B., and Nicotera, P. (2003). Regulation of cell death: the calcium–apoptosis link. *Nat Rev Mol Cell Biol* *4*, 552–565.

- Palmer, A.E., Jin, C., Reed, J.C., and Tsien, R.Y. (2004). Bcl-2-mediated alterations in endoplasmic reticulum Ca<sup>2+</sup> analyzed with an improved genetically encoded fluorescent sensor. *Proceedings of the National Academy of Sciences of the United States of America* *101*, 17404–17409.
- Palmer, A.E., Giacomello, M., Kortemme, T., Hires, S.A., Lev-Ram, V., Baker, D., and Tsien, R.Y. (2006). Ca<sup>2+</sup> Indicators Based on Computationally Redesigned Calmodulin-Peptide Pairs. *Chemistry & Biology* *13*, 521–530.
- van Panhuys, N., Klauschen, F., and Germain, R.N. (2014). T-cell-receptor-dependent signal intensity dominantly controls CD4(+) T cell polarization In Vivo. *Immunity* *41*, 63–74.
- Patterson, G.H., Piston, D.W., and Barisas, B.G. (2000). Förster distances between green fluorescent protein pairs. *Anal. Biochem.* *284*, 438–440.
- Pédélecq, J.-D., Cabantous, S., Tran, T., Terwilliger, T.C., and Waldo, G.S. (2005). Engineering and characterization of a superfolder green fluorescent protein. *Nature Biotechnology* *24*, 79–88.
- Piston, D.W., and Kremers, G.-J. (2007). Fluorescent protein FRET: the good, the bad and the ugly. *TRENDS in Biochemical Sciences* *32*, 407–414.
- Podor, B., Hu, Y., Ohkura, M., Nakai, J., Croll, R., and Fine, A. (2015). Comparison of genetically encoded calcium indicators for monitoring action potentials in mammalian brain by two-photon excitation fluorescence microscopy. *Neurophotonics* *2*.
- Popp, A.K., Valentine, M.T., Kaplan, P.D., and Weitz, D.A. (2003). Microscopic origin of light scattering in tissue. *Appl Opt* *42*, 2871–2880.
- Potter, J.D., and Gergely, J. (1975). The regulatory system of the actin-myosin interaction. *Recent Adv Stud Cardiac Struct Metab* *5*, 235–244.
- Ramsey, I.S., Delling, M., and Clapham, D.E. (2006). An introduction to TRP channels. *Annu. Rev. Physiol.* *68*, 619–647.
- Reddy Chichili, V.P., Kumar, V., and Sivaraman, J. (2013). Linkers in the structural biology of protein–protein interactions. *Protein Sci* *22*, 153–167.
- Reid, B.G., and Flynn, G.C. (1997). Chromophore formation in green fluorescent protein. *Biochemistry* *36*, 6786–6791.
- Rodriguez, E.A., Tran, G.N., Gross, L.A., Crisp, J.L., Shu, X., Lin, J.Y., and Tsien, R.Y. (2016). A far-red fluorescent protein evolved from a cyanobacterial phycobiliprotein. *Nat Meth advance online publication*.
- Romero, P.A., and Arnold, F.H. (2009). Exploring protein fitness landscapes by directed evolution. *Nat Rev Mol Cell Biol* *10*, 866–876.
- Romoser, V.A., Hinkle, P.M., and Persechini, A. (1997). Detection in Living Cells of Ca<sup>2+</sup>-Dependent Changes in the Fluorescence Emission of an Indicator Composed of Two Green Fluorescent Protein Variants Linked by a Calmodulin-Binding Sequence A NEW CLASS OF FLUORESCENT INDICATORS. *J. Biol. Chem.* *272*, 13270–13274.
- Rose, T., Goltstein, P.M., Portugues, R., and Griesbeck, O. (2014). Putting a finishing touch on GECIs. *Front Mol Neurosci* *7*, 88.
- Ruff, A.J., Dennig, A., and Schwaneberg, U. (2013). To get what we aim for--progress in diversity generation methods. *FEBS J.* *280*, 2961–2978.
- Russell, J.T. (2011). Imaging calcium signals in vivo: a powerful tool in physiology and pharmacology. *Br. J. Pharmacol.* *163*, 1605–1625.
- Rust, M.J., Bates, M., and Zhuang, X. (2006). Sub-diffraction-limit imaging by stochastic optical reconstruction microscopy (STORM). *Nat Meth* *3*, 793–796.

- Sakaue-Sawano, A., Kurokawa, H., Morimura, T., Hanyu, A., Hama, H., Osawa, H., Kashiwagi, S., Fukami, K., Miyata, T., Miyoshi, H., et al. (2008). Visualizing Spatiotemporal Dynamics of Multicellular Cell-Cycle Progression. *Cell* *132*, 487–498.
- Samtleben, S., Jaepel, J., Fecher, C., Andreska, T., Rehberg, M., and Blum, R. (2013). Direct Imaging of ER Calcium with Targeted-Esterase Induced Dye Loading (TED). *JoVE (Journal of Visualized Experiments)* e50317–e50317.
- Scharping, N.E., and Delgoffe, G.M. (2016). Tumor Microenvironment Metabolism: A New Checkpoint for Anti-Tumor Immunity. *Vaccines (Basel)* *4*.
- Schiffeler, M., and Griesbeck, O. (2012). A dynamic FRET reporter of gene expression improved by functional screening. *J. Am. Chem. Soc.* *134*, 15185–15188.
- Schimmel, P.R., and Flory, P.J. (1967). Conformational energy and configurational statistics of poly-L-proline. *Proc Natl Acad Sci U S A* *58*, 52–59.
- Schnitzler, C.E., Keenan, R.J., McCord, R., Matysik, A., Christianson, L.M., and Haddock, S.H.D. (2008). Spectral diversity of fluorescent proteins from the anthozoan *Corynactis californica*. *Mar. Biotechnol.* *10*, 328–342.
- Schultz, C., Zhang, J., and Mehta, S. (2015). *Optical probes in biology* (CRC Press).
- Shaner, N.C., Campbell, R.E., Steinbach, P.A., Giepmans, B.N.G., Palmer, A.E., and Tsien, R.Y. (2004). Improved monomeric red, orange and yellow fluorescent proteins derived from *Discosoma* sp. red fluorescent protein. *Nat Biotechnol* *22*, 1567–1572.
- Shaner, N.C., Lin, M.Z., McKeown, M.R., Steinbach, P.A., Hazelwood, K.L., Davidson, M.W., and Tsien, R.Y. (2008). Improving the photostability of bright monomeric orange and red fluorescent proteins. *Nat Meth* *5*, 545–551.
- Shcherbakova, D.M., and Verkhusha, V.V. (2013). Near-infrared fluorescent proteins for multicolor in vivo imaging. *Nat Meth* *10*, 751–754.
- Shcherbo, D., Merzlyak, E.M., Chepurnykh, T.V., Fradkov, A.F., Ermakova, G.V., Solovieva, E.A., Lukyanov, K.A., Bogdanova, E.A., Zaraisky, A.G., Lukyanov, S., et al. (2007). Bright far-red fluorescent protein for whole-body imaging. *Nat Methods* *4*, 741–746.
- Shimomura, O., Johnson, F.H., and Saiga, Y. (1962). Extraction, purification and properties of aequorin, a bioluminescent protein from the luminous hydromedusa, *Aequorea*. *J Cell Comp Physiol* *59*, 223–239.
- Shimotohno, A., Oue, S., Yano, T., Kuramitsu, S., and Kagamiyama, H. (2001). Demonstration of the Importance and Usefulness of Manipulating Non-Active-Site Residues in Protein Design. *The Journal of Biochemistry* *129*, 943–948.
- Shindo, A., Hara, Y., Yamamoto, T.S., Ohkura, M., Nakai, J., and Ueno, N. (2010). Tissue-Tissue Interaction-Triggered Calcium Elevation Is Required for Cell Polarization during *Xenopus* Gastrulation. *PLoS ONE* *5*, e8897.
- Shkrob, M.A., Yanushevich, Y.G., Chudakov, D.M., Gurskaya, N.G., Labas, Y.A., Poponov, S.Y., Mudrik, N.N., Lukyanov, S., and Lukyanov, K.A. (2005). Far-red fluorescent proteins evolved from a blue chromoprotein from *Actinia equina*. *Biochem J* *392*, 649–654.
- Sia, S.K., Li, M.X., Spyropoulos, L., Gagne, S.M., Liu, W., Putkey, J.A., and Sykes, B.D. (1997). Structure of Cardiac Muscle Troponin C Unexpectedly Reveals a Closed Regulatory Domain. *J. Biol. Chem.* *272*, 18216–18221.
- Simon-Loriere, E., and Holmes, E.C. (2011). Why do RNA viruses recombine? *Nat Rev Microbiol* *9*, 617–626.
- Smith, J.M. (1970). Natural selection and the concept of a protein space. *Nature* *225*, 563–564.

- Spyracopoulos, L., Lavigne, P., Crump, M.P., Gagne, S.M., Kay, C.M., and Sykes, B.D. (2001). Temperature Dependence of Dynamics and Thermodynamics of the Regulatory Domain of Human Cardiac Troponin C. *Biochemistry* *40*, 12541–12551.
- Stefan, M.I., and Novère, N.L. (2013). Cooperative Binding. *PLOS Computational Biology* *9*, e1003106.
- Stemmer, W.P.C. (1994). DNA shuffling by random fragmentation and reassembly: In vitro recombination for molecular evolution. *Proc. Natl. Acad. Sci. USA* *91*, 10747–10751.
- Stokes, G.G. (1852). On the Change of Refrangibility of Light. *Philosophical Transactions of the Royal Society of London* 463–562.
- Stryer, L., and Haugland, R.P. (1967). Energy transfer: a spectroscopic ruler. *Proc Natl Acad Sci U S A* *58*, 719–726.
- Sun, X.R., Badura, A., Pacheco, D.A., Lynch, L.A., Schneider, E.R., Taylor, M.P., Hogue, I.B., Enquist, L.W., Murthy, M., and Wang, S.S.-H. (2013). Fast GCaMPs for improved tracking of neuronal activity. *Nat Commun* *4*.
- Svoboda, K., and Yasuda, R. (2006). Principles of Two-Photon Excitation Microscopy and Its Applications to Neuroscience. *Neuron* *50*, 823–839.
- Swindle, N., and Tikunova, S.B. (2010). Hypertrophic Cardiomyopathy-Linked Mutation D145E Drastically Alters Calcium Binding by the C-Domain of Cardiac Troponin C. *Biochemistry* *49*, 4813–4820.
- Tallini, Y.N., Ohkura, M., Choi, B.-R., Ji, G., Imoto, K., Doran, R., Lee, J., Plan, P., Wilson, J., Xin, H.-B., et al. (2006). Imaging cellular signals in the heart in vivo: Cardiac expression of the high-signal Ca<sup>2+</sup> indicator GCaMP2. *PNAS* *103*, 4753–4758.
- Tang, J., van Panhuys, N., Kastenmüller, W., and Germain, R.N. (2013). The Future of Immuno-imaging – Deeper, Bigger, More Precise, and Definitely More Colorful. *Eur J Immunol* *43*, 1407–1412.
- Tee, K.L., and Schwaneberg, U. (2007). Directed evolution of oxygenases: screening systems, success stories and challenges. *Comb. Chem. High Throughput Screen.* *10*, 197–217.
- Thestrup, T., Litzlbauer, J., Bartholomäus, I., Mues, M., Russo, L., Dana, H., Kovalchuk, Y., Liang, Y., Kalamakis, G., Laukat, Y., et al. (2014). Optimized ratiometric calcium sensors for functional in vivo imaging of neurons and T lymphocytes. *Nat. Methods* *11*, 175–182.
- Tian, L., Hires, S.A., Mao, T., Huber, D., Chiappe, M.E., Chalasani, S.H., Petreanu, L., Akerboom, J., McKinney, S.A., Schreiter, E.R., et al. (2009). Imaging neural activity in worms, flies and mice with improved GCaMP calcium indicators. *Nat Meth* *6*, 875–881.
- Tikunova, S.B., Black, D.J., Johnson, J.D., and Davis, J.P. (2001). Modifying Mg<sup>2+</sup> binding and exchange with the N-terminal of calmodulin. *Biochemistry* *40*, 3348–3353.
- Trigo-Mourino, P., Thestrup, T., Griesbeck, O., Griesinger, C., and Becker, S. (2016). The structural base for FRET in a green fluorescent protein biosensor. Submitted.
- Tsien, R.Y. (1998). The Green Fluorescent Protein. *Annu. Rev. Biochem* *67*, 509–544.
- Tsutsui, H., Karasawa, S., Okamura, Y., and Miyawaki, A. (2008). Improving membrane voltage measurements using FRET with new fluorescent proteins. *Nat. Methods* *5*, 683–685.
- Vörös, J. (2004). The Density and Refractive Index of Adsorbing Protein Layers. *Biophys J* *87*, 553–561.
- Wachter, R.M., Elsliger, M.A., Kallio, K., Hanson, G.T., and Remington, S.J. (1998). Structural basis of spectral shifts in the yellow-emission variants of green fluorescent protein. *Structure* *6*, 1267–1277.
- Waite, J.C., Vardhana, S., Shaw, P.J., Jang, J.-E., McCarl, C.-A., Cameron, T.O., Feske, S., and Dustin, M.L. (2013). Interference with Ca(2+) release activated Ca(2+) (CRAC) channel function delays T-cell arrest in vivo. *Eur. J. Immunol.* *43*, 3343–3354.

- Wang, Q., Shui, B., Kotlikoff, M.I., and Sonderrmann, H. (2008). Structural Basis for Calcium Sensing by GCaMP2. *Structure* 16, 1817–1827.
- Westphal, V., and Hell, S.W. (2005). Nanoscale resolution in the focal plane of an optical microscope. *Phys. Rev. Lett.* 94, 143903.
- Wong, T.S., Roccatano, D., Zacharias, M., and Schwaneberg, U. (2006a). A statistical analysis of random mutagenesis methods used for directed protein evolution. *J. Mol. Biol* 355, 858–871.
- Wong, T.S., Zhurina, D., and Schwaneberg, U. (2006b). The diversity challenge in directed protein evolution. *Comb. Chem. High Throughput Screen* 9, 271–288.
- Wright, S. (1931). Evolution in Mendelian Populations. *Genetics* 16, 97–159.
- Yamada, Y., and Mikoshiba, K. (2012). Quantitative comparison of novel GCaMP-type genetically encoded Ca<sup>2+</sup> indicators in mammalian neurons. *Front Cell Neurosci* 6.
- Yamakage, M., and Namiki, A. (2002). Calcium channels - basic aspects of their structure, function and gene encoding; anesthetic action on the channels - a review: [Revue : notions de base sur la structure, la fonction et l'encodage genetique des canaux calciques et action des anesthesiques sur ces canaux]. *Can J Anesth* 49, 151–164.
- Yang, F., Moss, L.G., and Phillips, G.N. (1996). The molecular structure of green fluorescent protein. *Nat Biotechnol* 14, 1246–1251.
- Zhang, J., Campbell, R.E., Ting, A.Y., and Tsien, R.Y. (2002). Creating new fluorescent probes for cell biology. *Nat Rev Mol Cell Biol* 3, 906–918.
- Zhao, H., and Arnold, F.H. (1997). Combinatorial protein design: strategies for screening protein libraries. *Curr. Opin. Struct. Biol* 7, 480–485.
- Zhao, H., Giver, L., Shao, Z., Affholter, J.A., and Arnold, F.H. (1998). Molecular evolution by staggered extension process (StEP) in vitro recombination. *Nature Biotechnology* 16.
- Zhao, Y., Araki, S., Wu, J., Teramoto, T., Chang, Y.-F., Nakano, M., Abdelfattah, A.S., Fujiwara, M., Ishihara, T., Nagai, T., et al. (2011). An Expanded Palette of Genetically Encoded Ca<sup>2+</sup> Indicators. *Science* 333, 1888–1891.
- Zipfel, W.R., Williams, R.M., Christie, R., Nikitin, A.Y., Hyman, B.T., and Webb, W.W. (2003). Live tissue intrinsic emission microscopy using multiphoton-excited native fluorescence and second harmonic generation. *Proc Natl Acad Sci U S A.* 100, 7075–7080.

# Appendix – CHAPTER 2

## **Correlating Calcium Binding, Förster Resonance Energy Transfer, and Conformational Change in the Biosensor TN-XXL**

Anselm Geiger,<sup>†</sup> Luigi Russo,<sup>‡</sup> Thomas Gensch,<sup>§</sup> Thomas Thestrup,<sup>†</sup> Stefan Becker,<sup>‡</sup> Karl-Peter Hopfner,<sup>¶</sup> Christian Griesinger,<sup>‡</sup> Gregor Witte,<sup>¶</sup> and Oliver Griesbeck<sup>†</sup>

<sup>†</sup>Max-Planck-Institut für Neurobiologie, Martinsried, Germany; <sup>‡</sup>Max-Planck-Institut für biophysikalische Chemie, Göttingen, Germany; <sup>§</sup>ICS-4, Forschungszentrum Jülich, Jülich, Germany; and <sup>¶</sup>Genzentrum und Department Biochemie, Ludwig-Maximilians-University, Munich, Germany

### **Supporting Material**

**Supplementary Table 1: Fluorescence decay parameters for truncation and “Amber”-like constructs.**

	Ca <sup>2+</sup> conc. [nM]	$\alpha_1$ [%]	$\tau_1$ [ns]	$\alpha_2$ [%]	$\tau_2$ [ns]	$\alpha_3$ [%]	$\tau_3$ [ns]	$\tau_{ave}$ [ns]
<b>ECFP</b>	“Ca <sup>2+</sup> free”	38	0.720	20	2.00	42	3.87	2.31
	“high Ca <sup>2+</sup> ”	37	0.735	20	1.98	44	3.87	2.35
<b>TN-XXL <math>\Delta</math>cpCit</b>	“Ca <sup>2+</sup> free”	34	0.718	25	2.15	41	3.97	2.40
	“high Ca <sup>2+</sup> ”	33	0.704	22	2.10	45	3.95	2.48
<b>TN-XXL cpCit<sup>o</sup></b>	“Ca <sup>2+</sup> free”	32	0.722	26	2.00	41	3.92	2.38
	“high Ca <sup>2+</sup> ”	33	0.719	25	1.97	42	3.85	2.36
<b>cpCitrine</b>	“Ca <sup>2+</sup> free”	100	3.56	--	--	--	--	3.56
	“high Ca <sup>2+</sup> ”	100	3.57	--	--	--	--	3.57
<b>TN-XXL <math>\Delta</math>ECFP</b>	“Ca <sup>2+</sup> free”	100	3.45	--	--	--	--	3.45
	“high Ca <sup>2+</sup> ”	100	3.37	--	--	--	--	3.37
<b>TN-XXL ECFP<sup>o</sup></b>	“Ca <sup>2+</sup> free”	100	3.50	--	--	--	--	3.50
	“high Ca <sup>2+</sup> ”	100	3.27	--	--	--	--	3.27

**Supplementary Table 2: Fluorescence decay parameters in TN-XXL.**

	fit	$\alpha_1$ [%]	$\tau_1$ [ns]	$\alpha_2$ [%]	$\tau_2$ [ns]	$\alpha_3$ [%]	$\tau_3$ [ns]	$\chi^2$	$\tau_{ave}$ [ns]
TN-XXL cpCit <sup>o</sup> „Ca <sup>2+</sup> free“	bi-exp	47	1.16	---	---	53	3.76	1.202	2.53
	<b>tri-exp</b>	<b>30</b>	<b>0.762</b>	<b>25</b>	<b>1.97 (fix)</b>	<b>45</b>	<b>3.96</b>	<b>1.197</b>	<b>2.49</b>
TN-XXL cpCit <sup>o</sup> “high Ca <sup>2+</sup> ”	bi-exp	47	1.14	---	---	53	3.70	1.193	2.50
	<b>tri-exp</b>	<b>32</b>	<b>0.738</b>	<b>24</b>	<b>1.97 (fix)</b>	<b>44</b>	<b>3.88</b>	<b>1.123</b>	<b>2.414</b>
TN-XXL “Ca <sup>2+</sup> free“	bi-exp	52	1.11	---	---	48	3.51	1.202	2.26
	<b>tri-exp</b>	<b>36</b>	<b>0.705</b>	<b>30</b>	<b>1.97 (fix)</b>	<b>34</b>	<b>3.73</b>	<b>1.121</b>	<b>2.11</b>
TN-XXL “high Ca <sup>2+</sup> ”	bi-exp	71	0.758	---	---	29	3.24	1.476	1.47
	<b>tri-exp</b>	<b>64</b>	<b>0.511</b>	<b>24</b>	<b>1.97 (fix)</b>	<b>12</b>	<b>3.79</b>	<b>1.206</b>	<b>1.26</b>

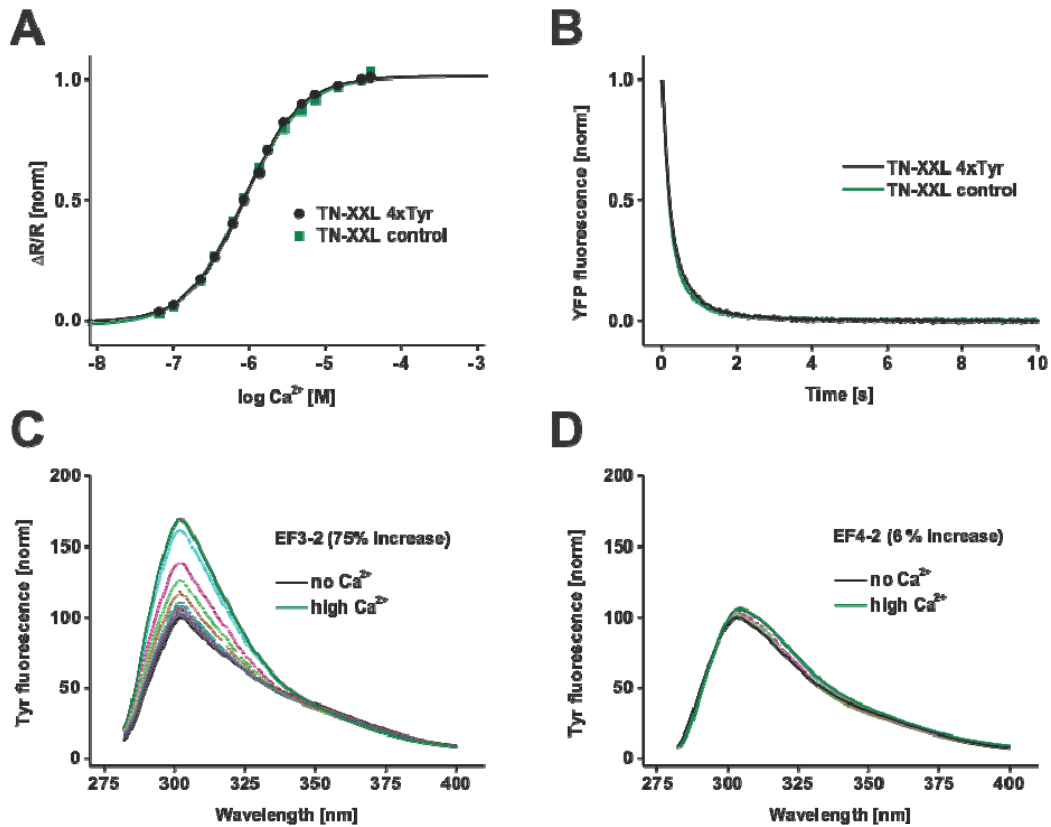
Donor excitation wavelength: 440 nm

Donor emission wavelength: 470 nm

These parameters represent the averages of the values obtained from three independent experiments. The  $\tau_2$  value fixed in the tri-exponential fits was obtained from averaging the  $\tau_2$  values from three Ca<sup>2+</sup> titrations of TN-XXL. Subsequently this value was kept fixed throughout further tri-exponential fits. The tri-exponential fits highlighted in bold letters were used further on in discussion and figures.

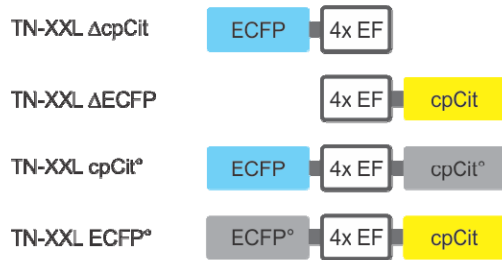
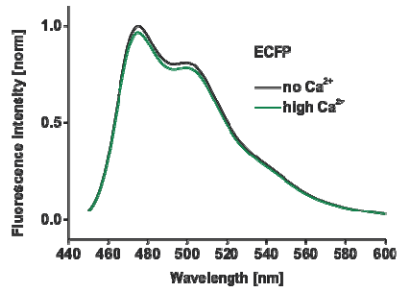
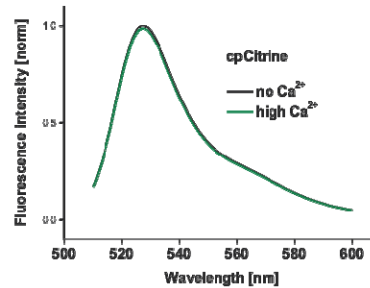
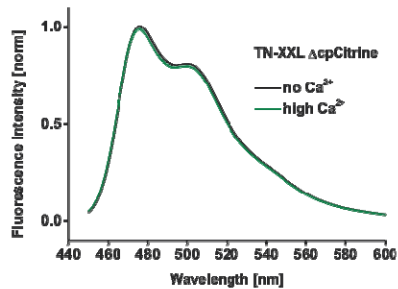
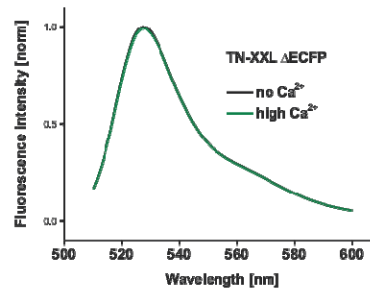
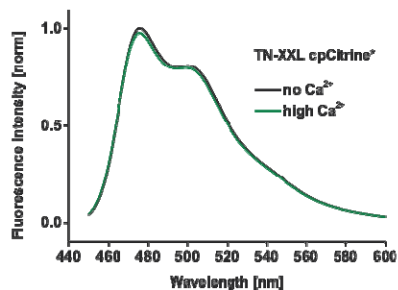
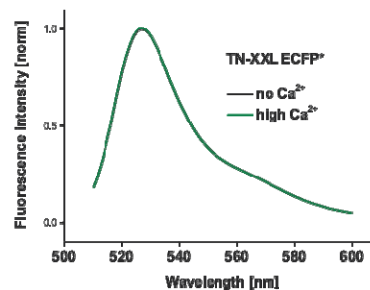
**Supplementary Table 3: Temperature and pH dependency of TN-XXL**

Condition		Affinity $K_d$ [nM]	Off-Kinetics $t_{decay}$ [ms]
23°C	pH = 6.5	1030	620
	pH = 7.2	830	--
	pH = 7.5	--	522
	pH = 8.0	451	425
30°C	pH = 7.2	946	--
	pH = 7.5	--	264
37°C	pH = 7.2	1210	--
	pH = 7.5	--	129



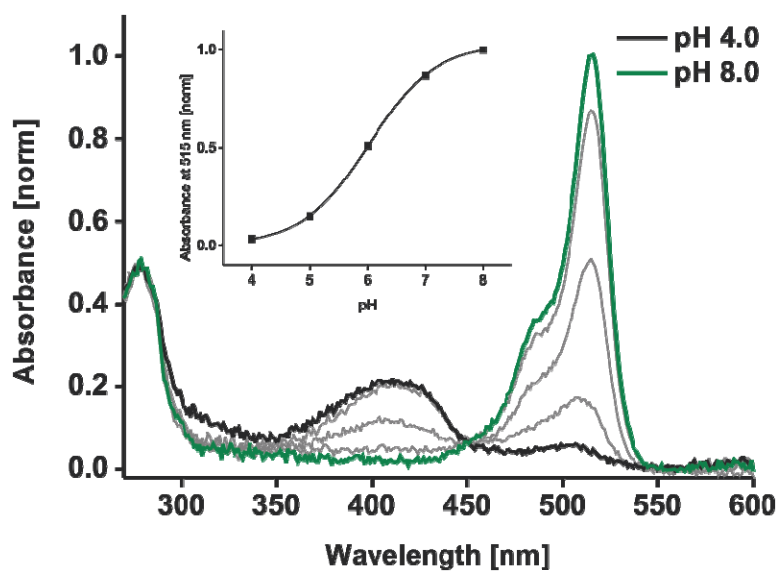
### Supplementary Figure S1 Tyrosine substitutions in TN-XXL.

(A and B) Tyrosine substitutions in all four EF-hands (TN-XXL 4xTyr) do not alter calcium binding properties of TN-XXL as monitored by FRET. Calcium affinity titrations (A) and calcium dissociation kinetics (B) of TN-XXL 4xTyr were indistinguishable from those of TN-XXL. Excitation was at 432 nm and emission recorded at 475/527 nm. (C and D) Emission spectra of calcium titrations with single tyrosine substitutions within TN-XXL. EF3-1 (C) and EF4-1 (D) showed comparable fluorescence modulation to EF3-2 and EF4-2, respectively (excitation at 275 nm with emission spectra recorded from 285-400 nm).

**A****B****E****C****F****D****G**

### Supplementary Figure S2 Truncation and Amber Substitutions in TN-XXL.

(A) TN-XXL truncation and Amber substitution constructs used to test the structure effects on the fluorescence signal of each FP variant. For ECFP emission (excitation: 432 nm) ECFP alone (B), TN-XXL  $\Delta$ cpCit (C) and TN-XXL cpCit<sup>°</sup> including the Amber mutation Y67C in cpCitrine (D) were tested and only a minor drop in fluorescence of  $\sim$ 2% upon addition of 40  $\mu$ M Ca<sup>2+</sup> was detected. cpCitrine emission (excitation: 500 nm) was tested with cpCitrine alone (E), TN-XXL  $\Delta$ ECFP (F) and TN-XXL ECFP<sup>°</sup> including the Amber mutation W67C in ECFP (G) without any fluorescence change upon addition of 40  $\mu$ M Ca<sup>2+</sup>.



**Supplementary Figure S3 pH effect on cpCitrine chromophore.**

UV Absorption spectra of cpCitrine recorded at different pH values of 4.0 (cyan), 5.0, 6.0, 7.0 and 8.0 (black). The inset shows the normalized absorption readout at 515 nm indicating ~88% absorption at pH 7.2 (i.e., 88% of the cpCitrine chromophores deprotonated).

# Appendix – CHAPTER 3

## **Supplementary Information**

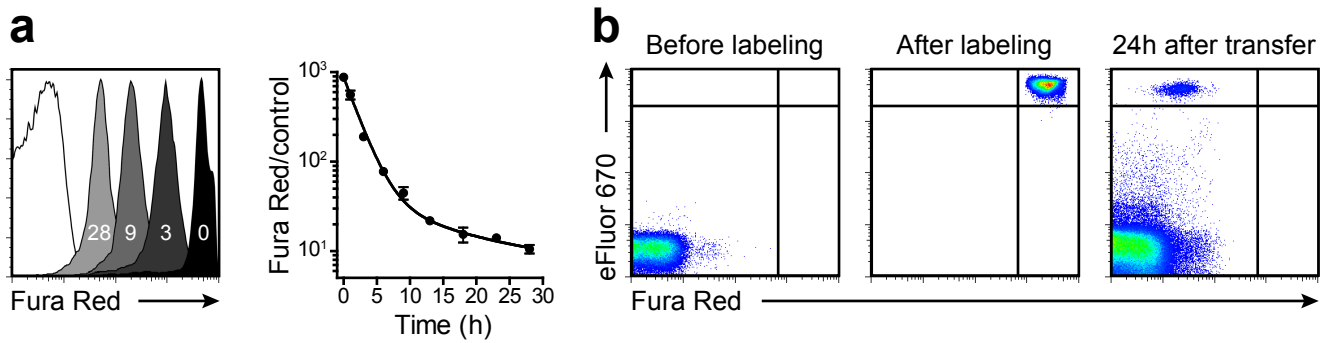
### **Real-time in vivo analysis of T cell activation in the central nervous system using a genetically encoded calcium indicator**

Marsilius Mues<sup>1</sup>, Ingo Bartholomäus<sup>1</sup>, Thomas Thestrup<sup>2</sup>, Oliver Griesbeck<sup>2</sup>, Hartmut Wekerle<sup>1</sup>, Naoto Kawakami<sup>1,3</sup>, and Gurumoorthy Krishnamoorthy<sup>1</sup>

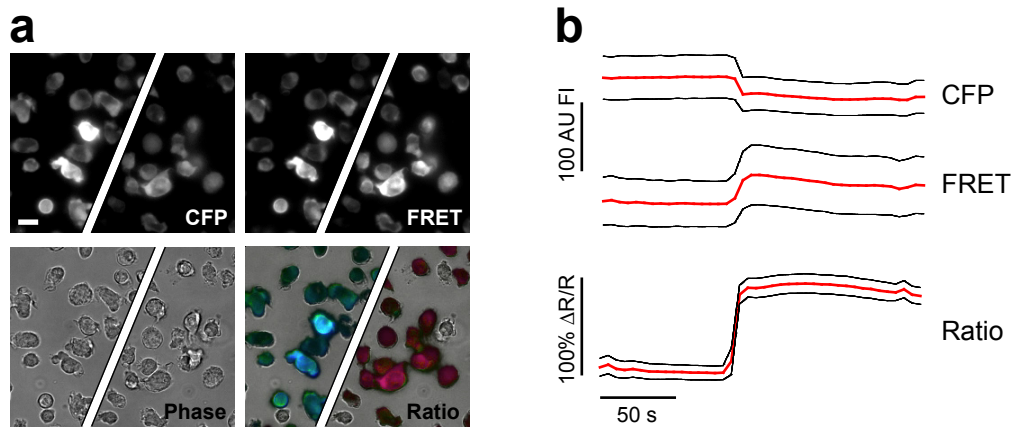
<sup>1</sup>Department of Neuroimmunology and <sup>2</sup>Research Group of Cellular Dynamics, Max Planck Institute of Neurobiology, Martinsried, Germany <sup>3</sup>Institute of Clinical Neuroimmunology, Ludwig Maximilians University, Munich, Germany

### **Inventory of Supplementary Information**

Supplementary Figures 1-12 Legends for Supplementary Videos Supplementary Methods TaqMan qPCR oligonucleotides



**Supplementary Figure 1** Synthetic calcium indicators are not stable in T cells. **(a)** Primary murine T cells were loaded *in vitro* with the visible light-excited calcium indicator Fura Red and its intracellular persistence was followed using flow cytometry (left). Quantification of the Fura Red label intensity in relation to unlabeled control cells showed loss of the synthetic calcium dye from T cells within hours (right). Data are presented as the mean $\pm$ SEM. **(b)** Murine splenocytes double-labeled with Fura Red and the cell tracking dye eFluor 670 (that irreversibly couples to cellular proteins) were adoptively transferred into WT host animals. FACS analysis showed selective loss of the synthetic calcium dye fluorescence from double-labeled cells *in vivo* 24 hours after transfer.



**Supplementary Figure 2** Microscopic characterization of TN-XXL in EL4 cells. **(a)** Epifluorescence and phase-contrast images of TN-XXL-expressing EL4 cells before (left) and after (right) the addition of 4  $\mu\text{M}$  ionomycin (taken from Video 1). The overlay shows the pseudocolor image of the emission ratio; scale bar 30  $\mu\text{m}$ . **(b)** Average fluorescence intensities of CFP and FRET and the average response of the ratiometric signal after the stimulation of calcium influx in TN-XXL-expressing EL4 cells using 4  $\mu\text{M}$  ionomycin (mean $\pm$ SEM). FI, fluorescence intensity; AU, arbitrary units.

**M V S K G E E L F T G V V P I L V E L D G D V N G H**  
 ATG GTG AGC AAG GGC GAG GAG CTG TTC ACC GGG GTG GTG CCC ATC CTG GTC GAG CTG GAC GGC GAC GTA AAC GGC CAC  
 \*\*\*

**K F S V R G E G E G D A T N G K L T L K F I C T T G**  
 AAG TTC AGC GTG CGC GGC GAG GGC GAG GGC GAT GCC ACC AAC GGC AAG CTG ACC CTG AAG TTC ATC TGC ACC ACC GGC  
 \*\*\*

**K L P V P W P T L V T T L T W G V Q C F S R Y P D H**  
 AAG CTG CCC GTG CCC TGG CCC ACC CTC GTG ACC ACC CTG ACC TGG GGC GTG CAG TGC TTC AGC CGC TAC CCC GAC CAC  
 \*\*\*

**M K Q H D F F K S A M P E G Y V Q E R T I F F K D D**  
 ATG AAG CAG CAC GAC TTC TTC AAG TCC GCC ATG CCC GAA GGC TAC GTC CAG GAG CGT ACC ATC TTC TTC AAG GAC GAC  
 \*\*\*

**G N Y K T R A E V K F E G D T L V N R I E L K G I D**  
 GGC AAC TAC AAG ACC CGC GCC GAG GTG AAG TTC GAG GGC GAC ACC CTG GTG AAC CGC ATC GAG CTG AAG GGC ATC GAC  
 \*\*\*

**F K E D G N I L G H K L E Y N Y I S H N V Y I T A D**  
 TTC AAG GAG GAC GGC AAC ATC CTG GGG CAC AAG CTG GAG TAC AAC TAC ATC AGC CAC AAC GTC TAT ATC ACC GCC GAC  
 \*\*\*

**K Q K N G I K A H F K I R H N I E D G S V Q L A D H**  
 AAG CAG AAG AAC GGC ATC AAG GCC CAC TTC AAG ATC CGC CAC AAC ATC GAG GAC GGC AGC GTG CAG CTC GCC GAC CAC  
 \*\*\*

**Y Q Q N T P I G D G P V L L P D N H Y L S T Q S K L**  
 TAC CAG CAG AAC ACC CCC ATC GGC GAC GGC CCC GTG CTG CTG CCC GAC AAC CAC TAC CTG AGC ACC CAG TCC AAG CTG  
 \*\*\*

**S K D P N E K R D H M V L L E F V T A A R M L S E E**  
 AGC AAA GAC CCC AAC GAG AAG CGC GAT CAC ATG GTC CTG CTG GAG TTC GTG ACC GCC GCC CGC ATG CTG AGC GAG GAA  
 \*\*\* **TCT \*\*\* GAG**

**E L A N C F R I F D K D A N G F I D I E E L G E I L**  
 GAG CTG GCC AAC TGC TTC CGC ATC TTC GAC AAG GAC GCT AAC GGG TTC ATC GAC ATC GAG GAG CTG GGT GAG ATT CTC  
 \*\*\* **TTG GCT** \*\*\* \*\*\* \*\*\* \*\*\* **ATA TTT GAT** \*\*\* \*\*\* **GCA** \*\*\* **GGC TTT** \*\*\* \*\*\* **ATA** \*\*\* **GAA CTC GGC** \*\*\* \*\*\* **CTG**

**R A T G E H V T E E D I E D L M K D S D K N N D G R**  
 AGG GCC ACT GGG GAG CAC GTC ACC GAG GAG GAC ATA GAA GAC CTC ATG AAG GAT TCA GAC AAG AAC AAT GAC GGC CGC  
**CGG GCT ACC GGC** \*\*\* **CAT GTA ACG** \*\*\* \*\*\* \*\*\* **ATC GAG GAT CTG** \*\*\* \*\*\* \*\*\* **TCC** \*\*\* \*\*\* \*\*\* **AAC GAT** \*\*\* **CGT**

**I D F D E F L K M M E G V Q G T S E E E L A N C F R**  
 ATT GAC TTC GAT GAG TTC CTG AAG ATG ATG GAG GGC GTG CAG GGT ACC AGC GAG GAA GAG CTG GCC AAC TGC TTC CGC  
 \*\*\* \*\*\* \*\*\* **GAC GAA TTT CTT AAA** \*\*\* \*\*\* \*\*\* **GGG** \*\*\* \*\*\* \*\*\* \*\*\* \*\*\* \*\*\* \*\*\* **GAA** \*\*\* **GCT AAT** \*\*\* **TTT AGG**

**I F D K D A N G F I D I E E L G E I L R A T G E H V**  
 ATC TTC GAC AAG GAC GCT AAC GGG TTC ATC GAC ATC GAG GAG CTG GGT GAG ATT CTC AGG GCC ACT GGG GAG CAC GTC  
 \*\*\* \*\*\* \*\*\* \*\*\* **GAT** \*\*\* \*\*\* **GGA** \*\*\* **ATA** \*\*\* **ATT** \*\*\* \*\*\* **CTA GGG** \*\*\* **ATC TTG CGG** \*\*\* \*\*\* **GGA** \*\*\* \*\*\* **GTG**

**T E E D I E D L M K D S D K N N D G R I D F D E F L**  
 ACC GAG GAG GAC ATA GAA GAC CTC ATG AAG GAT TCA GAC AAG AAC AAT GAC GGC CGC ATT GAC TTC GAT GAG TTC CTG  
 \*\*\* \*\*\* \*\*\* **GAT** \*\*\* \*\*\* **GAT CTT** \*\*\* **AAA GAC AGC GAT** \*\*\* **AAT AAC** \*\*\* \*\*\* **CGA ATC GAT TTT GAC** \*\*\* \*\*\* **TTG**

**K M M E G V Q E L M G G V Q L A D H Y Q Q N T P I G**  
 AAG ATG ATG GAG GGC GTG CAG GAG CTC ATG GGC GGC GTG CAG CTC GCC GAC CAC TAC CAG CAG AAC ACC CCC ATC GGC  
 \*\*\* \*\*\* \*\*\* **GAA** \*\*\* **GTT** \*\*\* \*\*\* \*\*\* \*\*\* **GGT GGG GTC** \*\*\* **CTT GCA GAT** \*\*\* \*\*\* \*\*\* \*\*\* **AAT ACT CCG** \*\*\* **GGG**

**D G P V L L P D N H Y L S Y Q S K L S K D P N E K R**  
 GAC GGC CCC GTG CTG CTG CCC GAC AAC CAC TAC CTG AGC TAC CAG TCC AAG CTG AGC AAA GAC CCC AAC GAG AAG CGC  
**GAT GGG CCG GTT CTC** \*\*\* **CCT** \*\*\* \*\*\* \*\*\* \*\*\* \*\*\* **TCA** \*\*\* \*\*\* \*\*\* \*\*\* **CTT TCC** \*\*\* **GAT CCT AAT GAA** \*\*\* **CGG**

**D H M V L L E F V T A A G I T L G M D E L Y K G G T**  
 GAT CAC ATG GTC CTG CTG GAG TTC GTG ACC GCC GCC GGG ATC ACT CTC GGC ATG GAC GAG CTG TAC AAG GGC GGT ACC  
 \*\*\* \*\*\* \*\*\* \*\*\* \*\*\* \*\*\* **GAA TTT GTC** \*\*\* \*\*\* \*\*\* **GGA** \*\*\* \*\*\* \*\*\* **GGA** \*\*\* \*\*\* \*\*\* \*\*\* \*\*\* **AAA GGT GGG** \*\*\*

**G G S M V S K G E E L F T G V V P I L V E L D G D V**  
 GGC GGC AGC ATG GTG AGC AAG GGC GAG GAG CTG TTC ACC GGG GTG GTG CCC ATC CTG GTC GAG CTG GAC GGC GAC GTA  
**GGG GGA TCT** \*\*\* \*\*\* \*\*\* \*\*\* \*\*\* **GAA GAA TTG** \*\*\* **ACT GGT GTA GTC CCT ATT TTG GTG GAA** \*\*\* **GAT GGG GAT GTC**

**N G H K F S V R G E G E G D A T N G K L T L K F/L I C**  
 AAC GGC CAC AAG TTC AGC GTG CGC GGC GAG GGC GAG GGC GAT GCC ACC AAC GGC AAG CTG ACC CTG AAG TTC ATC TGC  
 \*\*\* **GGT CAT AAA** \*\*\* \*\*\* \*\*\* **CGA GGG** \*\*\* **GGT** \*\*\* **GGG GAC GCA ACT AAT** \*\*\* **AAA TTG ACA CTC** \*\*\* **CTC** \*\*\* \*\*\*

**T T G K L P V P W P T L V T T L G Y G L M C F A R Y**  
 ACC ACC GGC AAG CTG CCC GTG CCC TGG CCC ACC CTC GTG ACC ACC CTG GGC TAC GGC CTG ATG TGC TTC GCC CGC TAC  
**ACA ACG GGG AAA** \*\*\* \*\*\* \*\*\* **CCA** \*\*\* \*\*\* **ACA** \*\*\* **GTT ACT ACT CTA GGA TAT** \*\*\* **CTT** \*\*\* **TGT** \*\*\* \*\*\* \*\*\* \*\*\*

**P D H M K Q H D F F K S A M P E G Y V Q E R T I F F**  
 CCC GAC CAC ATG AAG CAG CAC GAC TTC AAG TCC GCC ATG CCC GAA GGC GAC GTC CAG GAG CGC ACC ATC TTC TTC  
**CCA** \*\*\* **CAT** \*\*\* **AAA CAA** \*\*\* **GAT** \*\*\* **TTT AAA TCA** \*\*\* \*\*\* **CCA GAG GGG** \*\*\* \*\*\* \*\*\* \*\*\* **AGA ACT** \*\*\* \*\*\* \*\*\*

**K D D G N Y K T R A E V K F E G D T L V N R I E L K**  
 AAG GAC GAC GGC AAC TAC AAG ACC CGC GCC GAG GTG AAG TTC GAG GGC GAC ACC CTG GTG AAC CGC ATC GAG CTG AAG  
 \*\*\* \*\*\* **GAT GGT AAT** \*\*\* \*\*\* **ACT AGG** \*\*\* \*\*\* \*\*\* **AAA** \*\*\* **GAA GGG GAT ACA CTT GTC** \*\*\* **CGA** \*\*\* \*\*\* \*\*\* \*\*\*

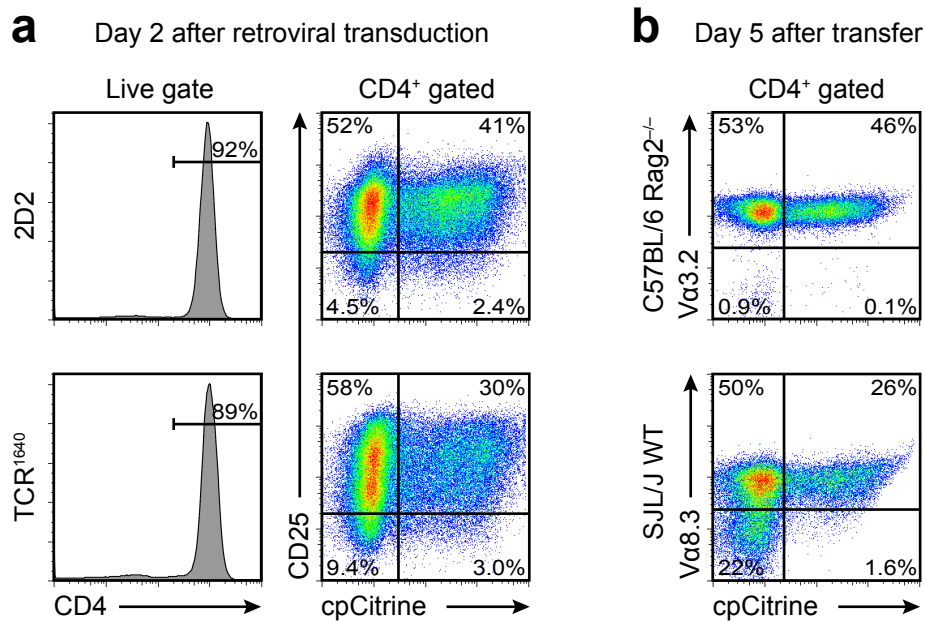
**G I D F K E D G N I L G H K L E Y N Y N S H N V Y I**  
 GGC ATC GAC TTC AAG GAG GAC GGC AAC ATC CTG GGG CAC AAG CTG GAG TAC AAC TAC AAC AGC CAC AAC GTC TAT ATC  
**GGA** \*\*\* \*\*\* **TTT** \*\*\* \*\*\* \*\*\* **GGA** \*\*\* **ATA CTC** \*\*\* **CAT** \*\*\* **TTG GAA** \*\*\* \*\*\* \*\*\* \*\*\* **AGT** \*\*\* **AAT GTT TAC** \*\*\*

**M-T A D K Q K N G I K A N F K I R H N I E D \***  
 ATG GCC GAC AAG CAG AAG AAC GGC ATC AAG GCC AAC TTC AAG ATC CGC CAC AAC ATC GAG GAC TAA  
**ACA** \*\*\* **GAT** \*\*\* **CAA** \*\*\* \*\*\* \*\*\* **ATT** \*\*\* **GCT AAT TTT** \*\*\* \*\*\* **CGT** \*\*\* \*\*\* **ATT** \*\*\* **GAT TGA**

**Supplementary Figure 3** Comparison of codon-diversified TN-XXL with the original sequence. The CFP (blue), Troponin C (red), and cpCitrine (yellow) amino acid sequences are shown with the altered codons highlighted.

pMSCVneo-TN-XXL	5'LTR	Ψ <sup>+</sup> signal	TN-XXL	PGKp	NeoR	s	3'LTR	5.24 kb
pMSCVneo-TN-XXL <sup>CD</sup>	5'LTR	Ψ <sup>+</sup> signal	TN-XXL <sup>CD</sup>	PGKp	NeoR	s	3'LTR	5.24 kb
pMSCVΔneo-TN-XXL <sup>CD</sup>	5'LTR	Ψ <sup>+</sup> signal	TN-XXL <sup>CD</sup>			s	3'LTR	3.91 kb
pMSCVneo-cpCitrine	5'LTR	Ψ <sup>+</sup> signal	cpCitrine	PGKp	NeoR	s	3'LTR	4.12 kb

**Supplementary Figure 4** Comparison of retroviral vector sizes. Removal of the PGK promoter (PGKp) and neomycin resistance cassette (NeoR) significantly reduces the retroviral vector size. LTR, long terminal repeats; Ψ<sup>+</sup>, extended packaging signal; s, spacer.



**Supplementary Figure 5** Stable expression of TN-XXL<sup>CD</sup> in TCR transgenic T cells. **(a)** FACS analysis of TCR transgenic MOG-specific 2D2 and TCR<sup>1640</sup> T cell cultures after transduction with TN-XXL<sup>CD</sup>. **(b)** Analysis of blood lymphocytes from recipient animals showed stable expression of TN-XXL<sup>CD</sup> in TCR transgenic T cells five days after adoptive transfer (right).

**M V S K G E E L F T G V V P I L V E L D G D V N G H**  
 ATG GTG AGC AAG GGC GAG GAG CTG TTC ACC GGG GTG GTG CCC ATC CTG GTC GAG CTG GAC GGC GAC GTA AAC GGC CAC  
 \*\*\*

**K F S V R G E G E G D A T N G K L T L K F I C T T G**  
 AAG TTC AGC GTG CGC GGC GAG GGC GAG GGC GAT GCC ACC AAC GGC AAG CTG ACC CTG AAG TTC ATC TGC ACC ACC GGC  
 \*\*\*

**K L P V P W P T L V T T L T W G V Q C F S R Y P D H**  
 AAG CTG CCC GTG CCC TGG CCC ACC CTC GTG ACC ACC CTG ACC TGG GGC GTG CAG TGC TTC AGC CGC TAC CCC GAC CAC  
 \*\*\*

**M K Q H D F F K S A M P E G Y V Q E R T I F F K D D**  
 ATG AAG CAG CAC GAC TTC TTC AAG TCC GCC ATG CCC GAA GGC TAC GTC CAG GAG CGT ACC ATC TTC TTC AAG GAC GAC  
 \*\*\*

**G N Y K T R A E V K F E G D T L V N R I E L K G I D**  
 GGC AAC TAC AAG ACC CGC GCC GAG GTG AAG TTC GAG GGC GAC ACC CTG GTG AAC CGC ATC GAG CTG AAG GGC ATC GAC  
 \*\*\*

**F K E D G N I L G H K L E Y N Y I S H N V Y I T A D**  
 TTC AAG GAG GAC GGC AAC ATC CTG GGG CAC AAG CTG GAG TAC AAC TAC ATC AGC CAC AAC GTC TAT ATC ACC GCC GAC  
 \*\*\*

**K Q K N G I K A H F K I R H N I E D G S V Q L A D H**  
 AAG CAG AAG AAC GGC ATC AAG GCC CAC TTC AAG ATC CGC CAC AAC ATC GAG GAC GGC AGC GTG CAG CTC GCC GAC CAC  
 \*\*\*

**Y Q Q N T P I G D G P V L L P D N H Y L S T Q S K L**  
 TAC CAG CAG AAC ACC CCC ATC GGC GAC GGC CCC GTG CTG CTG CCC GAC AAC CAC TAC CTG AGC ACC CAG TCC AAG CTG  
 \*\*\*

**S K D P N E K R D H M V L L E F V T A A R M P S E E**  
 AGC AAA GAC CCC AAC GAG AAG CGC GAT CAC ATG GTC CTG CTG GAG TTC GTG ACC GCC GCC CGC ATG CCT AGC GAA GAA  
 \*\*\*

**E L S E C F R I F D K D G N G F I D R E E F G D I I**  
 GAG CTA TCA GAG TGC TTT CGC ATT TTT GAC AAG GAT GGA AAT GGT TTC ATC GAC AGG GAG GAA TTT GGA GAC ATC ATC  
 \*\*\*

**R L T G E Q L T D E D V D E I F G D S D T D K N G R**  
 CGC CTT ACT GGA GAA CAG CTC ACA GAT GAG GAT GTC GAT GAG ATA TTT GGA GAT TCA GAC ACA GAC AAA AAT GGA AGG  
 \*\*\*

**I D F D E F L K M V E N V Q P E L M G G V Q L A D H**  
 ATT GAC TTT GAT GAG PTC CTG AAG ATG GTG GAG AAT GTC CAG CCT GAG CTC ATG GGC GGC GTG CAG CTC GCC GAC CAC  
 \*\*\* \*\*\* \*\*\* \*\*\* \*\*\* \*\*\* \*\*\* \*\*\* \*\*\* \*\*\* \*\*\* \*\*\* \*\*\* \*\*\* \*\*\* \*\*\* \*\*\* \*\*\* \*\*\* **GGT GGG GTC** \*\*\* **CTT GCA GAT** \*\*\*

**Y Q Q N T P I G D G P V L L P D N H Y L S Y Q S K L**  
 TAC CAG CAG AAC ACC CCC ATC GGC GAC GGC CCC GTG CTG CTG CCC GAC AAC CAC TAC CTG AGC TAC CAG TCC AAG CTG  
 \*\*\* \*\*\* \*\*\* **AAT ACT CCG** \*\*\* **GGG GAT GGG CCG GTT CTC** \*\*\* **CCT** \*\*\* \*\*\* \*\*\* \*\*\* \*\*\* **TCA** \*\*\* \*\*\* \*\*\* \*\*\* **CTT**

**S K D P N E K R D H M V L L E F V T A A G I T L G M**  
 AGC AAA GAC CCC AAC GAG AAG CGC GAT CAC ATG GTC CTG CTG GAG TTC GTG ACC GCC GCC GGG ATC ACT CTC GGC ATG  
**TCC** \*\*\* **GAT CCT AAT GAA** \*\*\* **CGG** \*\*\* \*\*\* \*\*\* \*\*\* \*\*\* \*\*\* **GAA TTT GTC** \*\*\* \*\*\* \*\*\* **GGA** \*\*\* \*\*\* \*\*\* **GGA** \*\*\*

**D E L Y K G G T G G S M V S K G E E L F T G V V P I**  
 GAC GAG CTG TAC AAG GGC GGT ACC GGC GGC AGC ATG GTG AGC AAG GGC GAG GAG CTG TTC ACC GGG GTG GTG CCC ATC  
 \*\*\* \*\*\* \*\*\* \*\*\* **AAA GGT GGG** \*\*\* **GGG GGA TCT** \*\*\* \*\*\* \*\*\* \*\*\* \*\*\* \*\*\* **GAA GAA TTG** \*\*\* **ACT GGT GTA GTC CCT ATT**

**L V E L D G D V N G H K F S V R G E G E G D A T N G**  
 CTG GTC GAG CTG GAC GGC GAC GTA AAC GGC CAC AAG TTC AGC GTG CGC GGC GAG GGC GAG GGC GAT GCC ACC AAC GGC  
**TTG GTG GAA** \*\*\* **GAT GGG GAT GTC** \*\*\* **GGT CAT AAA** \*\*\* \*\*\* \*\*\* \*\*\* **CGA GGG** \*\*\* **GGT** \*\*\* **GGG GAC GCA ACT AAT** \*\*\*

```

K L T L K F/L I C T T G K L P V P W P T L V T T L G Y
AAG CTG ACC CTG AAG TTC ATC TGC ACC ACC GGC AAG CTG CCC GTG CCC TGG CCC ACC CTC GTG ACC ACC CTG GGC TAC
AAA TTG ACA CTC *** CTC *** *** ACA ACG GGG AAA *** *** *** CCA *** *** ACA *** GTT ACT ACT CTA GGA TAT

G L M C F A R Y P D H M K Q H D F F K S A M P E G Y
GGC CTG ATG TGC TTC GCC CGC TAC CCC GAC CAC ATG AAG CAG CAC GAC TTC TTC AAG TCC GCC ATG CCC GAA GGC TAC
*** CTT *** TGT *** *** *** *** *** CCA *** CAT *** AAA CAA *** GAT *** TTT AAA TCA *** *** CCA GAG GGG ***

V Q E R T I F F K D D G N Y K T R A E V K F E G D T
GTC CAG GAG CGC ACC ATC TTC TTC AAG GAC GAC GGC AAC TAC AAG ACC CGC GCC GAG GTG AAG TTC GAG GGC GAC ACC
*** *** *** AGA ACT *** *** *** *** *** GAT GGT AAT *** *** ACT AGG *** *** *** AAA *** GAA GGG GAT ACA

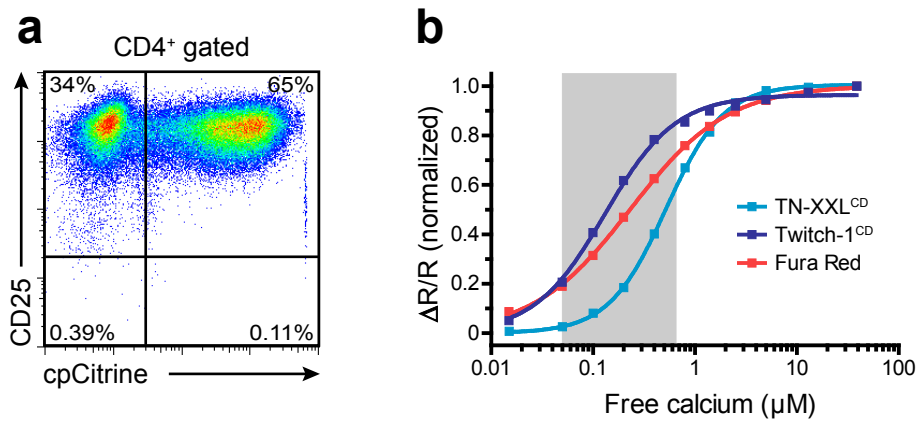
L V N R I E L K G I D F K E D G N I L G H K L E Y N
CTG GTG AAC CGC ATC GAG CTG AAG GGC ATC GAC TTC AAG GAG GAC GGC AAC ATC CTG GGG CAC AAG CTG GAG TAC AAC
CTT GTC *** CGA *** *** *** *** *** GGA *** *** TTT *** *** *** GGA *** ATA CTC *** CAT *** TTG GAA *** ***

Y N S H N V Y I M-T A D K Q K N G I K A N F K I R H N
TAC AAC AGC CAC AAC GTC TAT ATC ATG GCC GAC AAG CAG AAG AAC GGC ATC AAG GCC AAC TTC AAG ATC CGC CAC AAC
*** *** AGT *** AAT GTT TAC *** ACA *** GAT *** CAA *** *** *** ATT *** GCT AAT TTT *** *** CGT *** ***

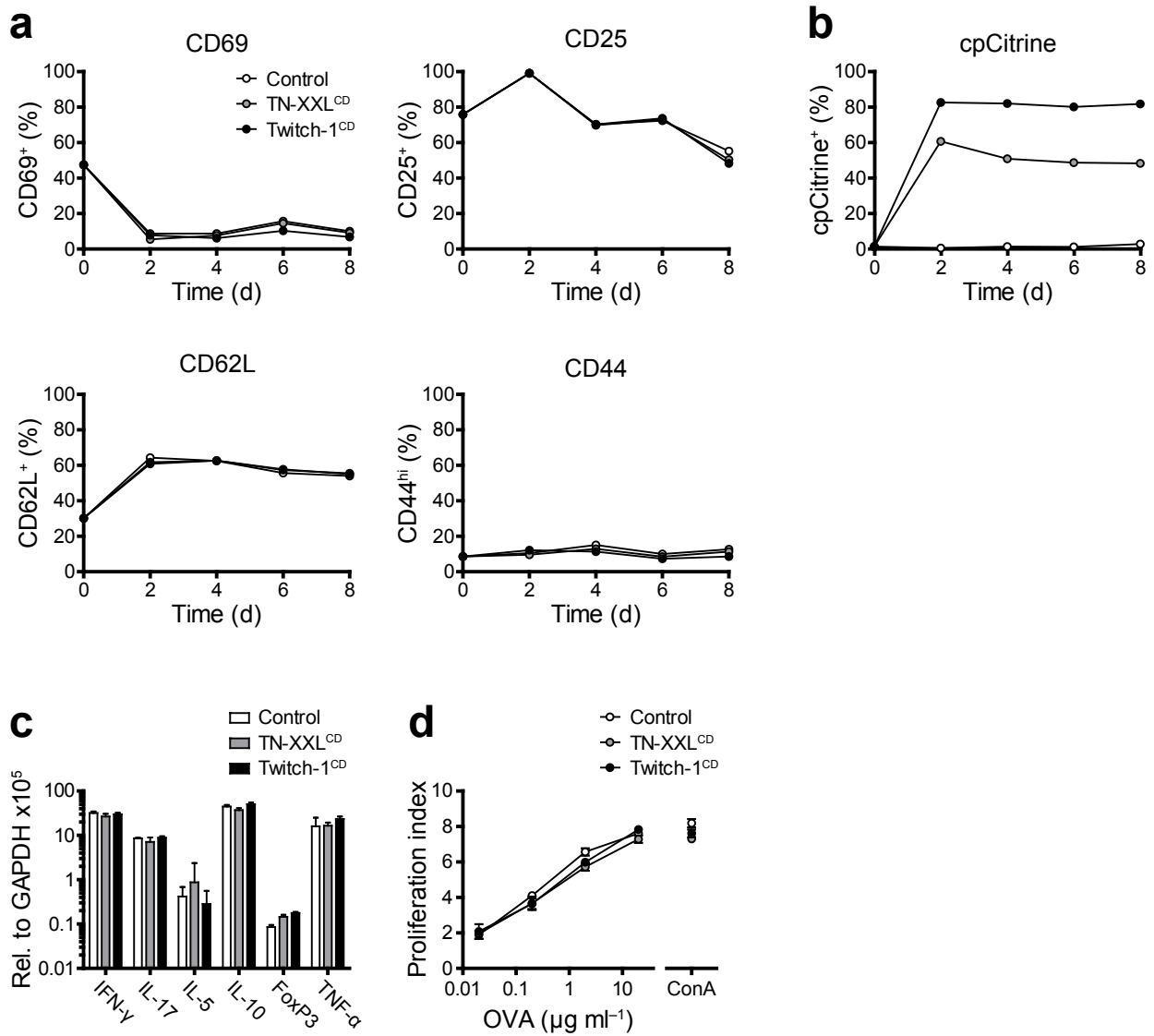
I E D *
ATC GAG GAC TAA
ATT *** GAT TGA

```

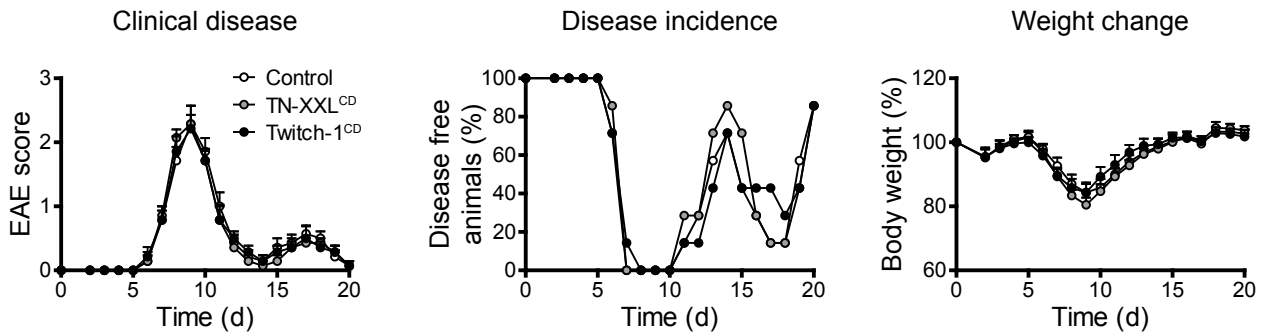
**Supplementary Figure 6** Comparison of codon-diversified Twitch-1 with the original sequence. The CFP (blue), Troponin C (red), and cpCitrine (yellow) amino acid sequences are shown with the altered codons highlighted.



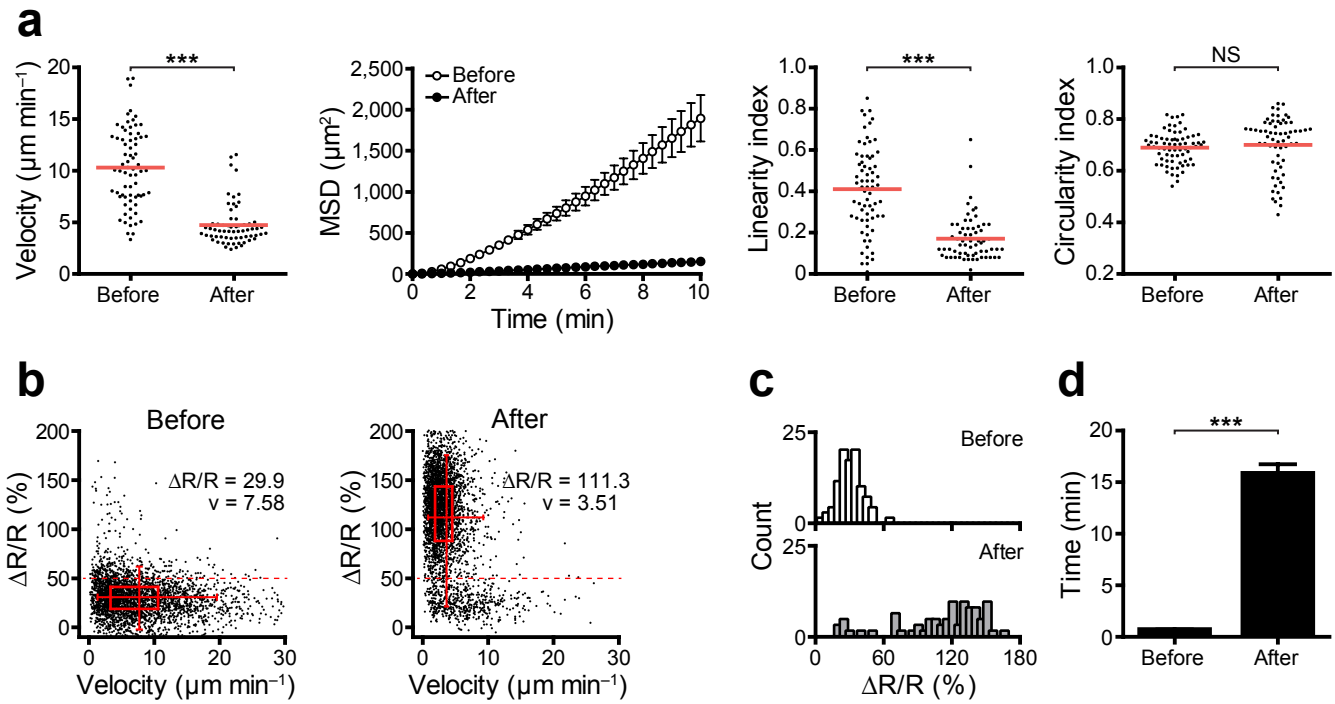
**Supplementary Figure 7** Expression of Twitch-1<sup>CD</sup> and dissociation constants of calcium indicators. **(a)** FACS analysis of 2D2 T cells transduced with Twitch-1<sup>CD</sup>. **(b)** *In situ* calcium calibration: titration curves of TN-XXL<sup>CD</sup>, Twitch-1<sup>CD</sup>, and Fura Red in T cells. The resulting dissociation constant  $K_d$  (indicating calcium affinity) and the corresponding Hill coefficient  $h$  (indicating cooperativity of binding) are  $K_d \approx 520$  nM and  $h \approx 1.5$  for TN-XXL<sup>CD</sup>,  $K_d \approx 140$  nM and  $h \approx 1.3$  for Twitch-1<sup>CD</sup>, and  $K_d \approx 230$  nM and  $h \approx 0.9$  for Fura Red, respectively. Grey area highlights the range of physiologically relevant calcium levels in T cells.



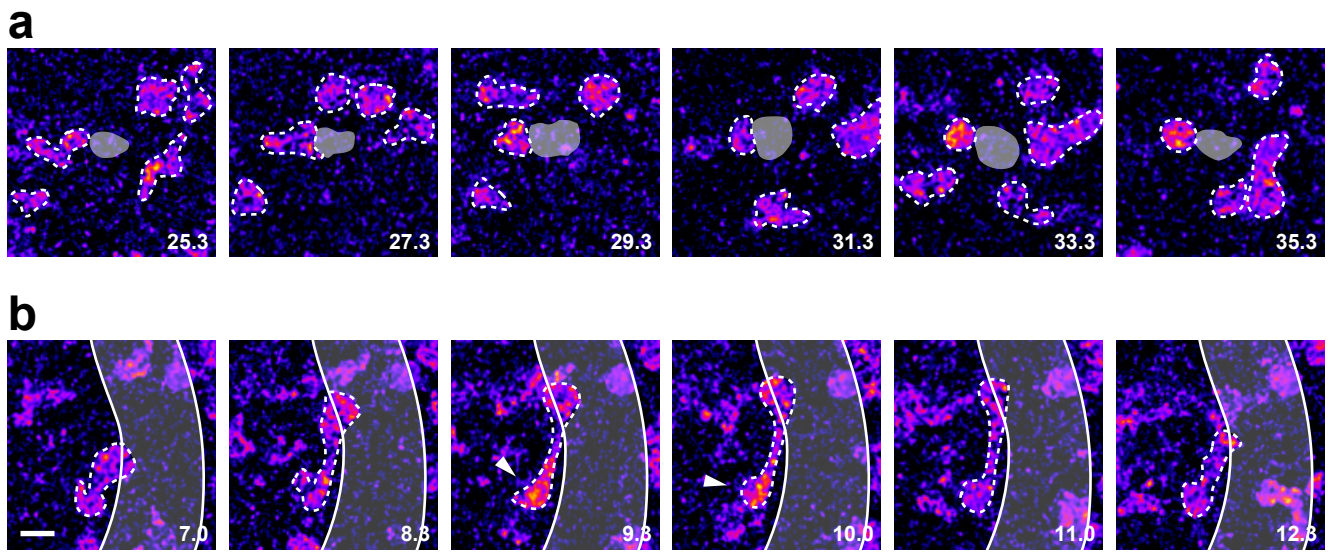
**Supplementary Figure 8** Calcium indicator expression does not alter T cell function. (a) FACS-analysis of various surface markers and (b) calcium indicator expression in transduced OT-II T cells over time. (c) Analysis of cytokine transcript levels in OT-II T cells on day 4 after transduction and (d) proliferation assay after restimulation with OVA peptide or 2  $\mu\text{g ml}^{-1}$  Concanavalin A on day 6 after transduction. Data are presented as the mean  $\pm$  SEM.



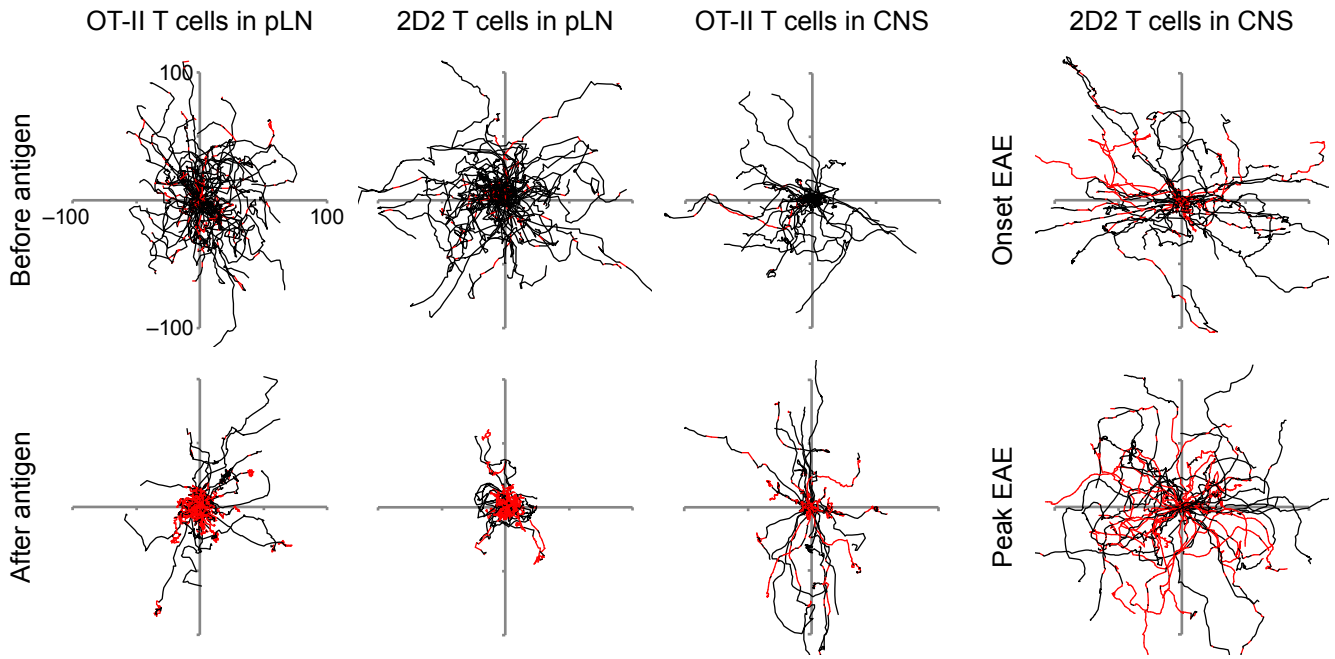
**Supplementary Figure 9** Calcium indicator expression does not alter the course of EAE. Calcium indicator-expressing TCR<sup>1640</sup> T cells induce EAE in recipient animals to a similar extent as control T cells. *n*=7 mice per group. Data are presented as the mean±SEM.



**Supplementary Figure 10** Calcium signaling in 2D2 T cells in the lymph node. **(a)** Quantification of T cell locomotion within the popliteal lymph node before ( $n=71$ ) and after ( $n=64$ ) the i.v. injection of 100  $\mu\text{g}$  of NF-M peptide. The average velocities, mean squared displacement ( $\text{MSD} \pm \text{SEM}$ ), movement linearity, and cell circularity are plotted. **(b)** Scatter plots showing the cell velocity vs. calcium indicator ratio change for each individual time point before ( $n=3350$ ) and after ( $n=3806$ ) antigen injection. Mean values for  $\Delta R/R$  and velocity ( $v$ ) are indicated along with a two-dimensional box plot. **(c)** Distribution of average intracellular calcium levels. **(d)** Duration of elevated calcium levels with a  $\Delta R/R$  above 50%. Data are presented as the mean  $\pm$  SEM; \*\*\* $P < 0.001$ . Results represent one of three similar experiments.



**Supplementary Figure 11** Differential calcium signaling in T cells during peak EAE (Video 9). **(a)** T cell arrest and elevated calcium levels after APC encounter (outlined in grey as seen by phagocytosed fluorescent dextran). **(b)** Subcellularly defined calcium signaling in the perikarya (arrowhead). The pseudocolor ratio images with the T cells encircled and the blood vessel walls retraced are shown. Time interval in minutes, scale bar 10  $\mu$ m.



**Supplementary Figure 12** Comparison of superimposed trajectories of OT-II and 2D2 T cells in the popliteal lymph node (Figure 3 and Supplementary Figure 10) and of OT-II T cells in the inflamed CNS (Figure 4) (all before and after the injection of cognate antigen), and of encephalitogenic 2D2 T cells at the onset and peak of transfer EAE. The time points with a  $\Delta R/R$  above 50% are indicated in red, the distance is shown in  $\mu\text{m}$ . Data are representative of at least three independent experiments.

## Legends for Supplementary Videos (available online)

**Video 1** Visualization of calcium influx in EL4 cells by TN-XXL (related to Supplementary Figure 2). EL4 lymphoma cells stably expressing TN-XXL were imaged *in vitro* before and after the addition of 4  $\mu$ M ionomycin.

**Video 2** CD3 binding triggers a strong calcium flux in T cells (related to Figure 2). TN-XXL<sup>CD</sup>-expressing 2D2 T cells interacting with anti-CD3/CD28 beads were imaged *in vitro*.

**Video 3** APC encounter triggers strong calcium flux in T cells (related to Figure 2). TN-XXL<sup>CD</sup>-expressing 2D2 T cells interacting with recombinant MOG-pulsed IgH<sup>MOG</sup> B cells were imaged *in vitro*.

**Video 4** T cells respond strongly to antigen presented by DCs (related to Figure 3). Twitch-1<sup>CD</sup>-expressing OT-II T cells were adoptively transferred into WT recipient hosts before the subcutaneous injection of SNARF-1-labeled DCs. After one day, *in vivo* two-photon microscopy of the popliteal lymph node was performed before and after the i.v. injection of 100  $\mu$ g of OVA peptide.

**Video 5** All T cells displaying strong calcium signals are engaged with DCs (related to Figure 3). The experimental settings are the same as in Video 4 after the injection of antigen but with highlighting the positions of DCs.

**Video 6** Encephalitogenic T cells also respond strongly to antigen presented by DCs (related to Supplementary Figure 10). The experimental settings are the same as in Video 4 but with 2D2 T cells and injection of 100  $\mu$ g of NF-M peptide.

**Video 7** CNS resident APCs efficiently present antigen to infiltrating T cells (related to Figure 4). Twitch-1<sup>CD</sup>-expressing OT-II T cells were adoptively transferred into MOG peptide-immunized WT mice, followed by two-photon microscopy of the spinal cord, before and after the i.v. injection of 100  $\mu$ g of OVA peptide and Texas Red dextran.

**Video 8** Extravasated encephalitogenic T cells showing calcium oscillations in the CNS (related to Figure 5). Twitch-1<sup>CD</sup>-expressing 2D2 T cells were adoptively transferred into Rag2<sup>-/-</sup> recipients and two-photon microscopy of the spinal cord was performed at the onset of EAE (score 0.5).

**Video 9** Differential calcium signaling in encephalitogenic T cells during peak EAE (related to Figure 5). The experimental settings are the same as in Video 8 but the imaging was performed at the peak of EAE (score >2).

## Supplementary Methods

**Plasmid construction.** For the generation of pcDNA3.1-TN-XXL, TN-XXL was excised from pRSETB-TN-XXL by restriction digestion with *Bam*HI and *Eco*RI (all cloning enzymes from NEB) and subcloned into the pcDNA3.1 expression vector (Invitrogen). For retroviral transduction, TN-XXL and derivatives were subcloned from the pRSETB cloning vector (Invitrogen) by excision with *Sac*II and *Eco*RI, and ligation into the pMSCVneo retroviral vector (Clontech) opened by *Sac*II and *Mfe*I. Modifications of the calcium biosensor TN-XXL were constructed in pRSETB. For the generation of TN-XXL  $\Delta$ TnC, the TnC C-terminal lobes in TN-XXL were replaced by an oligonucleotide linker coding for 2xGGGGS by restriction digestion with *Sph*I and *Sac*I. BFP was amplified from pTagBFP-actin (Evrogen) to replace CFP in TN-XXL  $\Delta$ TnC CFP $\rightarrow$ BFP by restriction digestion with *Sac*II and *Sph*I. The codon-diversified cpCitrine and the C-terminal lobe domains of TN-XXL<sup>CD</sup> were synthesized by Sloning BioTechnology. Deletion of the neomycin resistance cassette from pMSCVneo was done by restriction digestion with *Bgl*II and *Bam*HI, followed by re-ligation of the plasmid to yield pMSCV $\Delta$ neo. For the generation of Twitch-1<sup>CD</sup>, the C-terminal lobe domains of TN-XXL<sup>CD</sup> were replaced with a higher affinity moiety by restriction digestion with *Sph*I and *Sac*I.

**Cell culture.** Primary murine lymphocytes were cultured in RPMI, and Phoenix packaging and EL4 lymphoma cells were grown in DMEM (both Sigma-Aldrich). The culture media were supplemented with 10% FCS (Biochrome), 2 mM L-glutamine, 1 mM sodium pyruvate, 1x MEM non-essential amino acids, 100 U ml<sup>-1</sup> Penicillin, 100  $\mu$ g ml<sup>-1</sup> Streptomycin (all supplements from Invitrogen), and 50  $\mu$ M  $\beta$ -mercaptoethanol. For the generation of TN-XXL-expressing EL4 cells, pcDNA3.1-TN-XXL was transfected into EL4 cells using Lipofectamine 2000 (Invitrogen), and clones with stable and high expression of TN-XXL were obtained by neomycin selection and limiting dilution. The EL4 cell lysates were prepared by incubating cells in lysis buffer containing 20 mM HEPES, 10 mM KCl, 1.5 mM MgCl<sub>2</sub>, 1 mM DTT, 0.1 mM PMSF, and 1% Triton X-100, supplemented with the Complete Mini Protease Inhibitor Cocktail (Roche). The TN-XXL emission spectra were analyzed on a Cary-Eclipse spectrophotometer (Varian).

**Dye labeling of cells.** For labeling with the tracking dyes eFlour 450 or eFluor 670 (eBioscience), cells were incubated in PBS containing 5  $\mu$ M dye for 10 minutes at 37°C and subsequently washed with cold PBS. Labeling of T cells with the synthetic calcium indicator Fura Red was achieved by incubation of the cells in Hank's balanced salt solution with 1% FCS containing 10  $\mu$ M Fura Red (Invitrogen) for 30 minutes at 37°C.

**Flow cytometric analysis.** For the detection of cell surface markers, cells were stained with fluorochrome-labeled antibodies (BD Biosciences and eBioscience), and samples were acquired on a FACSCalibur system with CellQuest software (BD Biosciences). For FACS-based intracellular calcium measurements, samples were acquired on a FACSCanto system with FACSDiva software (BD Biosciences), equipped with a 405 nm laser for excitation of CFP and 465/30 nm and 530/30 nm band pass filters for CFP and FRET emission, respectively, along with a 488 nm laser with a 530/30 nm band pass filter for direct excitation and emission of cpCitrine. For functional intracellular calcium measurements, cells were kept at 37°C during acquisition using a custom built warming jacket. All FACS data were analyzed with FlowJo software (Tree Star).

***In situ* calcium calibration.** FACS-based intracellular calcium calibrations were done as described previously (June & Moore 2008 *Curr. Protoc. Immunol.*, Vol 5: 5.5). Briefly, cells were suspended in 10 mM MOPS buffer containing defined amounts of 10 mM CaEGTA and K<sub>2</sub>EGTA, poisoned with 4 μM ionomycin, 10 μM carbonyl cyanide m-chlorophenyl hydrazone, 40 mM 2-deoxyglucose, and 60 mM sodium azide. Cells were incubated for 90 minutes at 37°C to allow for clamping and calcium equilibration before acquisition.

***In vitro* proliferation assay.** 4 x 10<sup>4</sup> T cells labeled with eFluor 450 and 2 x 10<sup>5</sup> irradiated (30 Gy) WT splenocytes per well were seeded in 96-well round-bottom plates in a total volume of 200 μl growth medium in triplicates with varying concentrations of cognate antigen or 2 μg ml<sup>-1</sup> Concanavalin A. After a culture period of 72 hours, samples were harvested and analyzed for eFluor 450 dilution. The proliferative index is calculated from the sum of the cells in all generations divided by the number of original parent cells.

**Quantitative real-time PCR analysis.** Total RNA was isolated from cells by TRI Reagent (Sigma-Aldrich) extraction and, following DNase I treatment, converted into cDNA using oligo-dT primers and SuperScript II Reverse Transcriptase (Invitrogen). TaqMan qPCR analysis was done with gene-specific primers and probes (Metabion) and Absolute QPCR mixes (ABgene), run in triplicates on an ABI 7900 machine (Applied Biosystems). Results were analyzed and normalized to the housekeeping gene GAPDH.

***In vitro* widefield microscopy calcium imaging.** TN-XXL-expressing EL4 lymphoma or primary T cells were suspended in buffer containing 140 mM NaCl, 5 mM KCl, 1 mM CaCl<sub>2</sub>, 1 mM MgCl<sub>2</sub>, 1 mg ml<sup>-1</sup> glucose, and 10 mM HEPES, pH 7.4. Cells were seeded on a glass bottom culture dish (MatTek) coated with type I collagen (Invitrogen), and time-lapse images were acquired every 5-10 seconds on a Carl Zeiss Axiovert microscope equipped with a 37°C incubation chamber. Microscopy data were processed using MetaMorph (Molecular Devices) and ImageJ (NIH) software.

**Cell transfer for lymph node imaging.** On day one after retroviral transduction,  $5\text{--}15 \times 10^6$  OT-II T cells were adoptively transferred via i.v. injection into the tail vein of mildly irradiated (3.5 Gy) C57BL/6 recipients. The mice were allowed to recover for one week before the adoptive transfer of APCs. BMDCs were obtained from the femurs of C57BL/6 mice and were cultured in the presence of GM-CSF producing hybridoma-conditioned medium with repeated medium exchange to deplete the non-adherent cells. After 8 days in culture, the BMDCs were trypsinized and activated o/n in fresh medium supplemented with  $1 \mu\text{g ml}^{-1}$  LPS. The activated BMDCs were labeled using  $4 \mu\text{M}$  SNARF-1 (Invitrogen), and  $2 \times 10^6$  BMDCs were injected subcutaneously into the lower leg. Imaging of the draining popliteal lymph node was performed one day later.

**OT-II T cell transfer during active EAE.** C57BL/6 mice were subcutaneously immunized at the base of the tail with  $200 \mu\text{g}$  recombinant MOG emulsified in Freund's adjuvant supplemented with  $3 \text{ mg ml}^{-1}$  Mycobacterium tuberculosis (strain H37Ra).  $400 \text{ ng}$  of pertussis toxin was injected i.p. on days 0 and 2. One week after immunization  $10 \times 10^6$  retrovirally transduced OT-II T cells were adoptively transferred by i.v. injection into the tail vein, and 4-5 days later spinal cord imaging was performed.

**Adoptive transfer EAE.** One day after retroviral transduction  $5\text{--}15 \times 10^6$  2D2 or TCR<sup>1640</sup> T cells were adoptively transferred by i.v. injection into the tail vein of Rag2<sup>-/-</sup> or SJL/J recipients, respectively.  $400 \text{ ng}$  of pertussis toxin was injected i.p. on the day of adoptive transfer. The recipients developed EAE after approximately 12 days, with a classical monophasic disease course. Clinical scoring of animals was according to the classic EAE disease determination: 0, healthy animal; 1, animal with a flaccid tail; 2, animal with impaired righting reflex and/or gait; 3, animal with 1 paralyzed hind leg; 4, animal with both hind legs paralyzed; 5, moribund animal or death of the animal after preceding clinical disease.

**TaqMan qPCR primer/probe combinations (5' – 3' orientation)**

IFN- $\gamma$	sense	TCAAGTGGCATAGATGTGGAAGAA
	antisense	TGGCTCTGCAGGATTTTCATG
	probe	TCACCATCCTTTTGCCAGTTCTCCAG
IL-17	sense	AACTCCCTTGGCGCAAAGT
	antisense	GGCACTGAGCTTCCCAGATC
	probe	CCACGTCACCCTGGACTCTCCACC
IL-5	sense	CCGCTCACCGAGCTCTGTT
	antisense	AGATTTCTCCAATGCATAGCTGG
	probe	CAGGAAGCCTCATCGTCTCATTGCTTGT
IL-10	sense	CAGAGAAGCATGGCCCAGAA
	antisense	TGCTCCACTGCCTTGCTCTT
	probe	TGAGGCGCTTGTCATCGATTTCTCCC
mFoxP3	sense	AGGAGAAGCTGGGAGCTATGC
	antisense	TGGCTACGATGCAGCAAGAG
	probe	AAGGCTCCATCTGTGGCCTCAATGGA
mTNF- $\alpha$	sense	CATCTTCTCAAATTTCGAGTGACAA
	antisense	TGGGAGTAGACAAGGTACAACCC
	probe	CACGTCGTAGCAAACCACCAAGTGGA
GAPDH	sense	TCACCACCATGGAGAAGGC
	antisense	GCTAAGCAGTTGGTGGTGCA
	probe	ATGCCCCCATGTTTGTGATGGGTGT

# Appendix – CHAPTER 4

nature|methods

## Optimized Ratiometric Calcium Sensors for Functional *In Vivo* Imaging of Neurons and T-Lymphocytes

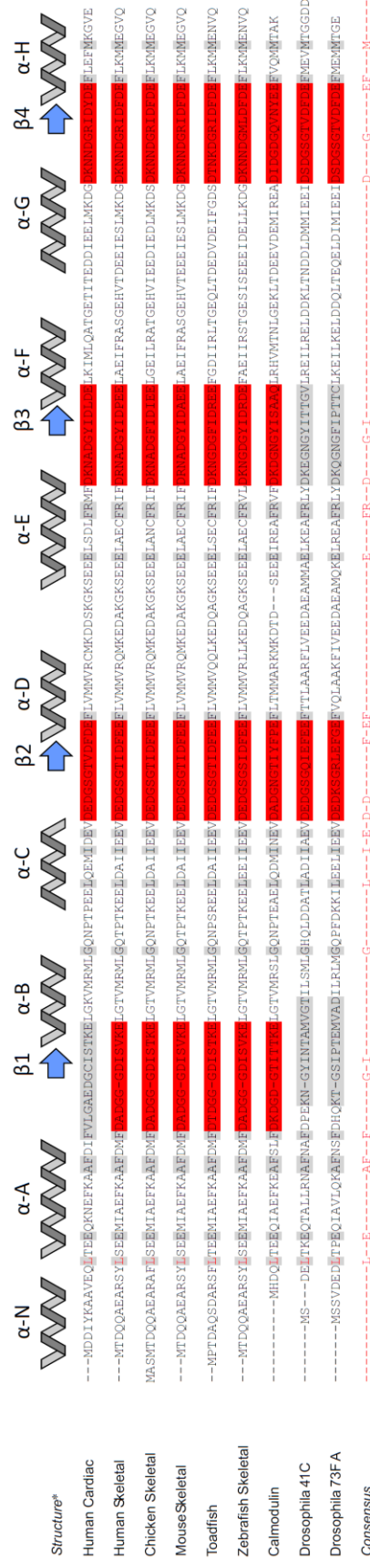
Thomas Thestrup, Julia Litzlbauer, Ingo Bartholomäus, Marsilius Mues, Luigi Russo, Hod Dana, Yuri Kovalchuk, Yajie Liang, Georgios Kalamakis, Yvonne Laukat, Stefan Becker, Gregor Witte, Anselm Geiger, Taylor Allen, Lawrence C Rome, Tsai-Wen Chen, Douglas S. Kim, Olga Garaschuk, Christian Griesinger, Oliver Griesbeck

### Supplementary materials

<b>Supplementary Figure 1</b>	Sequence alignment of various TnCs used for indicator construction
<b>Supplementary Figure 2</b>	Comparison of TN-L15 and Ts-L13 off-kinetics
<b>Supplementary Figure 3</b>	Incorporating the minimal domain into FRET sensors - Initial engineering of FRET change with small proline linker libraries
<b>Supplementary Figure 4</b>	NMR characterization of calcium loaded tsTnC minimal domain and $^1\text{H}$ - $^{15}\text{N}$ HSQC spectra used to monitor the $\text{Ca}^{2+}$ and $\text{Mg}^{2+}$ binding affinity.
<b>Supplementary Figure 5</b>	The structure of the tsTnC minimal domain compared to the C-terminal domain of Chicken TnC
<b>Supplementary Figure 6</b>	Measured SAXS curves of the sensors in absence and presence of calcium
<b>Supplementary Figure 7</b>	SAXS multi-domain modeling
<b>Supplementary Figure 8</b>	Diversified indicator libraries generated for screening
<b>Supplementary Figure 9</b>	Bacterial colony screening
<b>Supplementary Figure 10</b>	Comparison of selected FRET calcium sensors in dissociated neurons
<b>Supplementary Figure 11</b>	<i>In vivo</i> functional imaging of mouse visual cortex using Twitch-3
<b>Supplementary Figure 12</b>	Differences in baseline fluorescence between Twitch-3 and YC3.60 <i>in vivo</i>

<b>Supplementary Figure 13</b>	Emission spectra of purified "Twitch" variants <i>in vitro</i>
<b>Supplementary Table S1</b>	NMR structural statistics
<b>Supplementary Table S2</b>	SAXS data evaluation
<b>Supplementary Table S3</b>	Construct Overview

**Supplementary Figure 1.** Sequence alignment of various TnCs tested for indicator construction.



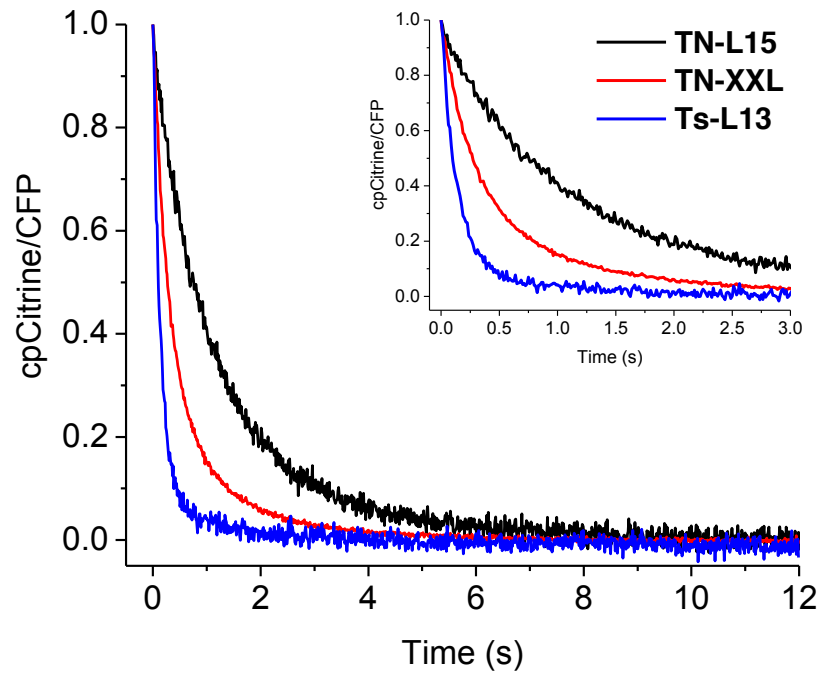
N-terminal lobe

C-terminal lobe

Sequence alignment of different TnC variants and calmodulin used as parental genes for construction of new calcium indicators. All indicated TnCs could be sandwiched between donor and acceptor FPs and yielded FRET sensors with varying FRET changes and Kds (data not shown). Sensors based on C-terminal lobe domains generally had higher calcium affinities than sensors based on full-length sequences or on N-terminal lobe domains. The red color indicates functional EF-hand domains whereas grey indicates non-functional domains. *Structure*\* illustrates the approximate position of the helices (grey helix) and  $\beta$ -sheets (blue arrow) in troponin c and calmodulin.

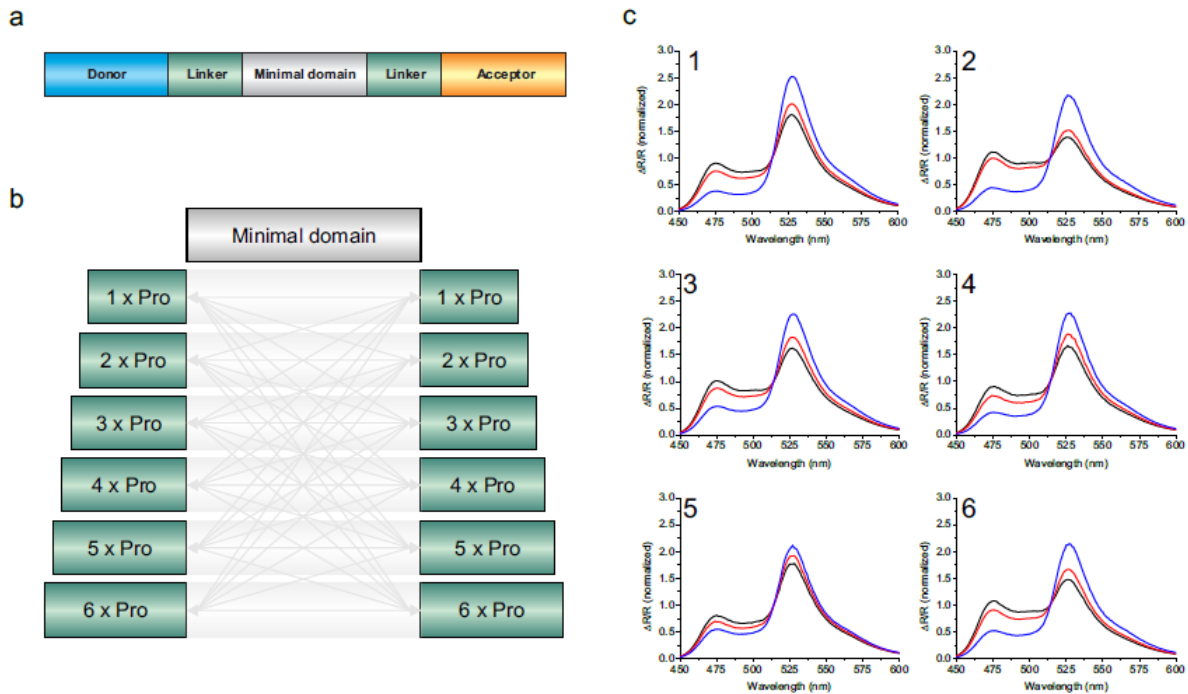
\* The CaBP Data Library – Troponin C (accessed 14.07.08) [http://structbio.vanderbilt.edu/cabp\\_database/general/prot\\_pages/tropc.html](http://structbio.vanderbilt.edu/cabp_database/general/prot_pages/tropc.html)

**Supplementary Figure 2.** Comparison of TN-L15 and Ts-L13 off-kinetics.



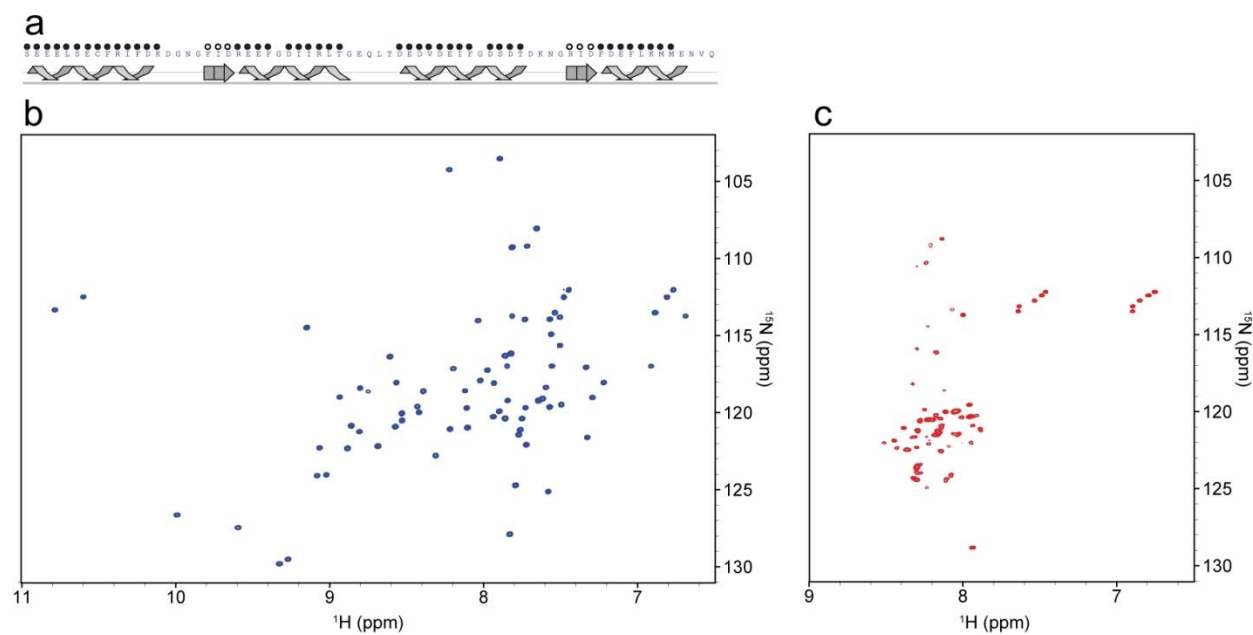
TN-L15 and Ts-L13 are simple FRET sensors based on wildtype chicken TnC truncated at leucin 15 (TN-L15) (Heim & Griesbeck, 2004) or toadfish white muscle/swim bladder TnC truncated at leucin 13 (Ts-L13). Both sensors based on the wild type proteins comprising both the N- and C-terminal domains had comparable calcium affinities of 1.2 and 1.3  $\mu\text{M}$ , respectively. Shown are *in vitro* stopped flow kinetics show calcium off-rates from the indicators TN-L15 ( $\tau = 1.230$  s), TN-XXL ( $\tau = 0.527$  s) and ts-L13 ( $\tau = 0.178$  s), taken at room temperature. The inlay shows a zoom in from 0-3 seconds. The experiments were conducted by mixing calcium saturated indicators with the strong calcium chelator BAPTA, and following the time course of signal relaxation. The two solutions were prepared as following: Calcium saturated indicator (5 ml): 10 mM MOPS, 4 mM  $\text{CaCl}_2$ , 1 mM  $\text{MgCl}_2$ , 50 mM KCl,  $\sim 0.2 - 1$   $\mu\text{M}$  indicator pH 7.5 and mixed with BAPTA solution (5 ml): 10 mM MOPS, 50 mM KCl, 20 mM BAPTA pH 7.5.

**Supplementary Figure 3.** Sandwiching the minimal domain into FRET sensors. Initial engineering of FRET change with small proline linker libraries.



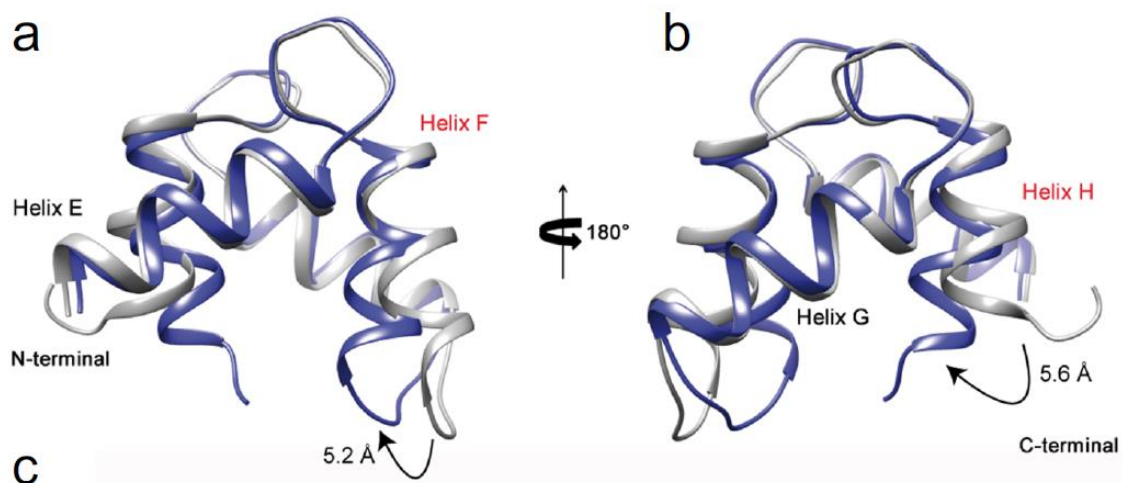
(a) A schematic representation of the sensor design in which the minimal calcium binding domain (grey) is sandwiched via amino acid linkers (green) between a donor (blue) and acceptor (yellow) fluorescent protein (b) Effects of linker insertions consisting of 0-6 prolines on basal and calcium induced FRET. A total of 49 sensors were assayed with combinations of 0-6 prolines at the N-terminal and C-terminal ends of the minimal domain. The light grey arrows indicate the different combinations. (c) Figure C1-C6 illustrates the differences in starting ratio and FRET change for a selection of sensors with proline linkers (C1: 1,1 Pro, C2: 2,2 Pro, C3: 3,3 Pro, C4: 4,2 Pro, C5: 6,0 Pro and C6: 2,5 Pro). Black lines represent the calcium free state, red;  $Mg^{2+}$  sensitivity (1 mM  $Mg^{2+}$ ) and blue line the maximum calcium response (10 mM  $Ca^{2+}$ ). C1 became the basis for the design of Twitch-1.

**Supplementary Figure 4.** NMR characterization of calcium loaded tsTnC minimal domain and  $^1\text{H}$ - $^{15}\text{N}$  HSQC spectra used to monitor the  $\text{Ca}^{2+}$  and  $\text{Mg}^{2+}$  binding affinity.



**(a)** Secondary structure elements in dependence of the sequence in tsTnC minimal domain as derived by the Chemical Shift Index (CSI) based on  $\text{C}\beta$  resonance assignments.  $^3\text{J}_{\text{H}_\text{N}\text{H}_\alpha}$  coupling constants are also reported and indicated by filled and open circles for values of  $^3\text{J}_{\text{H}_\text{N}\text{H}_\alpha} < 4.5$  Hz or  $> 8$  Hz, respectively.  $^1\text{H}$ - $^{15}\text{N}$  heteronuclear single quantum correlation (HSQC) spectra of tsTnC minimal domain in Calcium saturated **(b)** and calcium free forms in presence of magnesium **(c)**.

**Supplementary Figure 5.** The structure of the tsTnC minimal domain compared to the C-terminal domain of Chicken TnC.



Protein	Interhelical angles (°) <sup>1</sup>			
	Helix E / Helix F	Helix F / Helix G	Helix G / Helix H	Helix E / Helix H
tsTnC minimal domain <sup>2</sup>	120 ± 4	111 ± 7	132 ± 7	102 ± 5
C domain of Chicken TnC (X-ray) <sup>3</sup>	106	125	113	115
Protein	Interhelical distances (Å) <sup>1</sup>			
	Helix E / Helix F	Helix F / Helix G	Helix G / Helix H	Helix E / Helix H
tsTnC minimal domain <sup>2</sup>	13.7 ± 0.4	10.9 ± 0.9	13.0 ± 0.8	10.3 ± 0.5
C domain of Chicken TnC (X-ray) <sup>3</sup>	15.6	11.3	14.1	10.8

<sup>1</sup>Calculated using the software Interhix written by Kyoko Yap and Mitsuhiro Ikura (University of Toronto).

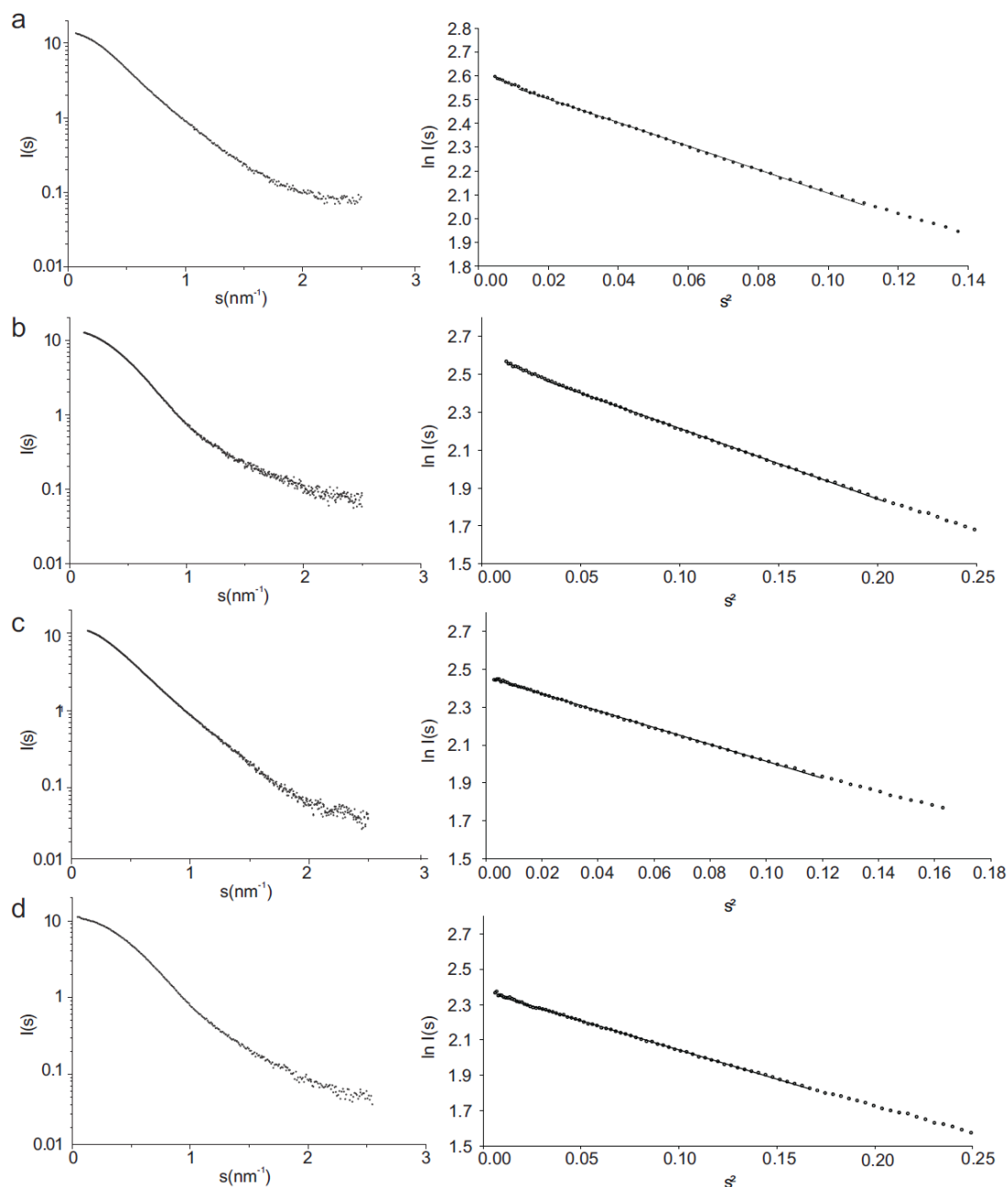
Helices E/F and G/H correspond to the helices forming calcium binding site EF3 and EF4, respectively.

<sup>2</sup>Listed are the mean ± standard error values calculated for twenty structures.

<sup>3</sup>PDB accession code: 1TOP. Helices are defined in the PDB file

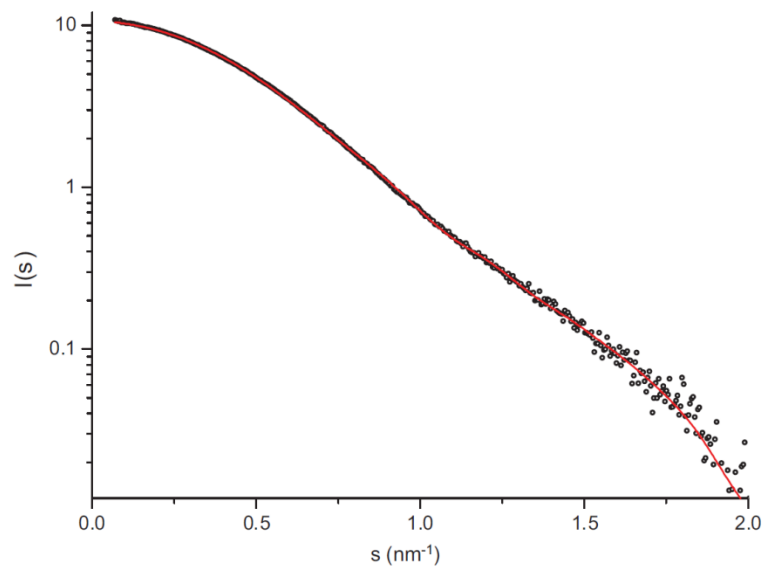
(a)-(b) Comparison of the average NMR structure of tsTnC minimal domain (*blue*) and the C-terminal domain of Chicken TnC (Protein Data Bank ID code: 1TOP) (*gray*) after superposition on the backbone atoms in two different orientations rotated 180° around z axis. (c) Helix-Helix angles and distances for the tsTnC minimal domain and C-terminal lobe domain of Chicken TnC. The two structures adopt a similar fold ( $rmsd_{bb} = 2.9 \text{ \AA}$ ), in which the secondary structure is conserved while the tertiary structure displays significant differences. We quantified the structural dissimilarity by measuring the interhelical angles. As reported in table (C) the minimal domain adopts a conformation in which the slight opening of the calcium binding loops drives the domain closing in a more compact four-helix bundle. Furthermore, the magnitude of the movement of helices F and H is characterized by a change in interhelical distance, resulting in displacements of 5.2 Å for the C-terminal end of helix F (A) and 5.6 Å for the C-terminal end of helix H.

**Supplementary Figure 6.** Measured Small-Angle X-ray Scattering curves of the sensors in absence and presence of calcium.



All curves show the buffer corrected scattering curves (left) and the corresponding Guinier-plot ( $\ln I(s)$  vs.  $s^2$ ) with linear region used for determination of  $R_g$  with  $s \cdot R_g < 1.3$  (right). **(a)** Twitch-0 without calcium,  $R_g=3.84$  nm **(b)** Twitch-0 in presence of calcium,  $R_g=3.35$  nm **(c)** Twitch-1 without calcium,  $R_g=3.65$  nm **(d)** Twitch-1 in presence of calcium,  $R_g=3.14$  nm. The comparison of a and b or c and d, respectively, show a change in shape to a more globular particle upon calcium binding.

**Supplementary Figure 7. SAXS multi-domain modeling.**



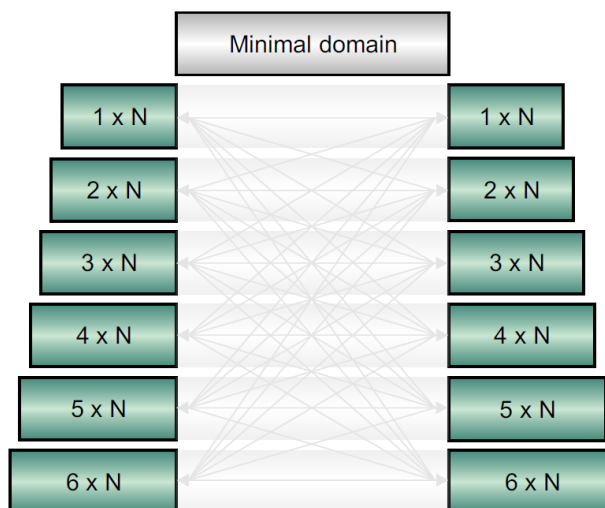
Fit of the modeled structure (see figure 2d in main text) of the calcium bound states of Twitch-1. Multi-domain modeling was performed using CORAL (Petoukhov, M.V. & Svergun, D.I., 2005) with ECFP (pdb code 2WSN), Citrine (pdb code 3DPX) and the structure of the calcium loaded minimal domain (this paper) and the respective scattering curves of calcium bound Twitch-1. To allow structural changes at the connecting termini of the fluorescent proteins induced by calcium binding to the minimal domain a “flexible linker stretch” of up to 5 residues was allowed for CORAL modeling to avoid clashes.

**Supplementary Figure 8.** Diversified indicator libraries generated for screening.

**a**

Helix	EF-hand
L5	<b>K14</b>
F9	<b>G16</b>
F12	<b>N17</b>
E23	<b>G18</b>
I28	<b>F19</b>
<b>V41</b>	<b>I20</b>
I44	<b>D21</b>
F45	<b>R22</b>
S48	<b>D57</b>
F58	
M64	
<b>M65</b>	
V68	

**c**

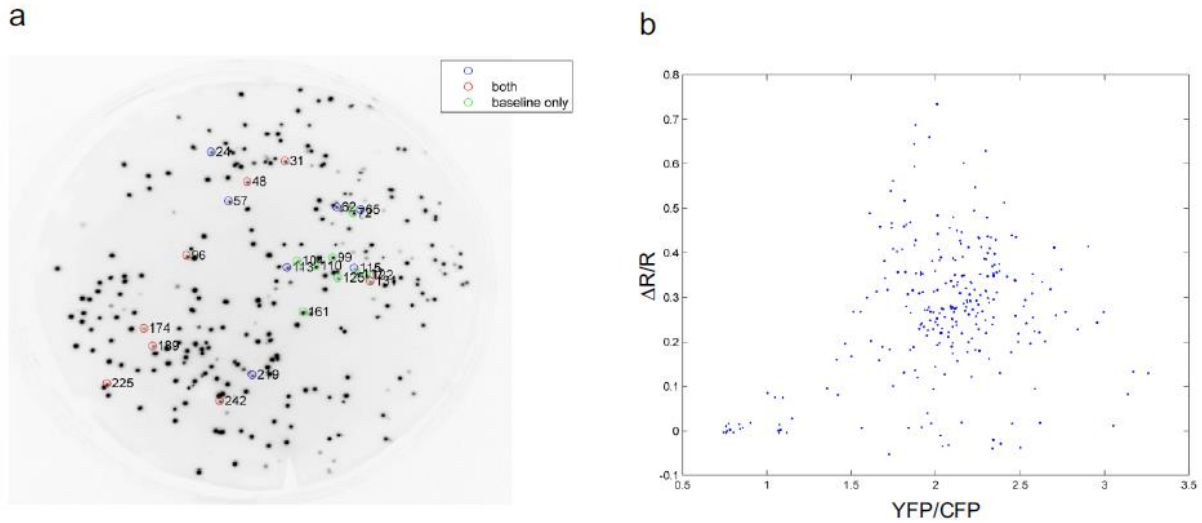


**b**

SEEELSECFRIFDKDGNGFIDREEFGDIIRLTGEQLTDEDVDEIFGSDTDKNGRIDDDEFCLKMENVQ

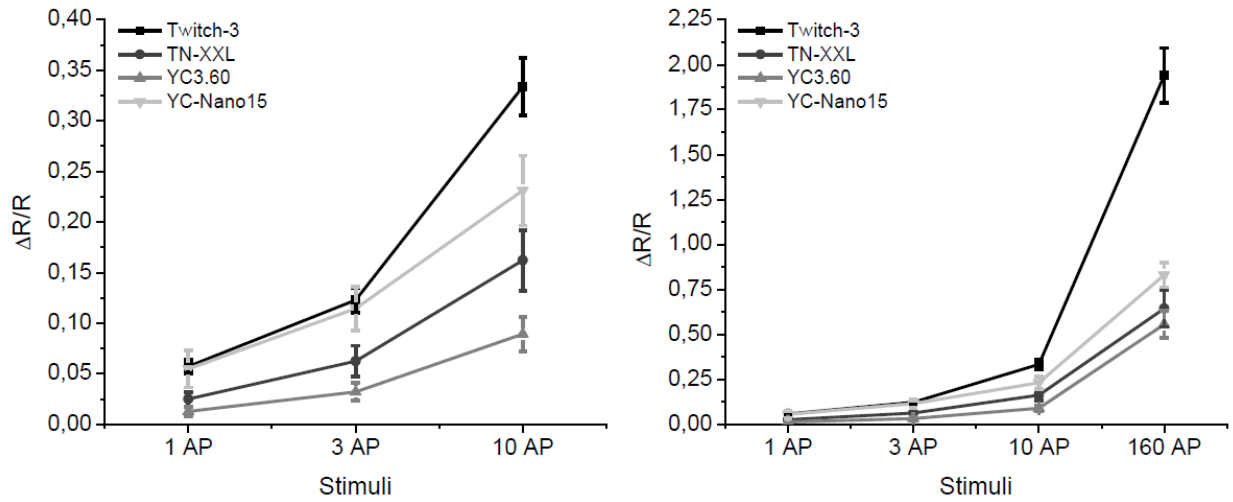
Summary of Twitch libraries based on hotspot mutations within the minimal domain and diversified linkers, as well as combinations hereof. **(a)** Several structural hotspots were identified through close examination of the C-lobe structure (see figure 2 of the main text). Both helix- (grey) and EF-hand (light green) residues were targeted to optimize calcium induced FRET change and calcium affinities. Three key mutation sites, K14, V41 and M65, are shown in large bold fonts, as they had significant effects on overall FRET change. **(b)** Amino acid sequence of the minimal calcium binding domain. K14, V41 and M65 are marked with bold and underscore, helices (grey) and EF-hand mutations (light green). For their localization within the structure see also figure 2 in the main text **(c)** To generate large scale diversified linker libraries, cassettes of 1-6 random linking amino acids were added to the N-terminal and C-terminal end of the minimal calcium binding domain as shown in B and sandwiched between donor and acceptor fluorescent proteins. N = random amino acid residue.

## Supplementary Figure 9. Bacterial plate screening.



Diversified Twitch sensor libraries were transformed into *E. coli* XL1 Blue, plated on Agar plates and screened for basal starting ratio and calcium induced FRET change via CCD camera wide field imaging. **(a)** False color representation of an Agar plate with bacterial colonies each expressing a diversified Twitch sensor variant. Up to 1000 colonies could be separated and imaged on a single Agar plate. Regions of interest were determined automatically and colonies were assigned an ID number. To avoid crowding the image only a few numbered colonies with good performers are shown. Colonies were imaged for basal starting ratio and subsequently after calcium permeabilization, for calcium induced FRET changes. The best variants are highlighted with colored rings and numbers for easy identification. Colonies marked with blue rings show the highest FRET change, green rings indicates mutants with a low starting ratio (YFP/CFP) and red rings constitute a combination between high FRET change and a favorable low starting ratio. Based on these criteria the top 1% fraction of each plate was picked. **(b)** Colony scatter plot of FRET ratio change ( $\Delta R/R$ ) and starting ratio (YFP/CFP) of each colony on the plate. Starting ratios of about 1 and high  $\Delta R/R$  were considered preferable. In this example the colonies with highest  $\Delta R/R$  lie within a starting ratio of 1.5-2.5.

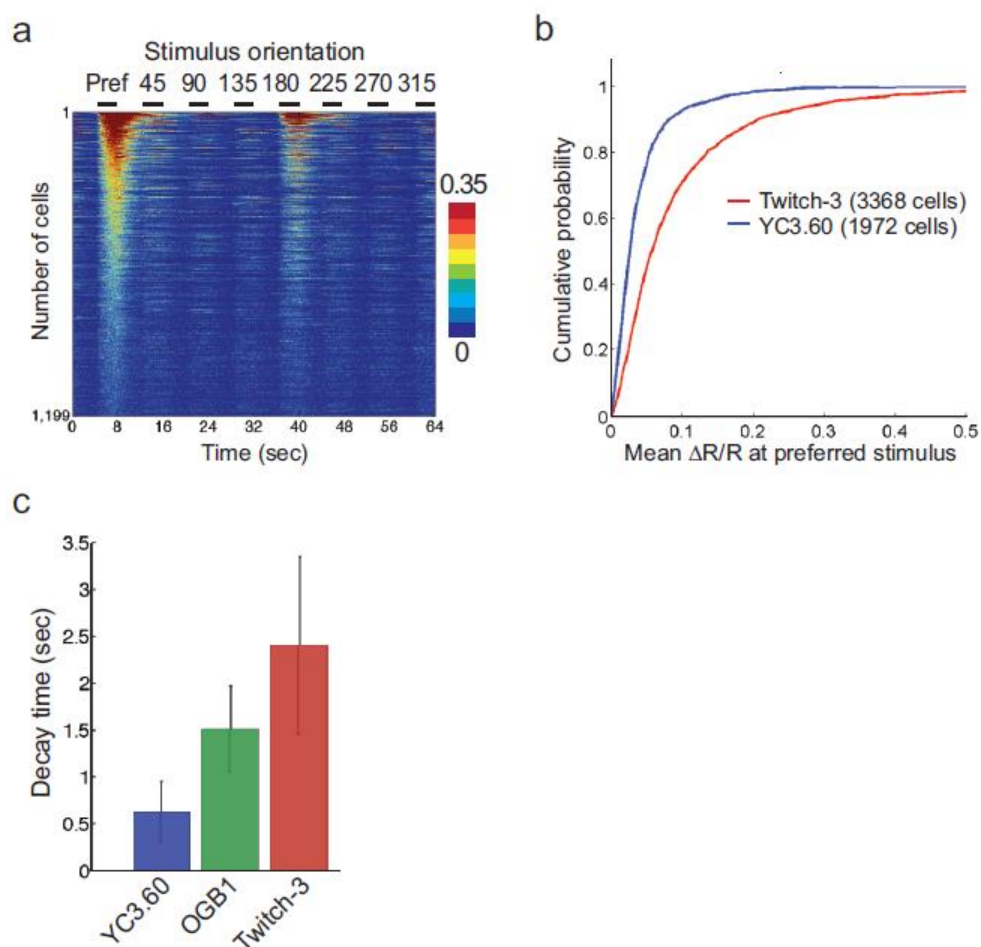
**Supplementary Figure 10.** Comparison of selected FRET calcium sensors in dissociated neurons



Sensor	# wells	# regions of interest	1 AP±SEM	3 AP±SEM	10 AP±SEM	160 AP±SEM
<b>Twitch-3</b>	14	168	5.7±0.7	12.3±1.2	33.4±2.8	194.1±15.2
<b>TN-XXL</b>	26	230	2.5±0.7	6.2±1.5	16.2±3.0	64.4±10.3
<b>YC3.60</b>	23	299	1.3±0.5	3.2±0.9	8.9±1.7	55.6±7.6
<b>YCNano 15</b>	16	253	5.5±1.8	11.4±2.2	23.1±3.5	83.1±6.8

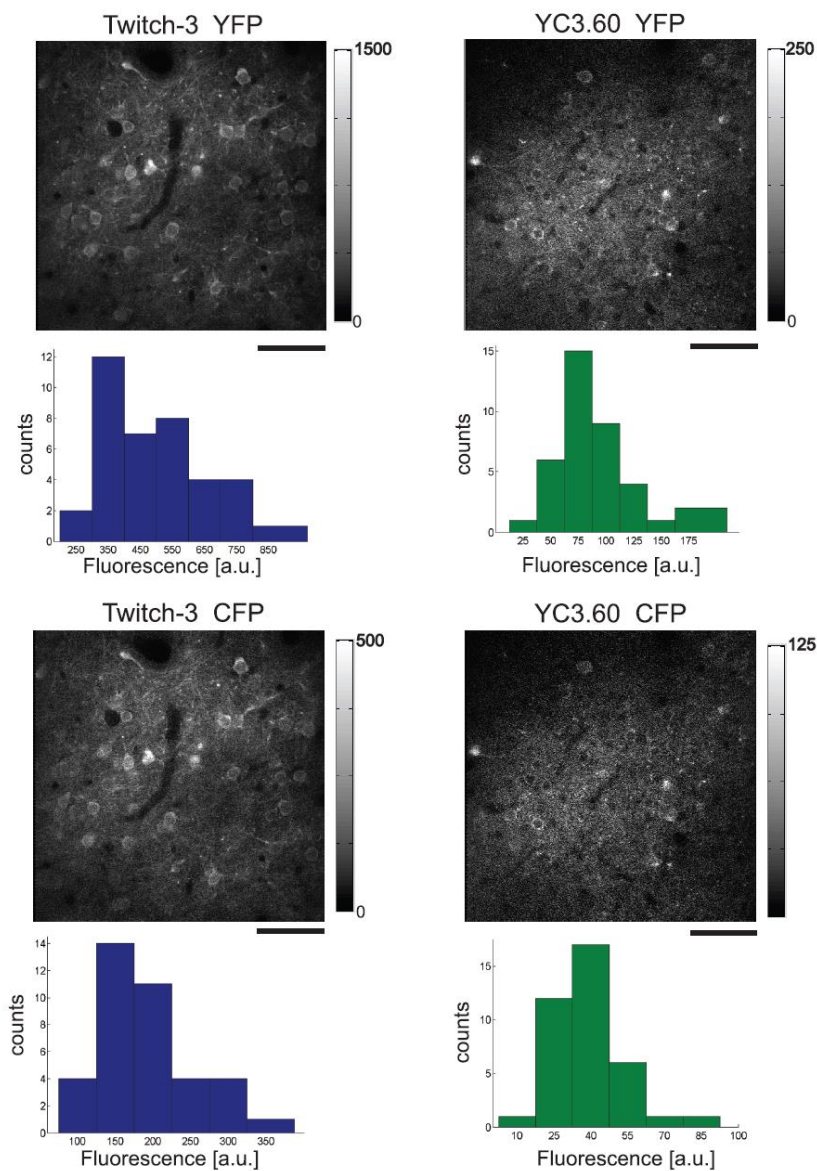
Two Troponin-C-based FRET sensors (TN-XXL, Twitch-3) and two calmodulin-M13-based FRET sensors (YC3.6, YCnano15) were compared under identical conditions. Rat primary hippocampal neuronal cultures in 96-well format were transfected by electroporation (Lonza Primary Cell Nucleofector P3 kit) of DNA constructs (3.2 micrograms). After 16 days in vitro, neurons were stimulated using a custom pair of electrodes, and responses were imaged with an Andor EMCCD camera (iXon 897, 35 fps) as previously described (Wardill et al., 2013, see Online References). Please note, however, that experimental conditions for this figure were not identical to what is described in Online Methods for Fig. 3. Different vector backbones and a different amount of DNA were used for transfection. In addition, one pair of electrodes (custom made, different than the electrodes used in Fig. 3) was used to sequentially stimulate cells in different wells.

**Supplementary Figure 11.** *In vivo* functional imaging of mouse visual cortex using Twitch-3.



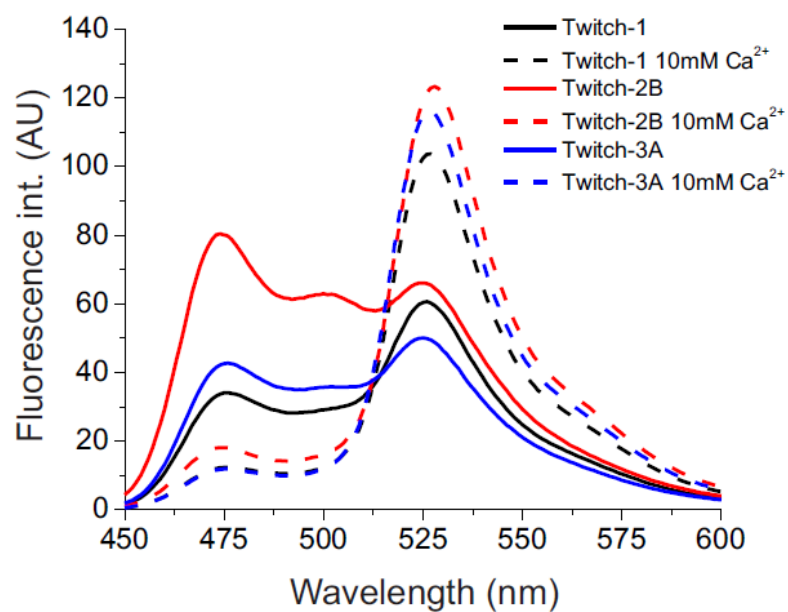
**(a)** Visual responses ( $\Delta R/R_0$ ) of 1199 responsive cells, rank ordered by signal level, to eight orientations aligned in columns starting with the preferred orientation for each cell. Black bars demonstrate when stimuli were presented. **(b)** Cumulative probability distribution of averaged responses to preferred orientation stimulus for Twitch-3 (3368 cells from 6 animals) and YC 3.60 (1972 cells from 5 animals). **(c)** Calculation of half decay time constants for OGB-1, YC 3.60, and Twitch-3. Left panel shows mean and standard deviation of half decay time for the 10% most responsive cells at their preferred orientation.

**Supplementary Figure 12.** Differences in baseline fluorescence between Twitch-3 and YC3.60 in vivo



All images were taken 150 μm under the cortical V1 surface with an average laser power of 10 mW, without any visual stimulus. Histograms show the distribution of the averaged fluorescence signal from cell bodies (n=38). Scale bar, 50 μm. As Twitch-3 was brighter than YC 3.60, average laser power for imaging Twitch-3 could be reduced compared to YC3.6 (20 mW and 45 mW respectively for imaging 150 μm under the brain dura) while maintaining equal brightness.

**Supplementary Figure 13.** Emission spectra of purified “Twitch” variants *in vitro*



Emission spectra of equimolar amounts of purified recombinant Twitch-1 (black), Twitch-2B (blue) and Twitch-3 (red) both at basal conditions (solid lines) and at calcium saturation (dashed lines). Note that the donor brightness is approximately 2 fold higher at resting state in Twitch-2B than in other variants.

**Supplementary Table S1.** NMR structural statistics.

---

**NMR constraints**

Completeness of resonance assignments	
Backbone (%)	99.4
Carbon $\beta$ (%)	100
Residual dipolar couplings ( $^1\text{H}$ - $^{15}\text{N}$ )	62

**Structure precision**

RMSD from mean structure (residues 2-65) (Å)	
All backbone atoms	0.90
All heavy atoms	1.31

**Structure quality**

MOLPROBITY	
Clash score	8.79 $\pm$ 1.87
Poor rotamers (%)	0.32 $\pm$ 0.65
MolProbity score	1.50 $\pm$ 0.13
Residues with bad bonds (%)	0 $\pm$ 0
Residues with bad angles (%)	0 $\pm$ 0
C $\beta$ deviations > 0.25 Å	0 $\pm$ 0
PROCHECK	
G-factors phi-psi/all dihedral angles	0.42 /0.55
Ramachandran plot statistics (%)	
Most favored regions	93.4
Additional allowed regions	6.6
Generously allowed regions	0
Disallowed regions	0

---

**Supplementary Table S2.** SAXS data evaluation.

Construct	Ca <sup>2+</sup>	Concentration mg/ml	Rg (nm)	Dmax (nm)	cpCitrine/CFP <sub>0</sub>	ΔR/R (%)
Twitch-1	+	1.6	3.14	10.56	9.74	400
	-	1.7	3.66	12.8	1.95	
TNXXL	+	0.86	3.33	11.16	3.48	260
	-	0.86	3.85	14.13	0.97	
tsL13	+	1.1	3.62	12.31	2.00	110
	-	1.1	3.66	14.5	0.97	
Twitch-0	+	1.1	3.37	10.86	10.48	130
	-	1.14	3.84	14.16	4.50	
2,1 Pro	+	1.52	3.06	9.71	6.66	230
	-	1.6	3.19	12.24	2.01	
2,2 Pro	+	1.7	3.23	10.38	4.91	290
	-	1.5	3.86	14.4	1.25	

Small angle X-ray scattering data were collected at zero calcium and at calcium saturation for several early Twitch constructs and Twitch-1, Ts-L13 (which harbors the full wild type TnC from *Opsanus tau* truncated at leucine 13), and TN-XXL. The construct 2,1 Pro is a FRET sensor that uses the minimal domain with a two prolines N-terminal linker and a 1 proline C-terminal linker amino acid, while 2,2 Pro uses two prolines on each side as linker amino acids. Rg values have been determined from analysis of the slope of the linear region ( $s \cdot R_g < 1.3$ ) of the guinier plot  $\ln(I)$  vs  $s^2$  using PRIMUS and maximum particle diameter was determined using GNOM as described (see Putnam, C.D., Hammel, M., Hura, G.L., & Tainer, J.A. X-ray solution scattering (SAXS) combined with crystallography and computation: defining accurate macromolecular structures, conformations and assemblies in solution. *Quarterly Reviews of Biophysics* **40**, 191-285 (2007)). cpCitrine/CFP<sub>0</sub> describes the basal acceptor/donor emission ratio at zero calcium. ΔR/R describes the maximal FRET ratio change of each construct from zero calcium to calcium saturation.

**Supplementary Table S3. Properties of selected Twitch sensors.**

High affinity sensors		Cuvette					Hippocampal neurons					
Name	FRET pair	Mutations**	Linkers	YFP/CFP (R <sub>0</sub> )	ΔR/R (%)	Kd (nM)	Decay time (s)	Hill slope "Coefficient"	Maximum ΔR/R @ 160FPs	YFP/CFP (R <sub>0</sub> )	Decay time 10AP (s)	
<b>tsL13</b>	ECFP cpCit174	TsTnC truncated at leucine 13	-	1.00	250	1300	0.15	1.22	-	-	-	
<b>Twitch-1</b>	ECFP cpCit174	M65V	P, P	1.95	400	250	0.80	1.18	80	2.08	1.50	
<b>Twitch-2</b>	ECFP cpCit174	K14F, M65V	DA, PIY	1.20	1000	150	2.80	1.34	209	1.21	1.81	
<b>Twitch-2B</b>	cpCit174 mCerulean3 cpVenus <sup>co</sup>	K14F, M65V	VADA, PIYP	0.80	800	200	2.80	1.31	104	1.53	2.11	
<b>Twitch-2C</b>	mTurquoise2 cpCit174	K14F, M65V	VADA, PIYP	0.80	700	450	2.60	1.31	-	-	-	
<b>Twitch-3</b>	ECFP cpCit174	V41P	DA, PLA	1.30	700	250	1.50	1.42	321	1.30	2.05	
<b>Twitch-3B</b>	ECFP cpVenus <sup>co</sup>	V41P	DA, PLA	1.15	900	150	2.98	1.13	185	1.53	2.55	
Low affinity sensors (Single EF-hand)												
Name	FRET pair	Mutations**	Linkers	YFP/CFP (R <sub>0</sub> )	ΔR/R (%)	Kd (μM)	Decay time (s)	Hill slope "Coefficient"	Maximum ΔR/R @ 160FPs	YFP/CFP (R <sub>0</sub> )	Decay time 10AP (s)	
<b>Twitch-4</b>	ECFP cpCit174	M65V, 54D+*	DA, PIY	1.20	600	2.80	0.50	1.04	100	1.40	0.615	
<b>2N1 390 54S+</b>	ECFP cpCit174	M65V, 54S+*	DA, PIY	1.22	500	2.60	0.45	1.06	90	1.50	0.814	
<b>Twitch-5</b>	ECFP cpCit174	18D+*, M65V	DA, PIY	1.25	550	9.25	0.16	1.37	-	-	-	
<b>2N1 390 18D+ B</b>	mCerulean3 cpVenus <sup>co</sup>	18D+*, M65V	DA, PIY	0.74	320	51.5	0.12	1.06	-	-	-	
<b>2N1 390 54S+ B</b>	mCerulean3 cpVenus <sup>co</sup>	54S+*, M65V	DA, PIY	0.74	330	257.0	0.07	1.06	-	-	-	
<b>Twitch-2B 18D+</b>	mCerulean3 cpVenus <sup>co</sup>	K14F, M65V, 54S+*	DA, PIY	0.80	220	139.0	0.15	1.06	-	-	-	
<b>Twitch-2B 54S+</b>	mCerulean3 cpVenus <sup>co</sup>	K14F, M65V, 54S+*	DA, PIY	0.78	320	174.0	0.07	1.06	-	-	-	

\* Amino acid insertion after the indicated numbered position, \*\* All sensors include the mutations N15D, D17N, N51D and D53N within the minimal domain to reduce Mg<sup>2+</sup>-binding.

# Acknowledgements

First and foremost, I want to thank my supervisor (Doktorvater) Oliver Griesbeck for giving me the opportunity to engulf on this long, interesting and challenging scientific journey. A journey that started back in 2007 with my masters thesis – time passes. Thank you for trusting in me, my work, the project and for trusting in people to get the job done. Thank you for the many great moments at conferences we have attended together, lab meetings and the yearly Griesbeck Christmas celebrations. I guess you can summarize the PhD journey like this: A “*Man in Slow Motion*” “*On the (Scientific) Prowl*” “*Walking on a Razor Blade*” where “*Something’s Missing*” searching for a “*Secret Passage*” to finally reach redemption, feeling like “*Water Falling*”.

I would also like to extend my gratitude to Axel Borst for always being supportive in all matters of life. It was a privilege to have you in my thesis committee and it was a pleasure to work in your department. You always brought great spirit with you.

I also need to thank my lovely colleagues from Se Griesbeck Group! We truly had something special and I cannot thank you enough for all the great times we shared and for the hard times, we pulled each other through. It was no doubt some of the hardest, but best times of my life. Thank you Marco for being my tutor in the art of GECI design. A special thank you to the honorary Smicker-Team and partners in crime Steph aka “Steph der Chef” aka “SMJ – Steph Man Joe”, Anselm aka “Oselm”, Jonny aka “Scottish” aka “Street Buddy” (my beloved Schwabing-Express passenger). A special thank you to my P29 crew, Gayane aka “Mother Russia” and Renate, for keepin’ it cool, now that we could not be part of the P1 dungeon. Gayane, you were a great desk-neighbor for many years! Thank you! I want to thank Martina aka “maRtiNA” for all the scientific support and crazy singing sessions (late nights in the lab). And not least Julia aka “Austria” aka “Julia Bulia” for being the backbone in our absolutely crazy screening sessions. 250,000 *E. coli* colonies do not screen themselves! I also need to thank our two “Lab Moms” Anja and Birgit. Anja, thank you for all the assistance you provided throughout the year. Birgit, thank you for all the help, for sharing the interest in BMWs and for keeping a steady supply of cultured cells.

I also want to thank the GECl-project and the Looger Lab at Janelia Farm Research Campus. Especially Doug for being an extremely efficient and dedicated mentor during my stay at "The Farm". Thank you, Eric, for being my daily support, friend and for making me feel welcome. Also a huge thanks to Jasper for the great times in and outside the lab – especially at your Beer-Brewing-BBQs. Damn we tasted many great and weird things. Thank you to Loren and Karel for great feedback on my work during the lab meetings. I also need to thank Melisa for the help and support during my cloning marathons and for letting me drive your husband's M3.

I also want to thank everyone in the whole Borst Department for contributing to a great, inspiring and fun place to work. Some of you I knew for a short time, others for many years. A special thanks to Mr. Plett, Jones, for supporting me during my masters project, for sharing whisky and for sharing an interest in hifi and random nonsense youtube clips.

I want to thank my friends and family back in Denmark for always being there, even though I have been abroad many years. I love you all very much. It is not always easy to be away from home – and away from you guys. I appreciate your support.

Finally, I want to thank my "CimCim" Ilcim for supporting me and giving me space and time to write my thesis. For always motivating me and keeping the spirit high for me. Muah!

I could probably thank more people, so in case I left you out; I thank you too.

# Curriculum Vitae

## Personal Data

Name Thomas Michael Thestrup  
Date, place of birth 07.11.1981, New Jersey, USA  
Nationality Danish, USA  
Profession Associate, Sunstone Life Science Ventures, Copenhagen, Denmark

## Education

01/2009 – **PhD student**, Max Planck Institute of Neurobiology, Martinsried, Germany  
Thesis: *Evolutionary Engineering of Green Fluorescent Protein Calcium Biosensors.*

09/2006 – 11/2008 **Master of Science (MSc) - Biology and Biotechnology**  
University of Copenhagen, Denmark

09/2002 – 09/2006 **Bachelor of Science (BSc) - Biology**  
University of Copenhagen, Denmark

08/1997 – 07/2000 **Studentereksamen (Upper Secondary Education)**  
Helsingør Gymnasium, Denmark

## Publications

**Biophys. Journal.** 2012: Geiger A, Russo L, Gensch T, **Thestrup T**, Becker S, Hopfner KP, Griesinger C, Witte G, Griesbeck O. *Correlating calcium binding, FRET and conformational change in the biosensor TN-XXL*

**Nature Medicine**, May 2013: Mues M, Bartholomäus I, **Thestrup T**, Griesbeck O, Wekerle H, Kawakami N, Krishnamoorthy G. *Real-time in vivo analysis of T cell activation in the central nervous system using a genetically encoded calcium indicator*

**Nature Methods**, Jan. 2014: **Thestrup T**, Litzlbauer J, Geiger A, Mues M, Bartholomäus I, Russo L, Griesinger C, Witte G, Chen TW, Kim D, Griesbeck O. *Optimized ratiometric calcium sensors for functional in vivo imaging of neurons and T lymphocytes*

**Optical Probes in Biology**, Jan., 2015: **Thestrup T** and Griesbeck O. *Protein-Based Calcium Sensors*

**Nature Communications**, Feb., 2015: Y. Kovalchuk, R. Homma, Y. Liang, A. Maslyukov, M. Hermes, **T. Thestrup**, O. Griesbeck, Y. Ninkovic, L. B. Cohen and O. Garaschuk. *In vivo odorant response properties of migrating adult-born neurons in the mouse olfactory bulb*

**PLOS ONE**, 2015 (Jun. 2015): Litzlbauer J, Schifferer M, Ng D, Fabritius A, **Thestrup T**, Griesbeck O. *Large Scale Bacterial Colony Screening of Diversified FRET Biosensors*

**Cell** (Submitted, Dec. 2016): Schnaitmann C, Haikala V, Abraham E, Oberhauser V, **Thestrup T**, Griesbeck O and Reiff DF. *Colour opponent processing in Drosophila inner photoreceptor terminals*

**Science Advances** (Submitted, Jun. 2016): Mourino PT, Paulat M, **Thestrup T**, Griesbeck O, Griesinger C & Becker S. *The Structural base for FRET in a green fluorescent protein biosensor*